

Electromagnetic methods for imaging subsurface injections

by

Lindsey J. Heagy

B.Sc. Geophysics, University of Alberta, 2012

A THESIS SUBMITTED IN PARTIAL FULFILLMENT
OF THE REQUIREMENTS FOR THE DEGREE OF

Doctor of Philosophy

in

THE FACULTY OF SCIENCE
(Earth, Ocean and Atmospheric Sciences)

The University of British Columbia
(Vancouver)

September 2018

© Lindsey J. Heagy, 2018

The following individuals certify that they have read, and recommend to the Faculty of Graduate and Postdoctoral Studies for acceptance, the thesis entitled:

Electromagnetic methods for imaging subsurface injections

submitted by **Lindsey J. Heagy** in partial fulfillment of the requirements for the degree of **Doctor of Philosophy in Earth, Ocean and Atmospheric Sciences**.

Examining Committee:

Douglas W. Oldenburg, Earth, Ocean and Atmospheric Sciences
Supervisor

Eldad Haber, Earth, Ocean and Atmospheric Sciences
Supervisory Committee Member

Michael Bostock, Earth, Ocean and Atmospheric Sciences
Supervisory Committee Member

Roger Beckie, Earth, Ocean and Atmospheric Sciences
University Examiner

Ian Mitchell, Computing Science
University Examiner

Abstract

The extraction of hydrocarbons from low-permeability formations is commonly achieved through hydraulic fracturing. In a hydraulic fracturing operation, fluid and particles, called proppant (commonly sand) are injected to create fracture pathways and to keep those pathways open so that hydrocarbons can flow from the reservoir to the wellbore. One of the key unknowns in hydraulic fracturing operations is the distribution and extent of proppant within the reservoir. If the electrical conductivity of the injected materials is distinct from the host rock, then electromagnetic geophysical methods can be used. In order for electromagnetics to be a viable imaging technique for this application, we must be able to: (a) collect data that are sensitive to the injected materials, and (b) have a method for estimating a representative model of the injected materials from those data through an inversion process. Numerical modelling is an essential tool for assessing feasibility of electromagnetics and for developing a suitable inversion procedure for extracting meaningful information from the collected data.

A complicating factor of using electromagnetics in reservoir settings is that steel-cased wells are commonly present. Steel has vastly different electrical and magnetic properties than the surrounding rock and therefore significantly alters the behavior of electromagnetic fields and fluxes. The success of electromagnetic methods for imaging subsurface injections, therefore, heavily relies on our ability to understand and simulate

the physical behavior of fields and fluxes in these settings.

Using hydraulic fracturing as a motivating application, this thesis examines aspects of both the imaging problem for subsurface injections as well as the fundamental behavior of electromagnetic fields and fluxes in settings with steel-cased wells. I present a strategy for estimating the electrical conductivity of a fractured volume of rock and incorporate this into the inverse problem. I also develop a numerical approach for accurately simulating electromagnetic surveys in settings with steel-cased wells. Using this software, I examine aspects of the fundamental physics, including how the magnetic properties of a pipe complicate the behavior of the fields and fluxes, and how this impacts measured data.

All of the software developed during the course of this research is open-source.

Revision: November 14, 2018

Lay Summary

Hydraulic fracturing is used for producing hydrocarbons from low-permeability reservoirs. Fluid and proppant (commonly sand) are injected to create fractures and to keep those fracture pathways open. One of the unknowns in this process is the distribution of the injected materials. If the electrical conductivity of the injected materials is distinct from the reservoir rock, electromagnetic geophysical data, which are sensitive to the distribution of those materials, can be collected. Through an inversion process, a 3D model of the injected materials can be estimated from those data. The presence of steel-cased wells complicates this procedure because steel has vastly different electrical and magnetic properties than the reservoir rock. As a result, it significantly alters the behavior of the electromagnetic fields. This thesis examines aspects of the fundamental physics of electromagnetics in settings with steel-cased wells and as well as strategies for estimating the distribution of injected materials from electromagnetic data.

Preface

The research I conducted for this dissertation was completed at the Geophysical Inversion Facility at the University of British Columbia under the supervision of Dr. Douglas Oldenburg. During my time as a PhD student, I also completed two internships, the first with the Schlumberger Electromagnetics Imaging group, under the advisement of Dr. Michael Wilt, and the second at Schlumberger Doll Research, under Dr. Dzevat Omeragic. These internships informed my understanding of hydraulic fracturing and industry practices for electromagnetic imaging. The research presented in this thesis has resulted in three peer-reviewed publications, seven conference proceedings and several auxiliary works.

Chapter 2 presents an approach for constructing a physical property model of a fractured volume of rock. Dr. Wilt had the initial idea to use effective medium theory to estimate the coarse-scale conductivity of a fractured volume of rock. I developed the two-step workflow, the algorithm used to solve for effective conductivity, and performed all numerical simulations in this chapter. Dr. Oldenburg advised on all of these developments. Earlier versions of this work were presented at three conferences (Heagy and Oldenburg, 2013; Heagy et al., 2014a; Wilt et al., 2014) and included in the patent Wilt et al. (2015).

Chapter 3 discusses a finite volume approach for simulating Maxwell's equations on

cylindrical meshes. This work has been submitted to *Computers and Geosciences* and is available on arXiv (Heagy and Oldenburg, 2018). Preliminary versions of this work were included in two conference abstracts (Heagy et al., 2015, 2017b). I implemented the software within the SimPEG framework and the code-review was conducted by Dr. Rowan Cockett. Dr. Oldenburg advised on the software development, testing, and content of the chapter. I performed the numerical simulations that comprise the examples in this chapter. Much of the numerical work in this chapter is supported by course material and instruction from Dr. Eldad Haber and Dr. Uri Ascher (Haber, 2014a; Ascher, 2008).

Chapter 4 discusses aspects of the fundamental physics of DC resistivity with steel-cased wells and demonstrates survey design considerations. This work was submitted to *Geophysical Journal International* for peer review. I conducted all of the numerical experiments in this chapter with advisement from Dr. Oldenburg. The application of DC resistivity to the casing integrity problem was prompted by conversations with Dr. Wilt.

Chapters 5 explores the physics of electromagnetics in settings with steel-cased wells. I conducted all of the experiments in this chapter with advisement from Dr. Oldenburg. Earlier versions of this work were included in (Heagy et al., 2015, 2017b).

Chapter 6 discusses the inverse problem for imaging a fractured volume of rock. I developed the idea of using effective medium theory in the inversion, implemented the necessary software components and performed the numerical experiments in this chapter, all with advisement from Dr. Oldenburg. An early version of the idea of using effective medium theory to invert for fracture concentration was presented in a conference publication (Heagy et al., 2014b). Dr. Cockett contributed to the development of examples in the conference publication.

Appendix B and Appendix C contain details relevant to Chapters 2 and 6. I per-

formed both derivations with advisement from Dr. Oldenburg. The derivation in B was inspired by a question from Dr. Frank Morrison.

Appendix D describes the SimPEG electromagnetics module which is the backbone for the numerical experiments conducted in this thesis. This work was published in *Computers & Geosciences* (Heagy et al., 2017a) and was conducted collaboratively with Dr. Cockett, Dr. Seogi Kang, and Mr. Gudni Rosenkjaer with advisement from Dr. Oldenburg. I led the development and implementation of the forward-simulation framework as well as the drafting of the manuscript. Dr. Kang performed the inversion of the Bookpurnong data as described in Section D.5.2. All authors contributed edits to the text.

Appendix E provides an overview of the GeoSci.xyz project (<https://geosci.xyz>) which is a collaborative effort to develop educational resources for the geosciences. This effort has been led by myself, Dr. Oldenburg, Dr. Kang, and Dr. Cockett, and has benefitted from a community of contributors. Notably, Mr. Dominique Fournier, Mr. Devin Cowan, Mr. Thibaut Astic, Dr. Sarah Devriese, Mr. Michael Mitchell, and Dr. Dianne Mitchenson, have invested significant efforts in contributing content.

Software development has been a critical part of this work. In particular, the research conducted in this thesis builds upon and contributes to the open-source SimPEG ecosystem, described in Cockett et al. (2015), of which I am a co-author. Excerpts of the background information on inversion in Section 1.5 are adapted from Cockett et al. (2015). My personal contribution to SimPEG exceeds 100,000 lines of code. In addition, I help maintain SimPEG and lead community development efforts by responding to code-usage questions and conducting code-reviews. The research in this thesis benefits from the efforts of all of those who are involved in the SimPEG community. Notably, Dr. Cockett and Dr. Kang have made substantial contributions to the architecture and

functionality of SimPEG that have been used to conduct the research in this thesis; they have also reviewed and provided input on much of the code that I have written.

The research in this thesis makes use of tools in the scientific Python ecosystem including Jupyter, Numpy, SciPy, and Matplotlib (Perez et al., 2015; van der Walt et al., 2011; Jones et al., 2001; Hunter, 2007) and relies upon the global community of contributors who develop and maintain these open-source resources.

Table of Contents

Abstract	iii
Lay Summary	v
Preface	vi
Table of Contents	x
List of Tables	xvi
List of Figures	xvii
Acknowledgments	lii
Dedication	liv
1 Introduction	1
1.1 Hydraulic Fracturing	2
1.2 Challenges to electromagnetics with steel-cased boreholes	7
1.3 Research motivation and thesis structure	12
1.3.1 Homogenization strategy for hydraulic fractures	13
1.3.2 Steel casings	14

1.3.3	Inversions for subsurface injections	16
1.3.4	Appendices	16
1.3.5	A note on reproducibility and dissemination	17
1.4	Background: Electromagnetic geophysics	18
1.4.1	Governing equations	18
1.4.2	Geophysical surveys	21
1.5	Background: Geophysical Inversions	24
1.5.1	Formulating and solving the inverse problem	25
2	A physical property model for a fractured volume of rock	31
2.1	Introduction	31
2.1.1	Proppant selection	32
2.1.2	Numerical Modelling	33
2.1.3	Chapter overview	35
2.2	Homogenization workflow using effective medium theory	36
2.2.1	Summary of self-consistent effective medium theory	37
2.2.2	Step 1: Effective conductivity of a proppant-fluid mixture	42
2.2.3	Step 2: Effective conductivity of fractured volume of rock	47
2.2.4	Summary	54
2.3	Feasibility of EM for detecting fractures	54
2.4	Conclusion	61
3	Modelling electromagnetics on cylindrical meshes	63
3.1	Numerical tools	66
3.1.1	Discretization	68
3.1.2	Validation	73

3.2	Numerical Examples	76
3.2.1	DC Resistivity Part 1: Electric fields, currents and charges in a long well	77
3.2.2	DC Resistivity Part 2: Finite Length Wells	80
3.2.3	Frequency Domain Electromagnetics Part 1: Comparison with scale model results	83
3.2.4	Frequency Domain Electromagnetics Part 2: Conductivity and permeability in the inductive response of a well	89
3.3	Summary and Outlook	94
4	Direct current resistivity with steel-cased wells	97
4.1	Introduction	97
4.2	DC resistivity for casing integrity	100
4.2.1	Basic experiment	101
4.2.2	Survey design considerations	106
4.2.3	Factors influencing detectability	108
4.2.4	Summary	118
4.3	Survey design for exciting targets at depth	120
4.3.1	Source location	121
4.3.2	Target properties	125
4.4	Coarse-scale approximations of the well	141
4.4.1	Replacing a hollow-cased well with a solid cylinder	142
4.4.2	Cartesian grid	146
4.5	Conclusion	150
5	Electromagnetics with steel cased wells	153

5.1	Introduction	153
5.2	EM response of a conductive casing	156
5.2.1	Data	160
5.2.2	Discussion	167
5.3	EM response of permeable casings	168
5.3.1	Data	172
5.3.2	Down-hole source	173
5.3.3	Discussion	174
5.4	Approximations to a steel cased well	179
5.4.1	Electrical conductivity	179
5.4.2	Magnetic permeability	185
5.5	Conclusions	190
6	An inversion approach for subsurface injections	193
6.1	Introduction	193
6.2	Choosing an inversion model	196
6.3	Inversions with steel-cased wells	203
6.3.1	Voxel inversion for conductivity	205
6.3.2	Parametric Inversion	210
6.3.3	Inversion for fracture concentration	216
6.3.4	Adding a-priori volume information	223
6.4	Conclusions	224
7	Conclusions and outlook	227
Bibliography		235

A	Source code	246
B	Concentric spheres in a uniform electrostatic field	248
B.1	Setup	248
B.2	Solving for the Potential	250
B.2.1	Solving for the coefficients	251
B.2.2	Sanity Checks	263
B.3	Effective Conductivity Expression	269
C	Self consistent effective medium theory derivatives	272
D	A framework for simulation and inversion in electromagnetics	275
D.1	Introduction	275
D.2	Background	279
D.2.1	Governing Equations	282
D.3	Motivation	284
D.4	Simulation Framework	285
D.4.1	Model and Physical Properties	291
D.4.2	Physics	293
D.4.3	Sources	297
D.4.4	Fields	299
D.4.5	Receivers	300
D.4.6	Summary	300
D.5	Examples	301
D.5.1	Cylindrically Symmetric Inversions	302
D.5.2	Bookpurnong Field Example	305
D.5.3	Steel-Cased Well: Sensitivity Analysis for a Parametric Model .	312

D.6 Conclusion	324
E Open source practices for education	326
E.1 Introduction	326
E.2 GeoSci.xyz Textbooks	329
E.3 Interactive content	331
E.4 Open development	334
E.5 Conclusions and outlook	336

List of Tables

Table 4.1	Integrated secondary charge over a target adjacent to the casing, as shown in Figure 4.14.	128
Table 4.2	Integrated secondary charge over a target that is not electrically connected to the casing, as shown in Figure 4.17.	134
Table D.1	Comparison of the maximum amplitude of the sensitivity with respect to each model parameter, and the approximate perturbation in that parameter required to produce a 10^{-9} V/m change in the measured data. The conversion from a perturbation in log-conductivity to conductivity is given by equation D.26. The perturbation in conductivity is also provided in terms of a percentage of the true model conductivity.	325

List of Figures

Figure 1.1 Conventional reservoirs contain oil and gas that have migrated upwards under pressure until they are trapped by a cap rock (left), while non-conventional tight or shale oil and gas reservoirs contain hydrocarbons that are trapped in low permeability formations (right).	4
Figure 1.2 The choice of whether to solve the EM equations in the time-domain (TDEM) or the frequency domain (FDEM) depends upon the transmitter waveform; a step-off-type waveform (left) lends itself to a solution approach in the time domain and a harmonic signal (right) is typically addressed in the frequency domain.	22
Figure 1.3 Time-domain inductive source experiment. (Left) a steady-state current is passed through the transmitter loop, generating a primary magnetic field. (Right) This current is shut-off, causing a change in magnetic flux. The changing magnetic flux induces secondary currents in conductors, which in turn create secondary magnetic fields that can be measured at receivers above, on, or within the earth. . .	22

Figure 1.4	(Left) Direct current resistivity experiment in which a steady-state current is injected into the earth, and (Right) a grounded source electromagnetic experiment which uses a time-varying source current.	23
Figure 1.5	Overview of a geophysical inversion workflow. Adapted from Cockett et al. (2015).	25
Figure 2.1	Fracture complexity, from simple planar fractures on the left to complex fracture networks on the right. The blue dot is the injection point in a horizontal well. After Cipolla et al. (2008a).	34
Figure 2.2	Constructing a physical property model for a fractured volume of rock using effective medium theory. The electrical conductivity of the proppant fluid mixture is given by σ_2 , the conductivity of the background reservoir rock by σ_1 . Using effective medium theory, the coarse-scale anisotropic conductivity, Σ^* describing the fractured volume of rock is computed.	38
Figure 2.3	Effective conductivity of a proppant-fluid mixture for five different proppant conductivities, each indicated in the legend. Panel (a) shows the conductivity on a linear scale, and panel (b) uses a log-scale. The conductivity of the fluid is 3 S/m, similar to the conductivity of sea-water.	43
Figure 2.4	Impact of the conductivity of the fluid on the effective conductivity of a proppant-fluid mixture. Panels (a) and (c) show the effective conductivity for mixtures with a 10^3 S/m proppant and panels (b) and (d) show the effective conductivity for mixtures with a 10^4 S/m proppant. The conductivity of the fluid is indicated by the legend.	44

Figure 2.5 Effective conductivity of a 3-phase proppant-fluid mixture consisting of resistive proppant (10^{-6} S/m), conductive proppant (10^5 S/m) and saline fluid (3 S/m). The legend indicates the percentage of conductive proppant in the proppant mixture and the x-axis is the volume fraction of proppant in the proppant-fluid mixture.	46
Figure 2.6 Effective conductivity of a 3-phase proppant-fluid mixture consisting of resistive proppant (10^{-6} S/m), conductive proppant (10^5 S/m) and saline fluid (3 S/m). The proppant mixture contains 25% conductive proppant and 75% resistive proppant. The legend indicates the aspect ratio of the elongated conductive proppant filler (prolate spheroids).	47
Figure 2.7 Oblate spheroid with normal along the x -axis. The y and z semi-axes are equal, and aspect ratio is $\alpha = b/a < 1$	49
Figure 2.8 Effective, anisotropic conductivity for a fractured rock with spheroidal cracks whose normal is oriented along the x -axis for five different aspect ratios, indicated by the legend. The black dashed lines show the upper and lower Wiener Bounds, which are identical to the volume-weighted arithmetic and harmonic averages of the conductivity of the rock (0.1 S/m) and proppant-fluid mixture (2500 S/m). The black dash-dot lines are the anisotropic Hashin-Shtrikman upper and lower bounds computed using an aspect ratio of 10^{-5} in equation 2.12. Panels (a) and (c) show the full range $0 \leq \varphi \leq 1$, and panels (b) and (d) zoom in to $0 \leq \varphi \leq 0.005$. Note that in (b), any curve that deviates from the lower bound is the $\sigma_{y,z}$ component; all σ_x values lie on the lower bound for the concentration range shown.	51

Figure 2.9 Effective, isotropic conductivity for a fractured rock with randomly oriented spheroidal cracks for five different aspect ratios, indicated by the legend. The black dashed lines show the upper and lower Wiener Bounds, which are identical the volume-weighted arithmetic and harmonic averages of the conductivity of the rock (0.1 S/m) and proppant-fluid mixture (2500 S/m).The black dash-dot lines are the isotropic Hashin-Shtrikman upper and lower bounds. The semi-transparent dotted lines show $\sigma_{y,z}$ from Figure 2.8 Panels (a) and (c) shows the full range $0 \leq \varphi \leq 1$, and panels (b) and (d) zooms in to $0 \leq \varphi \leq 0.01$ 53

Figure 2.10 Setup for the crosswell electromagnetic simulation. Ten fractures, each with 3 mm thickness and 50 m radius are spaced over a 10 m interval along the injection well. The dipole transmitter is positioned inside of the injection well and oriented along the x-axis. Receivers are located in an offset well and measure the real and imaginary parts of the x-component of the magnetic field. 56

Figure 2.11 Simulated secondary magnetic field data for: (a) the anisotropic fracture model and (b) the isotropic fracture model, in a crosswell survey conducted at 100Hz. The top row shows the real component and the bottom row shows the imaginary component of the measured magnetic flux (nT). In all plots, the x-axis shows the transmitter location relative to the center of the fracture, the y-axis shows the receiver location, and the color indicates the secondary magnetic flux with respect to a 0.1 S/m whole-space. Values beneath the noise floor of 10^{-4} nT have been masked and display as white. To display the signal as a percentage of the primary, we have included a semi-transparent overlay between 0% and 5%; low percentage values plot as darker greys.	59
Figure 2.12 Simulated secondary magnetic field data for: (a) the anisotropic fracture model and (b) the isotropic fracture model, in a crosswell survey conducted at 200Hz. The top row shows the real component and the bottom row shows the imaginary component of the measured magnetic flux (nT), similar to Figure 2.11	60
Figure 3.1 Anatomy of a finite volume cell in a (a) cartesian, rectangular mesh, (b) cylindrically symmetric mesh, and (c) a three dimensional cylindrical mesh.	68
Figure 3.2 Construction of a 3D cylindrical mesh from a cartesian mesh.	72

Figure 3.3 Depth slice (left) and cross section (right) through the 3D cylindrical mesh used for the comparison with Commer et al. (2015). The source and receivers are positioned along the $\theta = 90^\circ$ line. The mesh extends 3600 m radially and 3300 m vertically to ensure that the fields have sufficiently decayed before reaching the boundaries.	75
Figure 3.4 Time domain EM response comparison with (Commer et al., 2015). Each of the different line colors is associated with a different location; offsets are with respect to the location of the well.	76
Figure 3.5 (a) Total charge density, (b) secondary charge density, (c) electric field, and (d) current density in a section of the pipe near the source at $z = -500$ m.	78
Figure 3.6 (a) Current along a well for 5 different wellbore lengths. The x-axis is depth normalized by the length of the well. The black dashed line shows the short-well approximation (equation 45 in Kaufman and Wightman (1993)) for a 200 m long well. The black dash-dot line shows the long-well approximation (equation 53 in Kaufman and Wightman (1993)) for a 4000 m well. (b) Charge per unit length along the well for 5 different wellbore lengths.	81
Figure 3.7 Field strength ratio (FSR), the ratio of the measured vertical magnetic field with the free space magnetic field, as a function of frequency for two different receiver locations. In (a), the receiver is in the same plane as the source, in (b), the receiver is 1.49 m offset from the source.	85

Figure 3.8 Magnetic flux density at 0.1 Hz in the region of the pipe near the plane of the source for (a) the “infinite” pipe, where the source is located at -4.5 m and the pipe extends from 0 m to -9 m, (b) a “semi-infinite” pipe, where the source is located at 0 m and the pipe extends to -9 m. In (c), we zoom in to the top 5 cm of the “semi-infinite” pipe, and (d) shows the 5 cm at the top-end of the “infinite” pipe. . .	88
Figure 3.9 Field strength ratio, FSR, for a receiver positioned 3 cm beneath the plane of the source. For comparison, we have plotted the FSR for the permeable pipe when the source and receiver lie in the same plane ($L=0.00$ m) with the semi-transparent orange lines. Note that the infinite-pipe solutions for $L=0.03$ m and $L=0.00$ m overlap. . . .	89
Figure 3.10 Normalized secondary field, NSF, as a function of frequency for two wells. The NSF is the ratio of the secondary vertical magnetic field with the primary magnetic field at the receiver location ($z=-500$ m); the primary is defined as the whole-space primary.	92
Figure 3.11 Secondary magnetic flux density (with respect to a whole-space primary) at five different frequencies for a conductive pipe (top row) and for a conductive, permeable pipe (bottom row).	93
Figure 3.12 Normalized secondary field (NSF) through time. In the time-domain, we compute the NSF by taking the difference between the total magnetic flux at the receiver and the whole-space response and then taking the ratio with the whole-space magnetic flux prior to shutting off the transmitter. .	94

Figure 3.13 Secondary magnetic flux density for a conductive well (top row) and a conductive, permeable well (bottom row) through time. The source waveform is a step-off waveform.	95
Figure 4.1 Cross section showing: (a) electrical conductivity, (b) current density, (c) charge density, and (d) electric field for a top-casing DC resistivity experiment over (top) an intact 1000 m long well and (bottom) a 1000 m long well with a 10 m flaw at 500 m depth. . . .	102
Figure 4.2 (a) Charge along the length of the intact well (black), a 500 m well (“short”, grey dash-dot), and a well with a 10 m flaw at 500 m depth (blue), in a top-casing DC resistivity experiment. (b) Secondary electric field due on the surface of the earth due to the flaw in the casing. The primary is defined as the electric field due to the 1000 m long intact well. The return electrode is 2000 m away from the well.	104
Figure 4.3 Charge along the length of a 50 m long intact well (black), a 25 m well (“short”, grey dash-dot), and four wells, each with a flaw starting at 25 m depth and extending the length indicated by the legend (5×10^{-1} m (blue), 5×10^{-2} m (orange), and 5×10^{-3} m (green)) in a top-casing DC resistivity experiment. For reference, the diameter of the casing is 10^{-1} m and its thickness is 10^{-2} m. The return electrode is 50 m away from the well and a cylindrically symmetric mesh was used in the simulation.	105

Figure 4.4 (Top row) primary electric field, (second row) secondary electric field, and (third row) secondary electric field as a percentage of the primary radial electric field for a return electrode that is offset (a) 2000 m, (b) 750 m, (c) 500 m, and (d) 250 m from the well. The primary is defined as the response due to the 1000 m long, intact well. Electrode locations are denoted by the red dots. In the third row, the colorbar has been limited between 20% and 100%. The fourth and fifth rows show radial electric field data collected along the $\theta = 90^\circ$ azimuth (white dotted lines in the top three rows). The fourth row shows the primary (black line), the total electric field due to the flawed well (blue line), and the secondary radial electric field (orange line). The fifth row shows the secondary as a percentage of the primary. 107

Figure 4.5 Radial electric field as the depth of the flaw along a 1km long well is varied. The positive electrode is connected to the top of the casing, the negative electrode is positioned 500m away and data are measured along a line 90° from the source electrodes. In (a), we show the total electric field for four flawed wells, each with a 10m flaw at the depth indicated on the legend. The black line shows the radial electric field due to an intact well; we define this as the primary. In (b), the secondary radial electric field is plotted and in (c), we show the secondary radial electric field as a percentage of the primary. . . 110

- Figure 4.6 Radial electric field as the conductivity of the background is varied for a 1 km well with a 10 m flaw at 500 m depth. The positive electrode is connected to the top of the casing, the negative electrode is positioned 500 m away and data are measured along a line 90° from the source electrodes. In (a), we show the total electric field for five different background conductivities, each indicated on the legend. The solid lines indicate the response of the flawed well and the dashed lines indicate the response of the intact well (the primary). In (b), the secondary radial electric field is plotted and in (c), we show the secondary radial electric field as a percentage of the primary. 112
- Figure 4.7 Radial electric field as the conductivity of a 50 m thick layer positioned at 400 m depth is varied. The positive electrode is connected to the top of the casing, the negative electrode is positioned 500 m away and data are measured along a line 90° from the source electrodes. In (a), we show the total electric field five different layer conductivities. The black line shows the scenario where the layer has the same conductivity as the background. The dashed-lines indicate the intact well and the solid lines indicate the flawed well. In (b), the secondary radial electric field is plotted (with respect to an intact well primary) and in (c), we show the secondary radial electric field as a percentage of the primary. 113

Figure 4.8 Cross section showing: (a) electrical conductivity, (b) current density, (c) charge density, and (d) electric field for a top-casing DC resistivity experiment over models with a conductive layer (top two rows) and a model with a resistive layer (bottom two rows). The layer extends from 400 m to 450 m depth. The plots in the second and fourth correspond to models with a 10 m flaw at 500 m depth. . . 115

Figure 4.9 (a) Charge along the length of wells with three different conductivities (each indicated by a different color in the legend). The intact wells are denoted with dashed lines and the flawed wells are denoted with solid lines. (b) Secondary charge along the flawed and short wells. The primary is defined as the electric field due to the 1000 m long intact well. The return electrode is 2000 m away from the well. 116

Figure 4.10 Radial electric field as the conductivity of the casing is varied for a 1 km well with a 10 m flaw at 500 m depth. The positive electrode is connected to the top of the casing, the negative electrode is positioned 500 m away and data are measured along a line 90° from the source electrodes. In (a), we show the total electric field for three different casing conductivities, each indicated on the legend. The solid lines indicate the response of the flawed well and the dashed lines indicate the response of the intact well (the primary). In (b), the secondary radial electric field is plotted and in (c), we show the secondary radial electric field as a percentage of the primary. 117

Figure 4.11 Radial electric field as the vertical extent of the flaw is varied. The positive electrode is connected to the top of the casing, the negative electrode is positioned 500 m away and data are measured along a line 90° from the source electrodes. In (a), we show the total electric field four different flaw extents. The black line shows the response of the intact well. The dashed-lines indicate the partially flawed wells (50% of the circumference is compromised) and the solid lines flawed wells in which the entire circumference of the well has been compromised. In (b), the secondary radial electric field is plotted (with respect to an intact well primary) and in (c), we show the secondary radial electric field as a percentage of the primary. . . 119

Figure 4.12 Electrode locations to be compared. The top casing electrode (blue), centered electrode (green, 500 m depth), and downhole electrode (red, 500 m depth) are connected to the casing. The surface electrode (orange) is offset from the well by 0.1 m. The remaining electrodes are positioned along the axis of the casing. Panel (a) shows the entire length of the casing, while (b) zooms in to the bottom of the casing to show the separation between the electrodes beneath the casing. 122

Figure 4.13 Total current density along a vertical line offset (a) 25 m, (b) 50 m and (c) 100 m from the axis of the casing, which extends from the surface (0 m) to 1000 m depth. The electrode locations correspond to those shown in Figure 4.12. For reference, a simulation with an electrode 20 m below the casing when there is no casing present is shown in black. 124

Figure 4.14 Cross section showing: (a) electrical conductivity, (b) current density, (c) charge density, and (d) electric field for a DC resistivity experiment with a conductive target (top) and a resistive target (bottom). The positive electrode is positioned in the casing at the 912.5 m depth. The casing is shown by the black line that extends to 1 km depth in panel (a). 128

Figure 4.15 Cross section showing: (a) electrical conductivity, (b) current density, (c) charge density, and (d) electric field for a DC resistivity experiment with a conductive target (top) and a resistive target (bottom). The positive electrode is positioned at 912.5 m depth. No casing is included in this simulation. Note that the colorbars for the charge density (c) and electric field (d) are different than those used in Figure 4.14. For the resistive target, the colorbar is saturated, the charge density over the resistive target is on the order of 10^{-13} C/m³. 129

Figure 4.16 Radial electric field at the surface as the conductivity of a cylindrical target, in contact with the well, is varied. The target has a radius of 25 m and extends in depth from 900 m to 925 m. The return electrode is on the surface, 500 m from the well and data are measured along a line perpendicular to the source. The panels on the left show (a) the total electric field, (b) the secondary electric field with respect to a primary that does not include the target, and (c) the secondary electric field as a percentage of the primary for a survey in which the positive electrode is positioned downhole at 912.5 m depth. The panels on the right similarly show (d) the total electric field, (e) the secondary electric field, and (f) the secondary electric field as a percentage of the primary for a top-casing experiment. . . 130

Figure 4.17 Cross section showing: (a) electrical conductivity, (b) current density, (c) charge density, and (d) electric field for a DC resistivity experiment with a conductive target (top) and a resistive target (bottom) which is not in contact with the well. The positive electrode is positioned in the casing at the 912.5 m depth. The casing is shown by the black line that extends to 1 km depth in panel (a). 133

Figure 4.18 Radial electric field at the surface as the conductivity of a cylindrical target, which is not contact with the well, is varied. The target has a radius of 25 m and extends in depth from 900 m to 925 m. The return electrode is on the surface, 500 m from the well and data are measured along a line perpendicular to the source. The panels on the left show (a) the total electric field, (b) the secondary electric field with respect to a primary that does not include the target, and (c) the secondary electric field as a percentage of the primary for a survey in which the positive electrode is positioned downhole at 912.5 m depth. The panels on the right similarly show (d) the total electric field, (e) the secondary electric field, and (f) the secondary electric field as a percentage of the primary for a top-casing experiment. The data shown in Figure 4.16, for the target in contact with the well, are plotted in the dashed, semi-transparent lines for reference. 135

Figure 4.19 Depth slice showing the primary electric field due to a downhole electrode and a return electrode located on the surface at $x = -500$ m, $y = 0$ m. The red line indicates the azimuth of the source. We examine the 3 different target azimuths shown by the white outlines. The solid line indicates the target inline with the source, the dashed is 90° from the source line, and the dotted line is 180° from the source line. 137

Figure 4.20 Integrated anomalous current density (excitation), as defined in equation 4.2, for a $50\text{ m} \times 50\text{ m} \times 25\text{ m}$ target at 900 m depth in a DC experiment with the positive electrode (a) downhole at 912.5 m depth, and (b) a top-casing electrode. The return electrode is positioned on the surface 500 m from the well. Each line color indicates a different target conductivity. The different line styles correspond to different target azimuths relative to the plane of the source electrodes and correspond to those shown in Figure 4.19. The solid line indicates a target inline with the source, the dashed is 90° from the source, and the dotted line is 180° from the source. Offset is calculated from the center of the well to the edge of the target closest to the well. 138

Figure 4.21 (a) Sum of the primary and secondary radial electric field due to a dipolar target with moment of 38 Am centered 50 m from the well, either calculated with the casing (blue) or simply a dipole in a half-space (orange). (b) Secondary radial electric field due to a dipolar target in a halfspace with casing (blue) and without casing (orange). Secondary radial electric field as a percentage of the primary. The target is along a line 90° from the source electrodes; this is the same line along which we measure data at the surface. 140

Figure 4.22 Currents (top row) and charges (bottom row) along the length of a hollow steel-cased well (solid lines), solid cylinder with conductivity equal to that of the steel-cased well (dashed-lines), and a solid cylinder with a conductivity such that the product of the conductivity and the cross sectional area of the cylinder is equal to that of the hollow-pipe (dotted lines). Each of the line-colors corresponds to a different casing length, as indicated in the legend. In (a), we show the vertical current in the casing, (b) shows the difference from the true, hollow-cased well in the vertical current within the casing, and (c) shows that difference as a percentage of the true currents. In (d), we show the charge per unit length along the casing, (e) shows the difference from the true, hollow-cased well and (e) shows that differences as a percentage of the true charge distribution. The x-axis on all plots is depth normalized by the length of the casing. . . . 143

Figure 4.23 Radial electric field measured at the surface for a model of a hollow steel-cased well (solid lines), a solid cylinder with conductivity equal to that of the steel-cased well (dashed-lines), and a solid cylinder with a conductivity such that the product of the conductivity and the cross sectional area of the cylinder is equal to that of the hollow-pipe (dotted lines). Each of the line-colors corresponds to a different casing length, as indicated in the legend. In (a), we show the total radial electric field, (b) shows the difference in electric field from that due to the true, hollow-cased well, and (c) shows that difference as a percentage of the true electric fields. The x-axis on all plots is distance from the well normalized by the length of the casing. . . . 145

Figure 4.24 Three realizations of a 2 km long casing in a layered background, where the conductivity of the layers is assigned randomly. Each layer is 50 m thick, and the mean conductivity of the background is 0.1 S/m. The color of the title corresponds to the plots of the currents and charges in Figure 4.25 146

Figure 4.25 (a) Total vertical current through the casing for the three layered-earth models shown in Figure 4.24. The solid lines indicate the response of the true, hollow steel cased-well and the dotted lines indicate the response of a solid cylinder having the same cross-sectional conductance as the hollow well. (b) Difference between the currents along the casing in the solid well approximation and the true, hollow well. (c) Charge per unit length for each of the models. (d) Difference in charge per unit length between the true model of the casing and the approximation which preserves cross-sectional conductance. 147

Figure 4.26 Currents (top row) and charges (bottom row) along the length of a steel cased well. The “true” hollow-cased well is simulated on a 3D cylindrical mesh and has 4 cells across the width of the casing thickness (black line). The colored lines correspond to the currents and charges computed along the well represented on a cartesian mesh with cell widths shown in the legend. The finest vertical discretization is 2.5 m in all simulations. To represent the hollow cased well on the cartesian mesh, the cells intersected by the casing are assigned a conductivity that preserves the product of the conductivity and cross-sectional area of the well. In (a), we show the vertical current in the casing, (b) shows the difference from the true, hollow-cased well in the vertical current within the casing, and (c) shows that difference as a percentage of the true currents. In (d), we show the charge per unit length along the casing, (e) shows the difference from the true, hollow-cased well and (e) shows that differences as a percentage of the true charge distribution. 148

Figure 5.1 Current density for a time domain experiment over a 10^{-2} S/m half-space. The positive electrode is on the surface where the well-head will be and the return electrode is at $x = 1000$ m. Each row corresponds to different time, as indicated in the plots in panel (c). Panel (a) shows a cross section through the half-space along the same line as the source-wire. Panels (c) and (d) show depth-slices of the currents at 54 m and 801 m depth. 157

Figure 5.2	Current density for a top-casing time domain EM experiment with a conductive well (5×10^6 S/m). (a) Cross section in the immediate vicinity of the well. (b) Cross section through the formation. (c – d) depth-slices.	159
Figure 5.3	Difference in current density for a time domain experiment which includes a conductive steel-cased well (as in Figure 5.2) and an experiment over a halfspace (as in Figure 5.1).	161
Figure 5.4	Simulated electric field at the surface of the earth at (a) 0.01 ms and (b) 5 ms after shut-off for the halfspace model. (c) Radial electric field data measured along the survey line shown in white in (a) and (b) at 0.01 ms (blue) and 5 ms (green). (d) Radial electric field as a function of time at 300 m along the survey line (shown in the red dot in (a)). The red dots in (c) correspond to the data observed at 300 m offset and the blue and green dots in (d) correspond to the 0.01 ms and 5 ms data. Similar information is shown in (e), (f), (g) and (h) for the model with the conductive casing. The difference in the radial electric field data (casing minus halfspace) is shown in (i), (j), (k) and (l).	162

Figure 5.7	Current density for a top-casing time domain EM experiment over a 10^{-2} S/m half-space and a 1 km-long, conductive, permeable steel-cased well (5×10^6 S/m, $100\mu_0$)	169
Figure 5.8	Difference in current density for a time domain experiment which includes a conductive, permeable steel-cased well (as in Figure 5.7) and an experiment over a conductive well (as in Figure 5.2).	171
Figure 5.9	Sketch demonstrating how a vertical circulation of current can arise inside of a permeable casing in a top-casing TDEM experiment. A source current is applied and (a) currents flow downwards through the pipe. (b) Currents generate rotational magnetic fields according to Ampere's law. (c) Magnetic flux is concentrated in the permeable pipe according to the constitutive relation between \vec{b} and \vec{h} . (d) The magnetic flux varies with time after shut-off, and the time-varying magnetic flux creates rotational electric fields according to Faraday's law. (e) Currents associated with those electric fields are concentrated in conductive regions of the model in accordance with Ohm's law.	172
Figure 5.10	Simulated electric field at the surface of the earth, as was presented in 5.4. The top row (a – d) are the data simulated with the conductive casing. The second rows (e – h) are the data simulated with the conductive, permeable casing. The third row (i – l) is the difference (permeable and conductive minus conductive only), and the fourth row (m and n) show the difference as a percentage of the conductive solution.	174

Figure 5.11 Simulated db/dt at the surface of the earth, as was presented in 5.6.	
The top row (a – d) are the data simulated with the conductive casing. The second rows (e – h) are the data simulated with the conductive, permeable casing. The third row (i – l) is the difference (permeable and conductive minus conductive only), and the fourth row (m and n) show the difference as a percentage of the conductive solution.	175
Figure 5.12 Current density for a down-hole time domain experiment with a conductive, permeable steel-cased well (5×10^6 S/m, $100\mu_0$). The positive electrode is connected to the casing at 950 m depth and the return electrode is on the surface at $x = 1000$ m.	176
Figure 5.13 Difference in current density for a down-hole time domain experiment with a conductive, permeable steel-cased well (as in Figure 5.12) and a similar experiment with a conductive well.	177
Figure 5.14 Simulated electric field at the surface of the earth, as was presented in 5.10 for a TDEM experiment in which the positive electrode is coupled to the casing at a depth of 950m.	178

Figure 5.15 (a) Downward-directed current (a) within the casing at 0.01 ms (blue) and 5 ms (green) and (b) as a function of time at 500 m depth for the true, hollow-cased well. (c), (d) Current in the approximate model which treats the casing as a solid cylinder. The conductivity of the cylinder approximating the well is chosen so that both models have equal products of the conductivity and the cross sectional area. (e), (f) Difference between the current in the approximate model and the true model (approximate minus true). (g), (h) Difference as a percentage of the true solution. 181

Figure 5.16 Simulated electric field at the surface of the earth, as was presented in 5.4. The top row (a – d) are the data simulated with the true, conductive casing. The second rows (e – h) are the data simulated with the solid cylinder approximating the well. The third row (i – l) is the difference (approximate minus true), and the fourth row (m and n) show the difference as a percentage of the true solution. . . . 182

Figure 5.17 (a) True current density (b) difference between the currents in the simulation with the approximation to the conductive well and the true solution (secondary currents), (c) True charge density, (d) secondary charge density, (e) true electric field, (f) secondary electric field. 184

Figure 5.18 Sketch of the geometry of the dominant geometry of the current density, \vec{j} and magnetic flux density, \vec{b} , within the casing. Most of the current flows vertically while most of the magnetic flux density is rotational. 186

Figure 5.19 (a) Downward-directed current (a) within the casing at 0.01 ms (blue) and 5 ms (green) and (b) as a function of time at 500 m depth for the true, permeable, hollow-cased well. (c), (d) Current in the approximate model which treats the casing as a solid cylinder. The conductivity of the cylinder approximating the well is chosen so that both models have equal products of the conductivity and the cross sectional area. The permeability of the cylinder is chosen so that both models have equal products of the permeability and the thickness. (e), (f) Difference between the current in the approximate model and the true model (approximate minus true). (g), (h) Difference as a percentage of the true solution.	187
Figure 5.20 Simulated electric field at the surface of the earth, as was presented in 5.4. The top row (a – d) are the data simulated with the true, conductive, permeable casing. The second rows (e – h) are the data simulated with the solid cylinder approximating the well. The third row (i – l) is the difference (approximate minus true), and the fourth row (m and n) show the difference as a percentage of the true solution.	188
Figure 5.21 (a) True current density, (b) difference between the currents in the simulation with the approximation to the conductive, permeable well and the true solution (secondary currents), (c) true charge density, (d) secondary charge density, (e) true electric field, (f) secondary electric field.	189

- Figure 6.1 Approximation to a step function using an arctangent, as described in equation 6.6. The values in the legend indicate the value of the slope, a . Smaller values have a more gradual transition between zero and one, while larger values have a more rapid transition. 199
- Figure 6.2 Model of an electrically conductive propped fracture zone (3 S/m) in a halfspace ($100 \Omega \text{ m}$) with a steel-cased well. The well is modelled as a solid cylinder with a conductivity of $1.4 \times 10^4 \text{ S/m}$. The mesh has 4 cells across the radius of the casing. The fractured region extends vertically from 950 to 960 m depth and has a radius of 50 m. Panel (a) has a radial extent of 80 m to show the fractured zone and panel (b) has a radius of 0.4 m to show the casing. The a-electrode locations are shown in panel (b). 205
- Figure 6.3 (a) Synthetic data for the down-hole casing experiment for the background, prior to the fracture (solid lines), and after the fracture (dots), (b) secondary electric field (fracture - background), and (c) secondary electric field as a percentage of the primary (background). The color of the lines or dots indicates the depth of the source. . . . 206

Figure 6.4	(a) Observed and predicted radial electric field data, (b) difference between the observed and predicted data (V/m), (c) difference between the observed and predicted data as a percentage of the observed data, and (d) conductivity model recovered in the inversion. The colors in (a), (b), and (c) indicate the source location as shown in Figure 6.3. The white outline in (d) outlines the true geometry of the fracture zone and the grey line shows the location of the wellbore. The data are fit to a global χ -factor < 0.1 and the inversion took 3 iterations.	208
Figure 6.5	Integrated sensitivity for (a, b) a survey conducted in a 100 Ωm half-space and (c, d) the true model with the conductive target, shown in Figure 6.2. The inversion model is log-conductivity. The casing is shown by the grey line, and the source locations are shown by the red dots. The integrated sensitivity is computed by squaring the elements of the sensitivity matrix, summing along the rows of the sensitivity matrix and then taking the square-root. This gives a vector whose length is the number of model parameters.	209
Figure 6.6	Tikhonov inversion result, similar to that shown in 6.4 that fits the data to a global χ -factor < 0.05. The inversion took 5 iterations.	210
Figure 6.7	Tikhonov inversion result, similar to that shown in 6.6 that uses $\alpha_x = 100$. The inversion took 5 iterations.	211

Figure 6.8 Parametric inversion result for a starting model centered at 980 m depth with a thickness of 5 m and a radius of 5 m. The initial background conductivity is 10^{-2} S/m and the initial conductivity of the target is 3×10^{-2} S/m. The geometry of the starting model is shown by the white dashed-lines and the true model is shown by the solid white outline. The inversion reached a χ -factor < 0.05 and took 8 iterations.	212
Figure 6.9 Parametric inversion result for a starting model centered at 955 m depth with a thickness of 5 m and a radius of 5 m. The initial background conductivity is 10^{-2} S/m and the initial conductivity of the target is 3×10^{-2} S/m. The geometry of the starting model is shown by the white dashed-lines and the true model is shown by the solid white outline. The inversion reached a χ -factor < 0.05 and took 8 iterations.	213
Figure 6.10 Parametric inversion result for a starting model centered at 955 m depth with a thickness of 10 m and a radius of 5 m. The initial background conductivity is 10^{-2} S/m and the initial conductivity of the target is 3×10^{-2} S/m. The geometry of the starting model is shown by the white dashed-lines and the true model is shown by the solid white outline. The inversion reached a χ -factor < 0.05 and took 12 iterations.	214

Figure 6.11 Parametric inversion result where the center of the target is fixed at a depth of 955 m. The starting model has a thickness of 5 m and a radius of 75 m. The initial background conductivity is 10^{-2} S/m and the initial conductivity of the target is 3×10^{-2} S/m. The geometry of the starting model is shown by the white dashed-lines and the true model is shown by the solid white outline. The inversion reached a χ -factor < 0.05 and took 6 iterations. 215

Figure 6.12 Self-consistent effective medium theory estimation of electrical conductivity as a function of fracture concentration. The conductivity of the background is 10^{-2} S/m and the conductivity of the material filling the fractures is 2500 S/m. We use an aspect ratio of 3×10^{-5} , and the fractures are assumed to be randomly oriented. Panels (a) and (b) show the conductivity on a linear scale while panels (c) and (d) show the conductivity on a logarithmic scale. Panels (a) and (c) show the full range of possible φ values from 0 to 1, and panels (b) and (d) zoom into a smaller range, $0 \leq \varphi \leq 0.005$ 217

Figure 6.13 Integrated sensitivity, similar to that shown in 6.5, except here, the inversion model is fracture concentration. Panels (a, b) are the sensitivity for a $\varphi = 0$ half-space and (c, d) show the sensitivity calculated using the true model which includes the fracture. 218

Figure 6.14 (a) Observed and predicted radial electric field data, (b) difference between the observed and predicted data (V/m), (c) difference between the observed and predicted data as a percentage of the observed data, (d) fracture concentration model, φ , recovered in the inversion, and (e) electrical conductivity model obtained by converting φ to electrical conductivity using equation 6.9 The colors in (a), (b), and (c) indicate the source location as shown in Figure 6.3. The white outline in (d) outlines the true geometry of the fracture zone and the grey line shows the location of the wellbore. The data are fit to a global χ -factor < 0.05 and the inversion took 5 iterations. 219

Figure 6.15 Inversion result using a parametric model of the fracture concentration. The black dashed line outlines the geometry of the starting model. The initial fracture concentration is 10^{-10} in the background and 10^{-4} in the target. The data are fit to a global χ -factor < 0.05 and the inversion took 11 iterations. 220

Figure 6.16 Inversion result using a parametric model of the fracture concentration. The concentration is converted to electrical conductivity using the effective medium theory mapping shown in equation 6.9. The black dashed line outlines the geometry of the starting model. The initial fracture concentration is 10^{-10} in the background and 10^{-4} in the target. The data are fit to a global χ -factor < 0.05 and the inversion took 12 iterations. 221

Figure 6.17 Parametric inversion result where the center of the target is fixed at a depth of 955 m. The concentration is converted to electrical conductivity using the effective medium theory mapping shown in equation 6.9. The black dashed line outlines the geometry of the starting model. The initial fracture concentration is 10^{-10} in the background and 10^{-4} in the target. The data are fit to a global χ -factor < 0.05 and the inversion took 6 iterations.	222
Figure 6.18 Parametric inversion using effective medium theory and a volume data-misfit in the statement of the inverse problem. The uncertainty on the volume datum was 5%. The starting model was the same as used in Figure 6.17 The inversion reached a global χ -factor < 0.05 after 5 iterations.	225
Figure B.1 Problem setup. Concentric spheres in a uniform electric field.	249
Figure D.1 Inversion approach using the SIMPEG framework. Adapted from Cockett et al. (2015)	280
Figure D.2 Forward simulation framework.	286
Figure D.3 Location of variables in the finite volume implementation for both a unit cell in (a) cartesian and (b) cylindrical coordinates (after Heagy et al. (2015))	287
Figure D.4 (a) Contributions of each module to the sensitivity. (b) process for computing \mathbf{Jv} and (c) $\mathbf{J}^\top \mathbf{v}$; stars indicate where the source derivatives are incorporated.	289

Figure D.5	Mapping an inversion model, a 1D layered, log conductivity model defined below the surface, to electrical conductivity defined in the full simulation domain.	292
Figure D.6	Diagram showing the entire setup and organization of (a) the frequency domain simulation; (b) the time domain simulation; and (c) the common inversion framework used for each example. The muted text shows the programmatic inputs to each class instance. . .	303
Figure D.7	(a) True and recovered models for the FDEM and TDEM inversions; predicted and observed data for (b) the FDEM example, and (c) the TDEM example. In (b) the magnetic field data are in the negative z-direction.	306
Figure D.8	400 Hz In-phase RESOLVE data at (left) and High Moment SkyTEM data at 156μ s. The white dot at (462100m, 6196500m) on both images is the location of the stations chosen to demonstrate the 1D inversions in frequency and time.	308
Figure D.9	(a) Models recovered from from the 1D inversion of RESOLVE (back) and SkyTEM (blue) data at the location (462100m, 6196500m). (b) Observed (lines) and predicted (points) frequency domain data. (c) Observed and predicted time domain data. (d) Source waveform used in for the SkyTEM inversion, the x-axis is time (μ s) on a linear scale.	310
Figure D.10	(a) Conductivity model 9.9m below the surface from a stitched 1D inversion of RESOLVE data. (b) Real component of the observed RESOLVE data at 400Hz. (c) Real component of the predicted data at 400Hz.	311

Figure D.11 Setup of parametric models and calculation of the sensitivity for a primary secondary approach of simulating 3D geology and steel casing.	313
Figure D.12 Cross sectional slice of primary (casing + background) real current density. The colorbar is logarithmically scaled and shows the amplitude of the real current density.	317
Figure D.13 Depth slice at z=-950m showing the source current density for the secondary problem.	318
Figure D.14 Simulated real electric field data as measured at the surface using a primary secondary approach for casing and a conductive target (outlined in white). The upper panels show the total E_x (a) and E_y (b); the lower panels show the secondary (due to the conductive block) E_x (c) and E_y (d). Note that the colorbars showing the secondary electric fields are not on the same scale. The limits of the colorbars have been set so that the zero-crossing is always shown in the same color.	319
Figure D.15 Sensitivity of surface real E_x (left) and E_y (right) data with respect to the physical properties, $((V/m)/(\log(\sigma)))$	320
Figure D.16 Sensitivity of surface real E_x (left) and E_y (right) data with respect to the layer geometry, $((V/m)/m)$	321
Figure D.17 Sensitivity of surface real E_x (left) and E_y (right) data with respect to the block geometry, $((V/m)/m)$	322

Figure E.1	Web-page on a conducting sphere in a uniform electric field (https://em.geosci.xyz/content/max/electrostatic_sphere.html). The plot shown on this page is compiled from Python code and can be downloaded and run by users, or update by maintainers if there are improvements that can be made. . .	330
Figure E.2	Text source from which the web-page shown in Figure E.1 is built. The code used to build the plot starts under the plot-directive on line 134.	331
Figure E.3	A sample Jupyter notebook “app” that simulates a DC resistivity over a halfspace with a cylinder. The widgets control the visualization. The user can change the model parameters (e.g. the resistivity of the cylinder and of the background), the survey geometry, and select the visualization (e.g. electric field, currents, charges, etc.) .	333

Figure E.4 Seven step framework used for the case histories in <https://em.geosci.xyz>.

(1) Setup: describe the geoscientific question and objectives that are to be addressed. (2) Properties: identify the diagnostic physical properties (e.g. density, electrical conductivity, magnetic susceptibility, etc.). (3) Survey: design a survey that is suitable for detecting the physical property contrasts relevant to the application. (4) Data: carry out the field survey and collect the data set(s). (5) Processing: plot the data and apply the analysis steps needed to interpret the data (e.g. invert the data). (6) Interpretation: interpret the results in terms of the identified physical properties and original geoscience objective. (7) Synthesis: integrate the interpretation with geologic and other information relevant to the application in order to address the original geoscience objective. This image and caption are adapted from: https://em.geosci.xyz/content/geophysical_surveys/fundamentals/seven_steps.html 337

Acknowledgments

I am very fortunate to have been supported by a tremendous group of people during my academic and personal journeys as I conducted this research.

First and foremost, I am deeply grateful to my supervisor Dr. Doug Oldenburg – your endless enthusiasm and desire to make a positive impact, both in the field of geophysics and the daily lives of those around you, have enriched my life. You have opened doors for me and encouraged me to pursue projects I find meaningful. For these things and more, thank you.

Next, I thank Dr. Eldad Haber; the numerical work in this thesis has its foundation in your courses and resources on computational electromagnetics. Thank you for all you have taught me. Thanks to Michael Bostock for serving on my committee and for your input which helped improve this work.

To Dr. Michael Wilt, conversations with you helped shape the questions I pursued and the final content of this thesis. I am grateful for the investment you have made in me.

There are numerous educators who have inspired me and motivated my interest in pursuing science. In particular, Linda Legendre, David Westra, and Dr. David Lawrie, you have each had a meaningful impact on my career.

A special thanks to the friends who have supported me through my PhD. To name a

few: Dom Fournier, Sarah Devriese, Thibaut Astic, Gudni Rosenkjaer, Mike McMillan, Mike Mitchell, Devin Cowan, Luz Angelica Caudillo-Mata, Dikun Yang, Kris Davis, Dave Marchant, Jenn Fohring, Justin Granek, and Julie Nutini. I especially thank Rowan Cockett and Seogi Kang, I have learned so much from you both; I am grateful to count you as partners in much of this work and as supportive friends. To the growing number of contributors to SimPEG and resources in the open source ecosystem, I am inspired by your efforts.

To my family, who have been unwavering in their support including my encouraging brother, Josh Heagy, and my grandparents.

Finally, to my parents, I could not have done this without you. I am forever grateful for your love and support.

Funding for this work was provided by Vanier Canada Graduate Scholarship Program, the University of British Columbia Four Year Fellowship.

Dedication

To my parents.

The purpose of computing is insight, not numbers.

— Richard W. Hamming (1962)
Numerical Methods for Scientists and Engineers (Preface)

Chapter 1

Introduction

Exploration and development of unconventional resources such as shale gas formations has increased significantly over the past decades. The combination of horizontal drilling and hydraulic fracturing are key technologies for extracting hydrocarbons from shale and low permeability, “tight” reservoirs. As a byproduct of fracturing, wastewater, if not recycled, must be disposed of. In many cases this is achieved by injecting the wastewater into the subsurface through an injection well. Similarly, with recognition of the hazard that carbon-dioxide poses as a contributor to global warming, efforts are being made to capture and store CO₂ in the subsurface. In each of these scenarios, there are both environmental and economic motivations for characterizing the distribution of materials injected into the subsurface.

Electrical conductivity is a potentially diagnostic physical property in each of these application as the conductivity of the injected material is often distinct from the host rock it is being injected into. Electrical and electromagnetic geophysical techniques therefore have the potential of being viable methods for estimating the geometry of injected materials. To focus the research questions addressed in this thesis, I take the

application of hydraulic fracturing as the primary motivating context, keeping in mind the connections and similarities with other subsurface injections. In particular, reservoir settings often have steel-cased wells which complicate the electrical and electromagnetic responses.

In the sections that follow, I provide background and context on hydraulic fracturing and the questions I aim to address using electrical and EM methods, and discuss the challenges introduced when attempting to use electrical and electromagnetic methods in settings with steel-cased wells. At the end of this introductory chapter, I briefly introduce fundamental concepts of electromagnetism and geophysical inverse problems which are the foundation for my research and are applicable to all of the chapters in the thesis.

1.1 Hydraulic Fracturing

Hydraulic fracturing is used to extract hydrocarbons from tight (low-permeability) and shale formations where oil and gas will not easily flow. In such settings, hydraulic fracturing is used to create pathways for the hydrocarbons to flow (Figure 1.1). The process of inducing a fracture involves sealing off a section of the well and pumping fluid into that section under high pressure until the rock fails and cracks open up in the direction of the minimum principal stress. Typically, once the rock has fractured, sand or ceramic particles, referred to as proppant, are pumped into the formation to keep the newly created pathways open. Many of the wells drilled in the past two decades are horizontal wells, and typically 15 to 30 fracture stages (in some cases up to 60) are performed along the length of the well (Maxwell, 2014).

The extent of the fractures, complexity of the fractures, and distribution of proppant and fluid within these fractures are key factors that determine the available pathways for oil or gas to flow to the well, and thus, are important for the resulting production of the

resource (Brannon and Starks, 2008; Cipolla et al., 2009). One of the industry terms used to try to quantify the extent of the fractures within the reservoir is the “Stimulated Reservoir Volume” (SRV). Estimates of the SRV are used to make engineering decisions on the spacing between wells and completion design such as the number and spacing between fracture stages along the length of a well (Palisch et al., 2016). Hoversten et al. (2015) estimate that a 5% improvement in the characterization of the SRV for a 1 billion barrel field translates to over 0.5 billion U.S. dollars over 24 years with oil at US\$50 per barrel. Typically, an analysis to estimate the SRV is conducted using microseismic and / or tiltmeter data. Microseismic is sensitive to acoustic events generated as the fracture propagates through the reservoir (c.f. Mayerhofer et al. (2010); Cipolla et al. (2009); Maxwell et al. (2002); Warpinski (1996)), while tiltmeters are used to characterize the deformation of the rock due to the presence of a fracture or a change in the stress distribution ((Mayerhofer et al., 2010; Wright et al., 1998)). Though both techniques are valuable for estimating fracture geometry, complexity, and orientation, they provide no mechanism for delineating the extent of the proppant within the fractures; at most, they are a proxy for the extent of the fluid (Palisch et al., 2016). Two of the key factors in fracture performance are the fracture area and the hydraulic conductivity (Cipolla and Wallace, 2014), both of these are controlled by the distribution of proppant. Therefore, in order to assess how effectively the fracture treatment has stimulated the reservoir and how efficiently resources, such as water, have been used to create the fracture, we need a method to delineate the extent of the proppant and fluid within the reservoir.

To accomplish this task, I propose to use electromagnetic (EM) geophysical techniques. For EM to be a viable method for imaging the distribution of proppant and fluid within a fractured volume of rock, we require that: (1) the fractured volume of rock have physical properties which are distinct from the background, host rock, (2) the sur-

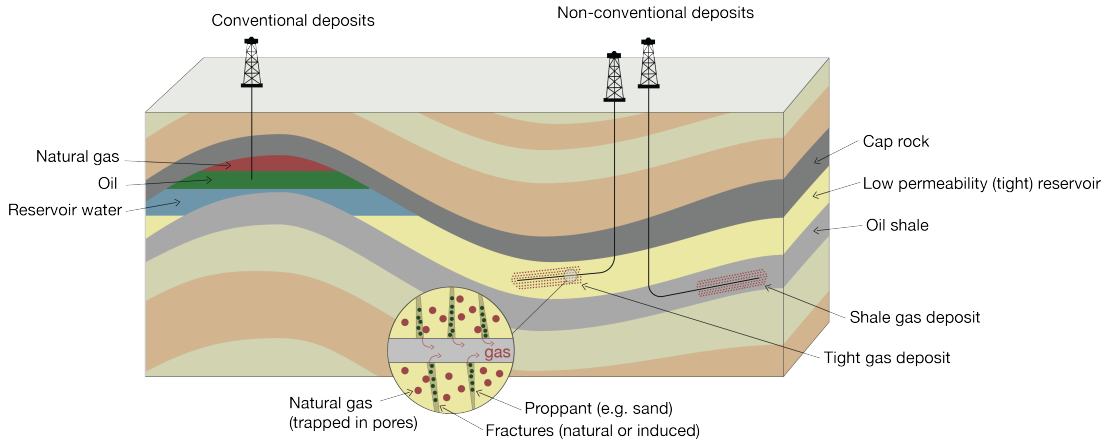


Figure 1.1: Conventional reservoirs contain oil and gas that have migrated upwards under pressure until they are trapped by a cap rock (left), while non-conventional tight or shale oil and gas reservoirs contain hydrocarbons that are trapped in low permeability formations (right).

vey must be sensitive to this contrast, and (3) once the data have been collected, they must be interpreted or inverted in a meaningful manner. Note that this is a time-lapse problem; that is, by inducing a fracture, the physical properties of the reservoir have been altered. In order to characterize such a change, we must view the imaging problem as a time-lapse one, and collect data to provide us with a before and an after data-view of the reservoir.

Variations in subsurface electrical conductivity have been used as a diagnostic physical property in sedimentary settings for characterizing geologic formations, and the properties and distribution of fluids within those formations. Hydrocarbons are much more resistive than saline formation fluids. In enhanced oil recovery projects, fluids are injected into the formation, which may be less resistive than the hydrocarbons they replace. These contrasts have been the target of cross-well, surface-to-borehole and borehole-to-surface electromagnetic (EM) methods for reservoir monitoring and char-

acterization applications (cf. Bevc and Morrison (1991); Wilt et al. (1995); Marsala et al. (2008, 2011, 2014)).

In the case of hydraulic fracturing, the physical properties of the fractured volume of the reservoir depend upon the properties of the injected fluid and proppant particles. Saline water may be used, as is often the case when recycled water is used, and electrically conductive proppant may be manufactured and injected (Cannan et al., 2014; Vengosh et al., 2014; King, 2010). One or both of these may be used to create a physical property contrast between the host reservoir rock and the fractured volume of the reservoir. This contrast is what we aim to excite using an electromagnetic survey.

Using additives to make a hydraulic fracture a geophysical target is not a new idea. Byerlee and Johnston (1976) suggested using magnetic particles and a magnetic survey to estimate fracture orientation at distances larger than can be determined by tracers and well logs. To create a fracture with a significant magnetic susceptibility, they suggested using finely crushed magnetite suspended in the fracturing fluid or iron shot, spherical particles of iron which do not crush easily and have a high magnetic susceptibility. They treated the fracture as a plate with a known magnetic susceptibility and collected measurements before and after the fracture operation; measurements of the horizontal magnetic field inside of the injection borehole are used to indicate the orientation of the fracture and surface measurements are used to estimate the fracture geometry. Using an analytic model for the magnetic response of a circular disc in a uniform inducing field, they demonstrated the potential of this technique for simple analog models of two fields sites: an engineered geothermal project at Los Alamos, where fractures are induced to circulate fluid through a dry geothermal reservoir and a hydraulic fracture operation for a tight-gas reservoir at Rio Blanco.

Similarly, Bartel et al. (1976) suggest using electrically conductive fracturing fluid

and measuring electric potentials at the surface in a DC resistivity experiment where one electrode is connected to the injection well and a return electrode is connected to a distant well casing. Potential electrodes are arranged in two concentric rings centered about the injection well with potential differences being measured between electrodes along the same azimuth in the inner and outer rings. Variations in the amplitude of the potential difference with azimuth are used to estimate the orientation of the fracture and to detect asymmetry (e.g. if the fracture extends further one side of the well than the other). Field tests were performed at two sites and demonstrated detectability of fractures in an experiment in the Wattenburg field for fractures at depths of ~ 2200 m depth. The source electrode was connected to the casing and centered at the depth of the induced fracture (see also Smith et al. (1978)).

Since these initial developments in the late 70's, there have been significant improvements in data quality as well as our ability to model and invert electrical and electromagnetic data in 3D. In conjunction, there have been advancements in fracture operations and imaging techniques such as the use of microseismic, tiltmeters, and pressure-transient analysis to characterize hydraulic fracture. As a result, the questions being asked are more detailed. How complex is the fracture? Is it a simple planar fracture or an extensive network? What is the extent of the propped volume of rock?

To assess if EM can provide insights for helping answer these questions, we need to be able to perform 3D numerical simulations of EM for fractured reservoirs. This prompts a question to be examined in the thesis:

- How do we construct a physical property model of a fractured volume of rock that can be used in numerical simulations?

1.2 Challenges to electromagnetics with steel-cased boreholes

Hydraulic fracture operations are typically conducted in steel cased wells. These wells presents several significant challenges for modelling and inverting EM geophysical data. Most wells are cased with carbon steel, which has both a large electrical conductivity ($\sim 5.5 \times 10^6$ S/m) and magnetic permeability ($> 50\mu_0$) (Wu and Habashy, 1994). This is a large contrast compared to typical geologic settings, which typically have conductivities less than 1 S/m and permeabilities similar to that of free space, μ_0 . As a result, the casing will have a significant impact on the behavior of the EM fields and fluxes. The properties of the casing, in particular, magnetic permeability, as well as casing thickness, can vary along the length of the well. They also depend on the quality of the steel and the state of corrosion; this adds another level of complexity to the situation. Well logging tools, such as that described by Brill et al. (2012) have been developed to characterize these variations.

Not only does casing introduce a large, variable, physical property contrast, its geometry and scale add to the difficulty. Well casing is cylindrical in shape, typically ~ 1 cm in thickness, ~ 10 cm in diameter, and may extend several kilometers in depth, while the geologic structures we aim to characterize with the geophysical survey have three dimensional variations in electrical conductivity on the scale of hundreds of meters to kilometers. Approaches tailored to accurately modelling the impact of the casing in simple 1D geologic settings may be geometrically incompatible or computationally prohibitive to use when reservoir-scale, three-dimensional geologic structures and targets are included in the conductivity model.

In much of the early literature, the casing was viewed as a nuisance which distorts the EM signals of interest. Distortion of surface direct current (DC) resistivity and in-

duced polarization (IP) data, primarily in hydrocarbon settings, was examined in (Wait, 1983; Holladay and West, 1984; Johnston et al., 1987) and later extended to grounded source EM and IP in (Wait and Williams, 1985; Williams and Wait, 1985; Johnston et al., 1992). Also in hydrocarbon applications, well-logging in the presence of steel cased boreholes is motivation for examining the behavior of electromagnetic fields and fluxes in the vicinity of casing. Initial work focussed on DC resistivity with (Kaufman, 1990; Schenkel and Morrison, 1990; Kaufman and Wightman, 1993; Schenkel and Morrison, 1994), and inductive source frequency domain experiments with (Augustin et al., 1989a). Kaufman (1990) derives an analytical solution for the electric field at DC in an experiment where an electrode is positioned along the axis of an infinite-length well. The mathematical solutions presented show how, and under what conditions, horizontal currents leak into the formation outside the well. Moreover, Kaufman (1990) showed, based upon asymptotic analysis, which fields to measure inside the well so that information about the formation resistivity could be obtained. This analysis is extended to include finite-length wells in Kaufman and Wightman (1993). Schenkel and Morrison (1994) show the importance of considering the length of the casing in borehole resistivity measurements, and demonstrate the feasibility of cross-well DC resistivity. They also show that the presence of a steel casing can improve sensitivity to a target adjacent to the well. In frequency domain EM, Augustin et al. (1989a) consider a loop-loop experiment, where a large loop is positioned on the surface of the earth and a magnetic field receiver is within the borehole. Magnetic permeability is included in the analysis and a “casing correction”, effectively a filter due to the casing on inductive-source data, is introduced. This work was built upon for considering cross-well frequency domain EM experiments (Uchida et al., 1991; Wilt et al., 1996).

For larger scale geophysical surveys, steel cased wells have been used as “extended

electrodes.” Rocroi and Koulikov (1985) used a pair of well casings as current electrodes for reservoir characterization in hydrocarbon applications. In near-surface settings (Ramirez et al., 1996; Rucker et al., 2010; Rucker, 2012) considered the use of monitoring wells as current and potential electrodes for a DC experiment aimed at imaging nuclear waste beneath a leaking storage tank. Similarly, Ronczka et al. (2015) considers the use of groundwater wells for monitoring a saltwater intrusion and investigates numerical strategies for simulating casings as long electrodes. Imaging hydraulic fractures has been a motivator for a number of studies at DC or EM, among them Weiss et al. (2016); Hoversten et al. (2017). Some of these have suggested the use of casings that include resistive gaps so that currents may be injected in a segment of the well and potentials measured across the other gaps along the well (Nekut, 1995; Zhang et al., 2018).

There has also been an increase in interest in examining the use of electrical or electromagnetic methods deployed on the surface to non-invasively look for flaws or breaks in the casing. Wilt et al. (2018b) introduces the idea of using electrical or electromagnetic methods for casing integrity which is further expanded upon in Wilt et al. (2018a). They show that low-frequency electromagnetic methods are sensitive to variations in wellbore length and demonstrate that their numerical simulations agree with field data collected over two different wellbores at the Containment and Monitoring Institute (CaMI) field site in southern Alberta, Canada. This work provides motivation for further delving into the physics and assessing under which circumstances we can expect to detect a flaw along a wellbore using electrical or electromagnetic methods.

As computing resources increased, our ability to forward-simulate more complex scenarios has improved. However, the large physical property contrasts and disparate length scales introduced when a steel cased well is included in a model still present

computational challenges. Even the DC problem, which is relatively computationally light, has posed challenges; those are exacerbated when solving the full Maxwell equations in the frequency (FDEM) or time domain (TDEM) and can become crippling for an inversion. For models where the source and borehole are axisymmetric, cylindrical symmetry may be exploited to reduce the dimensionality, and thus the number of unknowns, in the problem (e.g. Pardo and Torres-Verdin (2013); Heagy et al. (2015)).

To reduce computational load in a 3D simulation, a number of authors have employed simplifying assumptions. Several authors replaced the steel-cased well with a solid borehole, either with the same conductivity as the hollow-cased well (e.g. Um et al. (2015); Puzyrev et al. (2017)) or preserving the cross sectional conductance (e.g. Swidinsky et al. (2013); Kohnke et al. (2017)), so that a coarser discretization may be used; Haber et al. (2016) similarly replaces the borehole with a coarser conductivity structure and adopts an OcTree discretization to locally refine the mesh around the casing. Yang and Oldenburg (2016) uses a circuit model and introduces circuit components to account for the steel cased well in a 3D DC resistivity experiment; Weiss (2017) adopts a similar strategy in a Finite Element scheme. Another approach has been to replace the well with an “equivalent source”, for example, a collection of representative dipoles, inspired from Cuevas (2014b), or with linear charge distributions for a DC problem (Weiss et al., 2016). For the frequency domain electromagnetic problem, a method of moments approach, which replaces the casing with a series of current dipoles, has been taken in Kohnke et al. (2017).

For 3D survey geometries, only a handful of forward simulations which accurately discretize the casing have been demonstrated, and they have been achieved at significant computational cost. Recent examples, including Commer et al. (2015); Um et al. (2015); Puzyrev et al. (2017), perform time and frequency domain simulations with

finely-discretized boreholes; they required the equivalent of days of compute-time for a single forward simulation to complete. While these codes will undoubtedly see improvements in efficiency, there remains a need to accurately discretize the casing at modest computational cost both to serve as tool which these codes can compare against as well as a need for researchers to be able to interact with and explore the behavior of the currents, charges, electric and magnetic fields and fluxes to develop an understanding of the physics in these high-contrast settings.

There are a host of research questions to be explored in the context of highly conductive, permeable, steel cased wells in electromagnetic applications. This thesis is concerned with developing an understanding of the physics of electromagnetics in settings with steel cased wells. In order to delve into the physics, we must have a mechanism for simulating Maxwell's equations which raises the question:

- How do we develop a numerical approach that allows us to sufficiently discretize the steel casing so that we can not only simulate DC and EM data, but also explore the finer details of the currents, charges, electric and magnetic fields?

Assuming a numerical strategy can be developed, we can then begin to explore questions about the physics. At the DC limit,

- How do the currents, charges and electric fields behave in settings with steel cased wells? What are the implications for survey design?
- Are there physical insights which, when incorporated into numerical algorithms, reduce the computational cost of simulations with steel-cased wells?

Finally, electromagnetic experiments introduce the complication of time-variation in the fields and fluxes as well as the additional concern of variable magnetic permeability

in the model. Though the influence of the magnetic permeability of steel-casings has been explored for inductive source EM (e.g. where the source is a circular loop or magnetic dipole) (Wu and Habashy, 1994), the influence of magnetic permeability on grounded-source EM surveys (e.g. where two electrodes are used to inject current into the earth, similar to a DC resistivity experiment) is relatively unexplored. This prompts questions like:

- How do the fields and fluxes behave in an EM experiment which includes a steel-cased well?
- What impact does magnetic permeability have on the behavior of the fields and fluxes? How important is it to consider in numerical simulations?

These questions will serve as motivation for three chapters on steel-cased wells in the thesis.

1.3 Research motivation and thesis structure

The common theme throughout the thesis is the motivation to image subsurface injections – specifically proppant and fluid injected during a hydraulic fracturing operation. To this end, I consider three main topics that comprise five chapters in the thesis:

- Building a physical property model for a fractured volume of rock (Chapter 2)
- Developing a physical understanding of electrical and electromagnetic methods when steel-cased wells are present (Chapter 3, 4, and 5)
- Formulating and solving the inverse problem for a fractured volume of rock (Chapter 6)

Each of these topics is discussed in further detail below.

The research chapters in this thesis make use of fundamental knowledge that needs to be presented. Rather than insert that introductory material into the individual chapters, they are included at the end of this chapter. The background elements pertain to:

- Electromagnetic geophysics: introducing Maxwell's equations and EM geological surveys
- Geophysical inversions: formulating the inverse problem

These are successively presented in Sections 1.4 and 1.5 after I have introduced the research material in this thesis.

1.3.1 Homogenization strategy for hydraulic fractures

Chapter 2 develops a strategy for estimating a bulk conductivity of a fractured volume of rock. I break the problem into two steps, first estimating the effective conductivity of a mixture of electrically conductive proppant and fluid and second, estimating the conductivity of a fractured volume of rock where the fractures are filled with the proppant-fluid mixture. Having constructed a physical property model for a modest-sized fracture operation, I then demonstrate feasibility of detecting EM signal sensitive to the fracture using a well-established cross-well EM survey. At this stage, I neglect the influence of steel-cased wells.

The homogenization strategy taken in this chapter is based on established methods in effective medium theory (Bruggeman, 1935) which have previously been considered for fractured rocks (Berryman and Hoversten, 2013). The main contributions of this chapter are: algorithmic improvements to the effective conductivity calculation presented by Berryman and Hoversten (2013), and the discussion of the two-stage workflow

which allows various proppant-fluid mixtures to be considered (e.g. a fully conductive proppant-pack, mixture of standard sand or ceramic proppant and conductive proppant).

1.3.2 Steel casings

The intention in this thesis is to advance our understanding of the physics of EM in settings with steel-cased wells. This understanding can then be used to develop appropriate approximations in order to reduce computational cost, and to help calibrate our expectations of the results of more advanced numerical techniques. To this end, I consider three topics, each corresponding to one chapter in the thesis, to advancing our physical understanding.

Chapters 3, 4, and 5 contend with some of the challenges of performing DC and EM surveys in settings with steel-cased wells. In Chapter 3, I present a mimetic finite volume implementation for simulating Maxwell's equations at DC, in frequency and in time, on cylindrically symmetric and 3D cylindrical meshes (which include an azimuthal discretization). Although cylindrically symmetric meshes are common in EM modelling, cylindrical meshes which include an azimuthal discretization are not. A cylindrical mesh conforms to the geometry of a vertical borehole and thus, can greatly reduce the size of the mesh, and resultant cost of the computation, while still allowing for significant refinement in the vicinity of the borehole. The purpose of this implementation is to facilitate investigation into the physical behavior of EM fields and fluxes in this high-contrast setting. I consider two forms of validation: numerical validation and validation of the physical behavior. For numerical validation, I compare results of a forward simulation with independently developed codes (Haber et al., 2007; Commer et al., 2015; Yang and Oldenburg, 2016). For validation of the physical behavior, I compare features of the simulated currents, charges, and electric fields to the behavior expected

from the asymptotic analysis in Kaufman (1990); Kaufman and Wightman (1993) at DC, and similarly, compare the behavior of the magnetic fields and fluxes in the presence of conductive and permeable pipes with the lab studies and analytical work contained in Augustin et al. (1989a) for inductive source frequency-domain electromagnetics.

Chapter 4 focuses on developing an understanding of the physics of casings in a DC resistivity experiment. I start by considering the related application of casing integrity. In a casing integrity experiment, the aim is to detect a flaw or break in the casing which might be due to corrosion or failure under mechanical stresses. Wellbore integrity surveys are typically conducted with wireline tools, but more recently, Wilt et al. (2018b) introduced the idea of conducting a survey from the surface. This application provides the opportunity to build a physical understanding about the behavior of the currents, charges, and electric fields in a DC experiment with casing. I investigate factors that influence the feasibility of detecting a flaw, including the conductivity of the background and casing, depth to the flaw, and impact on the signal if the whole circumference or only a portion of the circumference of the casing is compromised. I also consider the location of the return electrode and its impact on the measured data. Many of the concepts developed in this section inform survey design elements in the next section, which considers DC resistivity survey for a conductive or resistive target adjacent to the well. I look at survey design elements, including the impact of the source electrode location on the resultant currents over the depth-interval of interest, and consider the impact of parameters such as the conductivity of the target and whether the target is electrically connected to the casing or not. The final topic in this chapter considers approximations to the steel-cased well in order to reduce the computational cost of the forward model. There is discrepancy among current literature as to whether the contrast between the background and the casing is the important quantity to conserve (e.g. Um et al. (2015))

or if the product of the conductivity and the cross-sectional area of the casing should be preserved (e.g. (Swidinsky et al., 2013)). I compare both approaches to resolve this question and discuss implications of choosing an incorrect approximation.

Chapter 5 explores important aspects of electromagnetics in settings with steel cased well. I begin by demonstrating the behavior of currents through time in time-domain EM simulation with a conductive well. The geometry of the currents through time is rather complex, even in this seemingly simple experiment. Building from this, I then consider magnetic permeability and demonstrate how permeability alters the behavior of the currents and in turn, discuss the impact permeability can have on data measured at the surface. Finally, I revisit approaches for approximating steel cased wells developed at DC and explore some of the subtleties that arise in EM experiments.

1.3.3 Inversions for subsurface injections

Chapter 6 returns to the application of hydraulic fracturing and examines the inverse problem for a fractured volume of rock. Using a DC resistivity experiment, I explore both voxel-based and parametric strategies for extracting information about the fractured volume of rock. These inversions demonstrate some of the challenges caused by steel cased wells and their influence on the sensitivity. Finally, I demonstrate how effective medium theory can be incorporated into the inversion and frame the inverse problem as an inversion for fracture concentration. This alters the sensitivity and provides the opportunity to incorporate a constraint on the volume of injected proppant and fluid.

1.3.4 Appendices

The thesis additionally includes 5 Appendices. Appendix A provides a listing of the source code used to perform all of the examples shown in the thesis. Following this,

there are two technical appendices, Appendix B and C, which support content in Chapters 2 and 6, respectively. Appendix D describes the open-source software used in this thesis to simulate and invert Maxwell’s equations. The final appendix, Appendix E, discusses how the open-source software development practices adopted in this thesis and the broader SimPEG community are similarly used for the development of interactive educational resources for geophysics in the GeoSci.xyz project (<https://geosci.xyz>).

1.3.5 A note on reproducibility and dissemination

Although simulating and inverting data in settings with steel-cased wells has practical applications, within the realm of geophysics, and even within EM geophysics, it is a narrow topic. The value in focussing on specific applications is that each application has its own subtleties and tangible details that must be worked through. In their own right, the discoveries that are made by working through these details are of value to the application-at-hand. However, this does not have to be the limit of their impact. If you choose to take the perspective that the problem-at-hand is an instance of a larger class of research questions, this allows you to view the methods and software needed to make incremental scientific discoveries as reusable components. It is then worth the investment of effort to develop and refactor these pieces so that they are modular building blocks that fit into a larger framework and are of use to a broader community. This is the perspective I have sought to take as I conducted the research described in this thesis.

The simulations and inversions build on and contribute to the SimPEG framework, which is described in Cockett et al. (2015); Heagy et al. (2017a); Cockett (2017). SimPEG is written in python and is open-source, licensed under the permissive MIT license. Source code for all of the examples shown are also openly licenced and are available on

GitHub as a combination of python scripts and Jupyter notebooks. Each chapter has a corresponding code-repository; Appendix A provides a summary of where these can be accessed. My intention in providing all of the source-code is to be transparent about the work completed; in addition, I hope these developments are of use and value to the broader geophysics community.

1.4 Background: Electromagnetic geophysics

Before moving into the research content of the thesis, I will provide a brief overview of the governing equations in electromagnetics and recommend Ward and Hohmann (1988) and GeoSci.xyz (2018) for more in-depth discussion on the physics. For an overview of how to numerically solve Maxwell's equations, I refer the reader to Haber (2014a).

1.4.1 Governing equations

The equations which govern the physics of EM are Maxwell's equations:

$$\begin{aligned} \nabla \times \vec{e} + \frac{\partial \vec{b}}{\partial t} &= 0 \\ \nabla \times \vec{h} - \frac{\partial \vec{d}}{\partial t} &= \vec{j} \end{aligned} \tag{1.1}$$

where \vec{e} is the electric field (V/m), \vec{b} is the magnetic flux density (T), \vec{h} is the magnetic field (A/m), \vec{d} is the electric displacement (C/m^2), \vec{j} is the current density (A/m^2). The first equation is Faraday's law; it describes how a time-varying magnetic flux generates rotational electric fields. The second equation is the Ampere-Maxwell equation (Maxwell's contribution was the addition of the displacement current term, $\partial \vec{d} / \partial t$). It describes how currents generate rotating magnetic fields.

It is sometimes also convenient to consider Maxwell's equations in the frequency do-

main. Using the $e^{i\omega t}$ Fourier transform convention and capital letters to denote variables in the frequency domain, Maxwell's equations are given by

$$\begin{aligned}\nabla \times \vec{E} + i\omega \vec{B} &= 0 \\ \nabla \times \vec{H} - i\omega \vec{D} &= \vec{J}\end{aligned}\tag{1.2}$$

These partial differential equations are coupled through the constitutive relations which relate the fields and fluxes through physical properties:

$$\begin{aligned}\vec{J} &= \sigma \vec{E} \\ \vec{B} &= \mu \vec{H} \\ \vec{D} &= \varepsilon \vec{E}\end{aligned}\tag{1.3}$$

where σ is electrical conductivity (S/m), μ is magnetic permeability (H/m), and ε is the dielectric permittivity (F/m). Electrical conductivity varies over many orders of magnitude; two examples on the extreme ends are the conductivity of air, $\sim 10^{-8}$ S/m and the conductivity of steel, $\sim 10^6$ S/m. The reciprocal of electrical conductivity is resistivity ($\rho = 1/\sigma$), which has units of Ωm . Throughout the thesis, resistivity and conductivity will be used interchangeably. The value of magnetic permeability is often taken to be that of free-space, $\mu_0 = 4\pi \times 10^{-7}$ H/m, in geophysical electromagnetic applications, as the permeability of most earth-materials ranges from 1-10 μ_0 (Telford et al., 1990a). The permeability of steel, however, is $\sim 100\mu_0$; thus, for settings with steel-cased wells the simplifying assumption that $\mu = \mu_0$ cannot necessarily be invoked. The value of dielectric permittivity varies between the free-space value of $\varepsilon_0 = 8.85 \times 10^{-12}$ F/m and the dielectric permittivity of water, $80\varepsilon_0$ (Telford et al., 1990a). Variations in dielectric permittivity are relevant at high frequencies, such as those used in ground penetrating

radar (GPR) surveys ($> 10^5$ Hz), but in most geophysical electromagnetic surveys, late-time or low frequencies are employed as the high-frequency signals attenuate rapidly in conductive earth-materials. As such, the quasi-static approximation, which neglects displacement currents (the $\partial \vec{d} / \partial t$ -term in equation 1.1 and the $i\omega \vec{D}$ term in equation 1.2), is commonly adopted, and will be used throughout the thesis. Under the quasi-static assumption, Maxwell's equations are given by:

$$\begin{aligned}\nabla \times \vec{e} + \frac{\partial \vec{b}}{\partial t} &= 0 \\ \nabla \times \vec{h} &= \vec{j}\end{aligned}\tag{1.4}$$

in time, and:

$$\begin{aligned}\nabla \times \vec{E} + i\omega \vec{B} &= 0 \\ \nabla \times \vec{H} &= \vec{J}\end{aligned}\tag{1.5}$$

in frequency.

In the electrostatic limit, the time-derivative terms vanish. Taking the divergence of Ampere's law, and recognizing that the electric field \vec{e} is curl-free and can therefore be expressed as the gradient of a scalar potential ϕ , gives us the governing equations for the DC resistivity problem:

$$\begin{aligned}\nabla \cdot \vec{j} &= I(\delta(\vec{r} - \vec{r}_{s+}) - \delta(\vec{r} - \vec{r}_{s-})) \\ \vec{e} &= -\nabla \phi\end{aligned}\tag{1.6}$$

Here \vec{j} is the current density, I is the magnitude of the source current, and \vec{r}_{s+} and \vec{r}_{s-} are the location of the positive and negative source electrodes, respectively. The electric field and the current density are related through Ohm's law (the first equation in equation

1.3), which we can invoke to reduce the two first-order partial differential equations in equation 1.6 to a single, second order equation in ϕ :

$$\nabla \cdot \sigma \nabla \phi = -I(\delta(\vec{r} - \vec{r}_{s+}) - \delta(\vec{r} - \vec{r}_{s-})) \quad (1.7)$$

This Poisson equation can be solved for the electric potential, ϕ , from which values of the currents and electric fields can be directly computed. In addition to considering the current density and electric fields, I will also present results in terms of charges throughout the thesis. The charge density is related to the electric field through

$$\nabla \cdot \vec{e} = \frac{\rho_f}{\epsilon_0} \quad (1.8)$$

1.4.2 Geophysical surveys

To generate data, we require that a source be used to excite a response and that receivers measure the resultant fields and/or fluxes. Sources can be natural, plane-wave sources, as in the case of the magnetotelluric method, or they can be controlled, man-made sources. Broadly speaking, two categories of controlled sources exist: inductive sources and grounded sources. Inductive sources consist of a loop of wire through which a time-varying current is passed, this in turn generates time-varying magnetic fields which act as the source fields, as shown in an Airborne EM example in Figure 1.3. The time-varying magnetic field created by these systems induces currents in the conductive earth which, in turn, create secondary magnetic fields which can be measured at or above the surface. Within reservoir settings, cross-well EM is a commonly applied inductive source survey (Wilt et al., 1995).

Grounded sources require an electrical connection between the source and the earth.

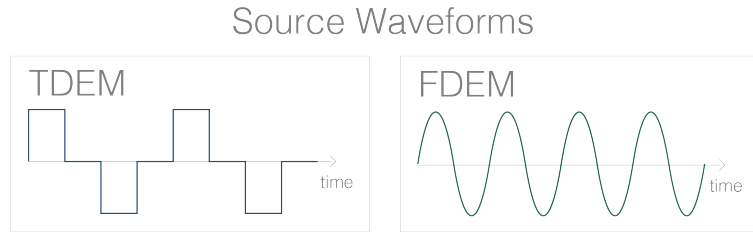


Figure 1.2: The choice of whether to solve the EM equations in the time-domain (TDEM) or the frequency domain (FDEM) depends upon the transmitter waveform; a step-off-type waveform (left) lends itself to a solution approach in the time domain and a harmonic signal (right) is typically addressed in the frequency domain.

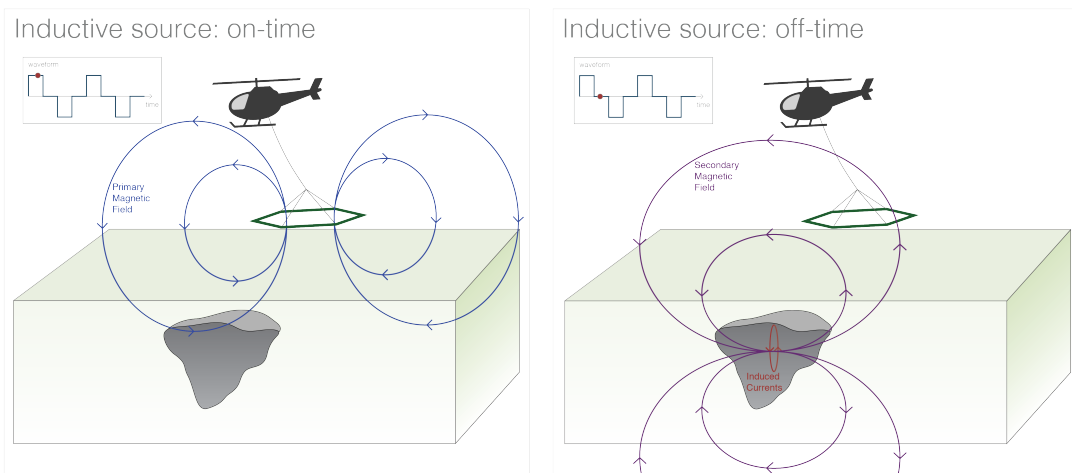


Figure 1.3: Time-domain inductive source experiment. (Left) a steady-state current is passed through the transmitter loop, generating a primary magnetic field. (Right) This current is shut-off, causing a change in magnetic flux. The changing magnetic flux induces secondary currents in conductors, which in turn create secondary magnetic fields that can be measured at receivers above, on, or within the earth.

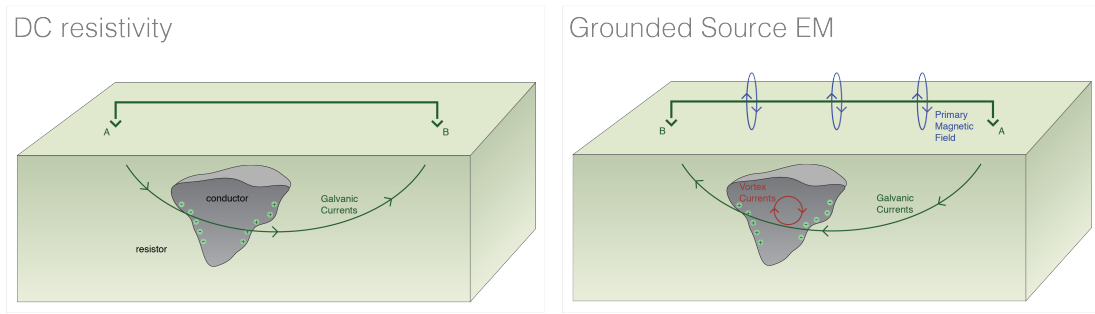


Figure 1.4: (Left) Direct current resistivity experiment in which a steady-state current is injected into the earth, and (Right) a grounded source electromagnetic experiment which uses a time-varying source current.

Two electrodes are positioned on, or in, the ground, the positive electrode injects current and a return electrode is a current-sink, as shown in Figure 1.4. In the electrostatic limit, a grounded-source experiment is simply a DC resistivity experiment. Galvanic currents flow through the earth and cause charges to build up at conductivity interfaces, generating electric potentials which can be measured at the surface or within boreholes. Electromagnetics introduces a time-varying component. The time-varying current flowing through the wire generates a time-varying primary magnetic field. This induces vortex currents in conductive structures within the earth. Receivers can measure electric fields, magnetic flux, or time-variations in the magnetic flux or some combination of these.

Two things are needed to generate data that are sensitive to a target or structure of interest. First, the source must be capable of getting EM energy to the target to excite a response, and second, the response must reach the receivers with sufficient amplitude to be measurable. A measurable signal is one which is (a) above the noise floor of the receivers, and (b) comprises a significant percentage of the primary (that is, the response with no target present). Numerical simulation of Maxwell's equations is

a critical component for assessing feasibility of detecting a target, and is an essential element of the inverse problem in which we aim to estimate a model from measured data. Within the thesis, I discuss the machinery used to perform numerical simulations in Chapter 3 and in Appendix D.

1.5 Background: Geophysical Inversions

Once data have been collected, an inverse problem can be formulated. The goal of the inversion is to extract information about the subsurface from the data. Formulating, implementing and solving the inverse problem can be viewed as a workflow consisting of inputs, implementation, and evaluation, as shown in Figure 1.5. The inputs are composed of the data, the governing equations, and prior knowledge or assumptions about the setting. In the case of the fracturing problem, this may include well-log resistivity measurements which provide information about the background, knowledge of where the fracture was initiated, and the volumes of proppant and fluid pumped to create the fracture. The implementation consists of two broad categories: the forward simulation and the inversion. The forward simulation is the means by which we solve the governing equations given a model, and the inversion components evaluate and update this model. I consider a gradient based approach, which updates the model through an optimization routine. The output of this implementation is a model, which, prior to interpretation, must be evaluated. This requires considering, and often re-assessing, the choices and assumptions made in both the input and implementation stages (c.f. Oldenburg and Li (2005b); Haber (2014b); Cockett et al. (2015)).

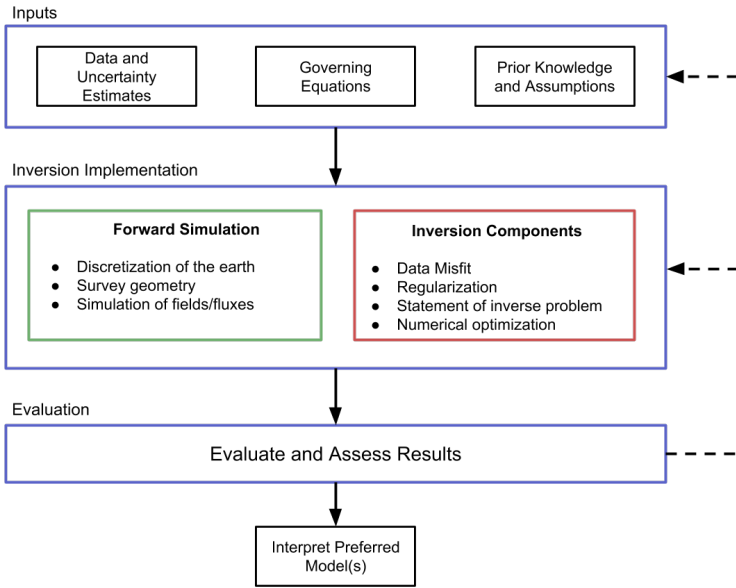


Figure 1.5: Overview of a geophysical inversion workflow. Adapted from Cockett et al. (2015).

1.5.1 Formulating and solving the inverse problem

In this section, I provide a brief overview of geophysical inversions, adapted from Cockett et al. (2015); for more detail and examples, the reader is referred to Oldenburg and Li (2005b); Cockett et al. (2015) as well as Appendix D for details specific to forward and inverse modelling in electromagnetics.

The aim of a geophysical inversion is to use the collected data to extract information about the subsurface. In a given survey, a datum can be written as

$$F_i[\mathbf{m}] + \boldsymbol{\varepsilon}_i = d_i \quad (1.9)$$

where $F[\cdot]$ is the forward simulation operator; for an electromagnetic problem, it simulates Maxwell's equations given a source and samples the relevant fields and fluxes

at the receiver locations. The physical properties of the subsurface are captured by the variable m , which I refer to as the inversion model. The noise is described by ε_i , and d_i is the observed datum. A survey usually includes multiple sources and receivers, resulting in the observed data $\mathbf{d}_{\text{obs}} = [d_1, \dots, d_N]$ and some estimate of their uncertainties – often assumed to be Gaussian. If the noise is Gaussian, then an appropriate measure of the data misfit is the l_2 -norm of the difference between the predicted data obtained through a forward simulation and the observed data, namely

$$\phi_d(\mathbf{m}) = \frac{1}{2} \|\mathbf{W}_d(F[\mathbf{m}] - \mathbf{d}_{\text{obs}})\|^2 \quad (1.10)$$

\mathbf{W}_d is a diagonal matrix whose elements are equal to $\mathbf{W}_{d_{ii}} = 1/\varepsilon_i$ where ε_i is an estimated standard deviation of the i^{th} datum. A good option is to assign a $\varepsilon_i = \text{floor} + \%|d_i|$. Percentages are generally required when there is a large dynamic range of the data. A percentage alone can cause great difficulty for the inversion if a particular datum acquires a value close to zero, and therefore we include a floor.

In addition to a metric that evaluates the size of the misfit, it is also required that we have a tolerance, ϕ_d^* ; models satisfying $\phi_d(\mathbf{m}) \leq \phi_d^*$ are considered to adequately fit the data (Parker, 1994a). If the data errors are Gaussian and we have assigned the correct standard deviations, then the expected value of $\phi_d^* \sim N/2$, where N is the number of data. Note that the division by 2 is because the statement of the data misfit includes the factor of 1/2 to simplify derivatives. When describing the “data-fit” of an inversion, it is common to quote a χ -factor, which is defined as

$$\phi_d^{\text{inv}} = \chi \phi_d^* \quad (1.11)$$

Where ϕ_d^{inv} is the final data-misfit in the inversion. Finding a model that has a misfit

substantially lower than this will result in a solution that has excessive and erroneous structure, that is, we are fitting the noise. Finding a model that has a misfit substantially larger than this will yield a model that is missing structure that could have been extracted from the data (see Oldenburg and Li (2005b) for a tutorial).

The goal of an inversion is to estimate the earth-model, m from the data. In reality, the physical property distribution of the subsurface is continuous; therefore, estimating this model from a finite number of data is an ill-posed problem, meaning no unique model explains the data. Thus, in order to obtain a meaningful model from the data, assumptions and additional information must be included. There are several mechanisms by which this can be achieved. One of the most common is to include consideration of a model regularization, ϕ_m in the inverse problem. This norm can penalize variation from a reference model, spatial derivatives of the model, or some combination of these. For example, the Tikhonov-style regularization function can be expressed as

$$\phi_m(\mathbf{m}) = \frac{\alpha_s}{2} \|\mathbf{W}_s(\mathbf{m} - \mathbf{m}_{\text{ref}})\|^2 + \frac{\alpha_x}{2} \|\mathbf{W}_x \mathbf{m}\|^2 + \frac{\alpha_y}{2} \|\mathbf{W}_y \mathbf{m}\|^2 + \frac{\alpha_z}{2} \|\mathbf{W}_z \mathbf{m}\|^2 \quad (1.12)$$

The first term is referred to as the “smallness” and penalizes difference between the inversion model and a reference model \mathbf{m}_{ref} . The matrix \mathbf{W}_s is a diagonal matrix; in the simplest case it is the identity matrix. The remaining three terms are the first-order smoothness in the x, y, and z directions; the matrices \mathbf{W}_x , \mathbf{W}_y and \mathbf{W}_z approximate the first order spatial derivatives in each direction. The α parameters weight the relative contribution of each term to the regularization. Their values should consider the length-scales in the problem (c.f. Oldenburg and Li (2005b)); for a typical 3D problem $\alpha_x = \alpha_y = \alpha_z = 1$ and α_s is generally chosen to be several orders of magnitude smaller than the smoothness weights.

To define the inverse problem, I take a deterministic approach to the inversion and treat it as an optimization problem. Additional strong constraints on the model such as upper and lower bounds (\mathbf{m}_u , \mathbf{m}_l) are also considered. The general form of the objective function I use combines the data misfit and regularization with a trade-off parameter, β , between them, giving a problem of the form

$$\begin{aligned} \underset{\mathbf{m}}{\text{minimize}} \quad & \phi(\mathbf{m}) = \phi_d(\mathbf{m}) + \beta \phi_m(\mathbf{m}) \\ \text{such that} \quad & \phi_d \leq \phi_d^*, \quad \mathbf{m}_l \leq \mathbf{m} \leq \mathbf{m}_u \end{aligned} \tag{1.13}$$

Since the value of β is not known *a priori*, the above optimization problem can be solved at many values of β to produce a trade-off, or Tikhonov, curve (cf. Parker (1994a)). An optimum value, β^* , can be found so that solving equation 1.13 with β^* produces a model with misfit ϕ_d^* . One approach to finding the value of β^* is to use cooling techniques where the β is progressively reduced from some high value and the process stopped when the tolerance is reached.

The optimization problem posed in equation 1.13 is non-linear for DC resistivity and electromagnetic forward simulations requiring that iterative optimization techniques be employed (c.f. Nocedal and Wright (1999)). Gradient-based techniques are commonly employed. In particular, Gauss-Newton methods are effective in geophysical inversions. To ease notation, I consider a more compact description of the model regularization, and write our objective function as

$$\phi(\mathbf{m}) = \frac{1}{2} \|\mathbf{W}_d(F[\mathbf{m}] - \mathbf{d}_{\text{obs}})\|^2 + \frac{\beta}{2} \|\mathbf{W}_m \mathbf{m}\|^2 \tag{1.14}$$

Note that if $\mathbf{m}_{\text{ref}} = \mathbf{0}$ and $\mathbf{W}_m = [\mathbf{W}_s^\top, \mathbf{W}_x^\top, \mathbf{W}_y^\top, \mathbf{W}_z^\top]^\top$, then the regularization is equiv-

alent to that stated in equation 1.12. The gradient is given by

$$\mathbf{g}(\mathbf{m}) = \mathbf{J}[\mathbf{m}]^\top \mathbf{W}_d^\top \mathbf{W}_d (F[\mathbf{m}] - \mathbf{d}_{\text{obs}}) + \beta \mathbf{W}_m^\top \mathbf{W}_m (\mathbf{m}) \quad (1.15)$$

where $\mathbf{J}[\mathbf{m}]$ is the sensitivity or Jacobian. The components $J[\mathbf{m}]_{ij}$ specify how the i^{th} datum changes with respect to the j^{th} model parameter,

$$\mathbf{J}[\mathbf{m}] = \frac{dF[\mathbf{m}]}{d\mathbf{m}} \quad (1.16)$$

I discuss the derivation of the sensitivity for time and frequency domain electromagnetic problems in depth in Appendix D.

At the k^{th} iteration, beginning with a model \mathbf{m}^k , we search for a perturbation $\delta\mathbf{m}$ that reduces the objective function. Linearizing the forward simulation by Taylor expansion,

$$F[\mathbf{m}^k + \delta\mathbf{m}] \simeq F[\mathbf{m}^k] + \mathbf{J}[\mathbf{m}^k] \delta\mathbf{m} + \mathcal{O}(\delta\mathbf{m})^2 \quad (1.17)$$

and setting the gradient equal to zero yields the standard Gauss-Newton equations to be solved for the perturbation $\delta\mathbf{m}$:

$$(\mathbf{J}[\mathbf{m}^k]^\top \mathbf{W}_d^\top \mathbf{W}_d \mathbf{J}[\mathbf{m}^k] + \beta \mathbf{W}_m^\top \mathbf{W}_m) \delta\mathbf{m} = -\mathbf{g}(\mathbf{m}^k) \quad (1.18)$$

The updated model is given by

$$\mathbf{m}^{k+1} = \mathbf{m}^k + \gamma \delta\mathbf{m} \quad (1.19)$$

where $\gamma \in (0, 1]$ is a coefficient that can be found by a line search. Setting $\gamma = 1$ is the default and a line search is necessary if $\phi(\mathbf{m}^{k+1}) \geq \phi(\mathbf{m}^k)$.

The iterative optimization process is continued until a suitable stopping criterion is reached. Completion of this iterative process yields a minimization for particular value of the trade-off parameter, β . If we are invoking a cooling schedule, and if the desired misfit tolerance is not yet achieved, β is reduced and the iterative numerical optimization procedure is repeated.

The forward simulation, computation of the sensitivities, and inversion machinery that I use throughout this thesis are implemented in the open source software package, SimPEG (Cockett et al., 2015; Heagy et al., 2017a).

Chapter 2

A physical property model for a fractured volume of rock

2.1 Introduction

For electromagnetic methods to be sensitive to a propped, fractured volume of rock, the fractured volume of rock must have physical properties which are distinct from the background, host rock. For EM methods, this means the electrical conductivity, magnetic permeability, or dielectric permittivity of the fractured rock must be distinct. Dielectric permittivity only plays a significant role when the frequency of the source is sufficiently high, in the hundreds of kilohertz to megahertz range, as is used in ground penetrating radar. Over the length-scales we need to consider for imaging fractures, hundreds to thousands of meters, attenuation of the EM signals due to skin depth effects make GPR impractical. Thus, we will work at lower frequencies, in the quasi-static regime of Maxwell's equations, and concern ourselves only with magnetic permeability and electrical conductivity. The materials traditionally used as proppant, typically sand

and ceramics, tend to have similar physical properties to the reservoir that they are being pumped into, making it difficult to detect them on the scale of the reservoir. However, if the proppant were made electrically conductive or magnetically permeable, for instance by coating it with graphite or including magnetite particles, it may create a sufficient physical property contrast that can be imaged using EM.

2.1.1 Proppant selection

To make the proppant electromagnetically distinct from the host rock, either the magnetic permeability or the electrical conductivity of the proppant could be targeted. Zawadzki and Bogacki (2016) provides an overview of possible magnetic proppants and highlights some practical considerations for the choice of material. For any proppant or additive, the constraints include: the mechanical strength of the particles must be able to withstand the pressure of the closing fracture without crushing and clogging the fracture pathways; the material should not be toxic or reactive; and the price-point should be reasonable since high volumes are needed. Zawadzki and Bogacki (2016) also provide a general classification of material types that could be considered: feedstock material, materials that are mixed with conventional proppant or replace conventional proppant, could include magnetite or steel particles. Both have a significant magnetic permeability, however, magnetite crushes easily, and although steel has significant mechanical strength, it is challenging to manufacture particles that are small enough (typically $< 2\text{mm}$ in diameter). They also consider ferrofluids, which contain microscopic ferromagnetic particles in suspension, and magnetic nanoparticles. Both are sufficiently small and remain in suspension so clogging is less of a concern. However, the cost of either material is quite significant and steps must be taken to reduce the environmental hazard posed. This is particularly important for nanoparticles as they tend to be much

more reactive than particles of the same material but larger in size (Zawadzki and Bogacki, 2016). Continuing advances in nanotechnology has prompted some authors, e.g. (Rahmani et al., 2014), to pursue analysis of the use of magnetic markers for mapping hydraulic fractures using electromagnetic techniques.

Magnetic permeability of common materials tends to vary over an order of magnitude (Telford et al., 1990a), while electrical conductivity of common materials can vary over > 8 orders of magnitude. Comparatively, there are many more materials that are electrically conductive than there are with a significant magnetic permeability. Materials such as coke breeze, a hardened graphite coating applied to conventional proppants, have been considered by numerous authors, as have a range of manufactured electrically conductive proppants (Pardo and Torres-Verdin, 2013; Hoversten et al., 2015; Weiss et al., 2015; Labrecque et al., 2016; Hu et al., 2018). For these reasons, I focus on electrically conductive proppants and treat the fractured region of the reservoir as an electrically conductive geophysical target.

2.1.2 Numerical Modelling

Numerical modelling is a critical component for assessing the feasibility of detecting a fractured volume of rock with an electromagnetic survey. To run a simulation, we need to discretize the modelling domain and represent the electrical conductivity of the earth on the simulation mesh. It is important to consider the large range of scales at play when considering fractures. The proppant which fills the fractures is micro-to-millimeters in diameter. The fractures are millimeters thick and we are aiming to characterize a region of the reservoir which extends hundreds of meters from the injection point at the well, tens to hundreds of meters in height, and tens of meters along the length of the well-bore. Furthermore, the numerical simulation domain must extend far enough to

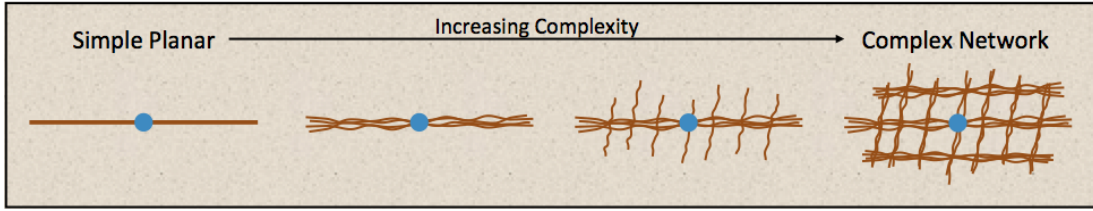


Figure 2.1: Fracture complexity, from simple planar fractures on the left to complex fracture networks on the right. The blue dot is the injection point in a horizontal well. After Cipolla et al. (2008a).

satisfy boundary conditions (typically that the fields have sufficiently decayed). This problem is exacerbated when one considers an inversion, where many forward simulations must be performed. We cannot expect a method to be capable of imaging both such a substantial volume of the subsurface while also having the resolution on the scale of the proppant particles. Thus, we require a characterization of the bulk impact of the conductive proppant within a fractured volume of rock. How we construct such a bulk physical property model depends on the geometry and complexity of the induced fractures, for instance, different approaches should be considered if the fracture is a simple planar fracture versus a complex fracture network, as depicted in Figure 2.1 (c.f. Cipolla et al. (2008b)).

To overcome these challenges, there are several approaches that may be taken; the appropriate choice will depend upon both the fracture complexity and the purpose of the simulation. If the fine-scale geometry of the fractures is defined, for example in a feasibility study built from a synthetic fracture model, then numerical upscaling (Durlofsky, 2003; Caudillo-Mata et al., 2014; Caudillo-mata et al., 2016) or multiscale techniques (Haber, 2014a) can be employed. In general, though, the fine-scale fracture geometry is not known; only a handful of studies have “ground-truthed” the geometry of an induced fracture by mining the fractured region (Cipolla et al., 2008a). Furthermore, in an inver-

sion, we cannot expect to resolve individual fractures, rather, the aim is to characterize the bulk impact due to electrically conductive fractures in a conductive medium. To estimate a bulk conductivity, effective medium theory is one approach that can be taken (c.f. Torquato (2002); Milton (2002); Berryman and Hoversten (2013)). These methods assume that the composite material is composed of a collection of randomly distributed spheres or ellipsoids (which may be preferentially aligned). The estimated conductivity depends upon the conductivity of each of the materials, their shape, and volume in the composite material. Looking forward to the inverse problem, these methods have the added benefit that they provide a conduit for incorporating a-priori information such as expected primary-fracture orientation, and volumes of proppant and fluid.

In this work, I adopt an effective medium theory approach. I take into account the conductivity of the host rock, the fracturing fluid and the proppant. The main simplifying assumption I employ is on the geometry of the fractures: I assume that they are composed of a collection of ellipsoidal cracks which may be preferentially or randomly aligned. The derivation I present follows similar derivations presented in the literature (in particular, Torquato (2002)), here I include details for preferentially aligned fractures resulting in a fully anisotropic conductivity.

2.1.3 Chapter overview

The purpose of this chapter is twofold: (1) I develop a workflow for estimating the physical properties of a fractured volume of rock containing proppant and fluid that have distinct electromagnetic properties from the host and (2) I assess if, using a commercially available electromagnetic survey, we can detect the anomaly introduced by the fracture in the data. All of the computations shown in this chapter are open-source and available as Jupyter notebooks (see Appendix A).

2.2 Homogenization workflow using effective medium theory

In this approach, I treat the fractures as being composed of a collection of preferentially (or randomly) oriented ellipsoidal cracks and based on the density of cracks within a given volume of rock, construct an anisotropic description of the coarse-scale conductivity.

Effective medium approximations range from applying simple harmonic or arithmetic averaging of conductivity values, for example when constructing a representative voxel conductivity model from well-log measurements, to more involved analytic or empirical relationships such as Archie's law (Archie, 1942), which is commonly applied for estimating the conductivity of a fluid-filled rock. Although discovered empirically, the simplest version of Archie's law is one example of a differential effective medium approximation which can be derived analytically. It assumes a background matrix, and uses an incremental approach to constructing a homogenized conductivity (c.f. Torquato (2002); Milton (2002)). However, for describing a fractured volume of rock, differential effective medium approximations are not appropriate as they assume that the rock-matrix is always connected (Torquato, 2002); in the composite material we are considering, a single computational voxel may be intersected by a fracture, meaning the rock matrix is not connected. The Maxwell-approximation (Maxwell, 1873) is yet another effective-medium approximation. It again makes a distinction between the background and the included phases, and assumes no interaction between inclusions.

I opt to consider self-consistent effective medium theory (SCEMT, also sometimes referred to as the Coherent Potential Approximation, CPS, or Bruggeman mixing). This is an effective medium approach which makes no distinction between background and included phases (e.g. see Torquato (2002)). Berryman and Hoversten (2013) similarly

suggest using self-consistent effective medium theory for fractured rocks where the fractures are filled with fluid.

Milton (1985) demonstrated the physical realizability of SCEMT; he showed that SCEMT is asymptotically the exact solution for the effective conductivity for fractal-like composites that are self-similar at many scales. Physical realizability means that the estimates given by SCEMT will always be within the Hashin-Shtrikman bounds (Torquato, 2002); at a minimum, this provides confidence that the conductivity estimates it provides are physically within a reasonable realm.

I construct the physical property model for a fractured volume of rock in two steps, as shown in Figure 2.2. Given the conductivity of the fluid and proppant particles, I estimate the effective conductivity, σ_2 , of a mixture of proppant and fluid. Next, I treat the fracture as consisting of a collection of ellipsoidal cracks filled with the proppant-fluid mixture. The ellipsoidal cracks may be preferentially aligned in a single or multiple directions or they may be randomly oriented. In both cases, I use the self-consistent effective medium theory, originally due to Bruggeman (1935) and further developed by Landauer (1952, 1978). In the following sections, I develop the theory and demonstrate its application for computing the effective conductivity of a proppant-fluid mixture as well as a fractured volume of rock.

2.2.1 Summary of self-consistent effective medium theory

Chapter 18 of Torquato (2002) provides an overview of effective medium theory approaches. The discussion presented in this section follows their presentation, but additionally considers preferentially aligned cracks, resulting in an anisotropic effective conductivity. Berryman and Hoversten (2013) present a similar overview but introduces several simplifying assumptions tailored for estimating the effective conductivity of a

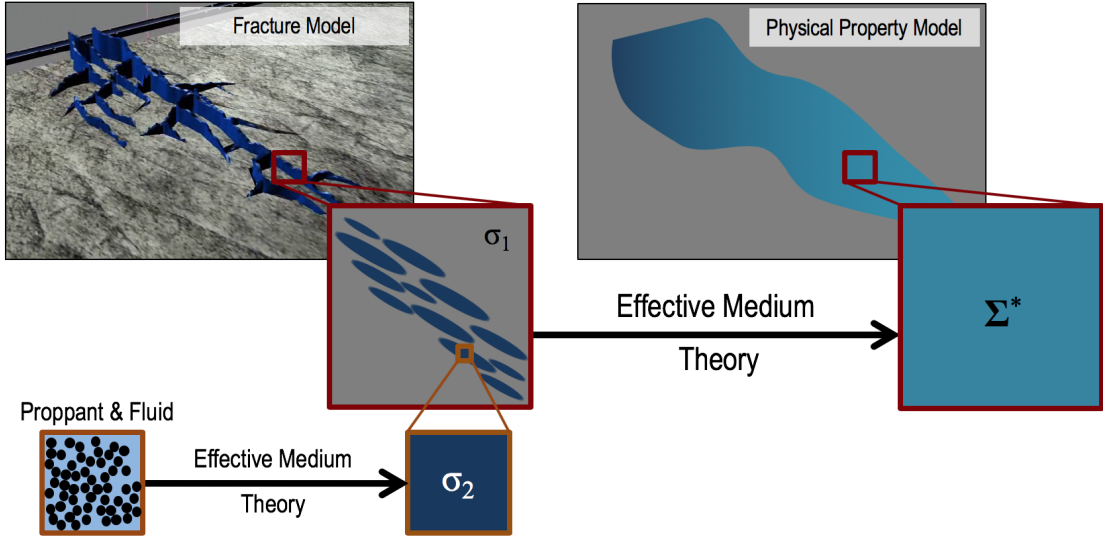


Figure 2.2: Constructing a physical property model for a fractured volume of rock using effective medium theory. The electrical conductivity of the proppant fluid mixture is given by σ_2 , the conductivity of the background reservoir rock by σ_1 . Using effective medium theory, the coarse-scale anisotropic conductivity, Σ^* describing the fractured volume of rock is computed.

naturally fractured rock where the fractures are a relatively small concentration with respect to the host rock. Here, I avoid such assumptions and work with the general formulation with the aim of being suitable for calculating both the effective conductivity of a proppant-fluid mixture as well as arbitrarily oriented fractures, each at potentially high concentrations.

Each material, or phase, in the composite is assumed to be made up of spherical or ellipsoidal particles with a known aspect ratio. Starting from the solution for a sphere or an ellipsoid in a uniform electric field, the effective conductivity of a heterogeneous medium is chosen to be the conductivity for which the average perturbation to the electric field – the difference between the electric field in the homogenized medium and the

true conductivity model – is zero. That is,

$$\sum_{j=1}^N \varphi_j (\Sigma^* - \sigma_j \mathbf{I}) \mathbf{R}^{(j,*)} = 0 \quad (2.1)$$

where N is the number of different phases of materials, φ_j is the volume fraction of the j -th phase, and σ_j is the electrical conductivity of the j -th phase. Σ^* is the 3×3 effective conductivity tensor, and \mathbf{I} is the 3×3 identity matrix. The matrix $\mathbf{R}^{(j,*)}$ is the electric field concentration tensor, and depends both on the shape of the inclusions (ie. proppant particles or cracks composing a fracture) and conductivity of the j -th phase, as well as the effective conductivity Σ^* .

For spherical particles, the electric field concentration tensor $\mathbf{R}^{(j,*)}$ reduces to a scalar, namely,

$$\mathbf{R}^{(j,*)} = \left[\mathbf{I} + \frac{1}{3} \Sigma^{*-1} (\sigma_j \mathbf{I} - \Sigma^*) \right]^{-1} \quad (2.2)$$

The resultant effective conductivity expression in 2.1 then reduces to a scalar equation.

If instead ellipsoidal inclusions are considered, the electric field concentration tensor is given by

$$\mathbf{R}^{(j,*)} = \left[\mathbf{I} + \mathbf{A} \Sigma^{*-1} (\sigma_j \mathbf{I} - \Sigma^*) \right]^{-1} \quad (2.3)$$

Where \mathbf{A} is the de-polarization tensor. For simplicity, I will assume that we are working with spheroids, either oblate (pancake-like) or prolate (needle-like) spheroids which have two semi-axes that are equal. The general solution for spheroids with three distinct semi-axes is presented in chapter 17 of Torquato (2002) and additionally discussed in Berryman and Hoversten (2013). For a spheroid with semi-axes $a_1 = a_2 = a$ and $a_3 = b$

that is aligned so that a_3 lies along the z-axis, the depolarization tensor is given by

$$\mathbf{A} = \begin{bmatrix} Q & & \\ & Q & \\ & & 1-2Q \end{bmatrix} \quad (2.4)$$

For prolate spheroids, with aspect ratio $\alpha = b/a > 1$, Q is given by

$$Q = \frac{1}{2} \left(1 + \frac{1}{\alpha^2 - 1} \left[1 - \frac{1}{2\chi_b} \ln \left(\frac{1+\chi_b}{1-\chi_b} \right) \right] \right) \quad (2.5)$$

and for oblate spheroids ($\alpha = b/a < 1$),

$$Q = \frac{1}{2} \left(1 + \frac{1}{\alpha^2 - 1} \left[1 - \frac{1}{\chi_a} \tan^{-1}(\chi_a) \right] \right) \quad (2.6)$$

with

$$\chi_a^2 = -\chi_b^2 = \frac{1}{\alpha^2} - 1 \quad (2.7)$$

For preferentially aligned spheroids, the matrix \mathbf{A} can be rotated as to align with the spheroidal axis using standard coordinate rotations. If the spheroids are randomly oriented, then we replace $\mathbf{R}^{(j,*)}$ with $1/3\text{trace}(\mathbf{R}^{(j,*)})$ in equation 2.1, and the effective conductivity expression reduces to a scalar equation. Note, that for spherical inclusions, $Q = 1/3$ and thus \mathbf{A} reduces to a scalar equal to $1/3$, showing that 2.3 is consistent with 2.2.

To solve for the effective conductivity, which is an implicit expression for Σ^* , we rearrange equation 2.1 to

$$\Sigma^* \sum_{j=0}^N \varphi_j \mathbf{R}^{(j,*)} = \sum_{j=0}^N \varphi_j \sigma_j \mathbf{R}^{(j,*)} \quad (2.8)$$

and solve

$$\Sigma^* = \sum_{j=0}^N \varphi_j \sigma_j \mathbf{R}^{(j,*)} \left(\sum_{j=0}^N \varphi_j \mathbf{R}^{(j,*)} \right)^{-1} \quad (2.9)$$

using fixed-point iteration as $\mathbf{R}^{(j,*)}$ depends on Σ^* . Gradient-based optimization techniques could additionally be considered to speed-up convergence, but as this is a simple 3×3 matrix equation and the fixed-point iteration is sufficiently fast for the problems I consider. Note that the matrix inverse in 2.9 is a 3×3 matrix inverse and thus is cheap to explicitly compute. The fixed-point iteration is performed until the recovered effective conductivity converges within a predefined tolerance. Berryman and Hoversten (2013) similarly use a fixed-point iteration to solve for the effective conductivity, however in their formulation, they isolate Σ^* by pulling out the first term in the summation in 2.1, leading to an update of the form

$$\Sigma^* = \sigma_0 \mathbf{I} - \frac{1}{\varphi_0} \mathbf{R}^{(0,*)}^{-1} \sum_{j=1}^N \varphi_j (\Sigma^* - \sigma_j \mathbf{I}) \mathbf{R}^{(j,*)}$$

This is equivalent to equation 10 in Berryman and Hoversten (2013) with the simplifications that $\mathbf{R}^{(j,*)}$ is replaced by $\mathbf{R}^{(j,0)}$ under the assumption that the fractures compose a small volume fraction of the fractured rock. In practice, this approach is suitable for low concentrations of included phases, but can cause instability in the algorithm at higher concentrations (it is possible for updates to be negative, and therefore unphysical); the authors noted challenges with algorithm convergence when the concentration of inclusions exceeded 0.2.

In the following sections, I use this formulation to estimate the effective conductivity of a range of proppant-fluid mixtures as well as for a fractured volume of rock.

2.2.2 Step 1: Effective conductivity of a proppant-fluid mixture

In general, an induced fracture will be filled with two types or phases of material: proppant and fluid. Often this mixture is referred to as a slurry. There are two principal types of mixtures I will consider, one where all of the proppant is conductive, and the second when there is a conductive filler added to a conventional proppant.

I start by considering the case of a proppant with uniform conductivity, for instance if a conductive proppant, or coated proppant were used. I assume the conductivity of the proppant is known; Appendix B includes a derivation for an effective conductivity of two concentric spheres for the scenario where the conductivity of a proppant particle and its coating are known independently.

For spherical proppant particles, the tensor-values in equation 2.1 reduces to a scalar-valued equation, and the resulting effective conductivity is isotropic. In Figure 2.3, I show the effective conductivity found using equations 2.1 and 2.2 for a proppant-fluid mixture as the concentration of proppant in the mixture (ϕ) is varied. The conductivity of the fluid is 3 S/m (similar to that of sea-water), and the proppant conductivity is varied logarithmically from 10 S/m to 10^5 S/m. For example, coke-breeze, a graphite based material has conductivities ~ 3000 S/m, and other authors have considered the use of contrast agents that reach conductivities of 10^5 S/m Weiss et al. (2015) and 10^6 S/m Pardo and Torres-Verdin (2013), which are similar to the conductivity of steel.

When the volume fraction of proppant is less than 1/3, the conductivity of the fluid is the dominant control on the resulting effective conductivity. Above a volume fraction of 1/3, the conductivity of the proppant is the primary contributor to the effective conductivity. The threshold between these behaviors is the *percolation threshold*. Below it, the concentration of conductive material is low enough that it is quite likely disconnected, above 1/3, the concentration is high enough to start forming connected, elec-

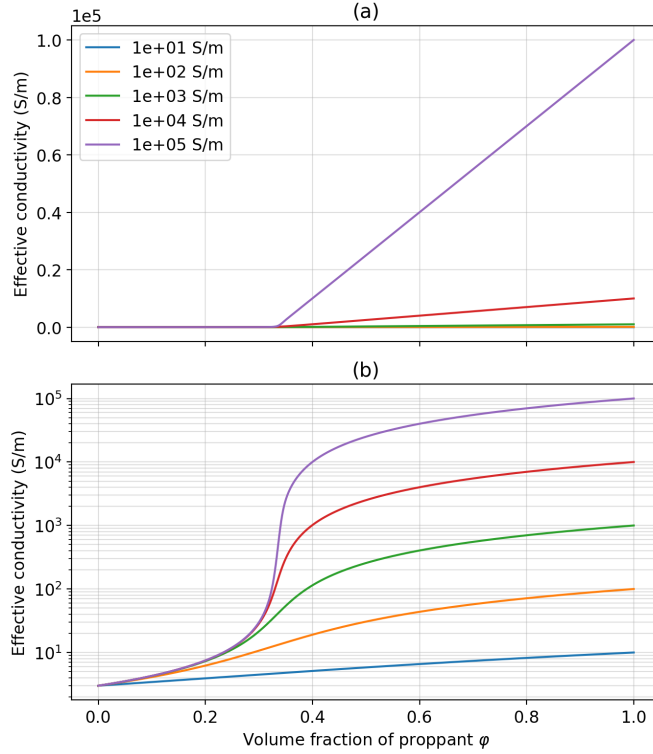


Figure 2.3: Effective conductivity of a proppant-fluid mixture for five different proppant conductivities, each indicated in the legend. Panel (a) shows the conductivity on a linear scale, and panel (b) uses a log-scale. The conductivity of the fluid is 3 S/m, similar to the conductivity of sea-water.

trically conductive pathways, causing a large jump in the effective conductivity of the system. Although proppant typically composes 10% to 20% of the injected slurry, some of the injected fluid leaks off into the surrounding geologic formation leaving proppant concentration that can be 50% in the fractures Novotny (1977); Hoversten et al. (2015).

The conductivity of the fluid also changes the resultant effective conductivity of the mixture. In Figure 2.4, I compare the effective conductivity for a mixture of conductive proppant (panel (a): 10^3 S/m, panel (b): 10^4 S/m) and four different fluid conductivities, ranging from 0.3 S/m to 300 S/m, as indicated in the legend. Although the conductivity of the fluid makes a significant difference at low proppant concentrations, above the

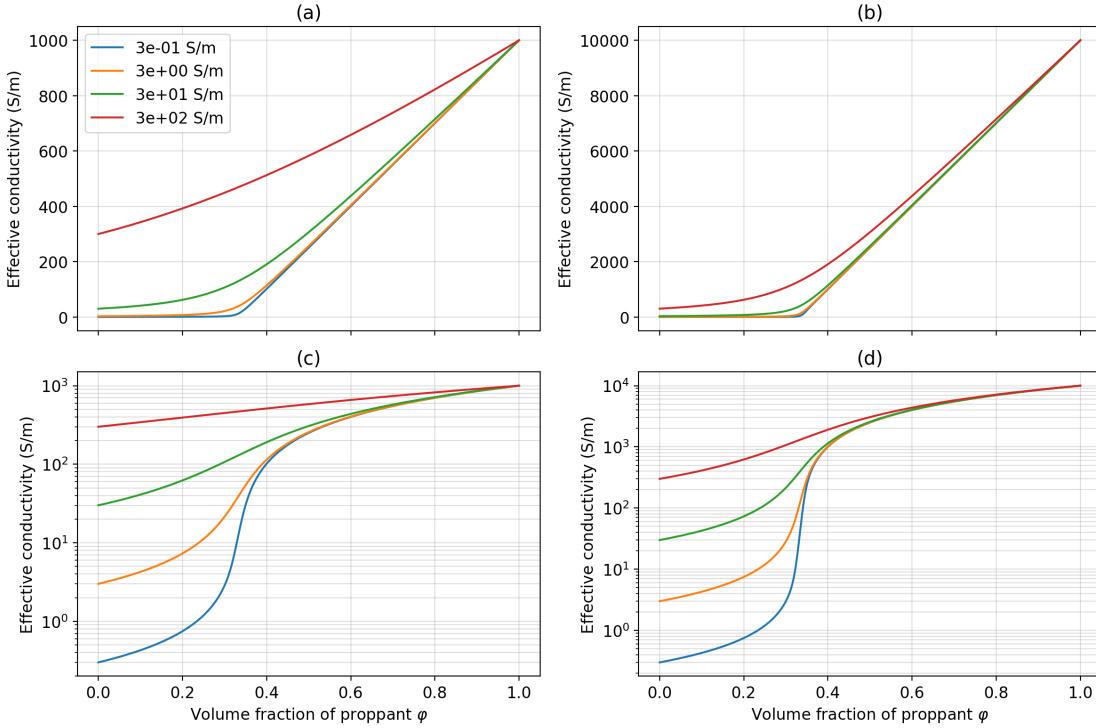


Figure 2.4: Impact of the conductivity of the fluid on the effective conductivity of a proppant-fluid mixture. Panels (a) and (c) show the effective conductivity for mixtures with a 10^3 S/m proppant and panels (b) and (d) show the effective conductivity for mixtures with a 10^4 S/m proppant. The conductivity of the fluid is indicated by the legend.

percolation threshold of 33%, the curves start to converge, particularly when the contrast between the conductivity of the proppant and the fluid exceeds 3 orders of magnitude. Thus, if the proppant can be made sufficiently conductive, its conductivity will be the controlling factor on the effective conductivity of the slurry that remains in the fractures.

The previous examples considered a 2-phase mixture in which all of the proppant was electrically conductive, however, depending on the setting and the cost to manufacture conductive proppant, it may be mixed in with conventional, resistive proppant. To examine this, I consider a proppant-fluid mixture composed of three materials, fluid (3 S/m), conventional, resistive proppant (10^{-6} S/m) and conductive proppant (10^5

S/m). The effective conductivities of proppant-fluid mixtures for five different proppant blends, where the relative concentration of the conductive proppant is varied from 0% to 100% of the proppant phase, are shown in Figure 2.5. Again, we see the impacts of the percolation threshold; when the conductive proppant composes less than 1/3 of the proppant pack, the effective conductivity is dominated by the resistive proppant. When the conductive proppant composes more than 1/3 of the proppant pack, we see that with increasing proppant concentration, the effective conductivity of the mixture is dominated by the conductive proppant. However, the percolation threshold for each of these mixtures is different. This is because it is the volume-fraction of the conductive proppant in the three-phase mixture, not the ratio of proppant to fluid, that determines when connected, electrically conductive pathways may be formed.

Another factor influencing the effective conductivity of a mixture is the shape of the materials. For the previous examples, the proppant was assumed to be composed of spherical particles. If elongated, conductive particles were included, we expect that connected, conductive pathways would form at lower concentrations. For instance, consider a 3 phase proppant mixture consisting of fluid (3 S/m), resistive, spherical proppant (10^{-6} S/m), and elongated, electrically conductive proppant (10^5 S/m). Assume that the ratio of conductive to resistive proppant is 0.25 (below the percolation threshold for spherical particles). If the elongated particles (prolate spheroids) are randomly oriented, then the resulting effective conductivity is isotropic, meaning it is independent of the directions of the inducing field and resulting current. The conductivity predicted by effective medium theory for mixtures with five different aspect ratios is shown in figure 2.6. The aspect ratio of the conductive particles influences the concentration at which we observe percolation. The more elongated the particles, the lower the concentration at which percolation occurs.

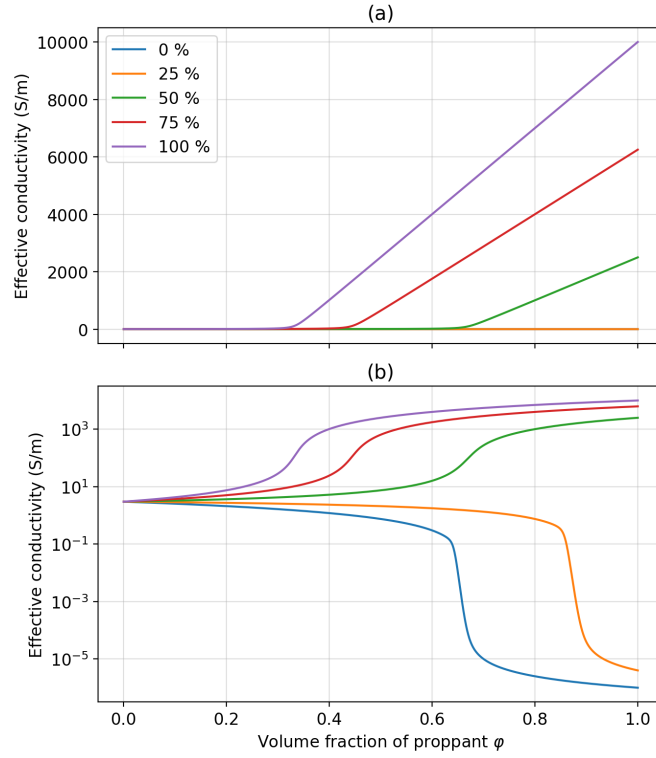


Figure 2.5: Effective conductivity of a 3-phase proppant-fluid mixture consisting of resistive proppant (10^{-6} S/m), conductive proppant (10^5 S/m) and saline fluid (3 S/m). The legend indicates the percentage of conductive proppant in the proppant mixture and the x-axis is the volume fraction of proppant in the proppant-fluid mixture.

In summary, there are several approaches that can be taken to create an electrically conductive proppant-fluid mixture. Spherical proppant particles which are themselves electrically conductive or coated with a conductive material can comprise the entire proppant pack. If conductive proppant is mixed with a conventional, resistive sand or ceramic particles, then at least 1/3 of the proppant mixture needs to be comprised of electrically conductive particles to create a conductive mixture. This ratio can be reduced if elongated particles, such as metallic strips, are used in the proppant mixture.

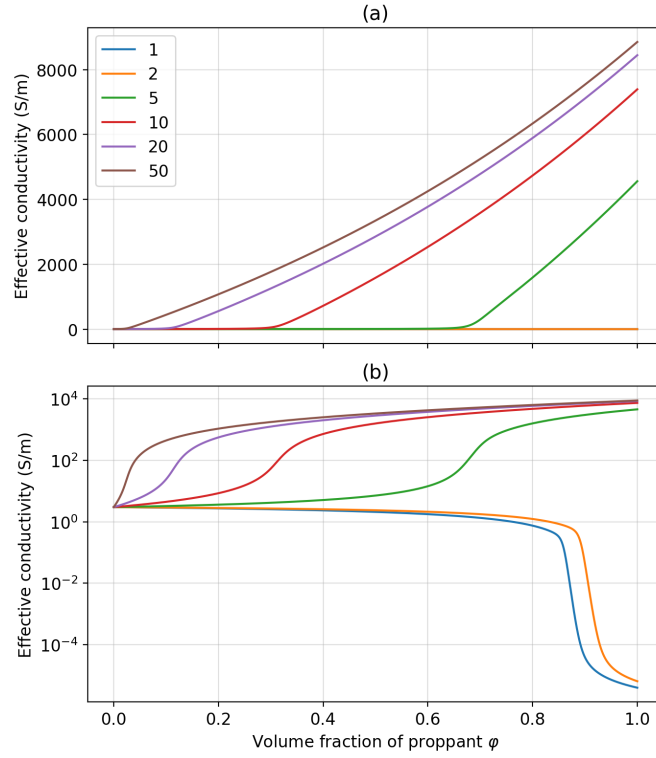


Figure 2.6: Effective conductivity of a 3-phase proppant-fluid mixture consisting of resistive proppant (10^{-6} S/m), conductive proppant (10^5 S/m) and saline fluid (3 S/m). The proppant mixture contains 25% conductive proppant and 75% resistive proppant. The legend indicates the aspect ratio of the elongated conductive proppant filler (prolate spheroids).

2.2.3 Step 2: Effective conductivity of fractured volume of rock

The next step is to estimate the effective conductivity of a fractured volume of rock. I again employ self-consistent effective medium theory as described in section 2.2.1 and consider the induced fractures to be composed of spheroidal cracks. Based on the analysis in the previous section, I consider a proppant-fluid mixture that has a conductivity of 2500 S/m. This could be achieved with spherical proppant particles having a conductivity of 10^4 S/m in a 50/50 mixture with water of 3 S/m (see Figure 2.3). Similar conductivities could be achieved with elongated particles mixed with conventional

proppant as shown in Figure 2.6. Lab measurements conducted by Zhang et al. (2016) showed that a proppant-fluid mixture composed of petroleum coke particles and seawater which fills the pore-spaces reached a conductivity of ~ 1000 S/m at 37.6% porosity. With further increase in confining pressure (thus reducing porosity and increasing the concentration of proppant), the observed conductivities range from 3000 – 5000 S/m. These results provide further confidence that conductivities > 1000 S/m for the mixture filling the hydraulic fractures are attainable.

For the following example, I will assume that the conductivity of the host-rock is 0.1 S/m. There are two scenarios I will consider. In the first, I assume the cracks are preferentially aligned, with the thin dimension of the oblate spheroid oriented along the x-axis, as shown in Figure 2.7. In this case, the recovered effective conductivity will be anisotropic, described by a diagonal matrix with entries $\sigma_y = \sigma_z \geq \sigma_x$:

$$\Sigma^* = \begin{bmatrix} \sigma_x & & \\ & \sigma_y & \\ & & \sigma_z \end{bmatrix} \quad (2.10)$$

Note that arbitrary, non-axes aligned, orientations can be considered; all that is required is that the depolarization tensor described in 2.4 is rotated to the desired orientation.

To estimate the effective conductivity of a fractured volume of rock, we must also specify the aspect ratio of the cracks. In estimating this, assume a fractal-like approximation, where the aspect ratio of the fracture is representative of the aspect ratio of the cracks that compose it. For example, if the fracture extends 50m laterally and has a width on the order of millimeters, then the aspect ratio is on the order of 10^{-5} . In Figure 2.8, I have plotted the diagonal elements of the effective conductivity for five different aspect ratios, indicated in the legend, as a function of the volume fraction of conductive

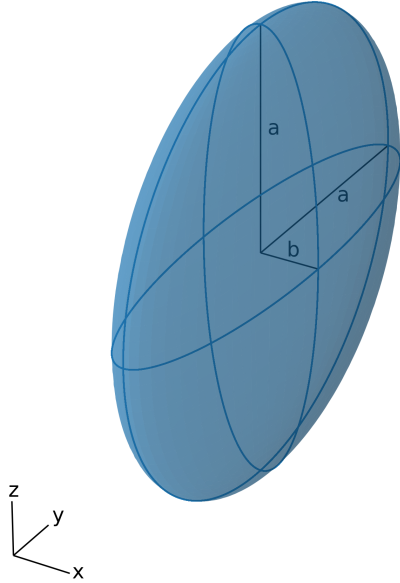


Figure 2.7: Oblate spheroid with normal along the x -axis. The y and z semi-axes are equal, and aspect ratio is $\alpha = b/a < 1$.

fractures in the rock volume sampled. Panel (a) shows the full range from $0 \leq \varphi \leq 1$ and panel (b) zooms in to lower concentrations ($0 \leq \varphi \leq 0.01$) which are more representative of a fractured rock volume, on the scale that we will consider for numerical modelling (e.g. if 10 fractures, each with 3mm width intersect a 10m \times 10m \times 10m cell, then $\varphi = 0.003$). In each of the plots, I have also included the upper and lower Wiener bounds (see equation 21.14 in Torquato (2002); originally attributed to Wiener (1912)):

$$\begin{aligned}\sigma_W^+ &= \sum_{j=0}^N \varphi_j \sigma_j \\ \sigma_W^- &= \left(\sum_{j=0}^N \frac{\varphi_j}{\sigma_j} \right)^{-1}\end{aligned}\tag{2.11}$$

in the black dashed lines; these can be understood as similar to parallel and series circuit

approximations to the conductivity. In the black dash-dot lines are the upper and lower Hashin-Shtrikman bounds for 2-phase anisotropic media in the black dash-dot (see equations 21.25 and 21.26 in Torquato (2002), which is the anisotropic generalization of the isotropic bounds derived by Hashin and Shtrikman (1962)):

$$\begin{aligned}\sigma_{\text{HS}}^+ &= \sigma_w^+ \mathbf{I} + (\sigma_1 - \sigma_0)^2 \tilde{\mathbf{A}} \cdot \left[\sigma_1 \mathbf{I} + \frac{\sigma_1 - \sigma_0}{\varphi_0} \tilde{\mathbf{A}} \right]^{-1} \\ \sigma_{\text{HS}}^- &= \sigma_w^+ \mathbf{I} + (\sigma_1 - \sigma_0)^2 \tilde{\mathbf{A}} \cdot \left[\sigma_0 \mathbf{I} + \frac{\sigma_0 - \sigma_1}{\varphi_1} \tilde{\mathbf{A}} \right]^{-1}\end{aligned}\quad (2.12)$$

For $\sigma_1 \geq \sigma_0$ and

$$\tilde{\mathbf{A}} = -\varphi_0 \varphi_1 \mathbf{A}_1 \quad (2.13)$$

where \mathbf{A}_1 is the depolarization tensor for the ellipsoidal cracks given by equation 2.4. For the bounds shown in the plot, the smallest aspect ratio, 10^{-5} was used to calculate the depolarization tensor. For the very significant aspect ratios used here, the Hashin-Shtrikman bounds are nearly identical to the Wiener bounds. Each component of the recovered effective conductivity should fall within these bounds.

For aspect ratios less than 10^{-3} , we see very little distinction between the estimate of $\sigma_{y,z}$ and σ_x ; the difference between the recovered effective conductivities for the aspect ratios of 10^{-4} and 10^{-5} is less than 1% for all values of φ . This indicates that for sufficiently thin cracks, the exact aspect ratio is not critical for estimating a representative conductivity of the fractured rock.

At the concentrations we expect to be observing in a hydraulic fracturing scenario (Figure 2.8b), we see that the effective conductivity along the normal of the fractures coincides with the lower bounds and remains nearly identical to the conductivity of the host rock for all aspect ratios shown, as may be expected. For the components of the conductivity along the cracks ($\sigma_{y,z}$), the effective conductivity mimics the behavior of

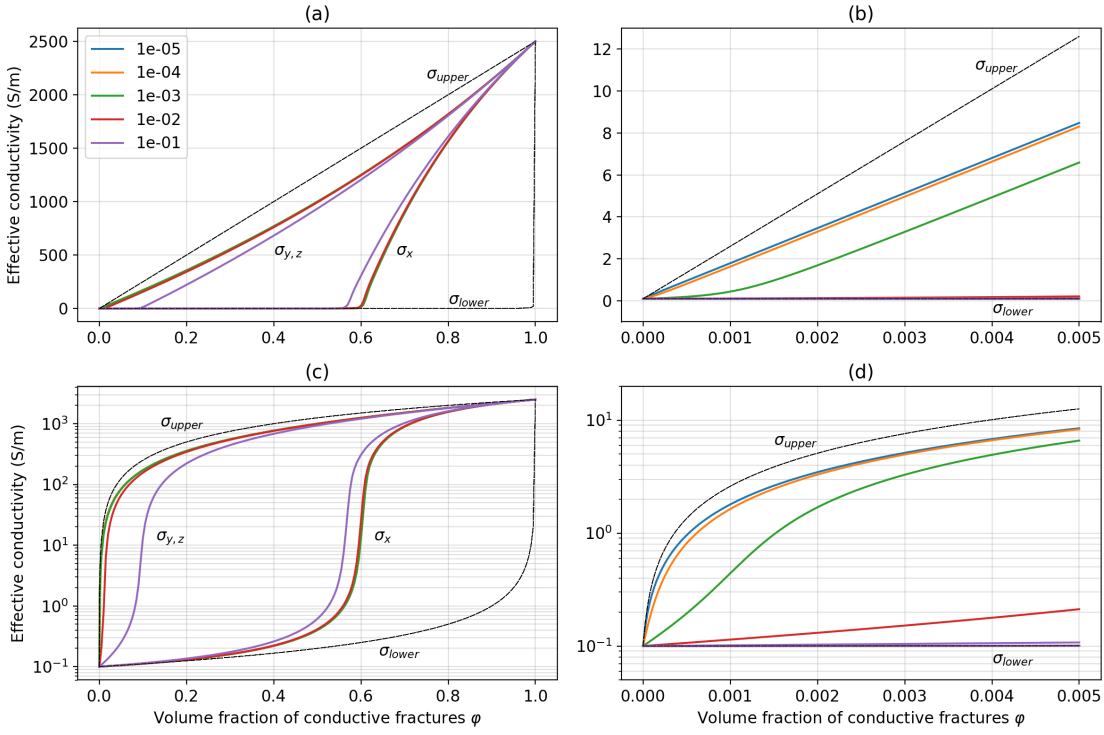


Figure 2.8: Effective, anisotropic conductivity for a fractured rock with spheroidal cracks whose normal is oriented along the x-axis for five different aspect ratios, indicated by the legend. The black dashed lines show the upper and lower Wiener Bounds, which are identical to the volume-weighted arithmetic and harmonic averages of the conductivity of the rock (0.1 S/m) and proppant-fluid mixture (2500 S/m). The black dash-dot lines are the anisotropic Hashin-Shtrikman upper and lower bounds computed using an aspect ratio of 10^{-5} in equation 2.12. Panels (a) and (c) show the full range $0 \leq \phi \leq 1$, and panels (b) and (d) zoom in to $0 \leq \phi \leq 0.005$. Note that in (b), any curve that deviates from the lower bound is the $\sigma_{y,z}$ component; all σ_x values lie on the lower bound for the concentration range shown.

the upper bounds. These components of the conductivity are similar to the behavior expected from a parallel-circuit approximation.

For settings where planar fractures are expected, a single orientation of the inclusions produces similar behavior to what would be expected if we performed simple series-and-parallel circuit approximations to the components perpendicular to and along the fracture. However, if more complex fracture networks are expected, it may be more appropriate to assume the cracks are randomly oriented. In this case, an isotropic conductivity describes the fractured volume of rock. Using the same aspect ratios shown in Figure 2.8 above, I compute the isotropic effective conductivity as a function of volume fraction of fractures in Figure 2.9. For reference, the conductivity along the fractures, $\sigma_{y,z}$ from Figure 2.8, is plotted in semi-transparent lines. As in the previous figure, panel (a) shows the full range from $0 \leq \varphi \leq 1$ and panel (b) zooms in to lower concentrations: $0 \leq \varphi \leq 0.01$.

Again, we see that for aspect ratios smaller than 10^{-3} there is little difference between the estimated effective conductivity of the fractured rock volume. The estimate of the effective conductivity largely follows the behavior of the upper bounds, while the magnitude of the effective conductivity is slightly reduced as compared to the component of the conductivity along the fractures in the anisotropic case. If we consider a $10\text{ m} \times 10\text{ m} \times 10\text{ m}$ computational cell with fractures having an aspect ratio of 10^{-5} and composing 0.3% of the total volume (e.g. 10 fractures, each with 3 mm width), we obtain $\sigma_{xy} = \sigma_z = 5.2\text{ S/m}$, $\sigma_x = 0.1\text{ S/m}$ for the case where the cracks are preferentially aligned while for the case where the cracks are randomly oriented, we obtain $\sigma^* = 3.5\text{ S/m}$.

Due to the large contrast between the conductive fractures and the host rock, the conductivity of the background has marginal effect on $\sigma_{y,z}$ in the anisotropic example

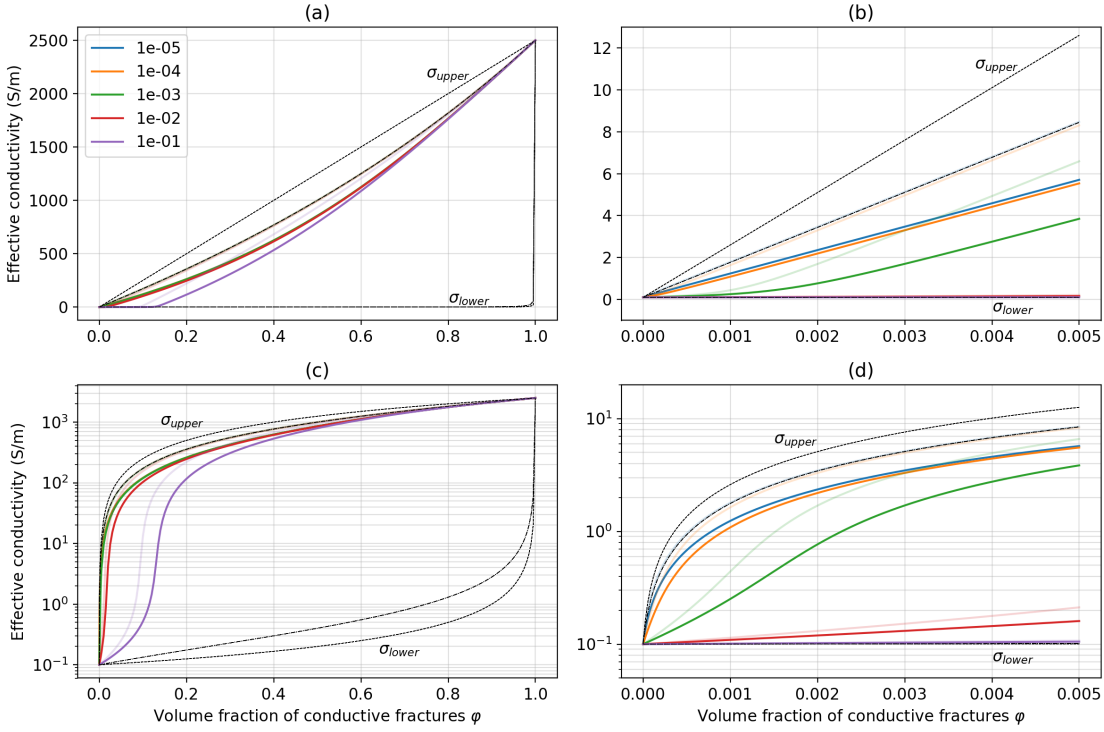


Figure 2.9: Effective, isotropic conductivity for a fractured rock with randomly oriented spheroidal cracks for five different aspect ratios, indicated by the legend. The black dashed lines show the upper and lower Wiener Bounds, which are identical the volume-weighted arithmetic and harmonic averages of the conductivity of the rock (0.1 S/m) and proppant-fluid mixture (2500 S/m). The black dash-dot lines are the isotropic Hashin-Shtrikman upper and lower bounds. The semi-transparent dotted lines show $\sigma_{y,z}$ from Figure 2.8. Panels (a) and (c) shows the full range $0 \leq \phi \leq 1$, and panels (b) and (d) zooms in to $0 \leq \phi \leq 0.01$.

or on σ^* . If we consider the example with $\phi = 0.003$, as before, and instead use a background conductivity of 0.01 S/m, the effective anisotropic conductivity is $\sigma_y = \sigma_z = 5.1$ S/m, $\sigma_x = 0.01$ S/m and for the isotropic case $\sigma^* = 3.4$ S/m. However, if the background is made more conductive and the contrast between the conductive fractures and the host reduced, we do see some impact. Setting the background to 1 S/m for this same example, we obtain $\sigma_y = \sigma_z = 6.4$ S/m, $\sigma_x = 1$ S/m for the anisotropic case and

$\sigma^* = 4.7 \text{ S/m}$ for the isotropic case.

2.2.4 Summary

To construct an approximate conductivity model of a fractured volume of rock, I use a two step process: first, I estimate the effective conductivity of a mixture of proppant and fluid that fills the fractures and second, I estimate the effective conductivity of a fractured volume of rock.

In the section that follows, I will compare numerical simulations of a crosswell electromagnetic survey for both anisotropic and isotropic conductivity models of a fractured volume of rock, representing planar and complex fracture networks, respectively.

2.3 Feasibility of EM for detecting fractures

I now examine the feasibility of detecting a conductive, fractured region of a reservoir with an electromagnetic survey. The purpose of this section is to demonstrate detectability for a simple model of a fracture with existing electromagnetic imaging techniques. The survey I consider is a frequency-domain crosswell electromagnetic survey. In a crosswell EM survey a transmitter coil, which produces a time-varying magnetic field at a single frequency is positioned inside of one well. Time-varying magnetic fields induce time-varying currents in the earth whose distribution and magnitude depends upon the conductivity of the earth. These currents in turn generate secondary magnetic fields. In a second well, an array of receiver induction coils, which measure the time rate-of-change of the magnetic flux (db/dt , in units of volts), are positioned. The measured voltages can be converted to magnetic field values. To conduct a survey, the position of the receivers is fixed and the transmitter is moved at a fixed rate along the borehole (typically 3-5 meters per minute). The receivers are repositioned, and the process repeated (Wilt

et al., 1995). Both the transmitter and receivers are oriented along the axis of the bore-hole; for vertical wells, this means the transmitter is a vertical magnetic dipole, and the receivers measure the z-component of the magnetic field. Since its development, cross-well surveys have been used for a range of reservoir imaging problems for enhanced oil recovery including monitoring steam injections (Wilt et al., 1997) and water floods (Wilt et al., 2012), including a survey conducted in a pair of horizontal wells (Marsala et al., 2015; Marsala* et al., 2015). In this section, I consider a crosswell survey and examine the feasibility of detecting signal due to a fractured volume of rock.

The setup I use is shown in Figure 2.10; a crosswell EM survey conducted in a pair of horizontal wells that are spaced 500 m apart, as shown in Figure 2.10. The transmitter is oriented along the x-axis and positioned in the same well as where the fracture stimulation was performed; the receivers are in the offset well and measure the real and imaginary parts of the x-component of the magnetic field. In the numerical modelling, I assume that the wells are sufficiently deep so that the background can be treated as a whole-space. I do not consider steel-cased boreholes in this example and instead assume that the boreholes are open-holes or cased with fibreglass casing as in Wilt et al. (2012). The additional complications due to steel cased wells will be discussed in the following three chapters.

Most hydraulic fracture operations involve injecting \sim 800 m³ to 4000 m³ (5000 to 25000 bbls) of proppant-fluid slurry into the reservoir rock, with the proppant comprising 10% to 20% of this mixture (Hoversten et al., 2015). In this example, I consider a fracture that is on the lower-end, with an 800 m³ slurry comprised of 15% proppant by volume. A significant portion of the fluid typically leaks off into the surrounding formation (Novotny, 1977), so I will assume that the final mixture filling the cracks contains 50% fluid and 50% proppant. This gives a total fracture volume of 240 m³. To distribute

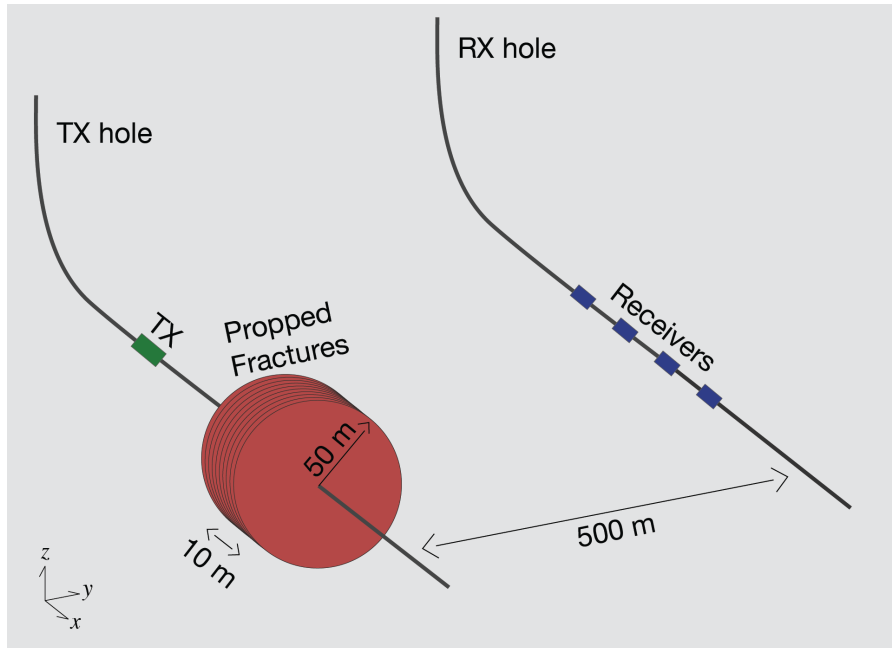


Figure 2.10: Setup for the crosswell electromagnetic simulation. Ten fractures, each with 3 mm thickness and 50 m radius are spaced over a 10 m interval along the injection well. The dipole transmitter is positioned inside of the injection well and oriented along the x-axis. Receivers are located in an offset well and measure the real and imaginary parts of the x-component of the magnetic field.

this volume, I assume that 10 fractures, each with 3 mm width are positioned within a 10 m interval along the well. Conserving volume and assuming circular fractures gives us a 50 m radius for each of the 10 fractures; I work with circular fractures that are centered along the borehole, as the resultant model is cylindrically symmetric. This significantly reduces the computational cost of the simulation.

For the physical properties, I treat the background as a whole-space with a conductivity of 0.1 S/m. Within the fractures, I use a two-phase proppant-fluid mixture, where all of the proppant is assumed to be spherical particles as in Figure 2.3. I use a proppant conductivity of 10^4 S/m and a fluid conductivity of 3 S/m; in a 50-50 mixture, the

effective conductivity computed using SCEMT, is 2500 S/m. To estimate the effective conductivity of the fractured volume of rock, I consider two scenarios: (1) the fractures are preferentially aligned and I estimate an anisotropic effective conductivity as in Figure 2.8; and (2) the fractures are sufficiently complex that I can approximate them as a collection of randomly oriented cracks, as in Figure 2.9. I estimate a single conductivity for the 10 m wide cylinder with 50 m radius that encloses the fractures. Within this region, the fractures comprise 0.3% of the total volume. To estimate the aspect ratio, I assume that the shape of the large fracture, with 3 mm width and 50 m radius (100 m diameter) is representative of the shape of the cracks that comprise it, thus the aspect ratio is 3×10^{-5} . The estimated effective conductivity for the anisotropic case is $\sigma_y = \sigma_z = 5$ S/m parallel to the fractures and $\sigma_x = 0.1$ S/m perpendicular to the fractures. For the second scenario, with randomly oriented cracks, the estimated isotropic conductivity is 3 S/m.

In terms of survey parameters, the dipole-moment of the transmitter is 5000 Am^2 and I use a transmitter frequency of 100 Hz, consistent with values stated in Wilt et al. (1995); Wilt (2003). For a signal to be detectable, we require that: (a) the secondary signal, that is, the difference between the data measured with and without the fractures present, be above the noise floor of the receivers, and (b) that the secondary signal comprises a significant percentage of the primary (model without the fractures). Marsala* et al. (2015) demonstrated noise levels of 0.5×10^{-5} nT and 0.5% repeatability between data profiles for a cross-well survey conducted between two open-hole horizontal wells, citing that “this was the lowest noise ever recorded with a crosswell EM system.” Using this as an upper-bound on our expectations, I adopt a more conservative noise level of 1×10^{-4} nT and select a percent-threshold of 5%. Thus, I consider signal above 1×10^{-4} nT and comprising > 5% of the primary as detectable.

Figure 2.11 shows the simulated secondary magnetic field data computed for (a) the anisotropic model and (b) the isotropic model at 100 Hz. The top row shows the real component and the bottom row shows the imaginary component. The x-axis shows the transmitter location relative to the center of the fracture, the y-axis shows the receiver location, and the color indicates the secondary magnetic field with respect to a 0.1 S/m whole-space. Regions of the plot which are colored, and are not covered by the semi-transparent overlay, indicate signal which is both above the noise floor and comprises a significant percentage of the primary.

As might be expected, when the transmitter and receiver are centered with the fracture, the secondary signal reaches its maximum amplitude in both the real and imaginary components. The anisotropic model produces stronger signals; the geometry of the survey is perfectly coupled to the radial components of the conductivity (σ_y and σ_z) as the resultant currents and electric fields are purely azimuthal in orientation. An isotropic simulation using $\sigma = 5$ S/m produces identical results to the anisotropic model for this survey geometry. Interestingly, the region over which data is measurable differs between the real and imaginary components. The real component is measurable over a larger range of transmitter positions, while the imaginary component is measurable over a larger range of receiver locations. The partition of EM energy into the real and imaginary components is a function of the conductivity of the medium as well as the frequency. For example, if I increase the frequency to 200 Hz, the amplitude of the imaginary component is larger than the real, and it is measurable over a larger set of source-receiver combinations, as shown in Figure 2.12.

For the simple setup shown here, there are a significant number of data that can be collected in a cross-well survey which are sensitive to both the anisotropic and isotropic fracture models. In both the 100 Hz and 200 Hz surveys, the extent over which either or

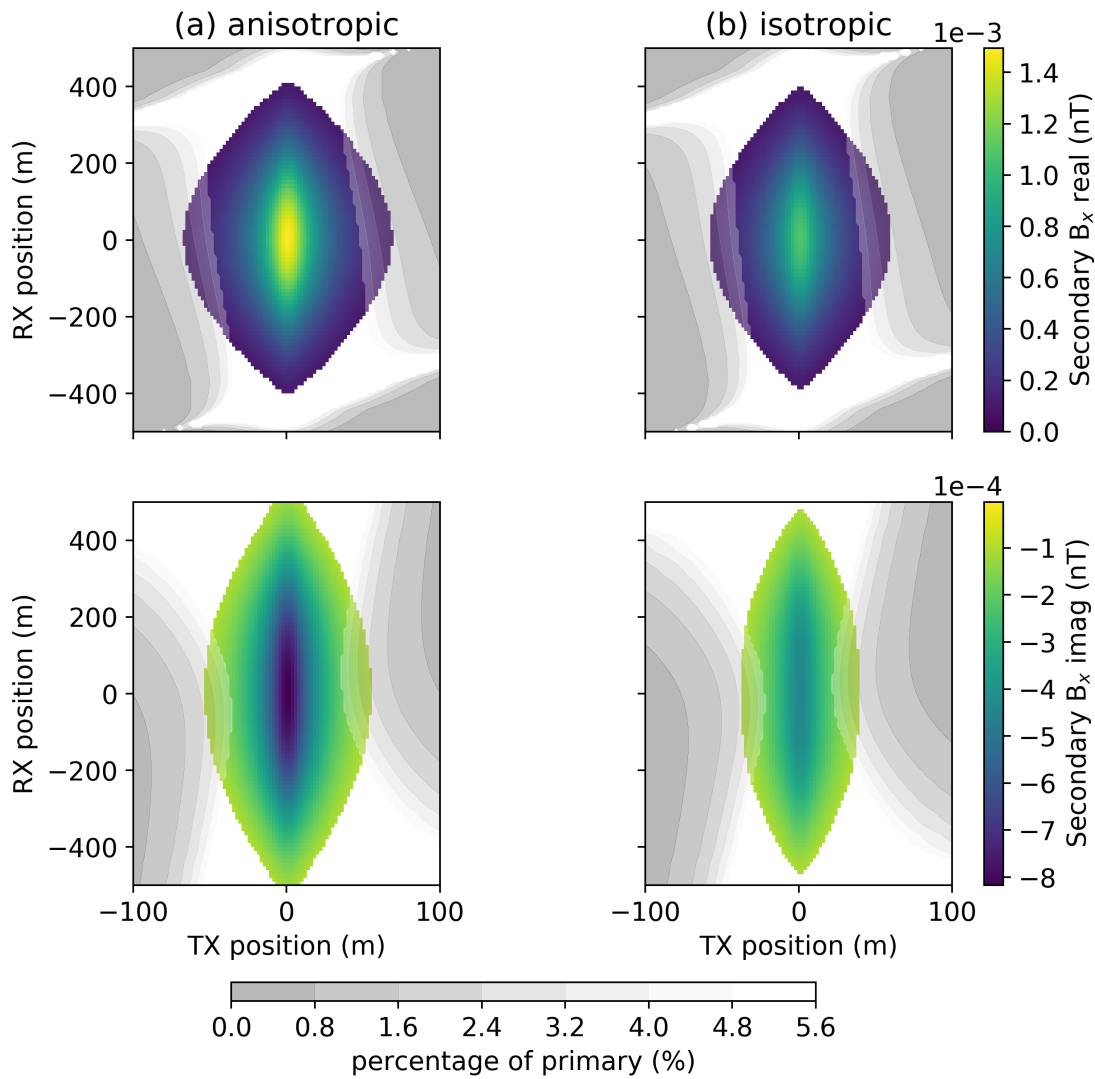


Figure 2.11: Simulated secondary magnetic field data for: (a) the anisotropic fracture model and (b) the isotropic fracture model, in a crosswell survey conducted at 100Hz. The top row shows the real component and the bottom row shows the imaginary component of the measured magnetic flux (nT). In all plots, the x-axis shows the transmitter location relative to the center of the fracture, the y-axis shows the receiver location, and the color indicates the secondary magnetic flux with respect to a 0.1 S/m whole-space. Values beneath the noise floor of 10^{-4} nT have been masked and display as white. To display the signal as a percentage of the primary, we have included a semi-transparent overlay between 0% and 5%; low percentage values plot as darker greys.

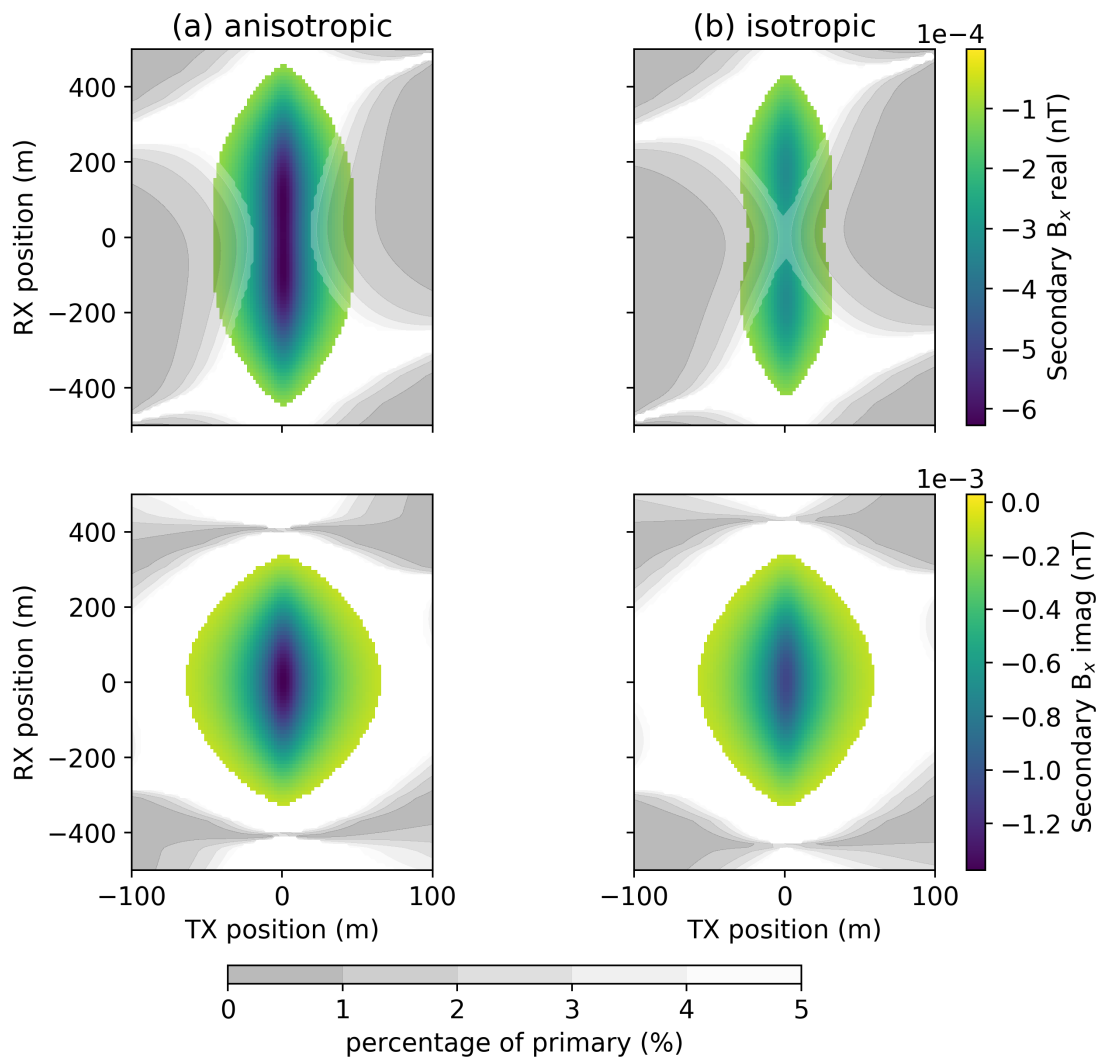


Figure 2.12: Simulated secondary magnetic field data for: (a) the anisotropic fracture model and (b) the isotropic fracture model, in a crosswell survey conducted at 200Hz. The top row shows the real component and the bottom row shows the imaginary component of the measured magnetic flux (nT), similar to Figure 2.11

both of the real and imaginary components of the data are above the noise floor and comprise a significant percentage of the primary field spanned ~ 100 m for the transmitter location and > 800 m for the receiver locations. These results provide confidence that EM is a potentially diagnostic tool for characterizing the propped region of a reservoir. Naturally, the success, or not, of EM in a given setting will depend upon the background conductivity, volume and conductivity of the proppant and fluid, as well as noise conditions in the field. Thus, forward modelling tailored to the setting is required to assess feasibility.

2.4 Conclusion

The large range of scales involved in describing a propped, fractured volume of rock as a geophysical target for an electromagnetic survey poses a challenge for performing numerical simulations. I approached this problem by using effective medium theory to estimate the electrical conductivity of a fracture volume of rock in two steps. First, I estimated the conductivity of a slurry containing proppant and fluid. I demonstrated several approaches for creating an electrically conductive slurry, including using conductive particles (or particles coated with a conductive material) as the proppant or including conductive particles, which might be elongated to enhance the conductivity at lower concentrations. General agreement with the values published in the laboratory experiment by Zhang et al. (2016) gives confidence that the estimates produced using effective medium theory are representative of the conductivities that can be achieved; a more rigorous comparison would require control on the conductivity of each of the constituents. In the second step, I estimated the effective conductivity of a fractured volume of rock by assuming that the fracture is composed of a collection of ellipsoidal cracks. These cracks may be preferentially oriented, if simple planar fractures are expected, or

randomly oriented if a more complex fracture network is anticipated.

Using this approach, I developed isotropic and anisotropic electrical conductivity models considering proppant and fluid volumes that are representative of current hydraulic fracture operations and simulated a crosswell EM survey. In this example, the fractured volume was detectable if I assume noise estimates that have demonstrated to be achievable in horizontal wells for a waterflood monitoring experiment. This provides evidence that EM has the potential to be a suitable method for characterizing the propped region of a hydraulically fractured reservoir.

The examples examined here neglect the effects of steel-cased well on EM signals. In the vast majority of settings where hydraulic fracturing is conducted, the wells are cased with steel, and therefore, this complication needs to be addressed. For induction problems, the concern is attenuation of the electromagnetic signals, as eddy currents may be induced in the steel cased well. However, there is increasing interest in using the steel casing as an “extended electrode” to help deliver current to depth. In the following chapters, I develop a strategy for including steel cased wells in the EM numerical simulations and examine their influence on EM signals.

Chapter 3

Modelling electromagnetics on cylindrical meshes

A number of geophysical electromagnetic (EM) problems lend themselves to cylindrical geometries. Airborne EM problems over a 1D layered earth or borehole-logging applications fall into this category; in these cases cylindrical modelling, which removes a degree of freedom in the azimuthal component, can be advantageous as it reduces the computation load. This is useful when running an inversion where many forward modellings are required, and it is also valuable when exploring and building up an understanding of the behaviour of electromagnetic fields and fluxes in a variety of settings, such as the canonical model of an airborne EM sounding over a sphere, as it reduces feedback time between asking a question and visualizing results (e.g. Oldenburg et al. (2017)).

Beyond these simple settings, there are also a range of scenarios where the footprint of the survey is primarily cylindrical, but 2D or 3D variations in the physical property model may be present. For example if we consider a single sounding in an Airborne EM

survey, the primary electric fields are rotational and the magnetic fields are poloidal, but the physical property model may have lateral variations or compact targets. More flexibility is required from the discretization to capture these features. In this case, a 3D cylindrical geometry, which incorporates azimuthal discretization may be advantageous. It allows finer discretization near the source where we have the most sensitivity and the fields are changing rapidly. Far from the source, the discretization is coarser, but it still conforms to the primary behaviour of the EM fields and fluxes and captures the rotational electric fields and poloidal magnetic flux.

In other cases, the most significant physical property variations may conform to a cylindrical geometry, for example in settings where vertical metallic well-casings are present, or in the emerging topic of using geophysics to “look ahead” of a tunnel boring machine. Of particular interest to the thesis is understanding the behavior of electromagnetic fields and fluxes in the presence of steel-cased wells. In addition to the hydraulic fracturing application, understanding EM in settings with steel-cased wells is of interest across a range of applications, from characterizing lithologic units with well-logs (Kaufman, 1990; Kaufman and Wightman, 1993; Augustin et al., 1989a), to identifying marine hydrocarbon targets (Kong et al., 2009; Swidinsky et al., 2013; Tietze et al., 2015), to mapping changes in a reservoir induced by hydraulic fracturing or carbon capture and storage (Pardo and Torres-Verdin, 2013; Börner et al., 2015; Um et al., 2015; Weiss et al., 2016; Hoversten et al., 2017; Zhang et al., 2018). Carbon steel, a material commonly used for borehole casings, is highly electrically conductive ($10^6 - 10^7$ S/m) and has a significant magnetic permeability ($\geq 100 \mu_0$) (Wu and Habashy, 1994); it therefore can have a significant influence on electromagnetic signals. The large contrasts in physical properties between the casing and the geologic features of interest, along with the large range of scales that need to be considered to model both the millimeter-thick

casing walls while also capturing geologic features, provide interesting challenges and context for electromagnetics in cylindrical geometries.

In this chapter, I introduce an approach and associated open-source software implementation for simulating Maxwell's equations over conductive, permeable models on 2D and 3D cylindrical meshes. The software is written in Python (Van Rossum and Drake Jr, 1995) and is included as an extension to the SimPEG ecosystem (Cockett et al., 2015); Appendix D provides a description of the SimPEG electromagnetic module. Within the context of current research connected to steel-cased wells, my aim with the development and distribution of this software is two-fold: (1) to facilitate the exploration of the physics of EM in these large-contrast settings, and (2) to provide a simulation tool that can be used for testing other EM codes. The large physical property contrasts in both conductivity and permeability means the physics is complicated and often non-intuitive; as such, we prioritize the ability of the researcher to access and visualize fields, fluxes, and charges in the simulation domain. This is particularly useful when the software is used in conjunction with Jupyter notebooks which facilitate exploration of numerical results (Perez et al., 2015). As the mesh conforms to the geometry of a vertical borehole, a fine discretization can be used in its vicinity without resulting in a onerous computation. This provides the opportunity to build an understanding of the physics of EM in settings with vertical boreholes prior to moving to settings with deviated and horizontal wells. I demonstrate the software with examples at DC, in the frequency domain, and in the time domain. Source-code for all examples is provided as Jupyter notebooks as outlined in Appendix A; they are licensed under the permissive MIT license with the hope of reducing the effort necessary by a researcher to compare to or build upon this work.

This chapter is organized in the following manner. In section 3.1, I introduce the

governing equations, Maxwell's equations, and describe their discretization in cylindrical coordinates. I then compare our numerical implementation to the finite element and finite difference results shown in (Commer et al., 2015) as well as a finite volume OcTree simulation described in (Haber et al., 2007). Section 3.2 contains numerical examples of the DC, frequency domain EM, and time domain EM implementations. The two DC resistivity examples (sections 3.2.1 and 3.2.2) are built upon the foundational work in (Kaufman, 1990; Kaufman and Wightman, 1993) which use asymptotic analysis to draw conclusions about the behavior of the electric fields, currents, and charges for a well where an electrode has been positioned along its axis. The final two examples, in sections 3.2.3 and 3.2.4, consider a frequency domain experiment inspired by (Augustin et al., 1989a). These examples demonstrate the impact of magnetic permeability on the character of the magnetic flux within the vicinity of the borehole and discusses the resulting magnetic field measurements made within a borehole.

3.1 Numerical tools

The governing equations under consideration are Maxwell's equations. I provided an overview in Section 1.4. This section is meant to provide a brief review and set the context for what is required of our numerical tools.

Under the quasi-static approximation, Maxwell's equations are given by:

$$\begin{aligned} \nabla \times \vec{e} + \frac{\partial \vec{b}}{\partial t} &= 0 \\ \nabla \times \vec{h} - \vec{j} &= \vec{s}_e \end{aligned} \tag{3.1}$$

where \vec{e} is the electric field, \vec{b} is the magnetic flux density, \vec{h} is the magnetic field, \vec{j} is the current density and \vec{s}_e is the source current density. Maxwell's equations can also be

formulated in the frequency domain, using the $e^{i\omega t}$ Fourier Transform convention, they are

$$\begin{aligned}\nabla \times \vec{E} + i\omega \vec{B} &= 0 \\ \nabla \times \vec{H} - \vec{J} &= \vec{S}_e\end{aligned}\tag{3.2}$$

The fields and fluxes are related through the physical properties: electrical conductivity (σ , or its inverse, resistivity ρ) and magnetic permeability (μ), as described by the constitutive relations

$$\begin{aligned}\vec{J} &= \sigma \vec{E} \\ \vec{B} &= \mu \vec{H}\end{aligned}\tag{3.3}$$

At the zero-frequency limit, we also consider the DC resistivity experiment, described by

$$\begin{aligned}\nabla \cdot \vec{j} &= I(\delta(\vec{r} - \vec{r}_{s^+}) - \delta(\vec{r} - \vec{r}_{s^-})) \\ \vec{e} &= -\nabla \phi\end{aligned}\tag{3.4}$$

where I is the magnitude of the source current density, \vec{r}_{s^+} and \vec{r}_{s^-} are the locations of the current electrodes, and ϕ is the scalar electric potential.

Of our numerical tools, we require the ability to simulate large electrical conductivity contrasts, include magnetic permeability, and solve Maxwell's equations at DC, in frequency and in time in a computationally tractable manner. Finite volume methods are advantageous for modelling large physical property contrasts as they are conservative and the operators "mimic" properties of the continuous operators, that is, the edge curl operator is in the null space of the face divergence operator, and the nodal gradient

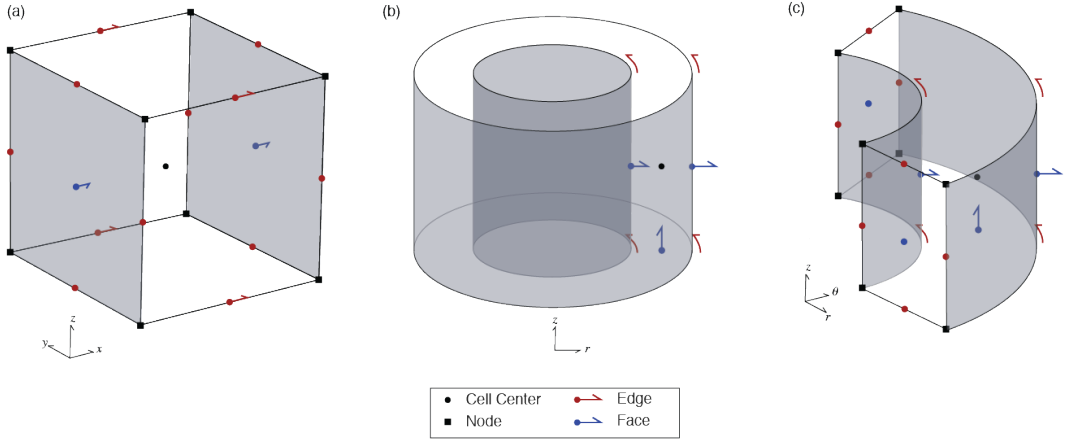


Figure 3.1: Anatomy of a finite volume cell in a (a) cartesian, rectangular mesh, (b) cylindrically symmetric mesh, and (c) a three dimensional cylindrical mesh.

operator is in the null space of the edge curl operator (Hyman and Shashkov, 1999). As such, they are common practice for many electromagnetic simulations (e.g. Horesh and Haber (2011); Haber (2014a); Jahandari and Farquharson (2014) and references within), and will be my method of choice.

3.1.1 Discretization

To represent a set of partial differential equations on the mesh, I use a staggered-grid approach (Yee, 1966) and discretize fields on edges, fluxes on faces, and physical properties at cell centers, as shown in Figure 3.1. Scalar potentials can be discretized at cell centers or nodes. I consider both cylindrically symmetric meshes and fully 3D cylindrical meshes; the anatomy of a finite volume cell for these scenarios is shown in Figure 3.1 (b) and (c).

To discretize Maxwell's equations in the time domain (equation 3.1) or in the frequency domain (equation 3.2), I invoke the constitutive relations to formulate our system

in terms of a single field and a single flux. This gives a system in either the electric field and magnetic flux (E-B formulation), or the magnetic field and the current density (H-J formulation). For example, in the frequency domain, the E-B formulation is

$$\begin{aligned} \mathbf{Ce} + i\omega \mathbf{b} &= \mathbf{s}_m \\ \mathbf{C}^\top \mathbf{M}_{\mu^{-1}}^f \mathbf{b} - \mathbf{M}_\sigma^e \mathbf{e} &= \mathbf{s}_e \end{aligned} \tag{3.5}$$

and the H-J formulation is

$$\begin{aligned} \mathbf{C}^\top \mathbf{M}_\rho^f \mathbf{j} + i\omega \mathbf{M}_\mu^e \mathbf{h} &= \mathbf{s}_m \\ \mathbf{Ch} - \mathbf{j} &= \mathbf{s}_e \end{aligned} \tag{3.6}$$

where $\mathbf{e}, \mathbf{b}, \mathbf{h}, \mathbf{j}$ are vectors of the discrete EM fields and fluxes; \mathbf{s}_m and \mathbf{s}_e are the discrete magnetic and electric source terms, respectively; \mathbf{C} is the edge curl operator, and the matrices $\mathbf{M}_{\text{prop}}^{e,f}$ are the edge / face inner product matrices. In particular, variable electrical conductivity and variable magnetic permeability are captured in the discretization. The time domain equations are discretized in the same manner; for time-stepping, a first-order backward Euler approach is used. Although the midpoint method, which is second-order accurate, could be considered, it is susceptible to oscillations in the solution, which reduce the order of accuracy, unless a sufficiently small time-step is used (Haber et al., 2004; Haber, 2014a). Appendix D provides more details on the discretization of Maxwell's equations in both the frequency and time-domains.

At the zero-frequency limit, each formulation has a complementary discretization for the DC equations. For the E-B formulation the discretization leads to a nodal dis-

cretization of the electric potential ϕ , giving

$$\begin{aligned} -\mathbf{G}^\top \mathbf{M}_\sigma^e \mathbf{e} &= \mathbf{q} \\ \mathbf{e} &= -\mathbf{G}\phi \end{aligned} \tag{3.7}$$

where \mathbf{G} is the nodal gradient operator, and \mathbf{q} is the source term, defined on nodes. Note that the nodal gradient takes the discrete derivative of nodal variables, and thus the output is on edges. The H-J formulation leads naturally to a cell centered discretization of the electric potential

$$\begin{aligned} \mathbf{V}\mathbf{D}\mathbf{j} &= \mathbf{q} \\ \mathbf{M}_\rho^f \mathbf{j} &= \mathbf{D}^\top \mathbf{V}\phi \end{aligned} \tag{3.8}$$

Where \mathbf{D} is the face divergence operator, \mathbf{V} is a diagonal matrix of the cell volumes, \mathbf{q} is the source term, which is defined at cell centers as is ϕ . Here, the face divergence takes the discrete derivative from faces to cell centers, thus its transpose takes a variable from cell centers to faces. For a tutorial on the finite volume discretization of the DC equations, see (Cockett et al., 2016b).

For the EM simulations, natural boundary conditions are employed; in the E-B formulation, this means $\vec{B} \times \vec{n} = 0|_{\partial\Omega}$, and in the H-J formulation, we use $\vec{J} \times \vec{n} = 0|_{\partial\Omega}$. Within the DC simulations, there is flexibility on the choice of boundary conditions employed. In the simplest scenario, for the nodal discretization, we use Neumann boundary conditions, $\sigma \vec{E} \cdot \vec{n} = 0|_{\partial\Omega}$, and for the cell centered discretization, we use Dirichlet boundary conditions $\phi = 0|_{\partial\Omega}$.

When employing a cylindrical mesh, the distinction between where the electric and magnetic contributions are discretized in each formulation has important implica-

tions. If we consider the cylindrically symmetric mesh (Figure 3.1b) and a magnetic dipole source positioned along the axis of symmetry (sometimes referred to as the TE mode), we must use the E-B formulation of Maxwell's equation to simulate the resulting toroidal magnetic flux and rotational electric fields. If instead, a vertical current dipole is positioned along the axis of symmetry (also referred to as the TM mode), then the H-J formulation of Maxwell's equations must be used in order to simulate toroidal currents and rotational magnetic fields. The advantage of a fully 3D cylindrical mesh is that it provides additional degrees of freedom, with the discretization in the azimuthal direction. This allows us to simulate more complex responses. However, in order to avoid the need for very fine discretization in the azimuthal direction, we should select the most natural formulation of Maxwell's equations given the source geometry being considered. For a vertical steel cased well and a grounded source, we expect the majority of the currents to flow vertically and radially, thus the more natural discretization to employ is the H-J formulation of Maxwell's equations.

Haber (2014a) provides derivations and discussion of the differential operators and inner product matrices; though they are described for a cartesian coordinate system and a rectangular grid, the extension to a three dimensional cylindrical mesh is straightforward. Effectively, a cartesian mesh is wrapped so that the x components become r components, and y components become θ components, as shown in Figure 3.2.

The additional complications that are introduced are: (1) the periodic boundary condition introduced on boundary faces and edges in the azimuthal direction, (2) the removal of radial faces and azimuthal edges along the axis of symmetry, and (3) the elimination of the degrees of freedom of the nodes and edges at the boundary and as well as the nodes and vertical edges along the axis of symmetry. The implementation of the 3D cylindrical mesh is provided as a part of the `discretize` package

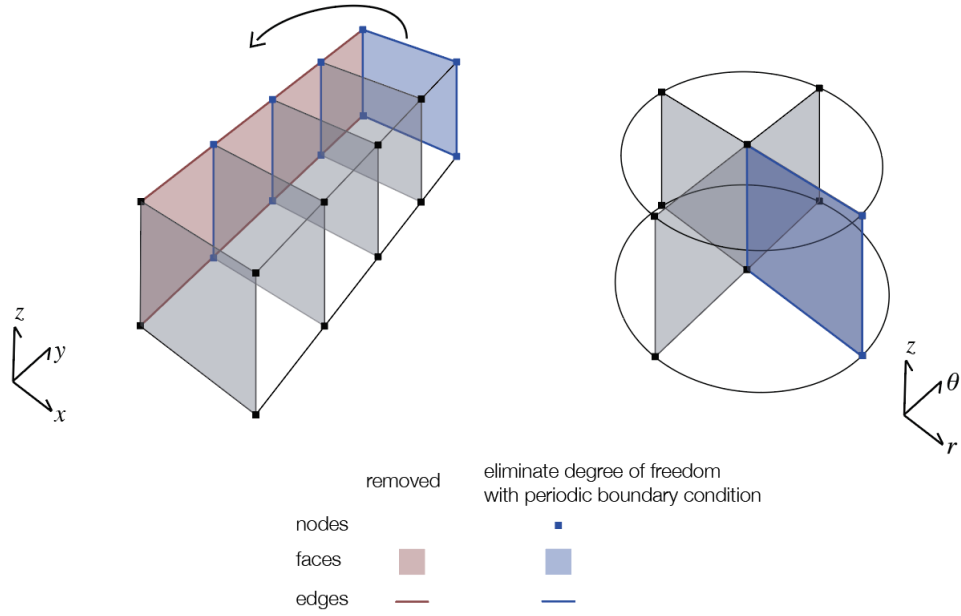


Figure 3.2: Construction of a 3D cylindrical mesh from a cartesian mesh.

(<http://discretize.simpeg.xyz>), which is an open-source python package that contains finite volume operators and utilities for a variety of mesh-types. All differential operators are tested for second order convergence and for preservation of mimetic properties (as described in Haber (2014a)). `discretize` is developed in a modular, object-oriented manner and interfaces to all of the SimPEG forward modelling and inversion routines, thus, once the differential operators have been implemented, they can be readily used to perform forward simulations (Cockett et al., 2015). One of the benefits of SimPEG for forward simulations is that values of the fields and fluxes are readily computed and visualized, which enables researchers to examine the physics as well as to simulate data. Development within the SimPEG ecosystem follows best practices for modern, opens-source software, including: peer review of code changes and additions, versioning, automated testing, documentation, and issue tracking.

3.1.2 Validation

Testing for the DC, TDEM, and FDEM implementations includes comparison with analytic solutions for a dipole in a whole-space. These examples are included as supplementary examples with the distributed notebooks. I have also compared the cylindrically symmetric implementation at low frequency with a DC simulation from a Resistor Network solution developed in MATLAB with (Figure 3 in Yang and Oldenburg (2016)).

Here, I include a comparison with the time domain electromagnetic simulation shown in Figures 13 and 14 of Commer et al. (2015). A 200m long well, with a conductivity of 10^6 S/m, outer diameter of 135 mm, and casing thickness of 12 mm is embedded in a 0.0333 S/m background. For the material inside the casing, I use a conductivity equal to that of the background. The conductivity of the air is set to 3×10^{-4} S/m and the permeability of the casing is ignored ($\mu = \mu_0$). A 10 m long inline electric dipole source is positioned on the surface, 50 m radially from the well. The radial electric field is sampled at 5 m, 10 m, 100 m, 200 m and 300 m along a line 180° from the source.

Two simulations are included in Commer et al. (2015): a finite element (FE) and a finite difference (FD) solution. Both simulation meshes capture the thickness of the casing with a single cell or single tetrahedral element. The finite element solution mesh consisted of over 8 million tetrahedral elements and the simulation completed in 63 hours on a single core of an Intel Xeon X5550 processor (2.67 GHz). For the finite difference solution, a conservative time-stepping was used ($\Delta t = 3 \times 10^{-10}$ s), resulting in a total of >120 million time steps. This simulation took 23.2 hours using 512 cores on an Intel Xeon architecture (2.33 GHz).

Additionally, I include a comparison with the 3D UBC finite volume OcTree time domain code (Haber et al., 2007). The OcTree mesh allows for adaptive refinement of the mesh around sources, receivers, and conductivity structures within the domain, thus

reducing the number of unknowns in the domain as compared to a tensor mesh. The mesh in the UBC simulation included 5,011,924 cells, with the finest cells being equal to the width of the casing; 154 time steps were taken and 10 different step-lengths were used (requiring 10 different matrix factorizations). This simulation took 57 minutes to run on a single Intel Xeon X5660 processor (2.80GHz).

For the 3D cylindrical simulation, I use a mesh that has 4 cells radially across the width of the casing, 2.5 m vertical discretization, and azimuthal refinement near the source and receivers (along the $\theta = 90^\circ$ line), as shown in Figure 3.3. The mesh has a total of 309 120 cells. For the time discretization, the smallest time-step I use is 10^{-6} s; the time-mesh is coarsened at later times. I used a moderately conservative time-stepping scheme with 187 time-steps total. Seven different step-lengths were employed, requiring seven matrix factorizations. To solve the system matrix, the direct solver PARDISO was used (Petra et al., 2014; Cosmin et al., 2016). The simulation took 14 minutes to run on a single Intel Xeon X5660 processor (2.80GHz).

In Figure 3.4, I show the absolute value of the radial electric field sampled at five stations; each of the different line colors is associated with a different location, and offsets are with respect to the location of the well. Solutions were interpolated to the same offset using nearest neighbor interpolation. The 3D cylindrical simulation (SimPEG) is plotted with a solid line and overlaps with the UBC solution (dash-dot line) for all times shown. The finite element (FE) solution from Commer et al. (2015) is shown with the dashed lines, and the finite difference (FD) solution is plotted with dotted lines. The 3D cylindrical (SimPEG) and UBC solutions are overall in good agreement with the solutions from Commer et al. (2015). There is a difference in amplitude and position of the zero-crossing (the v-shape visible in the blue and orange curves) between the Commer solutions and the SimPEG / UBC solutions at the shortest two offsets in the early

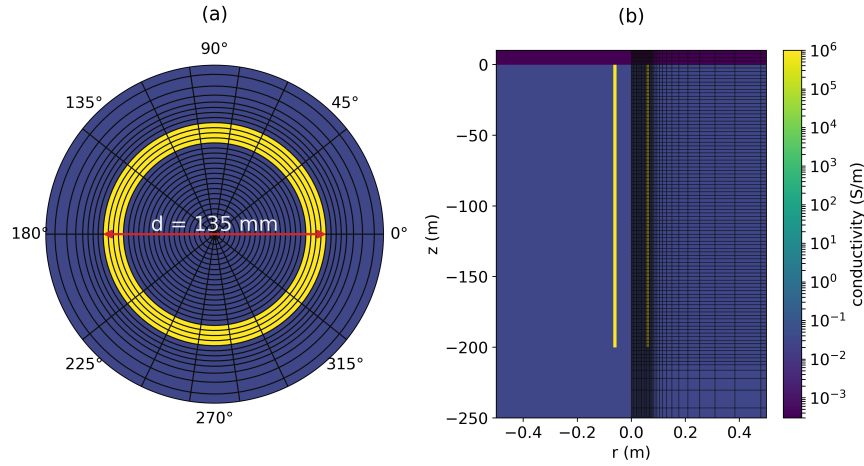


Figure 3.3: Depth slice (left) and cross section (right) through the 3D cylindrical mesh used for the comparison with Commer et al. (2015). The source and receivers are positioned along the $\theta = 90^\circ$ line. The mesh extends 3600 m radially and 3300 m vertically to ensure that the fields have sufficiently decayed before reaching the boundaries.

times. At such short offsets from a highly conductive target, details of the simulation and discretization, such as the construction of the physical property matrices in each of the various approaches become significant; this likely accounts for the discrepancies but a detailed code-comparison is beyond the scope of this chapter. My aim with this comparison is to provide evidence that the numerical simulation is performing as expected; the overall agreement with Commer’s and UBC’s results is provides confidence that it is.

This example demonstrates agreement between the 3D cylindrical solution and solutions obtained with independently developed codes. Importantly, it also shows how, by using a cylindrical discretization which conforms to the conductivity structure of interest, the size of the mesh and resultant cost of the computation can be greatly reduced. This is true even with relatively conservative spatial and temporal discretizations. Minimizing computation time was not a main focus in the development of the software and

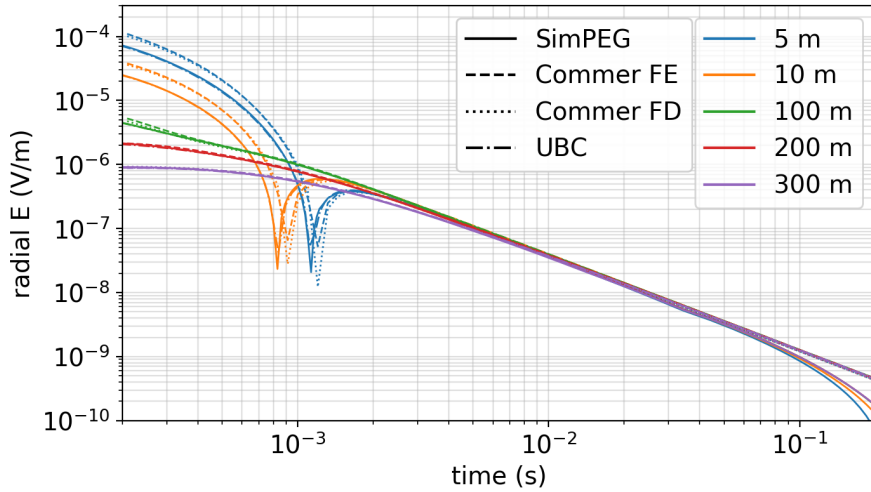


Figure 3.4: Time domain EM response comparison with (Commer et al., 2015). Each of the different line colors is associated with a different location; offsets are with respect to the location of the well.

there are still opportunities for improving efficiency. As an open-source project, contributions from the wider community are encouraged.

3.2 Numerical Examples

The numerical experiments I consider in this section are motivated by the need to use this software to delve into the physics of DC and EM in settings with steel cased wells. As such, the examples build upon examples in analytical derivations and asymptotic analyses in Kaufman (1990); Kaufman and Wightman (1993) at DC and Augustin et al. (1989a) for frequency domain EM. I do this to provide confidence that the physical phenomena we observe in the simulations are expected by theory as well as to build a foundation for discussion in the subsequent chapters.

3.2.1 DC Resistivity Part 1: Electric fields, currents and charges in a long well

In his two seminal papers on the topic, Kaufman uses transmission line theory to draw conclusions about the behaviour of the electric field when an electrode is positioned inside of an infinite casing. In this first example, I will revisit some of the physical insights discussed in (Kaufman, 1990; Kaufman and Wightman, 1993) that followed from an analytical derivation and compare those to my numerical results. In the second example, I look at the distribution of current and charges as the length of the well is varied and compare those to the analytical results discussed in (Kaufman and Wightman, 1993)

I start by considering a 1 km long well (10^6 S/m) in a whole space (10^{-2} S/m), with the conductivity of the material inside the borehole equal to that of the whole space. For modelling, I will use a cylindrically symmetric mesh. The positive electrode is positioned on the borehole axis in the mid-point of a 1 km long well; a distant return electrode is positioned 1 km away at the same depth.

Kaufman discusses the behavior of the electric field by dividing the response into three zones: a near zone, an intermediate zone and a far zone (Kaufman, 1990; Kaufman and Wightman, 1993). In the near zone, the electric field has both radial and vertical components, negative charges are present on the inside of the casing, and positive charges are present on the outside of the casing. The near zone is quite localized and typically, its vertical extent is no more than ~ 10 borehole radii away from the electrode. To examine these features in our numerical simulation, I have plotted in Figure 3.5: (a) the total charge, (b) secondary charges, (c) electric field, and (d) current density in a portion of the model near the source.

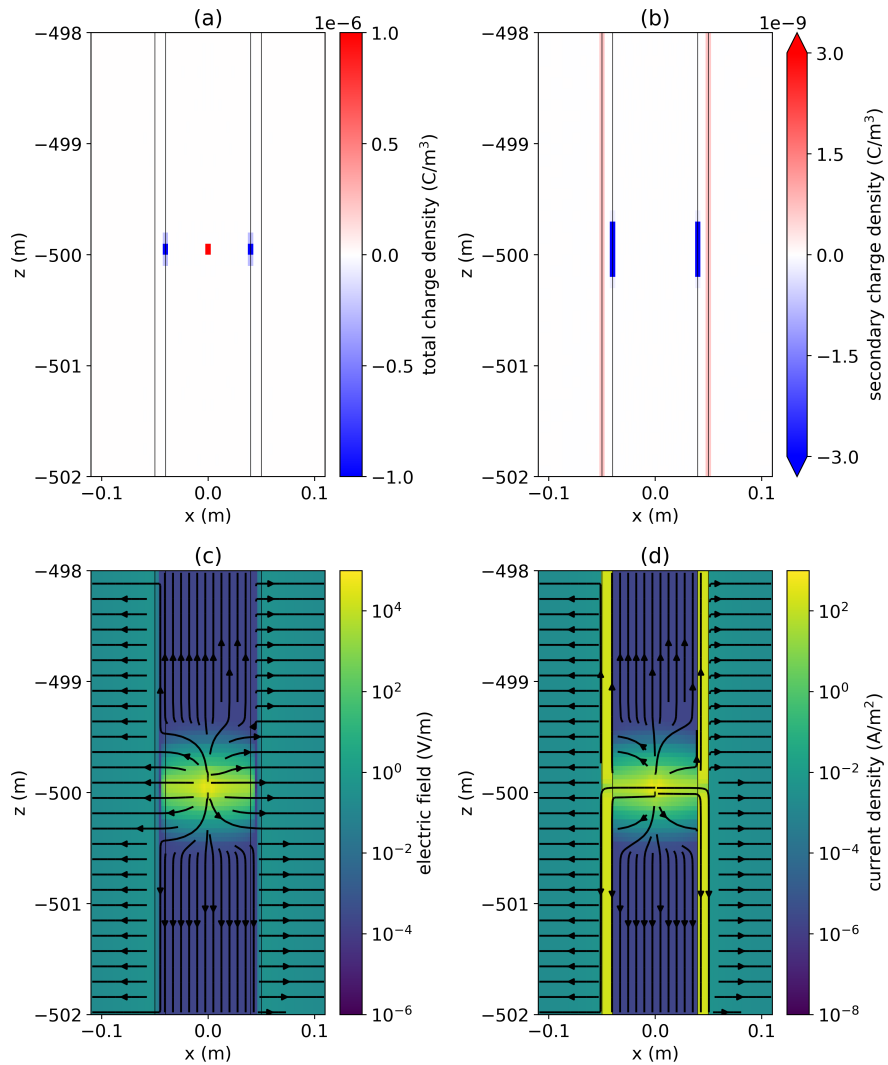


Figure 3.5: (a) Total charge density, (b) secondary charge density, (c) electric field, and (d) current density in a section of the pipe near the source at \$z = -500\$ m.

Discussion

Within the near-zone, the total charge is dominated by the large positive charge at the current electrode location and negative charges that exist along the casing wall where current is moving from a resistive region inside the borehole into a conductor. The extent of the negative charges along the inner casing wall is more evident when we look at the secondary charge, which is obtained by subtracting the charge that would be observed in a uniform half-space from the total charge (Figure 3.5b). Inside the casing, we can see the transition from near-zone behavior to intermediate zone behavior approximately 0.5 m above and below the source; that is equal to 10 borehole radii from the source location, which agrees with Kaufman's conclusion.

In the intermediate zone, Kaufman discusses a number of interesting aspects with respect to the behavior of the electric fields and currents which we can compare with the observed behavior in Figure 3.5. Among them, he shows that the electric field within the borehole and casing is directed along the vertical axis; as a result no charges accumulate on the inner casing wall. Charges do, however, accumulate on the outer surface of the casing; these generate radially-directed electric fields and currents, often referred to as leakage currents, within the formation. At each depth slice through the casing and borehole, the electric field is uniform, however, due to the high conductivity of the casing, most of the current flows within the casing. The vertical extent of the intermediate zone depends on the resistivity contrast between the casing and the surrounding formation and extends beyond several hundred meters before transitioning to the far zone, where the influence of the casing disappears (Kaufman, 1990).

The radially directed fields from the casing, and the length of the intermediate zone, have practical implications in the context of well-logging because they delineate the region in which measurements can be made to acquire information about the formation

resistivity outside the well. Within the intermediate zone, fields behave like those due to a transmission line (Kaufman, 1990), and multiple authors have adopted modelling strategies that approximate the well and surrounding medium as a transmission line (Kong et al., 2009; Aldridge et al., 2015). I will extend this analysis in the next example and discuss how the length of the well impacts the behavior of the charges, fields, and fluxes.

3.2.2 DC Resistivity Part 2: Finite Length Wells

In (Kaufman and Wightman, 1993), the transmission-line analysis was extended to consider finite-length wells. Inspired by the interest in using the casing as an “extended electrode” for delivering current to depth (e.g. Schenkel and Morrison (1994); Um et al. (2015); Weiss et al. (2016); Hoversten et al. (2017)), here I consider a 3D DC resistivity experiment where one electrode is connected to the top of the well. I will examine the current and charge distribution for wells ranging in length from 250 m to 4000 m and compare those to the observations in (Kaufman and Wightman, 1993). The conductivity of the well is selected to be 10^6 S/m. A uniform background conductivity of 10^{-2} S/m is used and the return electrode is positioned 8000 m from the well; this is sufficiently far from the well that we do not need to examine the impact of the return electrode location in this example. A 3D cylindrical mesh was used for the simulation.

Kaufman and Wightman (1993) derives a solution for the current within a finite length well and discusses two end-member cases: a short well and a long well. “Short” versus “long” are defined on the product of αL_c , where L_c is the length of the casing and $\alpha = 1/\sqrt{ST}$, where S is the cross-sectional conductance of the casing and has units of S·m ($S = \sigma_c 2\pi a \Delta a$, for a casing with radius a and thickness Δa), and T is the transverse resistance. The transverse resistance is approximately equal to the resistivity of the sur-

rounding formation (for more discussion on where this approximation breaks down, see Schenkel and Morrison (1994)). For short wells, $\alpha L_c \ll 1$, the current decreases linearly with distance, whereas for long wells, where $\alpha L_c \gg 1$, the current decays exponentially with distance from the source, with the rate of decay being controlled by the parameter α . In Figure 3.6 (a), I show current in the well for 5 different borehole lengths. The x-axis is the distance from the source normalized by the length of the well. I also show the two end-member solutions (equations 45 and 53) from Kaufman and Wightman (1993). There is significant overlap between the 250m numerical solution and the short well approximation. As the length of the well increases, exponential decay of the currents becomes evident. Since α is quite small, for this example $\alpha = 2 \times 10^{-3} \text{ m}^{-1}$, the borehole must be very long to reach the other end member which corresponds to the exponentially decaying solution.

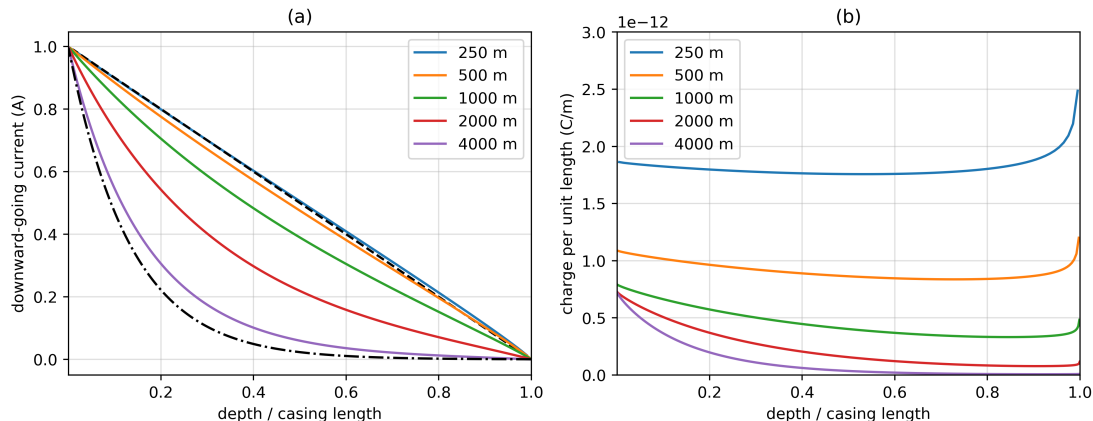


Figure 3.6: (a) Current along a well for 5 different wellbore lengths. The x-axis is depth normalized by the length of the well. The black dashed line shows the short-well approximation (equation 45 in Kaufman and Wightman (1993)) for a 200 m long well. The black dash-dot line shows the long-well approximation (equation 53 in Kaufman and Wightman (1993)) for a 4000 m well. (b) Charge per unit length along the well for 5 different wellbore lengths.

In Figure 3.6 (b), I have plotted the charges along the length of the well. In the short-

well regime, the borehole is approximately an equipotential surface and the charges are uniformly distributed; in the long well the charges decay with depth. What was surprising to me was the noticeable increase in charge accumulation that occurs near the bottom of the well. This is especially evident for the short well. Initially, I was suspicious and thought this might be due to problems with our numerical simulation; there was no obvious physical explanation that I was aware of. However, investigation into the literature revealed that the increase in charge density at the ends of a cylinder is a real physical effect, but an exact theoretical solution does still not appear to exist (Griffiths and Li, 1997) (see figure 4, in particular).

Discussion

The results shown in Figure 3.6 have implications when testing approaches for reducing computational load by approximating a well with a solid tube or prism, as in Um et al. (2015), or replacing the well with a distribution of charges, as in Weiss et al. (2016). For a short well, the behaviour of the currents is independent of conductivity, so, as long as the borehole is approximated by a sufficiently conductive target, the behaviour of the fields and fluxes will be representative of the fine-scale model. However, as the length of the well increases, the cross-sectional conductance of the well becomes relevant as it controls the rate of decay of the currents in the well and thus the rate that currents leak into the formation. A similar result holds when a line of charges is used to approximate the well as a DC source; a uniform charge is suitable for a sufficiently short or sufficiently conductive well, whereas a distribution of charge which decays exponentially with depth needs to be considered for longer wells. Thus, when attempting to replace a fine-scale model of a well with a coarse-scale model, either with a conductivity structure or by some form of “equivalent source”, validations should be

performed on models that have the same length-scale as the experiment to ensure that both behaviors are being accurately modeled.

3.2.3 Frequency Domain Electromagnetics Part 1: Comparison with scale model results

In the DC example, we discussed how charges are distributed along the well and currents flow into the formation. From a historical perspective, practical developments in EM were pursued in the frequency domain; the mathematics is more manageable in the frequency domain, and technological advances were being made in the development of induction well-logging tools (Doll, 1949; Moran and Kunz, 1962). Although conductivity of the pipes is generally plays the most dominant role in attenuating the signal, the magnetic permeability is non-negligible (Wait and Hill, 1977); it is the product of the conductivity and permeability that appears in the description of EM attenuation. Also, the fact that permeable material becomes magnetized in the presence of an external field complicates the problem. Augustin et al. (1989a) is one of the first papers on induction logging in the presence of steel cased wells that aims to understand and isolate the EM response of the steel cased well. Using a combination of scale modelling and analytical mathematical modelling, they examine the impacts of conductivity and magnetic permeability on the magnetic field observed in the pipe. In this example and the one that follows, I attempt to unravel this interplay between conductivity and magnetic permeability.

The first experiment Augustin et al. (1989a) discuss is a scale model using two different pipes, a conductive copper pipe and a conductive, permeable iron pipe; each pipe is 9 m in length. The copper pipe had an inner diameter of 0.063 m and a thickness of 0.002 m, while the iron pipe had a 0.063 m inner diameter and 0.0043 m wall thickness.

A source-loop, with radius 0.6 m was co-axial with the pipe and in one experiment positioned at one end of the pipe (which they refer to as the “semi-infinite pipe” scenario). In another experiment the source loop is positioned at the midpoint of the pipe (which they refer to as the “infinite pipe” scenario); for both experiments, magnetic field data are measured as a function of frequency at the central axis of the pipe. Their results are presented in terms of a Field Strength Ratio (FSR), which is the ratio of the absolute value of the magnetic field at the receiver with the absolute value of the magnetic field if no pipe is present (Figure 3 in Augustin et al. (1989a)). At low frequencies, for the data collected within the iron pipe, static shielding ($\text{FSR} < 1$) was observed for the measurements where the receiver was in the plane of the source loop for both the “infinite” and “semi-infinite” scenarios. When the receiver was positioned within the pipe, 1.49 m offset from the plane of the source loop, static enhancement effects ($\text{FSR} > 1$) were observed for both the infinite and semi-infinite scenarios. Using this experiment for context, I will compare the behaviour of our numerical simulation with the observations in (Augustin et al., 1989a) and examine the nature of the static shielding and enhancement effects.

For our numerical setup, the pipes are 9 m in length and have an inner diameter of 0.06 m. The copper pipe has a casing-wall thickness of 0.002 m and the iron pipe has a thickness of 0.004 m. Following the estimated physical property values from Augustin et al. (1989a), I use a conductivity of 3.5×10^7 S/m and a relative permeability of 1 for the copper pipe. For the iron pipe, a conductivity of 8.0×10^6 S/m and a relative permeability of 150 is used. A background conductivity of 10^4 Ωm is assumed. The computed FSR values for the axial magnetic field as a function of frequency are shown in Figure 3.7.

Consider the response of the conductive pipe. At low frequencies, the FSR for the

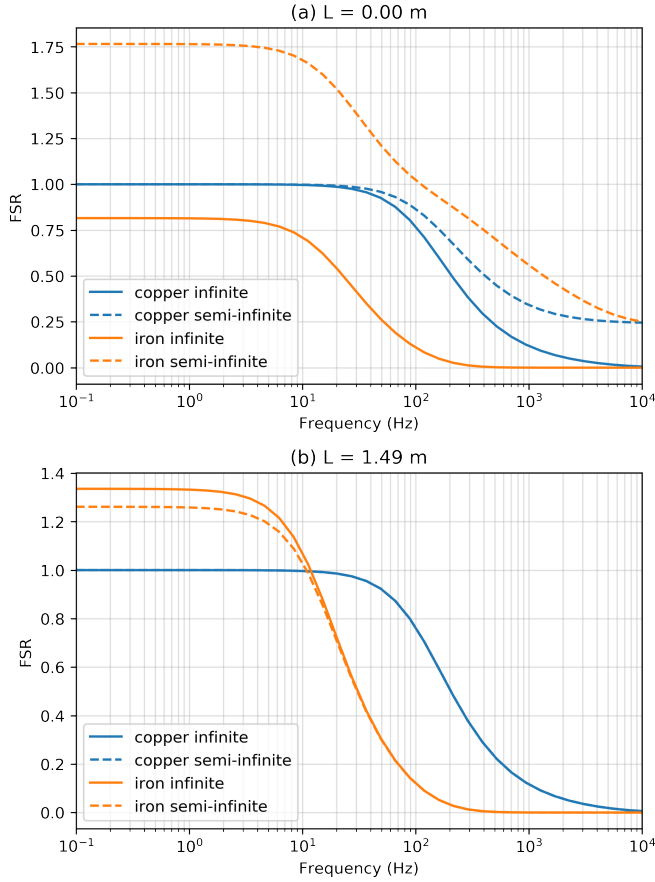


Figure 3.7: Field strength ratio (FSR), the ratio of the measured vertical magnetic field with the free space magnetic field, as a function of frequency for two different receiver locations. In (a), the receiver is in the same plane as the source, in (b), the receiver is 1.49 m offset from the source.

copper pipe (blue lines) is 1 for both the infinite (solid line) and semi-infinite (dashed line) scenarios, as the field inside the copper pipe is equivalent to the free-space field. With increasing frequency, eddy currents are induced in the pipe which generate a magnetic field that opposes the primary, causing a decrease in the observed FSR. When the source and receiver are in the same plane ($L=0.00 \text{ m}$), the rate of decrease is more rapid in the infinite scenario than the semi-infinite. Since there is conductive material on both sides of the receiver in the infinite case, we would expect attenuation of the fields to

occur more rapidly than in the semi-infinite case. This observation is consistent with Figure 3a in Augustin et al. (1989a). For the offset receiver ($L=1.49$ m), they observed a slight separation in the infinite and semi-infinite curves which I do not; however, they attributed this to potential errors in magnetometer position. Thus, overall, the numerical results for the copper pipe are in good agreement with the scale model results observed by Augustin et al. (1989a).

Next, we examine the response of the conductive, permeable pipe. In Figure 3.7b, we observe a static enhancement effect ($FSR > 1$) at low frequencies. The enhancement is larger in the infinite scenario than the semi-infinite scenario; this is in agreement with Figure 3b in Augustin et al. (1989a). There is however, a significant discrepancy between our numerical simulations and the scale model for the semi-infinite pipe when the source and receiver lie in the same plane (Figure 3.7a). Augustin et al. (1989a) observed a static shielding effect for both the infinite and semi-infinite scenarios, whereas we observe a static shielding for the infinite scenario, but a significant static enhancement for the semi-infinite case. To examine what might be the cause of this, I will examine the magnetic flux density in this region of the pipe.

In Figure 3.8, I have plotted: (a) the secondary magnetic flux in the infinite-pipe scenario near the source ($z = -4.5$ m), (b) the secondary magnetic flux in the semi-infinite scenario ($z=0$ m for the source), and (c) top 5 cm of the semi-infinite pipe. All plots are at 0.1 Hz. The primary magnetic field is directed upwards within the regions I have plotted, so upward-going magnetic flux indicates a static enhancement effect, and downward-oriented magnetic flux indicates static shielding effects. In (a) we see a transition between the static shielding in the vicinity of the source to a static enhancement approximately 0.5 m above and below the plane of the source. Similarly in (b), we notice a sign-reversal in the z-component of the secondary magnetic flux at a depth of 0.6

m.

Discussion

The behaviors observed in Figure 3.8 are quite comparable to Augustin et al.'s observation of a transition from shielding to enhancement occurring at distances greater than 0.8 m from the source. Numerical experiments show that the vertical extent of the region over which static shielding is occurring increases with increasing pipe diameter, and similarly increases with increasing loop radius while the magnitude of the effect decreases. This can be understood by considering how the pipe is magnetized; for a small loop radius, the magnetization is largely localized near the plane of the source and rapidly falls off with distance from the plane of the source. Localized, large amplitude magnetization causes the casing to act as a collection of dipoles around the circumference of the casing. As the radius of the loop increases, the magnetization spreads out along the length of the well resulting in longer, lower-amplitude dipoles, thus both increasing the extent of the region over which static shielding is occurring as well as decreasing its amplitude.

This explains the nature of the static enhancement and static shielding effects, but to explain the discrepancy between the static shielding observed in the semi-infinite pipe when $L=0$ m by Augustin et al., and the static enhancement we observe in Figure 3.7a, I examine the magnetic flux density in the top few centimeters of the pipe. Figure 3.8c shows the top 5 cm of the secondary magnetic flux in the semi-infinite pipe; the source is in the $z=0$ m plane. Zooming in reveals there is yet another sign reversal near the end of the pipe. This is evident even in the infinite-pipe scenario (Figure 3.7d), where the source is offset by several meters from the end of the pipe. This edge-effect perhaps bears some similarities to what we observed in Figure 3.6b, where we saw a build up

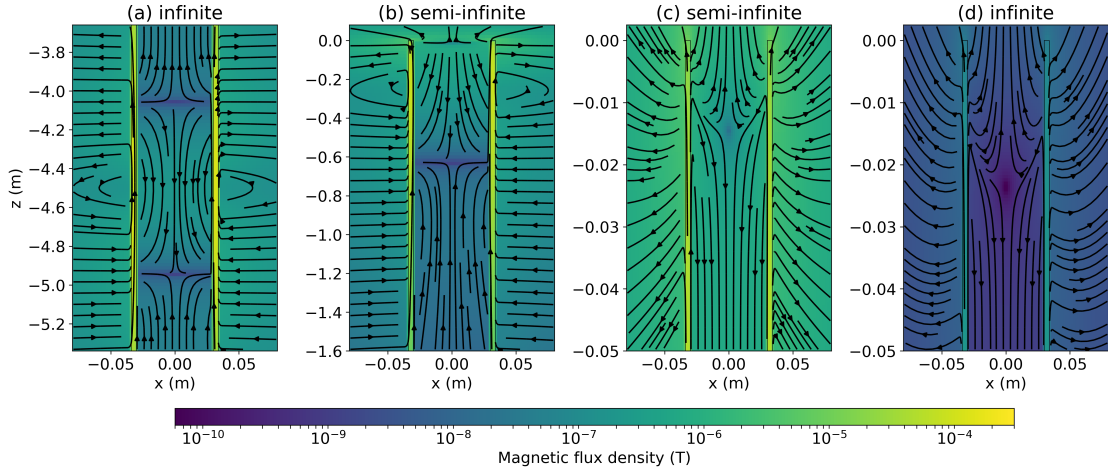


Figure 3.8: Magnetic flux density at 0.1 Hz in the region of the pipe near the plane of the source for (a) the “infinite” pipe, where the source is located at -4.5 m and the pipe extends from 0 m to -9 m, (b) a “semi-infinite” pipe, where the source is located at 0 m and the pipe extends to -9 m. In (c), we zoom in to the top 5 cm of the “semi-infinite” pipe, and (d) shows the 5 cm at the top-end of the “infinite” pipe.

of charge near the end of the pipe in the DC scenario. At the end of the pipe, we encounter the situation where the normal component of the flux (\vec{j}, \vec{b}) from the pipe to the background needs to be continuous both in the radial and vertical directions at the end of the pipe as does the tangential component of the fields (\vec{e}, \vec{h}). The interplay of these two constraints at the end of the pipe results in more complexity in the resultant fields and fluxes. Within the span of a few centimeters we transition from static enhancement at the top of the pipe to a static shielding further down. An error as small as a few centimeters in the position of the magnetometer causes a reversal in behavior; in Figure 3.9, I have plotted the FSR for a magnetometer positioned 3 cm beneath the plane of the source, and the static-shielding behavior observed for the semi-infinite pipe is much more aligned with that observed in Figure 3a in Augustin et al. (1989a).

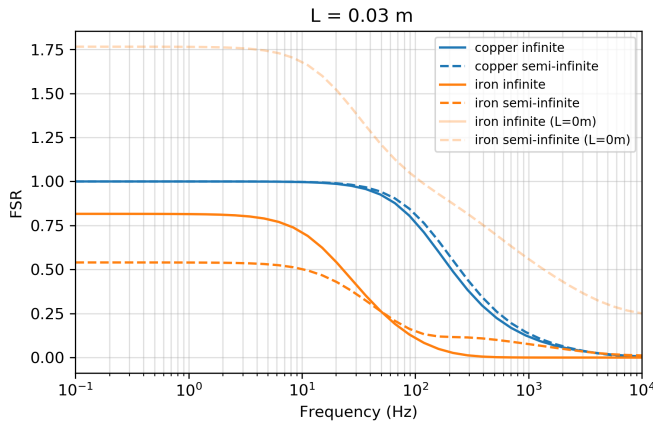


Figure 3.9: Field strength ratio, FSR, for a receiver positioned 3 cm beneath the plane of the source. For comparison, we have plotted the FSR for the permeable pipe when the source and receiver lie in the same plane ($L=0.00\text{ m}$) with the semi-transparent orange lines. Note that the infinite-pipe solutions for $L=0.03\text{ m}$ and $L=0.00\text{ m}$ overlap.

3.2.4 Frequency Domain Electromagnetics Part 2: Conductivity and permeability in the inductive response of a well

The experiments shown in the previous section revealed some insights into the complexity of the fields within the pipe and illustrated the role of permeability in the character of the responses at low frequency. Next, we move to larger scales and examine the role of conductivity and permeability in the responses we observe in the borehole.

In this example, I consider a 2 km long well with an outer diameter of 10 cm and thickness of 1 cm in a whole-space which has a resistivity of $10^4 \Omega\text{m}$. A loop with radius 100 m is coaxial with the well and positioned at the top-end of the well. A receiver measuring the z-component of the magnetic flux density is positioned 500 m below the transmitter loop, along the axis of the well. I will consider both time domain and frequency domain responses.

In electromagnetics, it is often the product of permeability and conductivity that

is considered to be the main controlling factor on the EM responses. To assess the contribution of each to the measured responses, I will investigate two scenarios. In the first, the well has a conductivity of 10^8 S/m and a relative permeability of 1, and in the second, the well has a conductivity of 10^6 S/m and a relative permeability of 100; thus the product of conductivity and permeability is equivalent for both wells.

Similar to the analysis done by Augustin et al. (1989a) when looking at the role of borehole radius in the behaviour of the magnetic response (e.g. figure 8), I will examine the normalized secondary field (NSF) which is the ratio of the secondary field with the amplitude of the primary, where the primary is defined to be the free-space response. In Figure 3.10, I have plotted the normalized secondary field for the two pipes considered, the conductive pipe (blue) and the conductive, permeable pipe (orange). Let us start by examining the conductivity response in Figure 3.10. Where the value of the NSF is zero, the primary dominates the response; this is the case at low frequencies where induction is not yet contributing to the response. As frequency increases, currents are induced in the pipe which generate a secondary magnetic field that opposes the primary, hence the NSF becomes negative. When the real part of the NSF (solid line) is -1, the secondary magnetic field is equal in magnitude but opposite in direction to the free-space primary and the measured real field is zero. Values less than -1 indicate a sign reversal in the real magnetic field. Similarly, when the imaginary part of the response function goes above zero, there is a sign reversal in the imaginary component. Note that these sign reversals occur even in a half-space and are a result of sampling the fields within a conductive medium; in this case the receiver was 500 m below the surface.

As compared to the conductive pipe, the frequency at which induction sets in is higher for the conductive, permeable pipe. We also notice that the amplitude variation of both the imaginary and real parts is larger for the permeable pipe. To examine the con-

tribution of conductivity and permeability to the responses, I have plotted the real part of the secondary magnetic flux density, \mathbf{b} , in Figure 3.11. The top row shows the response within the conductive pipe and the bottom row shows the conductive, permeable pipe. The primary magnetic flux is oriented upwards and we can see that all of the secondary fields generated are oriented downwards. Similar to the previous example, we see that at low frequencies, there is magnetostatic response due to the permeable pipe. However, due to the larger length scales of the source loop and the casing in this example, there is no measurable contribution at the receiver. At 1 Hz, we can see that induction is starting to contribute to the signal for the conductive pipe, while for the permeable pipe, it is not until ~ 10 Hz that we begin to observe the contribution of induction. At 100 Hz, the secondary magnetic field is stronger in amplitude than the primary, and the NFS is less than -1 for both the conductive and permeable pipes. The amplitude of the secondary within the permeable pipe is stronger than that in the conductive pipe. At 1000 Hz, we have reached the asymptote of $\text{NSF}=-1$ for both the conductive and permeable pipes; the secondary magnetic flux is equal in magnitude but opposite in direction to the primary.

Conducting a similar experiment in the time domain, we can compare the responses as a function of time. For this experiment, a step-off waveform is employed and data are measured after shut-off, the NSF is plotted in Figure 3.12. Note here that the secondary field is in the same direction as the primary, so after the source has been shut off, the secondary field is oriented upwards, as shown in Figure 3.13. Shortly after shut-off, the rate of increase in the secondary field is the same for both the conductive and the conductive, permeable wells. A maximum normalized field strength of approximately 1 is reached for both cases. The responses begin to differ at 10^{-3} s where the conductive well maintains a $\text{NFS} \sim 1$ for approximately 1 ms longer than the permeable well before the fields decay away.

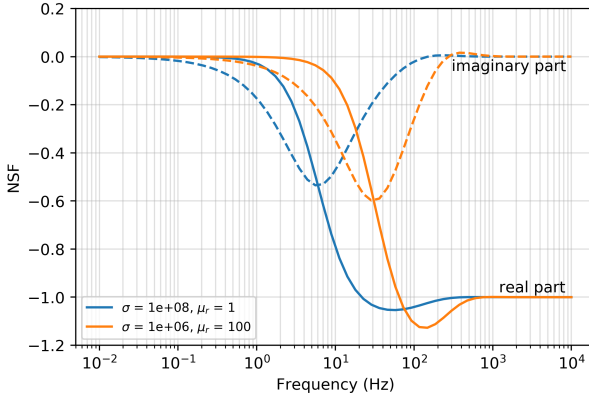


Figure 3.10: Normalized secondary field, NSF, as a function of frequency for two wells. The NSF is the ratio of the secondary vertical magnetic field with the primary magnetic field at the receiver location ($z = -500$ m); the primary is defined as the whole-space primary.

Discussion

It is important to note that although the product of the conductivity and permeability is identical for these wells, the geometry of the well and inducing fields results in different couplings for each of the parameters. For a vertical magnetic dipole source, the electric fields are purely rotational while the magnetic fields are primarily vertical. An approximation we can use to understand the implications of these geometric differences is to assume the inducing fields are uniform (e.g. the radius of the source loop is infinite) and to examine the conductance and permeance of the pipe. For rotational electric fields, the conductance is

$$\mathcal{S} = \sigma \frac{tL}{2\pi r} \quad (3.9)$$

where t is the thickness of the casing, r is the radius of the casing and L is the length-scale of the pipe segment contributing to the signal. For vertical magnetic fields, the

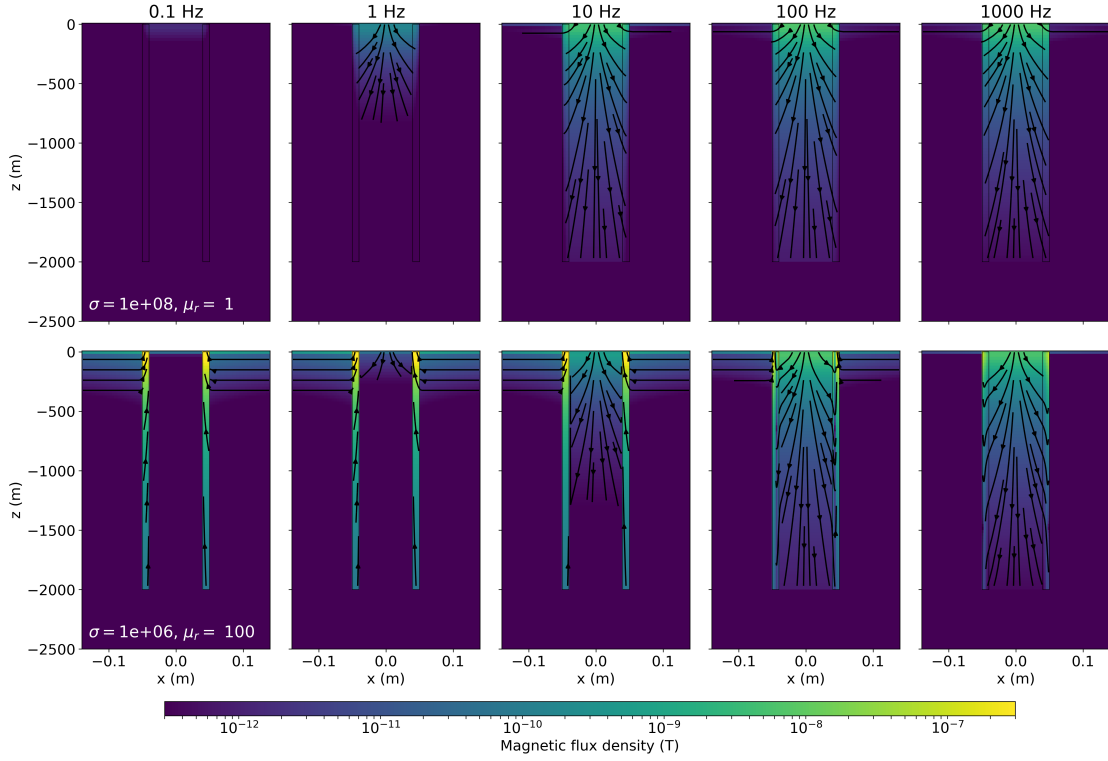


Figure 3.11: Secondary magnetic flux density (with respect to a whole-space primary) at five different frequencies for a conductive pipe (top row) and for a conductive, permeable pipe (bottom row).

permeance is

$$\mathcal{P} = \mu \frac{t^2 \pi r}{L} \quad (3.10)$$

As the length-scale, L , is larger than the circumference of the pipe ($2\pi r$) the geometric contribution to the conductance is larger than that to the permeance.

An important take-away from this example is that the contributions of conductivity and permeability to the observed EM signals are not simply governed by their product. The geometry of the source fields plays an important role in how each contributes. Thus to accurately model conductive, permeable pipes, over a range of frequencies or times, a numerical code must allow both variable conductivity and variable permeability to be

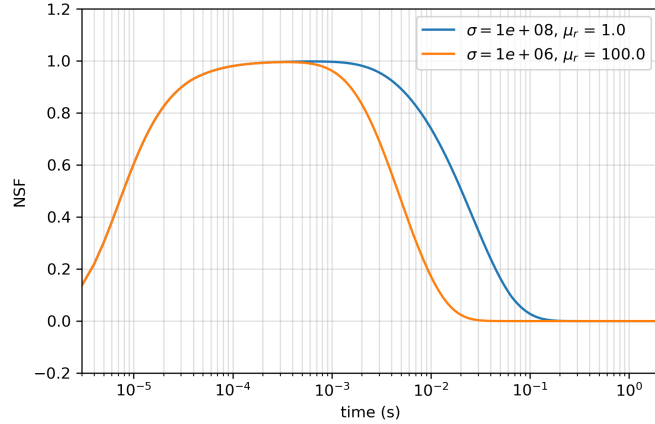


Figure 3.12: Normalized secondary field (NSF) through time. In the time-domain, we compute the NSF by taking the difference between the total magnetic flux at the receiver and the whole-space response and then taking the ratio with the whole-space magnetic flux prior to shutting off the transmitter.

considered.

3.3 Summary and Outlook

I have developed software for solving Maxwell's equations on 2D and 3D cylindrical meshes. The medium can have variable electrical conductivity and magnetic permeability. The 2D solution is especially computationally efficient and has a large number of practical applications. When cylindrical symmetry is not valid, the 3D solution can be implemented; a judicious design of the mesh can often generate a problem with fewer cells than would be required with a tensor or OcTree mesh, thus reducing the computational cost of a simulation. I demonstrated the versatility of the codes by modelling the electromagnetic fields that result when a highly conductive and permeable casing is embedded in the earth.

I presented a number of different experiments involving DC, frequency-domain, and time-domain sources. The first two examples considered a simple DC resistivity exper-

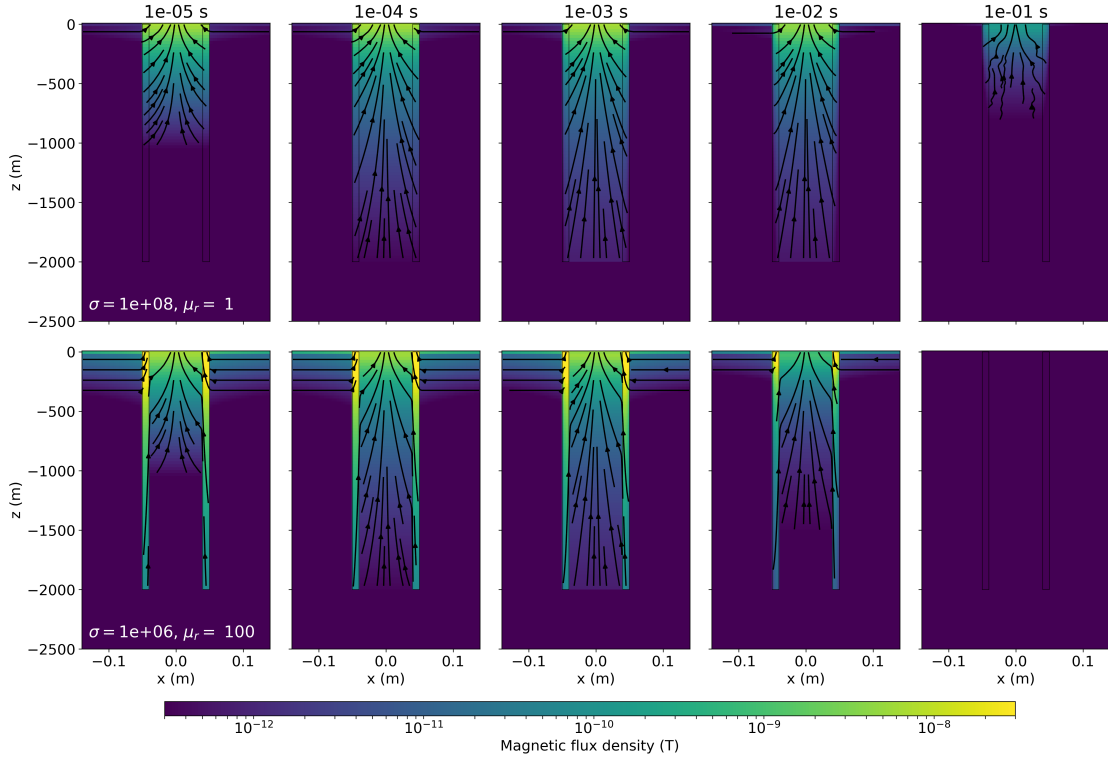


Figure 3.13: Secondary magnetic flux density for a conductive well (top row) and a conductive, permeable well (bottom row) through time. The source waveform is a step-off waveform.

iment. In the first, I demonstrated that the numerically obtained currents, electric fields, and charges emulated those predicted by the asymptotic analysis in Kaufman (1990) for long wells. The second example looked at the transition in behavior of currents and charges between short and long wells. Even in this relatively simple example, the physics was more complex than I originally anticipated; I had not intuitively expected to see the large increase in charge density that was observed near the ends of the well.

In the subsequent examples, I considered electromagnetic experiments and incorporated magnetic permeability in the simulations. I showed that for a conductive and permeable casing, excited by a circular current source, there is a complicated magnetic

field that occurs in the top few centimeters of the pipe. Furthermore, the role of conductivity and permeability in the observed responses is more complex than their product; the source geometry and coupling with the casing are important to consider.

As new strategies and software are developed to handle more complex well-geometries, such as deviated or horizontal wells, it is important that we establish an understanding of the physics. Of critical importance is the ability to plot the charges, fields, and fluxes in the simulations. This is valuable for understanding the responses obtained from the experiment and it is a solid foundation for designing a field survey. I anticipate that the software provided with this thesis can be a resource for building understanding and additionally, serve as a tool for testing 3D simulations with boreholes present.

The software implementation is included as a part of the SimPEG ecosystem. SimPEG also includes finite volume simulations on 3D tensor and OcTree meshes as well as machinery for solving inverse problems. This means that the cylindrical codes can be readily connected to an inversion and additionally, simulations and inversions of more complex 3D geologic settings can be achieved by coupling the cylindrical simulation with a 3D tensor or OcTree mesh using a primary-secondary approach (e.g. example 3 in Appendix D). Beyond modelling steel cased wells, the 3D cylindrical mesh could prove to be useful in conducting 3D airborne EM inversions where a domain-decomposition approach, similar to that described in Yang et al. (2014), is adopted.

Chapter 4

Direct current resistivity with steel-cased wells

4.1 Introduction

Subsurface resistivity can be a valuable part of a geologic interpretation, whether that be identifying lithologic units, characterizing changes within a reservoir, or imaging subsurface injections associated with carbon capture and storage or hydraulic fracturing. In many of these settings, steel-cased wellbores are present. Steel has a significant electrical conductivity, which is generally six or more orders of magnitude larger than that of the surrounding of the geologic formation. Clearly, such a large contrast is important to consider when conducting a direct current (DC) resistivity survey. On one-hand, the role of the steel casing may be viewed as “distortion” which complicates the signals of interest (Wait, 1983; Holladay and West, 1984; Johnston et al., 1987). In other scenarios, a wellbore may be beneficial in that it can serve as an “extended electrode” so that current-injection and sampling of the resultant electrical potentials can take place

beneath near surface heterogeneities (Ramirez et al., 1996; Rucker et al., 2010; Rucker, 2012; Ronczka et al., 2015) or so that currents injected at the surface can reach significant depths (Schenkel and Morrison, 1994; Weiss et al., 2016; Hoversten et al., 2017). The use of casings as extended electrodes extends back several decades. Sill and Ward (1978) used the well casing as a buried electrode for their mis-à-la-masse experiment at the Roosevelt Hot Springs geothermal field in Utah, as did ?auahikaua et al. (1980) for their mis-à-la-masse mapping of a high temperature geothermal reservoir in Hawaii. Sill (1983) used the well as a source to monitor an injection test at Raft River, Idaho to determine if measurable changes that might indicate the direction of fluid flow could be observed. Rocroi and Koulikov (1985) delineated a known resistive hydrocarbon deposit in the USSR by injecting current into two cased wells. More recently, applications for hydraulic fracturing, enhanced oil recovery and carbon capture and storage have been of much interest (Commer et al., 2015; Um et al., 2015; Weiss et al., 2016; Hoversten et al., 2017).

To build a physical understanding of electrical and electromagnetic methods in settings where steel-cased wells are present, there are several areas to be investigated. First, the significant conductivity of the steel will impact the behavior of the charges, currents, and electric fields. This is true at the electrostatic limit, relevant to DC resistivity surveys, as well as when the source fields are time-varying, as in electromagnetic (EM) surveys. When considering EM surveys, induction effects also influence the responses, and magnetic fields and fluxes become relevant, meaning that the magnetic permeability of the steel then introduces further complexity into the signals we measure. This chapter is concerned with the first set of physical phenomena: understanding the physics of steel casings at DC.

Much of the initial theory and understanding of the behavior of electric fields, cur-

rents, and charges, was developed in the context of well-logging. Kaufman (1990) and Kaufman and Wightman (1993) provide a theoretical basis for our understanding; the first paper derives an analytical solution for a DC experiment where an electrode is positioned along the axis of an infinite length well, and discusses where charges accumulate and how currents leak into the surrounding formation. From this, Kaufman (1990) shows that by measuring the second derivative of the electric potential, information about the formation resistivity can be obtained. The second paper extends the analysis for finite length wells. Schenkel and Morrison (1990); Schenkel (1991); Schenkel and Morrison (1994) pioneered numerical work analyzing the influence of steel-cased wells on geophysical data using an integral equation approach for solving the DC resistivity problem. They expand upon the logging-through-casing application and discuss limitations of the transmission line solution presented in Kaufman (1990) for this application. They also explored the feasibility of cross-hole and borehole-to-surface surveys where one electrode is placed within, or beneath, a cased borehole. These examples demonstrated that the casing can improve detectability of a conductive target as compared to the scenario where no cased well is present.

In this chapter, I focus on three aspects of DC resistivity in the presence of steel-cased well. In section 4.2, I examine the feasibility of conducting a surface DC survey to detect a flaw in the casing and discuss factors that influence detectability of a flaw. In section 4.3, I examine the use of DC resistivity for geophysical imaging when a steel-cased well is present. Finally, in section 4.4, I assess strategies applied in the literature for approximating a steel-cased well with a coarse-scale model to reduce computational cost.

Source codes for all of the simulations shown are open source, licensed under the MIT license, and are available as Jupyter notebooks (see Appendix A). The examples

in the paper have been selected with an emphasis on examining physical principles; however, I envision that the Jupyter notebooks included with this chapter could serve as useful survey design tools.

4.2 DC resistivity for casing integrity

Degraded or impaired wells can pose environmental and public-health hazards. A flaw in the cement or casing can provide a conduit for methane to migrate from depth into groundwater aquifers or into the atmosphere. This is particularly of concern for shale gas wells. Elevated levels of thermogenic methane, which are attributed to deep sources (rather than biogenic methane which can be generated closer to the surface), in groundwater wells in Pennsylvania has been positively correlated with proximity to shale gas wells in the Marcellus and Utica (Osborn et al., 2011; Jackson et al., 2013), and failure rates of unconventional wells (e.g. shale gas wells) is estimated to be 1.57 times larger than that of a conventional well drilled in the same time-period (Ingraffea et al., 2014). Wells can fail if there is a compromise in the cement or the casing. To diagnose the integrity of a well with electrical methods, we require a contrast in electrical conductivity to be associated with the flaw, thus I will focus attention to detecting flaws in the highly conductive casing.

Under what circumstances should we be able to detect a flaw in the casing using DC resistivity from the surface? To address this question, I begin by examining how a flaw which comprises the entire circumference of the pipe along some depth interval changes the charge distribution and thus the resultant electric fields we measure on the surface. From there, I investigate the role of parameters including the depth of the flaw and the background conductivity on our ability to detect it from the surface. Finally, I examine the scenario in which only a portion of the circumference of the pipe is flawed.

4.2.1 Basic experiment

The experiment I consider is a “top-casing” DC resistivity experiment where one electrode is connected to the wellbore at the surface and a return electrode is positioned some distance away. The concept and basic physics is the same as a mis-à-la-masse survey in which the positive electrode is connected to a conductive target. When the source is turned on, positive charges are distributed on the interface between the conductive target and the resistive host. Electric potentials are measured on the surface and these data are then used to infer information about the extent of the conductor (Telford et al., 1990a). Applying the same principles to a casing integrity experiment, I connect a positive electrode to the casing, and for an intact casing, positive charges will be distributed on the outer interface of the casing along its entire length. If corrosion causes a flaw across the diameter of the casing, the continuity of the conductive flow-path for charges is interrupted, thus we expect a larger charge on the top portion of the flawed casing than we would if it were intact. This results in a larger electric field at the surface than would be observed if the casing were intact. The difference in electric field (or electric potentials) from the expected electric field that results from an intact well could then be an indicator that there is a problem with the well.

To demonstrate the principles, I start by considering a simple model of a casing in a half-space. The intact well is 1 km long, has an outer diameter of 10 cm, a thickness of 1 cm and a conductivity of 5×10^6 S/m. The background is 10^{-1} S/m background, and the conductivity of the inside of the well is taken to be equal to that of the background. The positive electrode is connected to the top of the casing and the return electrode is positioned 2 km away. To simulate the physics, the 3D cylindrical DC code described in Chapter 3 was employed. In Figure 4.1 I show cross-sections of the: (a) electrical conductivity model, (b) current density, (c) charge density, and (d) electric field for

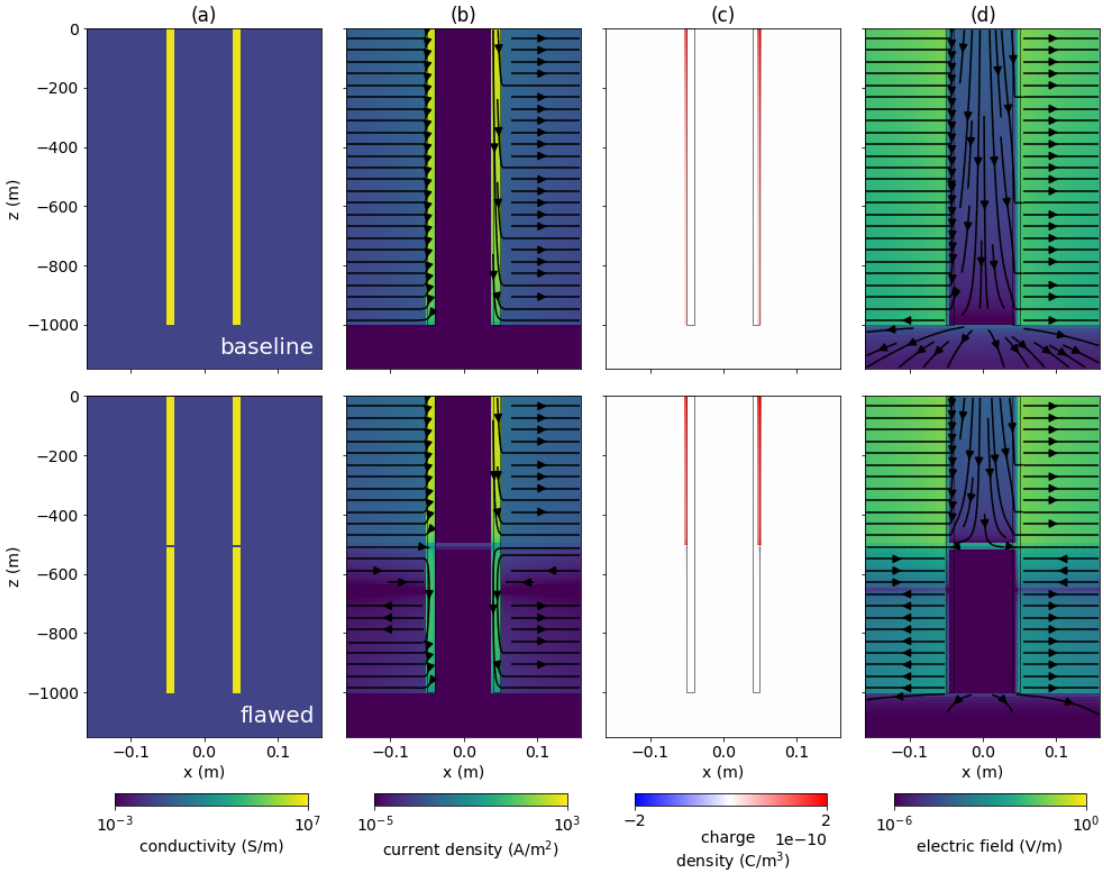


Figure 4.1: Cross section showing: (a) electrical conductivity, (b) current density, (c) charge density, and (d) electric field for a top-casing DC resistivity experiment over (top) an intact 1000 m long well and (bottom) a 1000 m long well with a 10 m flaw at 500 m depth.

the intact well (top row) and a flawed well (bottom row) that contains a 10 m gap in the casing at 500 m depth. As expected, the introduction of a resistive flaw prevents currents from reaching the bottom portion of the well. This results in increased currents, charge density and thus electric fields within the top 500 m.

To quantify the charge along the length of the well, I have plotted the charge as a function of depth for the intact well (black), flawed well (blue), and also a short well of 500 m length (grey dash-dot) in Figure 4.2a. In each of the wells, we observe that there

is an increase in charge density near the end of the discontinuity along the length of the well. This was also noted in Griffiths and Li (1997) and in Chapter 3 – this behavior is attributed to edge effects. At an interface between materials with two different conductivities, the normal component of the current density must be conserved, as well as the tangential component of the electric field; the discontinuity at the end of the pipe, and at the location of the flaw, means the continuity conditions must be preserved simultaneously in the radial and vertical directions, and this complicates the behavior of the fields, fluxes and charges. Another observation is that the flawed and short wells have nearly identical charge distributions in the top 500 m. In the bottom portion of the flawed well, where the remaining conductive material is, a small dipolar charge is introduced, but this is nearly an order of magnitude smaller than the charge in the top portion of the pipe. The signal due to the flaw can be defined as the difference between the total response due to a flawed well and the total response due to an intact well (the primary); I will refer to this difference as the secondary response. The secondary charge is dipolar in nature with positive charge above the flaw and negative charge beneath the flaw. Note that the charge distributions along the short well, truncated where the flaw starts at 500 m depth, and along the top portion of the flawed well are almost identical; these charges are the source of signal for a surface electric field measurement. This suggests that an inversion strategy, where one attempts to estimate the length of a well, may be an effective approach for characterizing the depth to a flaw.

Impact of the vertical extent of the flaw

A 10 m flaw is quite long and it is of interest to see how the results are changed if the flaw has a smaller vertical extent. The distribution of charges shown in Figure 4.2 hints that the flaw may not need to be very long in order to still significantly influence the

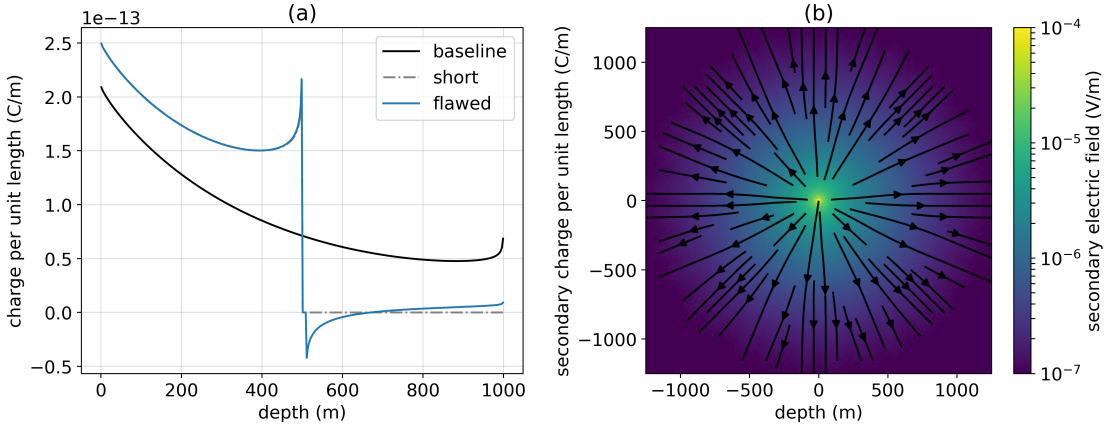


Figure 4.2: (a) Charge along the length of the intact well (black), a 500 m well (“short”, grey dash-dot), and a well with a 10 m flaw at 500 m depth (blue), in a top-casing DC resistivity experiment. (b) Secondary electric field due on the surface of the earth due to the flaw in the casing. The primary is defined as the electric field due to the 1000 m long intact well. The return electrode is 2000 m away from the well.

response. To confirm this, I adopt a much finer vertical discretization in order to model smaller flaws. Here, I use a shorter, 50 m long well in order to reduce computational load. The flaw is positioned at 25 m depth, and the length of the impairment is varied. This simulation is conducted on a cylindrically symmetric mesh, the positive electrode is connected to the casing, and a return electrode is positioned 50 m away.

The resultant charge distributions are shown in Figure 4.3. For comparison, I again show the charge on a well that is truncated at the location of the flaw; this is the “short” well and results are displayed using the grey dash-dot line. The charge distribution is similar for all of the flawed-well scenarios, even for flaws smaller than the thickness of the casing (10^{-2} m). We see similar behavior to that shown in Figure 4.2, where positive charge accumulates within the top portion of the well and a small dipole charge is present in the bottom portion of the well. There are minor differences in amplitude as the vertical extent of the flaw is changed; as the extent of the flaw decreases, the ampli-

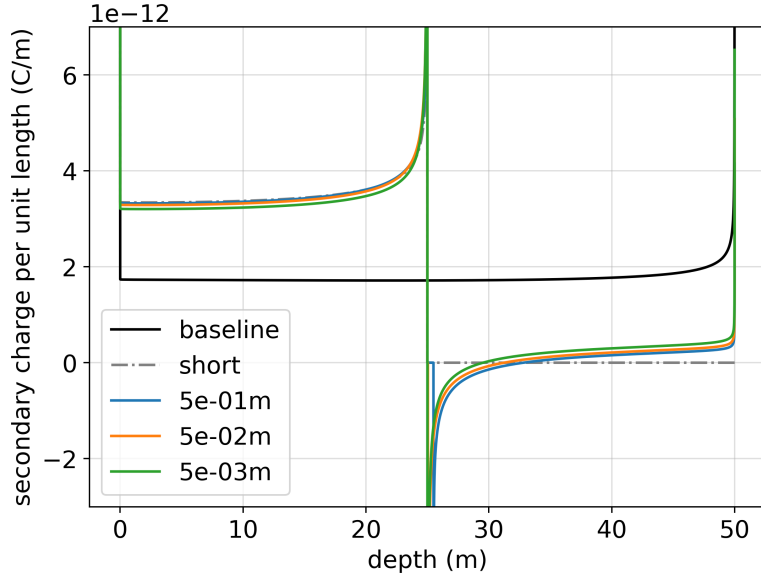


Figure 4.3: Charge along the length of a 50 m long intact well (black), a 25 m well (“short”, grey dash-dot), and four wells, each with a flaw starting at 25 m depth and extending the length indicated by the legend (5×10^{-1} m (blue), 5×10^{-2} m (orange), and 5×10^{-3} m (green)) in a top-casing DC resistivity experiment. For reference, the diameter of the casing is 10^{-1} m and its thickness is 10^{-2} m. The return electrode is 50 m away from the well and a cylindrically symmetric mesh was used in the simulation.

tude of the dipolar charge on the bottom portion of the well increases slightly while the amplitude of the positive charge on the top portion of the well decreases. These distinctions, however, are small in magnitude, and even if the background is more conductive, the casing is still orders-of-magnitude larger in conductivity than any geologic material we are likely to encounter. Thus, I conclude that, so long as the impairment affects the entire circumference of the casing, the extent of that flaw has little impact on the charge that accumulates in the top portion of the well. As such, I will proceed in our analysis using a 10 m flaw in the 1 km well so that a fine vertical discretization is not necessary.

4.2.2 Survey design considerations

When examining detectability of a signal, there are two aspects to consider: (1) the signal must be larger than the noise floor of the instrument, and (2) the signal must be a significant percentage of the primary; for the casing integrity experiment, the primary is the signal due to the intact well. Due to the cylindrical symmetry of the charge on the well, we expect the electric field at the surface to be purely radial, thus only radial electric field data need be collected at the surface.

In Figure 4.4, I have plotted the primary field (top row), secondary field (second row) and secondary field as a percentage of the primary (third row) for four different return electrode locations. In (a), the return electrode is 2000 m offset from the well, in (b) the offset is 750 m, in (c) the offset is 500 m, and in (d) the offset is 250 m. In addition to the plan view, I have plotted the primary electric field (black), total electric field for the flawed well (blue) and secondary radial electric field (orange) along the $\theta = 90^\circ$ azimuth in the fourth row of Figure 4.4. The fifth row shows the secondary as a percentage of the primary.

At the furthest offset (Figure 4.4a), there is nearly complete cylindrical symmetry in the primary field. With complete cylindrical symmetry there is no preferential direction along which to collect data. As I move the return electrode closer, for example to 750 m from the well, we notice that the secondary electric field does not change substantially. However, if I examine the ratio of the secondary to the primary (second and fifth rows), we see that the ratio has increased. Although the primary field has similar, if not larger amplitude near the well, it also has considerable curvature. As a result, the proportion of the primary field that is in the radial direction has decreased in amplitude. Hence the important characteristic, the ratio of the secondary to primary of the radial components, has increased. The above principles are further enhanced as the return current is brought

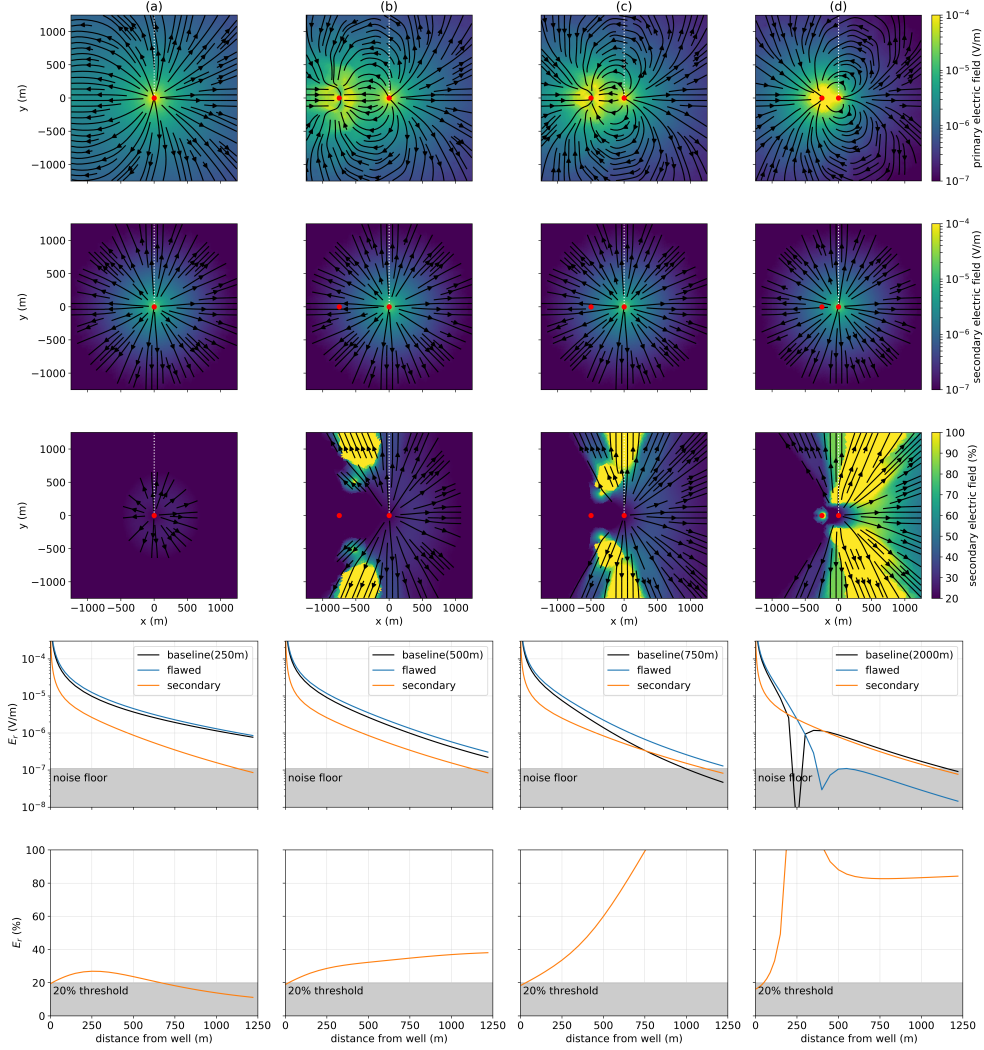


Figure 4.4: (Top row) primary electric field, (second row) secondary electric field, and (third row) secondary electric field as a percentage of the primary radial electric field for a return electrode that is offset (a) 2000 m, (b) 750 m, (c) 500 m, and (d) 250 m from the well. The primary is defined as the response due to the 1000 m long, intact well. Electrode locations are denoted by the red dots. In the third row, the colorbar has been limited between 20% and 100%. The fourth and fifth rows show radial electric field data collected along the $\theta = 90^\circ$ azimuth (white dotted lines in the top three rows). The fourth row shows the primary (black line), the total electric field due to the flawed well (blue line), and the secondary radial electric field (orange line). The fifth row shows the secondary as a percentage of the primary.

closer to the well as in panels (c) and (d), where the return electrode is brought to 500 m and 250 m from the well. Again, for all of these examples the amplitude of the secondary field at the surface is quite similar. However, the choice of azimuth for the survey line will greatly affect the size of the ratio. In terms of survey design, we can take advantage of the return electrode to reduce coupling with the primary.

For our following examples I will place the return electrode at 500 m from the well and collect radial data along a line that is perpendicular to the source line. I will examine several factors influencing detectability of a flaw, including the depth of the flaw and the conductivity of the background in the following sections. I will also examine the scenario where only a portion of the circumference of the well has been compromised.

4.2.3 Factors influencing detectability

Depth of the flaw

The introduction of a flaw in the well changes the distribution of charges along the length of the well and causes a secondary dipolar charge centered about the flaw. The position and strength of this dipole will affect our ability to detect the flaw. To examine this, I have taken the same model of a 1km pipe in a 10^{-1} S/m background and varied the depth of the flaw from 300 m to 900 m. In Figure 4.5, I plot radial electric field results along a line perpendicular to the source electrodes; the return electrode is positioned 500 m from the well. In (a), I show total radial electric field, in (b) the secondary radial electric field (with the primary being the electric field resulting from the intact well, shown in black in panel a), and in (c) I show the secondary radial electric field as a percentage of the primary. I have also indicated where values fall below a 10^{-7} V/m noise floor on Figure 4.5 (a) and (b), as well as those that fall below a 20% threshold in (c). A threshold of 20% may be conservative, however, it does depend on knowledge

of the background conductivity as well as the geometry and physical properties of the well. In many scenarios, these may not be well-constrained, thus I select a conservative threshold for this analysis. Any detectability analysis will be site-dependent and I have therefore made all source-code available so that a similar workflow may be followed and adapted to include setting-specific parameters.

When a well is impaired, the total radial electric field is larger than that due to the baseline, intact well. The strength of the secondary response decreases as the depth of the flaw increases. For this example of a 1000 m long well in a 10^{-2} S/m background, a flaw at 900 m depth is not detectable; there is no overlap between the region in which the secondary electric field (Figure 4.5b) is above the noise floor and the region in which the secondary comprises a significant percentage of the primary (Figure 4.5c). This might be expected, as the difference between the charges distributed along a 900 m long segment versus the 1000 m long well are not drastically different. For a flaw at 700 m depth, there is a window between 400 m offset and 800 m offset over which the radial electric field data are sensitive to the flaw. As the depth to the impairment decreases, both the spatial extent over which data are sensitive to the flaw, and the magnitude of the secondary response in those data, increase.

Background conductivity

The total charge on the well is controlled by the contrast in conductivity between the steel-cased well and the surrounding geology. Increasing the conductivity of the background reduces that contrast thus reducing the amount of charge on the well. The result is a decrease in the total electric field at the surface. Similarly, the strength of the secondary dipolar charge introduced with the presence of an impairment also depends upon the available charge and will also be reduced with increasing background conductivity.

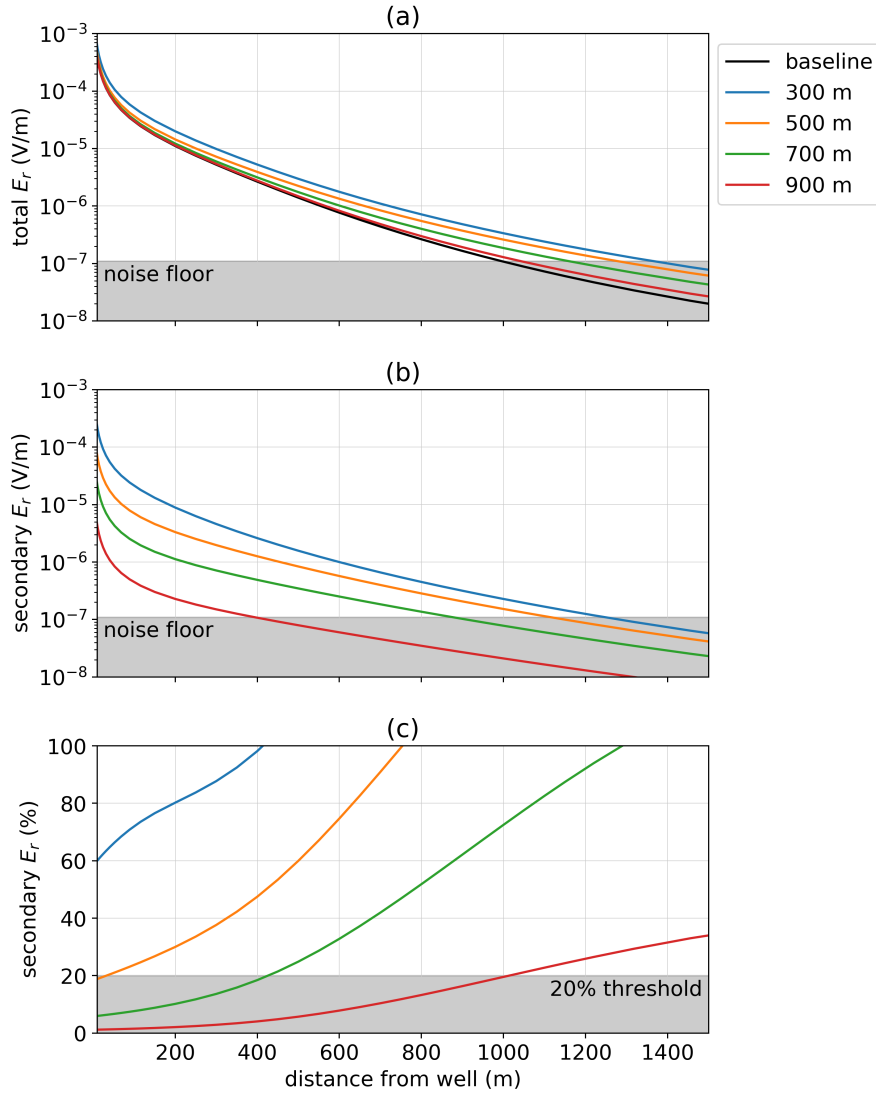


Figure 4.5: Radial electric field as the depth of the flaw along a 1km long well is varied. The positive electrode is connected to the top of the casing, the negative electrode is positioned 500m away and data are measured along a line 90° from the source electrodes. In (a), we show the total electric field for four flawed wells, each with a 10m flaw at the depth indicated on the legend. The black line shows the radial electric field due to an intact well; we define this as the primary. In (b), the secondary radial electric field is plotted and in (c), we show the secondary radial electric field as a percentage of the primary.

In Figure 4.6, I have adopted the same model of a 1 km well with a 10 m impairment at 500 m depth, and show the radial electric field for the flawed (solid lines) and intact (dashed lines) well as the background conductivity is varied. A resistive background promotes the strongest total and secondary signals. As the conductivity increases, detectability becomes more challenging; at a conductivity of 3×10^{-1} S/m, the flaw at 500 m depth is undetectable as there is no overlap in the regions where the secondary signal is above the noise floor and where it comprises a significant percentage of the primary.

Variations in the background geology will also influence the distribution of charges and thus the measured signal at the surface. To examine the challenges introduced when variable geology is considered, I will introduce a layer into the model and vary its conductivity. The layer is 50 m thick and its top is at 400 m depth. The flaw will again be positioned at 500 m depth, and the background conductivity is 10^{-1} S/m. The return electrode is 500 m from the well, and radial electric field data are measured along a line perpendicular to the source. In Figure 4.7, I show data for a flawed well (solid) and intact well (dashed) for scenarios in which a conductive or resistive layer is positioned above the flaw. The presence of a resistive layer improves detectability, while a conductive layer reduces detectability.

To understand the physical phenomena governing this, I have plotted a cross section through: (a) the model, (b) the currents, (c) the charges, and (d) the electric field in Figure 4.8 for (first row) a model of an intact well with a conductive layer present, (second row) a flawed-well model including a conductive layer, (third row) a model of an intact well with a resistive layer, and (fourth row) a flawed-well model including the resistive layer. For the comparison, there is two orders of magnitude difference between the background and the layer. When a conductive layer is present, we see that it acts to “short-circuit” the system as there is significant current leak-off into that layer. This

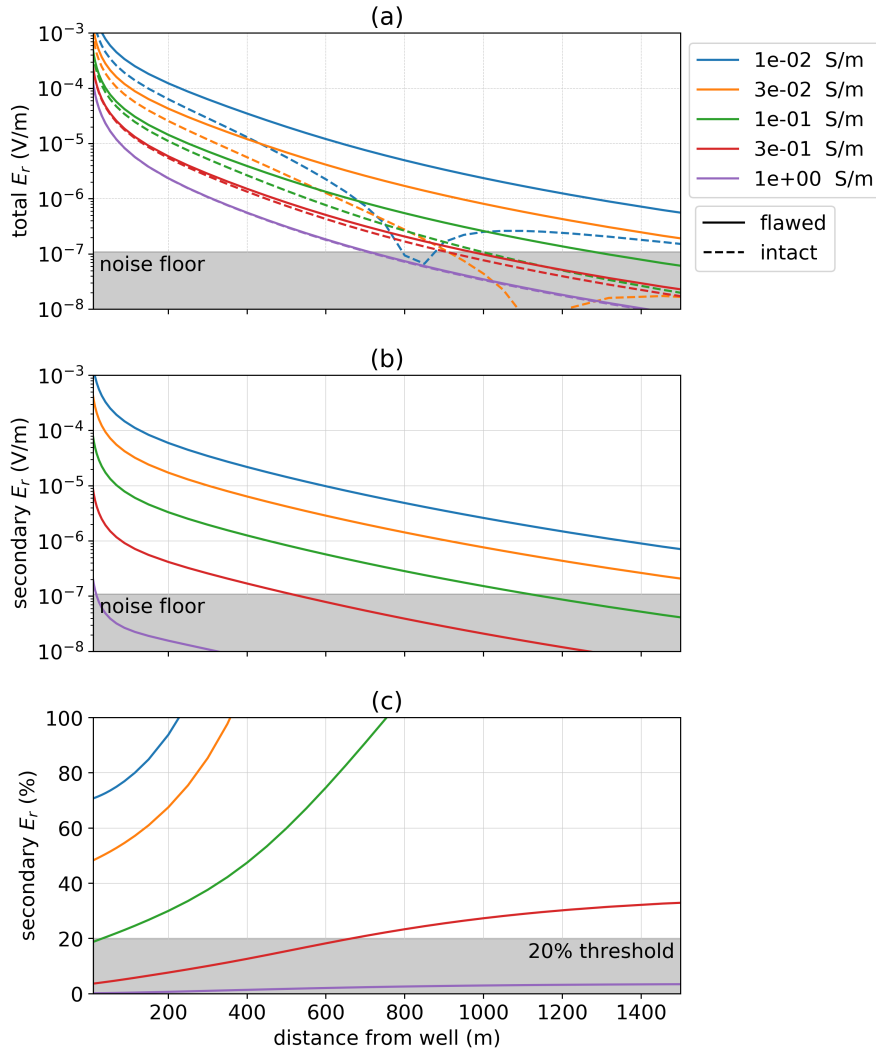


Figure 4.6: Radial electric field as the conductivity of the background is varied for a 1 km well with a 10 m flaw at 500 m depth. The positive electrode is connected to the top of the casing, the negative electrode is positioned 500 m away and data are measured along a line 90° from the source electrodes. In (a), we show the total electric field for five different background conductivities, each indicated on the legend. The solid lines indicate the response of the flawed well and the dashed lines indicate the response of the intact well (the primary). In (b), the secondary radial electric field is plotted and in (c), we show the secondary radial electric field as a percentage of the primary.

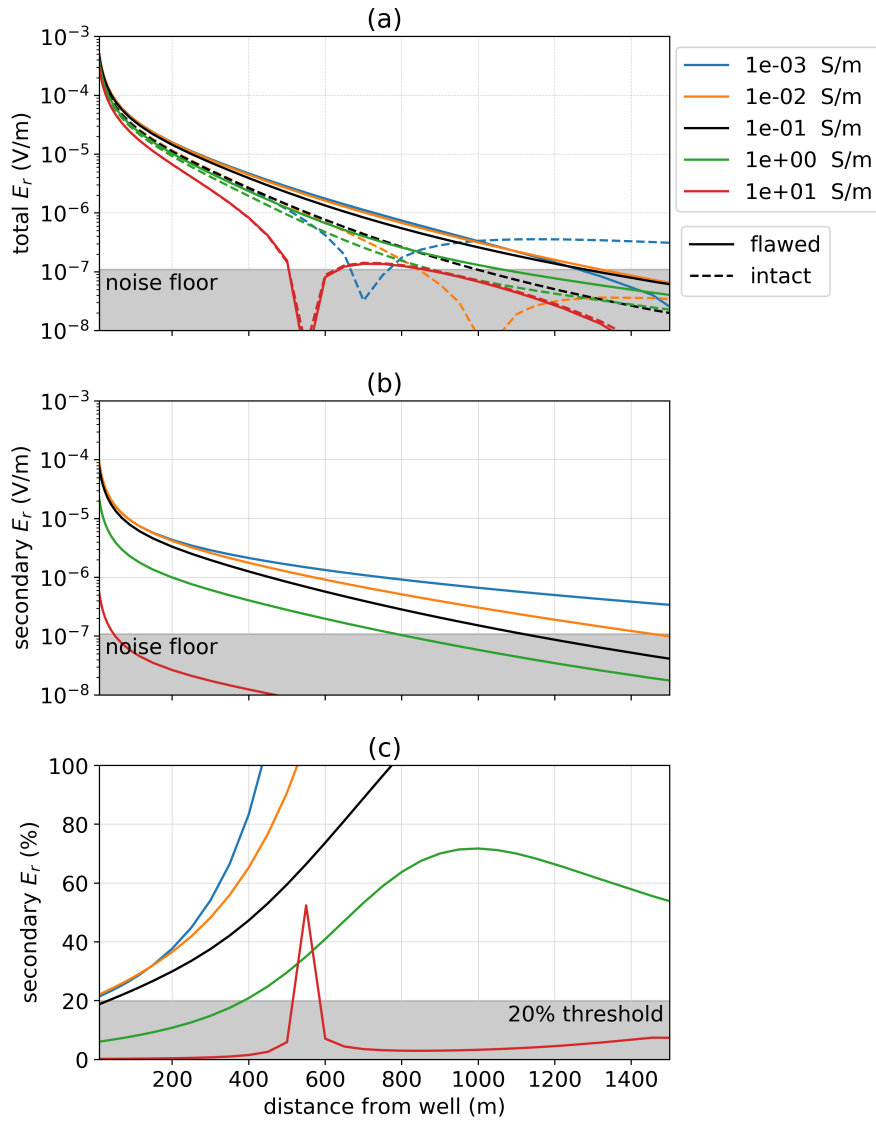


Figure 4.7: Radial electric field as the conductivity of a 50 m thick layer positioned at 400 m depth is varied. The positive electrode is connected to the top of the casing, the negative electrode is positioned 500 m away and data are measured along a line 90° from the source electrodes. In (a), we show the total electric field five different layer conductivities. The black line shows the scenario where the layer has the same conductivity as the background. The dashed-lines indicate the intact well and the solid lines indicate the flawed well. In (b), the secondary radial electric field is plotted (with respect to an intact well primary) and in (c), we show the secondary radial electric field as a percentage of the primary.

reduces the amount of current that reaches the flawed section of the well and decreases the total charge on the well, which is the source of our signal. Conversely, when a resistive layer is present, there is less leak-off of currents. In fact, Yang and Oldenburg (2016) showed that rather than leaking-off, currents can enter the casing if a resistive layer is present. In terms of detecting a flaw beneath a resistive layer, this means that the current density and charge along the well increases, thus amplifying the response due to the flaw.

Conductivity of the casing

The conductivity of the casing is also relevant to how the charges are distributed along its length. For highly conductive wells, the charge along the length of the well is approximately uniform, for more resistive wells, the charges follow an exponential decay, as shown in Figure 4.9. Schenkel (1991) described the decay of currents, and thus the distribution of charges along the length of a well, in terms of the conduction length,

$$\delta_L = \sqrt{\frac{S_c}{\sigma_0}} = \sqrt{\frac{2\pi r t \sigma_c}{\sigma_0}} \quad (4.1)$$

Where S_c is the cross-sectional conductance of the casing ($S_c = 2\pi r t \sigma_c$ for a casing with radius r , thickness t , conductivity σ_c and has units of $[S \cdot m]$) and σ_0 is the conductivity of the background. The conduction length is akin to skin depth in electromagnetics and is the depth at which the amplitude of currents have decreased by a factor of e^{-1} . Casing conductivities of 5×10^5 S/m, 5×10^6 S/m, and 5×10^7 S/m correspond to conduction lengths of ~ 180 m, 560 m, 1800 m. For the most resistive well shown, 5×10^5 S/m, the vast majority of current has decayed well before it reaches the flaw; the majority of charges are concentrated where the currents leak off, near the top of the well. Correspondingly, there is greater sensitivity to a flaw in a conductive well than in a resistive

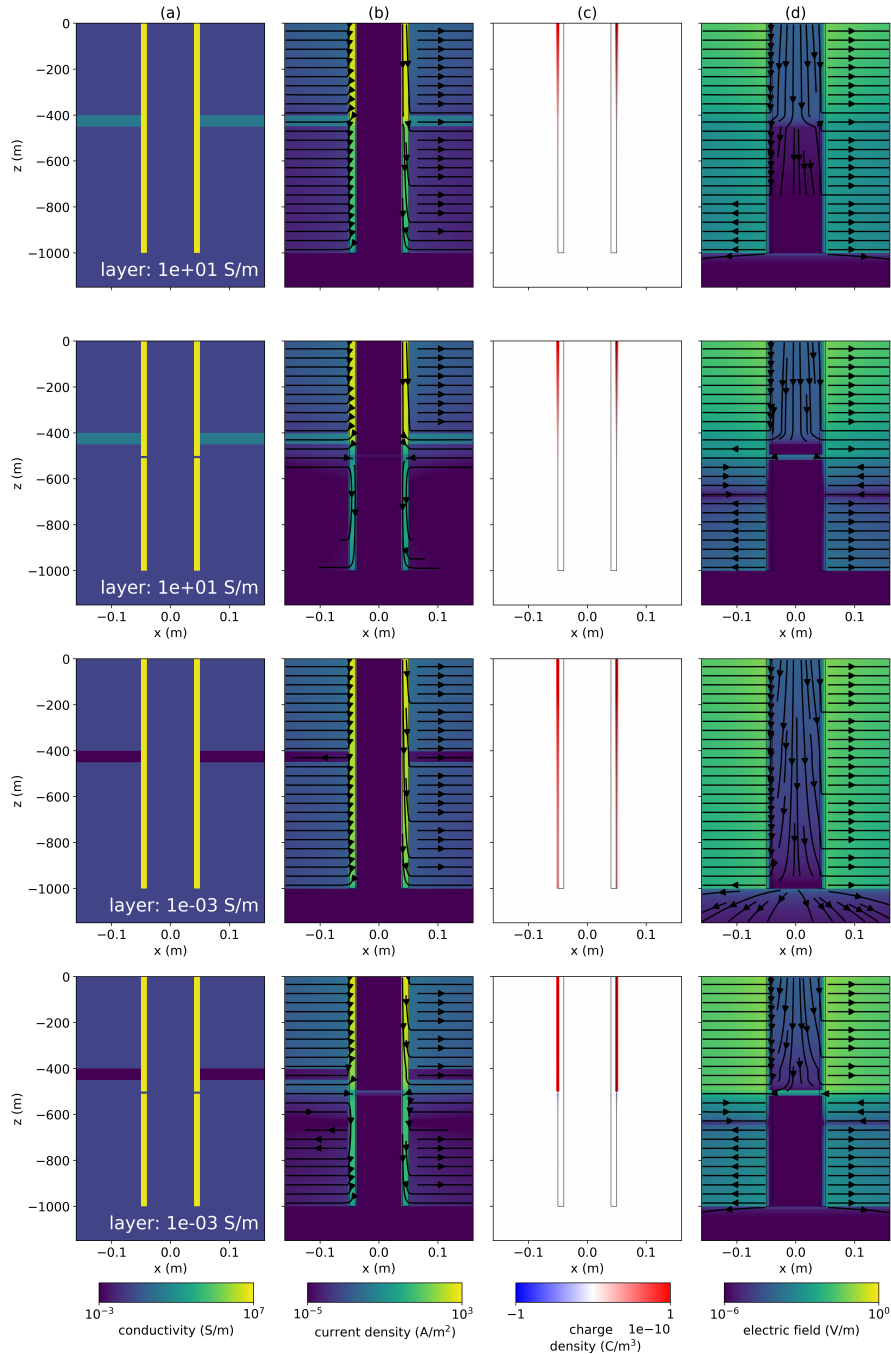


Figure 4.8: Cross section showing: (a) electrical conductivity, (b) current density, (c) charge density, and (d) electric field for a top-casing DC resistivity experiment over models with a conductive layer (top two rows) and a model with a resistive layer (bottom two rows). The layer extends from 400 m to 450 m depth. The plots in the second and fourth correspond to models with a 10 m flaw at 500 m depth.

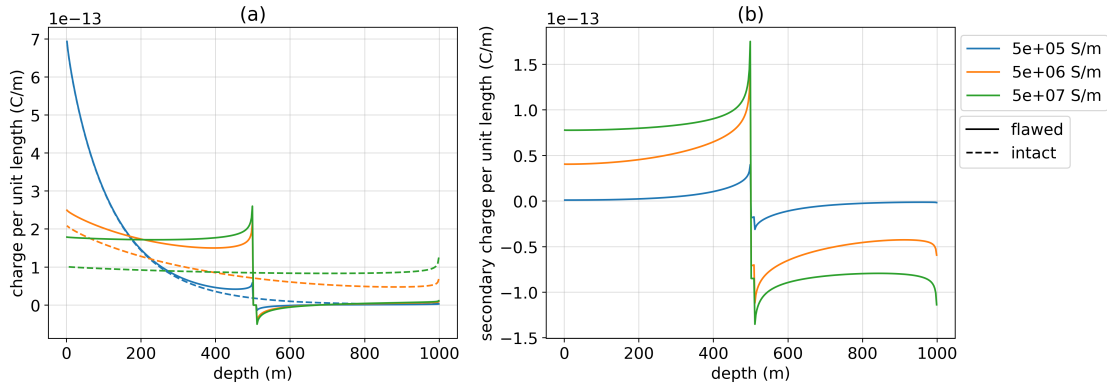


Figure 4.9: (a) Charge along the length of wells with three different conductivities (each indicated by a different color in the legend). The intact wells are denoted with dashed lines and the flawed wells are denoted with solid lines. (b) Secondary charge along the flawed and short wells. The primary is defined as the electric field due to the 1000 m long intact well. The return electrode is 2000 m away from the well.

well, as is reflected in the radial electric field data shown in Figure 4.10.

Partial flaw

The above examples considered an impairment that affects the entire circumference of the casing. This may be suitable in some scenarios where a particular geologic unit subjects the well to corrosive conditions, however, flaws may also be vertical cracks along the well (e.g. if pipe burst occurs). This is a much more challenging problem for DC resistivity because, if only a portion of the circumference is impaired, there is still a high-conductivity pathway for currents to flow along the entire length of the well. To examine the feasibility of detecting a partial flaw, I have run simulations where half of the circumference of the casing is compromised, leaving the other-half intact.

I consider four different depth extents of the flaw between 10 m and 300 m; in all scenarios the top of the flaw is at 500 m. In Figure 4.11a, I have plotted the total radial electric field resulting from an intact well (black), wells where the entire circumference

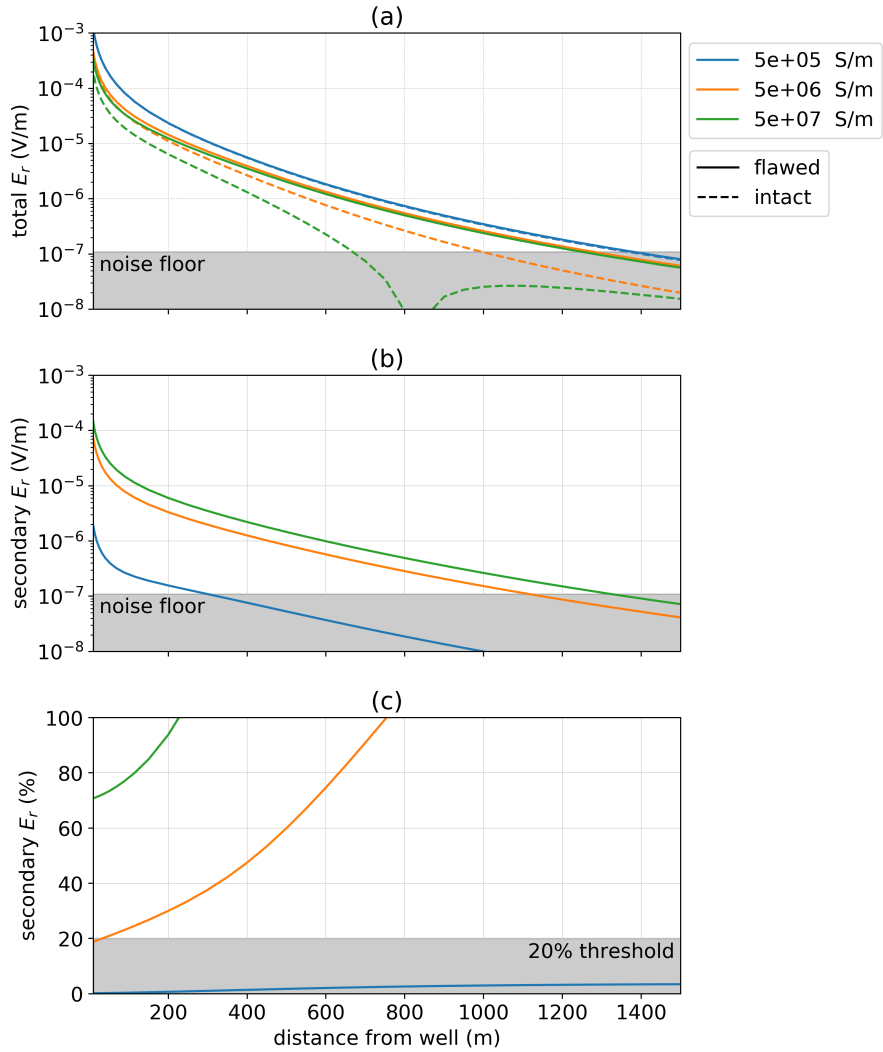


Figure 4.10: Radial electric field as the conductivity of the casing is varied for a 1 km well with a 10 m flaw at 500 m depth. The positive electrode is connected to the top of the casing, the negative electrode is positioned 500 m away and data are measured along a line 90° from the source electrodes. In (a), we show the total electric field for three different casing conductivities, each indicated on the legend. The solid lines indicate the response of the flawed well and the dashed lines indicate the response of the intact well (the primary). In (b), the secondary radial electric field is plotted and in (c), we show the secondary radial electric field as a percentage of the primary.

is compromised (solid) and wells in which 50% of the circumference has been compromised (dashed); (b) and (c) show the secondary radial electric field and the secondary as a percentage of the primary, respectively. We see that the depth-extent of the flaw has little impact on the fully-compromised wells, which is consistent with the observations in our previous examples. However, if the well is partially flawed, we do see variation in the secondary response. By compromising 50% of the circumference of the well, we have reduced the effective cross-sectional conductance over that portion of the well. Numerical experiments show that if, instead of introducing a flaw which comprises 50% of the circumference of the well, we reduce the conductivity of the intact well by 50% over the same depth extent as the flaw, we obtain similar, but not identical, responses at the surface. Although for extensive flaws, there is a small region over which the secondary signal is above the noise floor, there are no regions where this coincides with measurements where the secondary fields are a significant percentage of the primary. There may be a subset of circumstances, such as if the flaw is near to the surface, or if the background geology is sufficiently well-known so that the percent threshold can be reduced, where a partial flaw may be diagnosed, however, these results demonstrate that a partial flaw is a challenging target for a DC resistivity survey.

4.2.4 Summary

In summary, I provided an overview of the fundamental physics governing the behavior of currents, charges, and electric fields in a top-casing DC resistivity experiment to detect an impairment in the well. If a flaw comprises the entire circumference of some depth interval along the casing, then the charges are concentrated in the portion of the well above the flaw, and to first approximation, the charge distribution is equal to that of a well which has been truncated at the depth of the flaw. This excess charge is the source

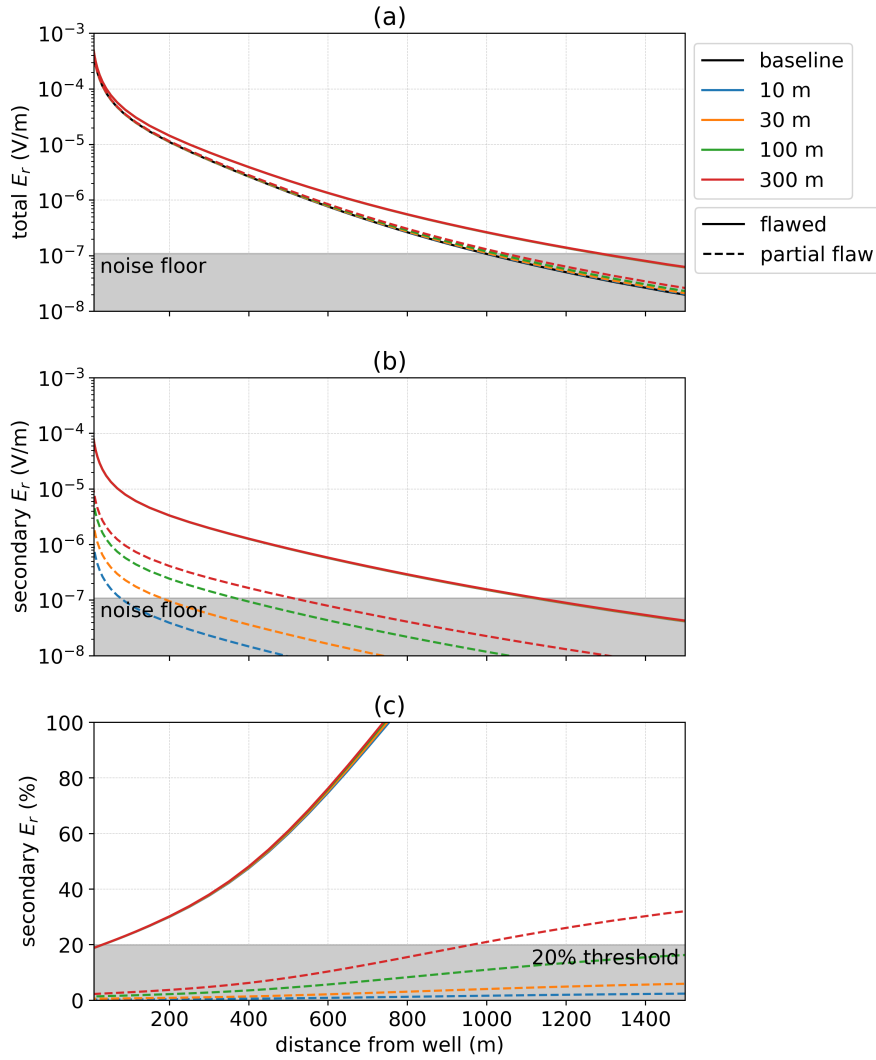


Figure 4.11: Radial electric field as the vertical extent of the flaw is varied. The positive electrode is connected to the top of the casing, the negative electrode is positioned 500 m away and data are measured along a line 90° from the source electrodes. In (a), we show the total electric field for four different flaw extents. The black line shows the response of the intact well. The dashed-lines indicate the partially flawed wells (50% of the circumference is compromised) and the solid lines flawed wells in which the entire circumference of the well has been compromised. In (b), the secondary radial electric field is plotted (with respect to an intact well primary) and in (c), we show the secondary radial electric field as a percentage of the primary.

of our signal. As it is cylindrically symmetric, the resultant secondary electric fields due to the flaw are purely radial. In terms of survey-design, we can take advantage of this knowledge and use the return electrode location to reduce coupling with the primary electric field in our data (as shown in Figure 4.4). Our ability to detect a flaw across the entire circumference of the casing depends upon the conductivity of the background and casing, as well as the depth of the flaw. Larger contrasts between the casing and the background (e.g. a more resistive background and / or a more conductive casing) increase the secondary response, as does decreasing the depth of the flaw. If only a portion of the circumference is impaired, leaving a conductive pathway connecting the top and bottom portions of the casing, the secondary signal is small and thus will be challenging to detect under most circumstances.

For the subset of scenarios where we do have data sensitivity to the flaw, an inverse problem can be solved to estimate the depth of the impairment. One approach would be to use a reduced modeling procedure whereby only a few parameters are sought. For the case presented here, we might invert for a smooth background, the length of the well, and potentially the conductivity of the casing, if it is not known a-priori.

In the next section, I transition from viewing the casing as the target to working on the scale of a geophysical imaging application in reservoir monitoring and viewing the casing as a high-conductivity feature present in that setting.

4.3 Survey design for exciting targets at depth

There are many problems in hydraulic fracturing, carbon capture and storage and enhanced oil recovery that require targets to be illuminated and data to be acquired and inverted. Typically these experiments include steel-cased wells and the target of interest could be resistive or conductive. The target could be immediately adjacent to a well or

offset from it, and the survey may employ electrodes on the surface or positioned down-hole. Similarly, receivers may be positioned on the surface or in adjacent boreholes. Each of these factors influences our ability to detect a target in our data.

Detectability of a target requires two steps: (1) source fields must excite the target, and (2) receivers must be positioned so that the secondary response is measurable. In this section, I focus on the first point – exciting the target. I will examine the impact of source electrode locations, the physical properties of the target and the geometry of the target on our ability to excite a response.

4.3.1 Source location

I begin by examining the impact of the source electrode location on our ability to deliver current to a region of interest in the model. The model I consider is 1 km long well in a 10^{-1} S/m background. The well has a conductivity of 5×10^6 S/m, an outer diameter of 10 cm thickness, and a 1 cm thickness; these are the same parameters used for the casing integrity experiment described in the previous section. The conductivity of the fluid filling the casing is identical to that of the background. I am interested in effects near the well and thus the modeling can be carried out using the 2D cylindrical mesh provided that the return electrode is sufficiently far away. The return electrode is physically a disc of current at a radius equal to the distance of the return electrode from the well, in this case 2 km. The assumption of cylindrical symmetry and the use of a distant return electrode has similarly been applied in Schenkel (1991).

To examine the impact that the source electrode location has on our ability to excite a target, I consider the electrode locations shown in Figure 4.12. Three of the electrodes are connected to the casing (tophole - blue, centered - green, and downhole - red); the remaining electrodes are not connected to the casing; these include the surface electrode

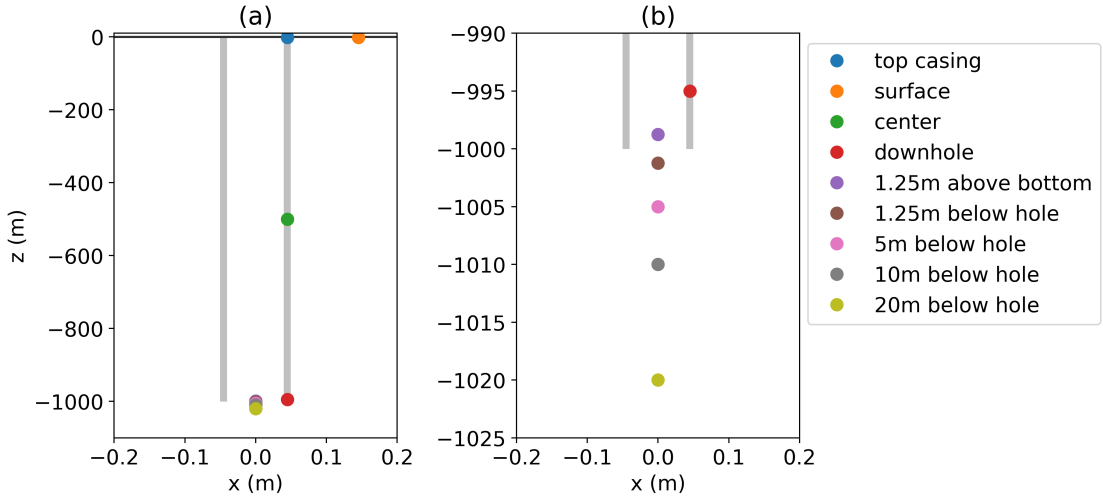


Figure 4.12: Electrode locations to be compared. The top casing electrode (blue), centered electrode (green, 500 m depth), and downhole electrode (red, 500 m depth) are connected to the casing. The surface electrode (orange) is offset from the well by 0.1 m. The remaining electrodes are positioned along the axis of the casing. Panel (a) shows the entire length of the casing, while (b) zooms in to the bottom of the casing to show the separation between the electrodes beneath the casing.

(orange) as well as the five electrodes near the end of the pipe (purple - within the pipe, brown, pink, grey and yellow are beneath the end of the pipe). The surface electrode is offset from the well by 0.1 m.

To assess the ability of each electrode configuration to excite a geologic target of interest, I will examine the current density in the formation. In Figure 4.13, I have plotted the amplitude of the current density along a vertical line (a) 25 m, (b) 50 m, and (c) 100 m radially offset from the well. In terms of survey design, we wish to choose a source location that maximizes the total current density within the depth region of interest. If the target is near the surface, we choose an electrode which is connected to the top of the casing, or near the casing at the surface. Interestingly, at depth, there is little distinction between these two scenarios. Thus, if one is limited to deploying

electrodes at the surface, and for practical purposes, connecting infrastructure to the well-head presents a challenge, then grounding the electrode near the well still results in a survey that benefits from the well acting as a high-conductivity pathway to help deliver current to depth. If the aim however, is to excite a deeper target, we see that positioning the electrode downhole can significantly increase the current density delivered to that depth. For example, if we have a target near 500 m depth, positioning the electrode near that depth nearly doubles the current density as compared to an electrode at the surface. If a target is near the end of the well, between 800 m and 1000 m depth, then positioning an electrode near the end of the well triples the current density. This effect will be amplified if the well is lengthened, since we observe exponential decay of the currents carried along according to the conduction length (equation 4.1).

Kaufman (1990) pointed out that the difference between an electrode positioned along the axis of the casing and one coupled to the casing at depth is highly localized around the source, and thus is not an important distinction at the scales we consider for a geophysical imaging survey. I can test this numerically by comparing the currents arising from the electrode which is connected to the casing 5 m above the bottom of the casing (red in Figures 4.12 and 4.13), and the electrode positioned along the axis of the casing 1.25 m above the bottom of the casing (purple in Figures 4.12 and 4.13). Indeed, we see that the red and purple lines overlap for all offsets in Figure 4.13, indicating that both situations result in the same distribution of currents within the formation.

For electrodes beneath the casing, the distribution of currents is significantly different. For electrodes 1.25 m, 5 m, 10 m and 20 m below the pipe, we see that within a ~ 100 m above and below the electrode location, the currents are nearly symmetric, following the expected response of a point source. I have included a simulation with the electrode 20 m below the pipe when there is no casing present; this is shown in black in

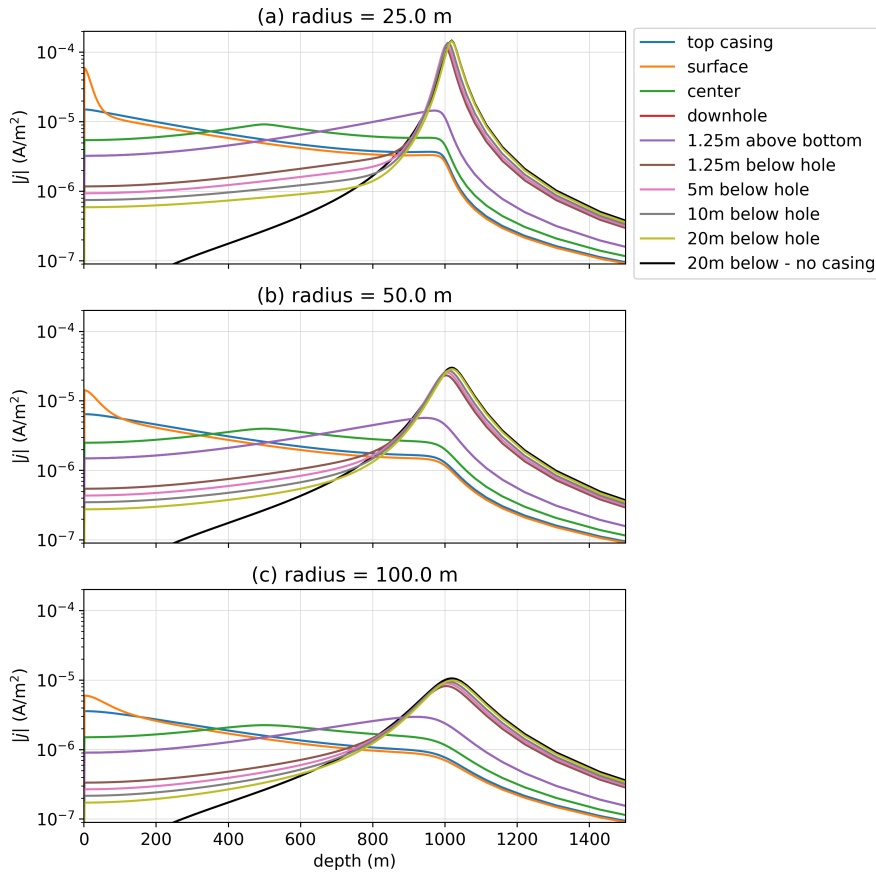


Figure 4.13: Total current density along a vertical line offset (a) 25 m, (b) 50 m and (c) 100 m from the axis of the casing, which extends from the surface (0 m) to 1000 m depth. The electrode locations correspond to those shown in Figure 4.12. For reference, a simulation with an electrode 20 m below the casing when there is no casing present is shown in black.

Figure 4.13. The main difference between the distribution of currents for each of these scenarios is the reduction in current density in the top 1000 m, with increasing electrode depth; as the electrode is moved deeper, less current is channeled into the casing. Schenkel and Morrison (1990) noted that for electrodes positioned beneath a well, if the electrode is more than 100 casing diameters beneath the casing, then the casing has little impact on the fields below or far from the pipe. The current is much more localized if

the electrode is beneath the casing, and thus if a target is beneath or very near the end of the well, then it is advantageous to position the electrode beneath the well.

Not surprisingly, if the source electrode can be positioned near the depth region of interest, the current density delivered to that region is larger. Numerical experiments show that the position of the return electrode makes minimal impact on the currents at depth. However, if the return electrode is within 10's of meters of the well, the near surface currents are significantly altered. This is consistent with our observations in section 4.2, where I showed that the return electrode location has little impact on the magnitude of the secondary signals, but its position alters the geometry of the source fields and this can be used to reduce coupling of receivers to the primary field.

4.3.2 Target properties

The physical property contrast between the target and the background, the target's geometry and proximity to the well, all influence our ability to observe its impact on the data we measure. The purpose of this section is to explore the impact of these factors on the excitation and detection of the target. In the first example, I examine the role of the conductivity of a cylindrical target which is in contact with the well. The second example is again a cylindrically symmetric co-axial disc target but there is a gap between the casing and the target. The final example is fully 3D; the target is a block and I look at the excitation as a function of the distance of a block from the well.

Target in contact with the well

First, I consider a cylindrical target that is in contact with the well. Schenkel and Morrison (1994) examined such a scenario for a conductive target (e.g. a steam injection or water flood) in a mis-à-la-masse type experiment where a source electrode is connected to the casing at the same depth as the center of the target. They considered a cross-well

experiment with potential electrodes in an offset, uncased well, and compared two scenarios for the source well: one in which the source well is an open-hole, and the second in which it was cased. They demonstrated that the casing enhances the response, and thus the data sensitivity to the target, as compared to an experiment where current is injected directly into the target and no casing is present. In this example, I build upon those findings and examine the role of the conductivity of the target on our ability to excite it as well as the impact on the data if the target is not directly in contact with the well.

The model I use is a 1 km casing in a half-space with a target. The target extends 25 m vertically and has a 25 m radius and the depth to its top is 900 m. The model is cylindrically symmetric and thus we expect that the secondary electric field at the surface due to the target will be purely radial. As such, I apply the lessons learned from the casing integrity example and use the return electrode to reduce coupling with the primary field along a line perpendicular to the source. I position the return electrode 500 m from the well-head and compare both top-casing and down-hole source electrode locations.

We begin by examining the physical behavior governing the DC response of a conductive and resistive target. Figure 4.14 shows the (a) conductivity model, and resultant: (b) current density, (c) charge density, and (d) electric fields for a conductive target (10 S/m , top row) and a resistive target (10^{-3} S/m , bottom row) in a down-hole experiment where the source electrode is positioned at the center of the target. The extent of the steel-cased well is noted by the vertical black line in panel (a). For the conductive target, we see an accumulation of positive charges along the radial and vertical boundaries of the target. This is consistent with currents that have been channeled into the conductor and exit into a more resistive background. Conversely, for the resistive target, we

see an accumulation of negative charge on the radial boundary, consistent with current moving from a resistive region to a more conductive material. We also notice some positive charge accumulation on the top and bottom boundaries of the target; some of the currents deflected around the resistor do enter from the top and bottom, resulting in an accumulation of positive charge. This is not observed in a traditional mis-à-la-masse experiment, where a point source is positioned within the target. Figure 4.15 shows the current density, charges and electric fields for a mis-à-la-masse experiment in which no steel cased well is present.

In a DC experiment, the electric field response we measure is a result of the distribution of charges within the domain. As a metric for quantifying excitation, I integrate the secondary charge over this depth interval containing the target. In Table 4.1, I show the secondary charge integrated over the depth interval containing the target; the secondary charge on the casing within this region is included in the calculation. To examine how the charge relates to the electric field data, I have plotted (a) total radial electric field, (b) secondary radial electric field (with respect to a primary that includes the casing in a halfspace), and (c) the secondary radial electric field as a percentage of the primary for a down-hole source and similarly for a top-casing source (d, e, f) in Figure 4.16. I adopt the same noise floor and percent threshold as in the casing integrity examples (10^{-7} V/m and 20%, respectively). For time-lapse surveys where a baseline survey has been taken and the background is well-characterized, this threshold could likely be reduced. The black line in panels (a) and (d) corresponds to the baseline model in which no target is present; each of the colored lines corresponds to a different target conductivity as indicated in the legend.

First, we examine the impact of the conductivity of the target and notice that there is an asymmetry between secondary charge on conductive targets and resistive targets. For

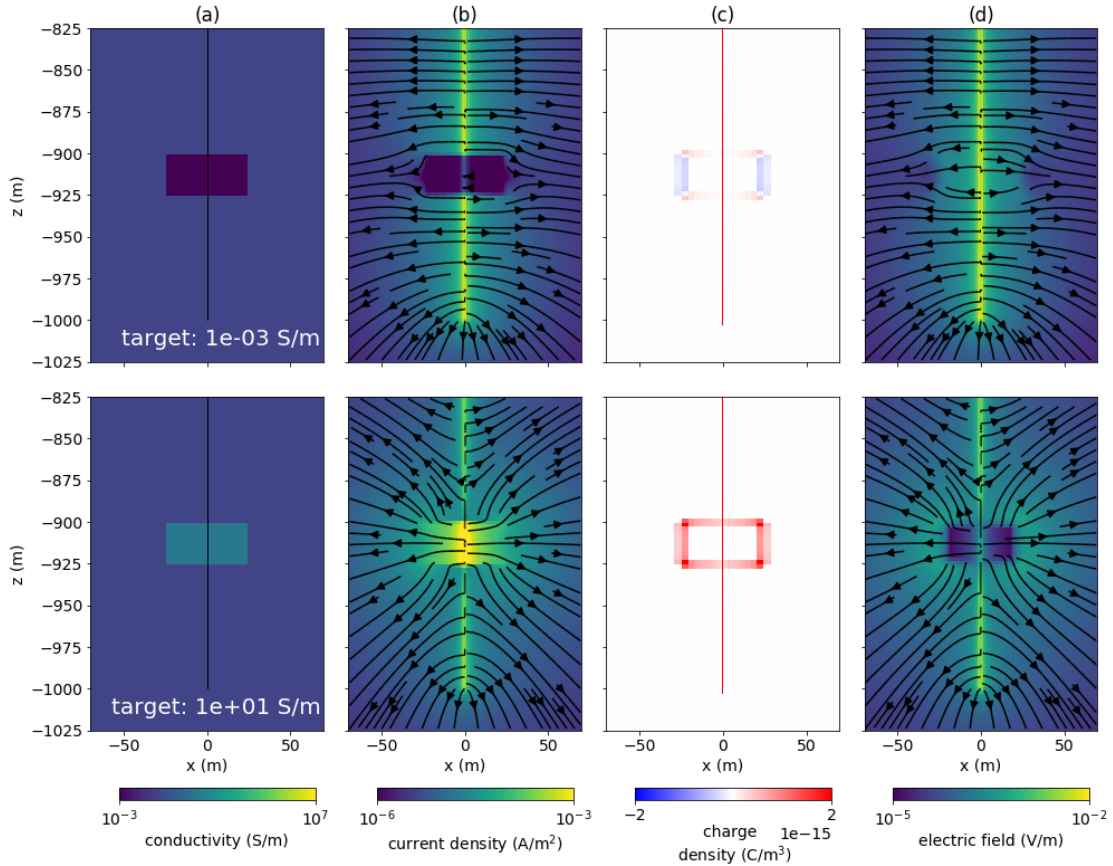


Figure 4.14: Cross section showing: (a) electrical conductivity, (b) current density, (c) charge density, and (d) electric field for a DC resistivity experiment with a conductive target (top) and a resistive target (bottom). The positive electrode is positioned in the casing at the 912.5 m depth. The casing is shown by the black line that extends to 1 km depth in panel (a).

Table 4.1: Integrated secondary charge over a target adjacent to the casing, as shown in Figure 4.14.

target conductivity (S/m)	integrated secondary charge (C)	
	downhole source	top-casing source
$1e-03$	-4.24e-12	-1.08e-12
$1e-02$	-3.82e-12	-9.68e-13
$1e-01$	0.00e+00	0.00e+00
$1e+00$	1.75e-11	4.46e-12
$1e+01$	3.26e-11	8.28e-12

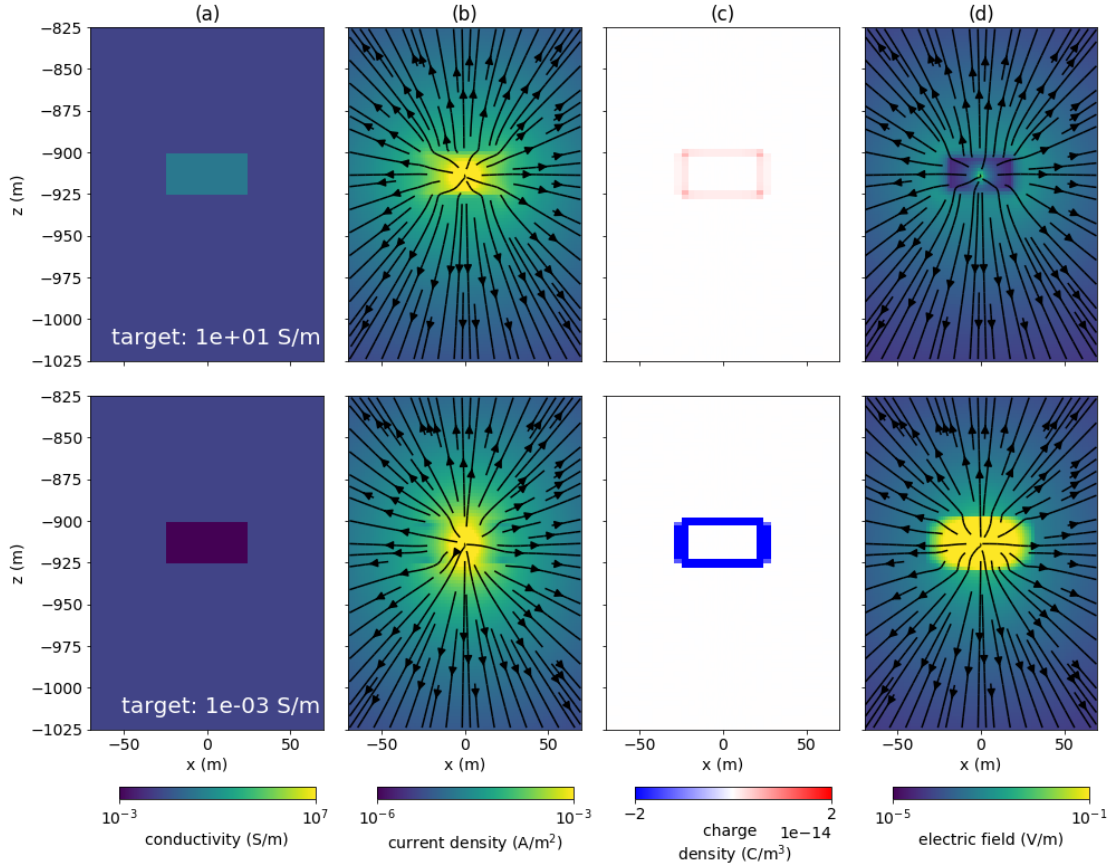


Figure 4.15: Cross section showing: (a) electrical conductivity, (b) current density, (c) charge density, and (d) electric field for a DC resistivity experiment with a conductive target (top) and a resistive target (bottom). The positive electrode is positioned at 912.5 m depth. No casing is included in this simulation. Note that the colorbars for the charge density (c) and electric field (d) are different than those used in Figure 4.14. For the resistive target, the colorbar is saturated, the charge density over the resistive target is on the order of 10^{-13} C/m^3 .

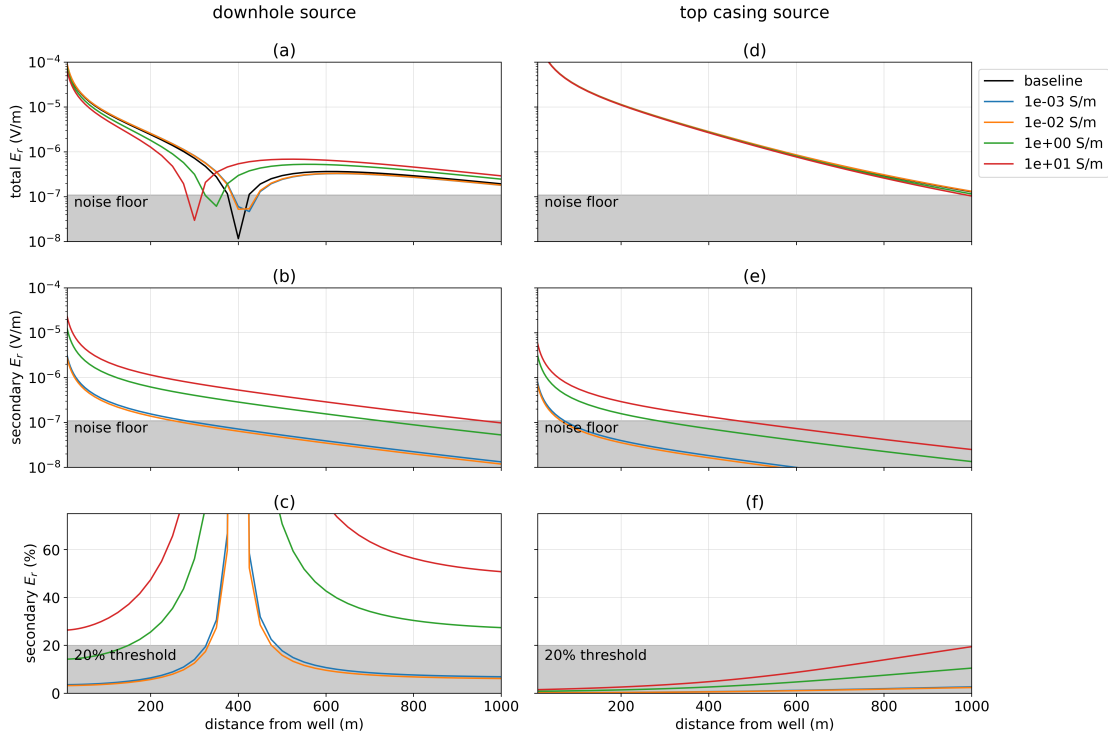


Figure 4.16: Radial electric field at the surface as the conductivity of a cylindrical target, in contact with the well, is varied. The target has a radius of 25 m and extends in depth from 900 m to 925 m. The return electrode is on the surface, 500 m from the well and data are measured along a line perpendicular to the source. The panels on the left show (a) the total electric field, (b) the secondary electric field with respect to a primary that does not include the target, and (c) the secondary electric field as a percentage of the primary for a survey in which the positive electrode is positioned downhole at 912.5 m depth. The panels on the right similarly show (d) the total electric field, (e) the secondary electric field, and (f) the secondary electric field as a percentage of the primary for a top-casing experiment.

a 1 S/m target, which is one order of magnitude more conductive than the background, the integrated secondary charge is $1.75 \times 10^{-11} \text{ C}$, while for a $1 \times 10^{-2} \text{ S/m}$ target, which is one order of magnitude more resistive than the background, the integrated secondary charge is $-3.82 \times 10^{-12} \text{ C}$ for the downhole casing experiment. Thus, there is a factor of 4.6 between the magnitude of the secondary charge for these targets; this is equivalent to the ratio we see between the secondary electric field measurements at the surface observed in Figure 4.16b. When also considering the influence of the primary electric field on our ability to detect a target, we see that for a down-hole casing experiment, the conductive targets are detectable; they both have a significant region where the secondary is above the noise floor and the secondary comprises a significant percentage of the primary. The resistive targets, however, are not. Although within 200 m of the well, the secondary signal is above the noise floor, this also corresponds to where the primary field is large; the percent threshold would need to be reduced to less than 5% in order to have confidence in the signals due to the resistive targets.

When comparing the downhole source to the top-casing source experiments for a fixed conductivity, there is a factor of 3.9 between the integrated secondary charge shown in 4.1; this is reflected in the secondary electric field data in Figure 4.16b & e. For the top-casing experiment, none of the targets is detectable. There are two factors that make this a more challenging experiment than the downhole scenario: (1) less current is available to excite the target, as reflected in Table 4.1 and (2) the primary field is stronger at the receivers (200 m from the well the primary field has an amplitude of 10^{-5} V/m , while for the down-hole source experiment, the primary has an amplitude of $2 \times 10^{-6} \text{ V/m}$). Addressing the excitation of the target requires that the source electrode be positioned downhole, closer to the target. The second point may be overcome if receivers can be positioned closer to the target, for example within an adjacent borehole.

In summary, the integrated secondary charge provides a metric for a survey's ability to excite a target, and shows that conductive targets are easier to excite than resistive targets. As expected, if the source electrode can be positioned near the target, excitation is enhanced. This also has the added benefit of reducing the strength of the primary electric field at the surface, as compared to a top-casing survey; this increases the potential for detecting a target with surface-based receivers. In the next section, I examine the significance of the electrical connection between the casing and the target.

Target not in contact with the well

How significant is the electrical connection between the casing and the target for our ability to excite a response? To examine this, I introduce a small gap equal to the thickness of the casing (1 cm) between the casing and the target. This has negligible effect on the volume of the target, but it changes the electrical characteristics of the problem. Consider a conductive target; if it is in-contact with the well, we are effectively conducting a mis-à-la-masse experiment, and the conductor will have a net positive charge. When the target is isolated from the casing, the total charge on the target must be zero, and thus dipolar effects, in which negative charges build up on the inner interface of the cylinder target and positive charges build up on the outer interface of the target, will be the source of our signal. This is demonstrated in Figure 4.17.

The corresponding secondary charge integrated over the target depth and radial electric field data are shown in Table 4.2 and Figure 4.18. For comparison, the data resulting from the target in contact with the well are plotted in the dashed, semi-transparent lines. While there is little difference in the integrated secondary charge or the electric field measurements for the resistive targets, we see that there is a factor of 1.3 difference (i.e. 30%) between the integrated secondary charges and correspondingly, the secondary

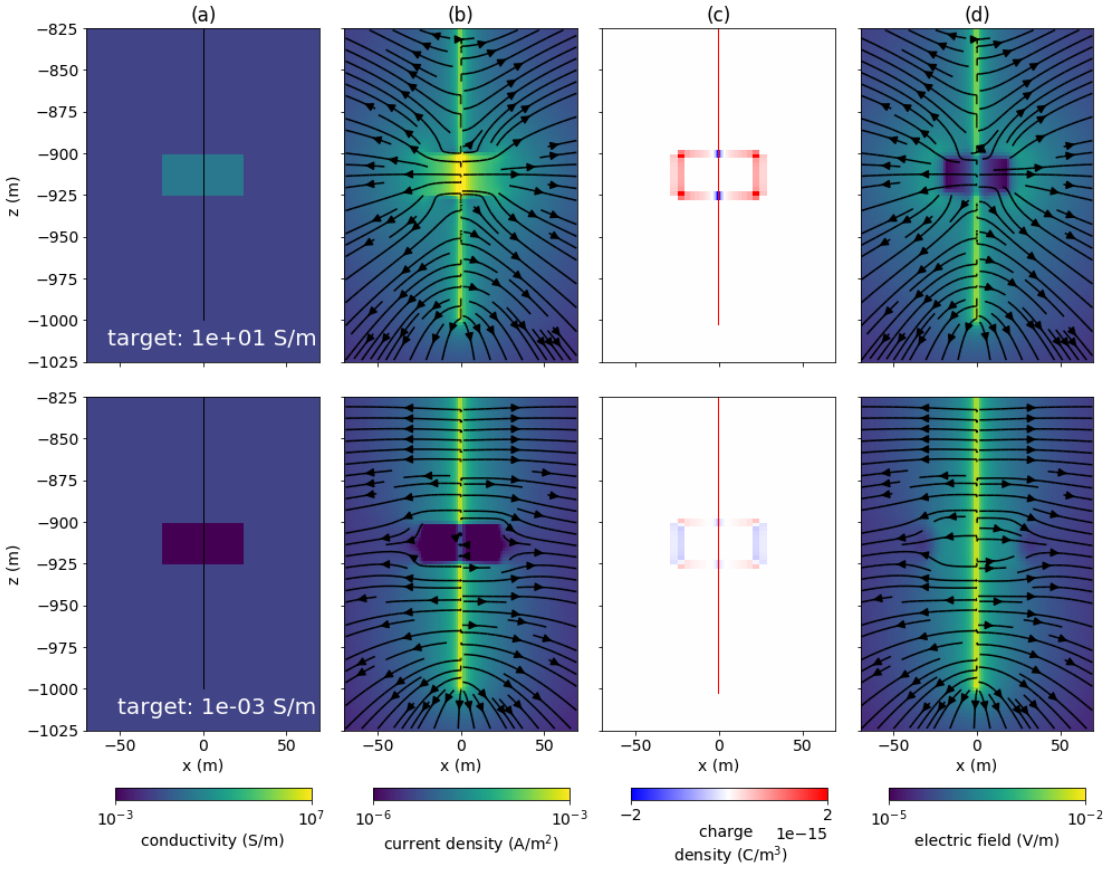


Figure 4.17: Cross section showing: (a) electrical conductivity, (b) current density, (c) charge density, and (d) electric field for a DC resistivity experiment with a conductive target (top) and a resistive target (bottom) which is not in contact with the well. The positive electrode is positioned in the casing at the 912.5 m depth. The casing is shown by the black line that extends to 1 km depth in panel (a).

electric fields, from a 10 S/m target in contact with the well versus not. Similarly, there is a factor of 1.2 between a 1 S/m target in contact with the well versus not for both the downhole and top-casing sources. Increasing the gap between the target and the casing decreases the integrated charge and correspondingly reduces the secondary electric field at the surface. The integrated secondary charge for a 10 S/m target with a 10 cm gap between the target and casing in a downhole source experiment is $1.7 \times 10^{-11} \text{ C}$, which is

Table 4.2: Integrated secondary charge over a target that is not electrically connected to the casing, as shown in Figure 4.17.

target conductivity (S/m)	integrated secondary charge (C) downhole source	integrated secondary charge (C) top-casing source
1e-03	-4.24e-12	-1.08e-12
1e-02	-3.80e-12	-9.64e-13
1e-01	0.00e+00	0.00e+00
1e+00	1.49e-11	3.79e-12
1e+01	2.51e-11	6.39e-12

a factor of 2.2 smaller than the connected target; correspondingly the electric field data at the surface are reduced by a factor of 2.2 as compared to the connected target. Thus, a direct, electrical connection between the target and the well in which we connect the source is preferable for exciting and detecting conductive targets. In the next section, I further examine the impact of the separation between the target and casing.

Target offset from the well

The examples thus far have focused on a particular geometry where the target is symmetric about the well and is either connected or not. The more general case is where there is a target located anywhere in the medium and we wish to use DC or EM to characterize it. For example, in some scenarios, instrumenting a well for a geophysical survey may not be possible if it is also actively being used for an injection. Using another well, offset from the injection well, may then be preferable for positioning electrodes. In such circumstances, the physical property model is fully 3D and there are more factors that influence our ability to excite the target; in addition to the conductivity and geometry of the target, the distance between the well where the source electrode is positioned is now relevant. To address these potential applications, I examine a fully 3D scenario in which a target block is located away from the source well. Our primary goal is compare relative excitations that arise from using different survey parameters. It

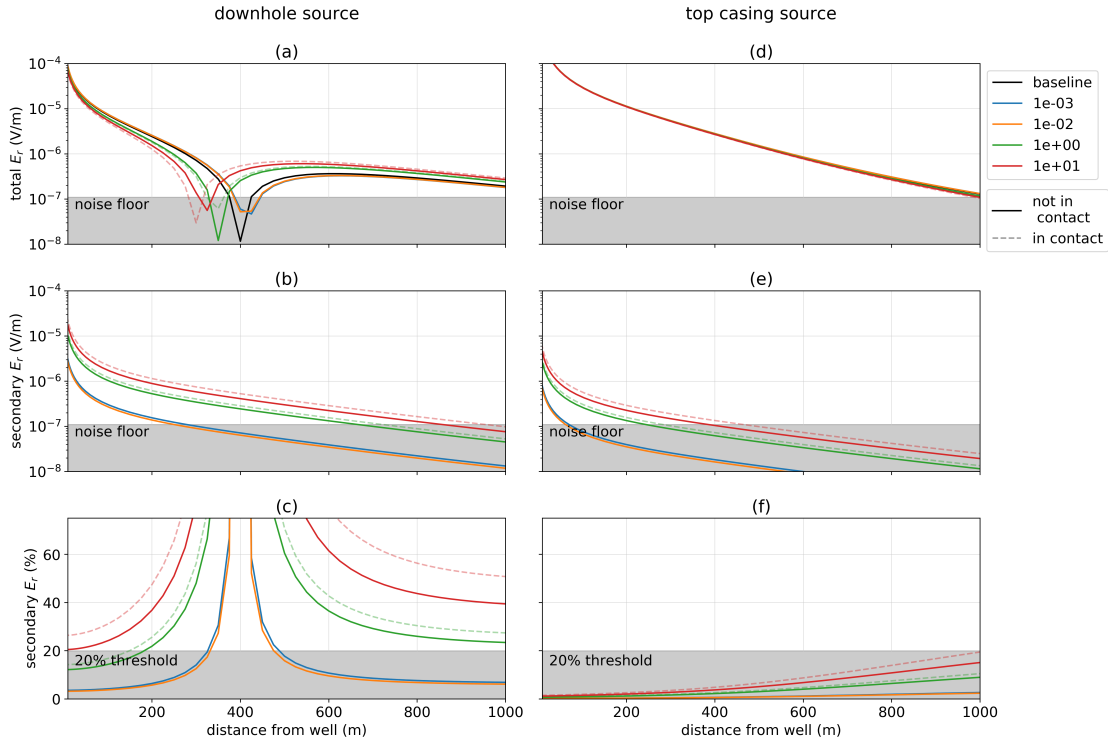


Figure 4.18: Radial electric field at the surface as the conductivity of a cylindrical target, which is not contact with the well, is varied. The target has a radius of 25 m and extends in depth from 900 m to 925 m. The return electrode is on the surface, 500 m from the well and data are measured along a line perpendicular to the source. The panels on the left show (a) the total electric field, (b) the secondary electric field with respect to a primary that does not include the target, and (c) the secondary electric field as a percentage of the primary for a survey in which the positive electrode is positioned downhole at 912.5 m depth. The panels on the right similarly show (d) the total electric field, (e) the secondary electric field, and (f) the secondary electric field as a percentage of the primary for a top-casing experiment. The data shown in Figure 4.16, for the target in contact with the well, are plotted in the dashed, semi-transparent lines for reference.

is sufficient to evaluate an electric dipole moment of the target that is evaluated with a Born approximation.

For a target offset from the pipe, we expect the secondary response due to that target to be dipolar. Thus, a natural proxy for excitation is the dipole moment of the target. I will adopt a Born-approximation approach to quantify the excitation and take the norm of the integrated anomalous current density over the target volume, that is,

$$\begin{aligned} m &= \left\| \int \vec{j}_a dV \right\| \\ &= \left\| \int \sigma_s \vec{e}_p dV \right\| \end{aligned} \quad (4.2)$$

where $\sigma_s = \sigma - \sigma_p$ is the secondary conductivity (the difference between the conductivity of the target and the conductivity of the background), \vec{e}_p is the primary electric field (the electric field due to the source, casing, and half-space background), and \vec{j}_a is the anomalous current density which is non-zero only over the volume where the target is located.

The target I consider is 50 m wide in both horizontal dimensions and is 25 m in height. Its top is at 900 m depth, as in the previous examples. I will examine both downhole source and top-casing experiments. A depth slice showing the primary electric field for the downhole electrode is shown in Figure 4.19; the return electrode is on the surface at $x = -500$ m, $y = 0$ m. The three different target positions relative to the borehole are outlined in white. The solid line shows the target which is inline with the return electrode, the dashed is 90° from the source electrode and the dotted line shows the target which is 180° from the return electrode. I vary the distance from the well to the target and have plotted the Born-approximated dipole moment for four different target conductivities in Figure 4.20 for a (a) downhole experiment, and (b) a top-casing

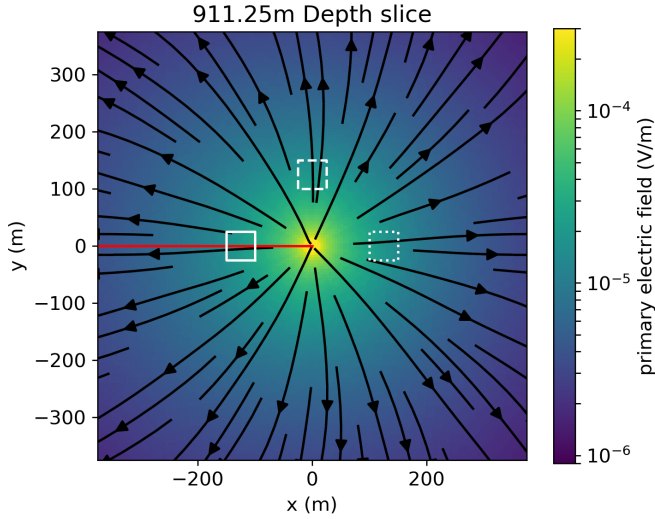


Figure 4.19: Depth slice showing the primary electric field due to a downhole electrode and a return electrode located on the surface at $x = -500$ m, $y = 0$ m. The red line indicates the azimuth of the source. We examine the 3 different target azimuths shown by the white outlines. The solid line indicates the target inline with the source, the dashed is 90° from the source line, and the dotted line is 180° from the source line.

experiment. The offset is calculated from the center of the well to the nearest edge of the target that is excited by a downhole source. As before, conductive targets are much easier to excite than resistive targets, and for a given conductivity, a downhole source provides greater excitation than a top-casing source. Naturally, as the target is moved further from the well, the geometric decay of source fields reduces our ability to excite the target. Positioning the return electrode along the same azimuth as the target acts to mitigate some of these effects for targets that are at distances greater than 200 m from the well, while for targets nearer to the well, the return electrode location has little effect on the excitation.

The next step to consider is detection of the secondary response due to this target. Consistent with the Born-approximation approach, I simulate the target as a dipole with

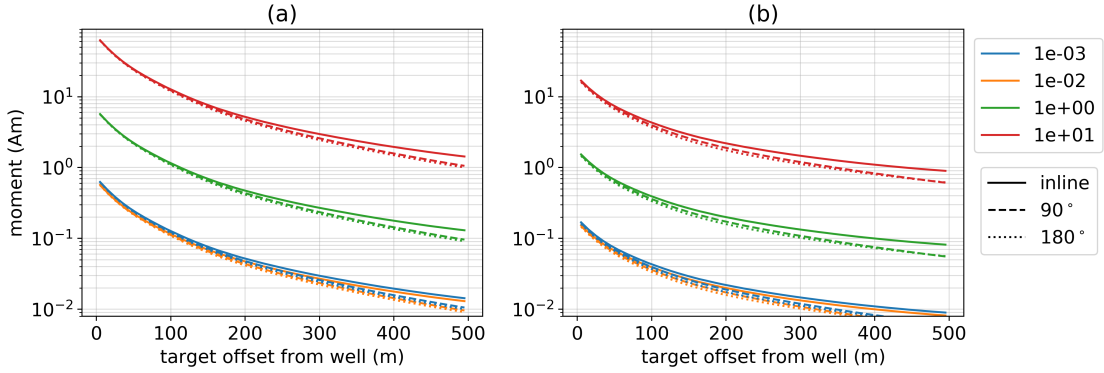


Figure 4.20: Integrated anomalous current density (excitation), as defined in equation 4.2, for a $50\text{ m} \times 50\text{ m} \times 25\text{ m}$ target at 900 m depth in a DC experiment with the positive electrode (a) downhole at 912.5 m depth, and (b) a top-casing electrode. The return electrode is positioned on the surface 500 m from the well. Each line color indicates a different target conductivity. The different line styles correspond to different target azimuths relative to the plane of the source electrodes and correspond to those shown in Figure 4.19. The solid line indicates a target inline with the source, the dashed is 90° from the source, and the dotted line is 180° from the source. Offset is calculated from the center of the well to the edge of the target closest to the well.

a moment computed with equation 4.2 and compare the secondary electric field data at the surface for models with, and without, the casing. For this example, I select the model of a conductive target (10 S/m) with center 50 m offset from the well. The target is along a line 90° from the source (e.g. along the same line as the dashed-outline in Figure 4.19). This gives a dipole moment of 38 Am for the target. The electric field data, measured along the same line as the target, are shown in Figure 4.21. The secondary response with the casing is shown in blue, and the response of the same dipole in a half-space is shown in orange. The secondary response due to the dipole in a half-space falls below the 10^{-7} V/m noise floor for all offsets, whereas, when the casing is included, the secondary response is above the noise floor until beyond offsets of 600 m from the well. The casing not only helps excite a target, as was demonstrated in

Schenkel and Morrison (1994), it also provides a conductive pathway for the secondary currents, thus increasing the secondary signal observed at the surface; this was similarly noted in Yang and Oldenburg (2016). In the model with the casing, the secondary signal comprises a significant percentage of the primary between offsets of ~ 200 m and ~ 650 m, providing a window between 200 m and 600 m where the secondary electric field is above the noise floor and comprises a significant percentage of the primary.

If I move the target further from the well, positioning its center 75 m from the well, then the dipole moment is reduced to 24 Am. If I use the criterion that the secondary electric field must be above the noise floor and be at least 20% of the primary field, then the region over which we can expect to collect data is reduced to a 50 m window between 300 m and 350 m offset from the well. For this given survey, then, we can consider ~ 25 Am as a threshold for detectability of a target.

Summary

The examples presented here showed that conductive targets are much easier to excite than resistive targets. For deep targets, a downhole electrode is preferable to a top-casing source as it delivers more current at depth to excite the target and reduces the strength of the primary at the surface; this makes the secondary field a larger percentage of the primary. For targets in close proximity to the well, if the target is in contact with the well, that electrical connection enhances the response. Additionally, I showed that beyond helping excite a target, as was demonstrated by Schenkel and Morrison (1994), the casing also improves detectability of secondary signals at the surface.

Designing a survey for a specific setting may require incorporation of 3D geologic structures and may include inversions to examine a survey's ability to recover a target. In this case, it is desirable to have a coarse-scale representation the steel-cased well on

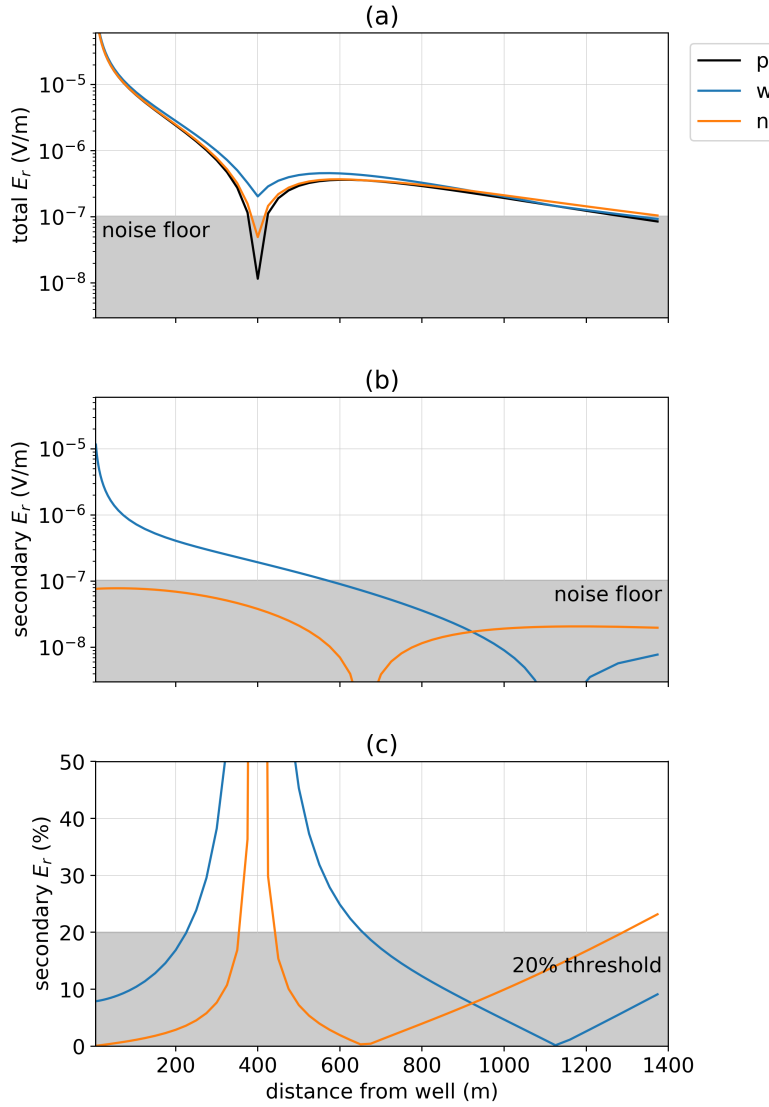


Figure 4.21: (a) Sum of the primary and secondary radial electric field due to a dipolar target with moment of 38 Am centered 50 m from the well, either calculated with the casing (blue) or simply a dipole in a half-space (orange). (b) Secondary radial electric field due to a dipolar target in a halfspace with casing (blue) and without casing (orange). Secondary radial electric field as a percentage of the primary. The target is along a line 90° from the source electrodes; this is the same line along which we measure data at the surface.

the simulation mesh. This is the topic of the next section.

4.4 Coarse-scale approximations of the well

When approaching the inverse problem, many forward simulations are required, and typically, a 3D cartesian mesh, with cells that vary on the length scales of the geology, is desired. Thus, rather than performing a fine-scale simulation of the steel-cased well, we may wish to represent the well on a coarse mesh. In the literature, two main approaches arise: the first approximates the well as some form of “equivalent source,” such as a charge distribution (e.g. Weiss et al. (2016)); the second approach represents the well as a conductivity feature on the coarse-mesh (e.g. Swidinsky et al. (2013); Um et al. (2015); Yang and Oldenburg (2016); Kohnke et al. (2017); Puzyrev et al. (2017), among others). Here, I will focus on the second approach, noting that a charge distribution along the length of the well can be computed with the 2D or 3D cylindrical code described in Chapter 3. Within the literature, there is disagreement among approaches for selecting the conductivity of the coarse-scale feature approximating the well. Um et al. (2015) replaces the fluid-filled cylinder with a solid rod having the same conductivity as the casing, arguing that it is the contrast between the conductivity of the well and the conductivity of the surrounding geology that is the most important factor; Puzyrev et al. (2017) also adopts this approach. Other authors have opted to preserve the cross-sectional conductance of the well (Swidinsky et al., 2013; Kohnke et al., 2017); this is consistent with the transmission-line model of the well discussed in Kaufman (1990). The aim of this section is to analyze these approaches.

4.4.1 Replacing a hollow-cased well with a solid cylinder

I consider a steel-cased well with a conductivity of 5×10^6 S/m that is embedded in a 0.1 S/m halfspace; the conductivity of the material that fills the well is the same as the background. The well has an outer diameter of 10 cm and a thickness of 1 cm, and I will vary its length. I will perform a top-casing experiment, where the positive electrode is connected to the casing at the surface. The return electrode is positioned 8 km away, and a cylindrically symmetric mesh is used in the simulations. I examine approximations that treat the casing as a solid cylinder with the same outer-diameter as the true, hollow-cased well.

The distribution of charges, or equivalently, the current in the casing, is the source of the electric response of the casing. Thus to judge if two models of the casing are “equivalent”, I examine the current and charges as a function of depth. In Figure 4.22, I have plotted the vertical current and charges along the casing for the true, hollow cased well (solid), solid cylinder with conductivity equal to that of the casing, 5×10^6 S/m (dashed), and solid cylinder with a conductivity that preserves the product of the conductivity and the cross-sectional area of the conductor, 1.8×10^6 (dotted), for four different casing lengths, each indicated by a different color. Figure 4.22 shows: (a) the vertical current along the casing, (b) the difference in current between the approximate model and the true model, (c) that difference as a percentage of the true solution (d) the charge per unit length, (e) difference in charge per unit length and (f) difference in charge per unit length as a percentage of the true solution.

For short wells, we see that the current decays linearly and that the charge distribution is nearly uniform above the end of the well, while for longer wells, the decay of the current is exponential in nature, as is the charge distribution. This behavior is consistent with that predicted by the transmission line solution described in Kaufman

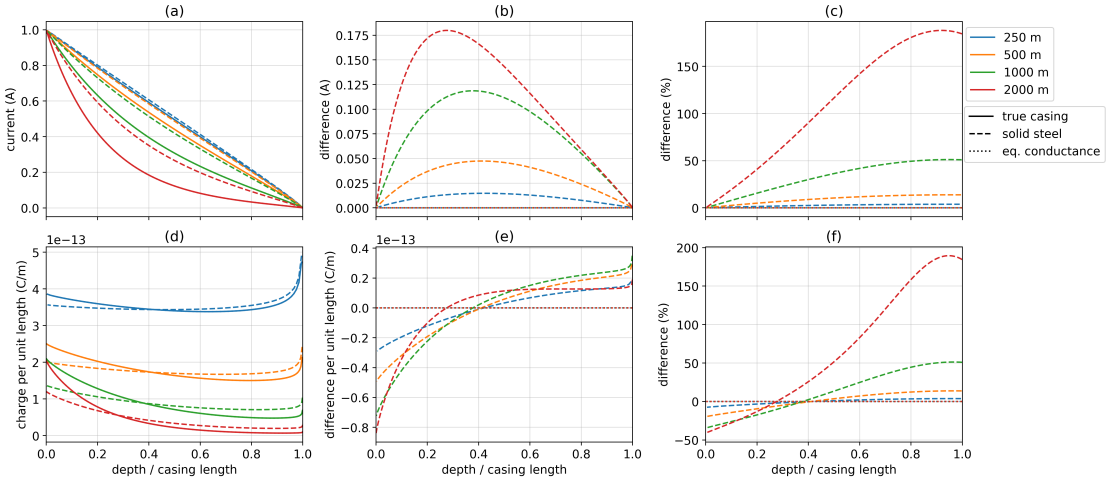


Figure 4.22: Currents (top row) and charges (bottom row) along the length of a hollow steel-cased well (solid lines), solid cylinder with conductivity equal to that of the steel-cased well (dashed-lines), and a solid cylinder with a conductivity such that the product of the conductivity and the cross sectional area of the cylinder is equal to that of the hollow-pipe (dotted lines). Each of the line-colors corresponds to a different casing length, as indicated in the legend. In (a), we show the vertical current in the casing, (b) shows the difference from the true, hollow-cased well in the vertical current within the casing, and (c) shows that difference as a percentage of the true currents. In (d), we show the charge per unit length along the casing, (e) shows the difference from the true, hollow-cased well and (e) shows that differences as a percentage of the true charge distribution. The x-axis on all plots is depth normalized by the length of the casing.

and Wightman (1993). Kaufman and Wightman (1993) showed that the transition between the linear decay of currents and the exponential decay of currents is controlled by three factors: the cross sectional conductance of the well, the resistivity of the surrounding formation, and the length of the well. Schenkel (1991) similarly summarized this behavior in the definition of the conduction length (equation 4.1), which is the length over which the currents in the casing have decayed by a factor of $1/e$. For sufficiently conductive and short wells (e.g. $L_c/\delta \ll 1$, where L_c is the length of the casing), the current decay is linear and independent of the conductivity, whereas for longer wells,

$(L_c/\delta \gg 1)$, the rate of decay of the currents is controlled by the conduction length (see equations 45 and 53 in Kaufman and Wightman (1993)).

In preserving the cross-sectional conductance, we see that the difference in currents and charges along the length of the well is negligible; the maximum difference in currents for the 2000 m long well which has equivalent cross-sectional conductance is 7×10^{-7} A as compared to the difference of 0.18 A when using the conductivity of the casing. This difference is important as it changes how much current is available to excite a target at depth. For a 2000 m long well, the current is overestimated by $> 150\%$ if the well is replaced by a solid cylinder with the same conductivity of the steel-cased well. It also changes the distribution of charges and thus the electric field due to the well. Figure 4.22e shows us that the extra conductance introduced when approximating the well using the conductivity equal to the casing results in a secondary dipolar charge on the casing. This in turn reduces the electric field we observe at the surface, as shown in Figure 4.23. For a long well, the difference can be as large as 40% near the well.

The numerical time-domain EM experiment used in Um et al. (2015) to justify the approximation of the well by a solid, conductive rod having the same conductivity as the steel-cased well used a 200 m long well with a thickness of 12.223 mm, outer diameter of 135 mm, conductivity of 10^6 S/m in 0.033 S/m half-space. The conduction length of this well is 560 m; this is more than twice the length of the well. Therefore, the behavior of the currents falls into the linear regime, where the decay of currents is mostly independent of the conductivity, and thus the difference between using the conductivity of the casing or preserving cross-sectional conductance is less significant. However, if longer wells such as those typically employed in hydrocarbon settings, are considered, the behavior of the currents and charges depends upon the conductance of the casing, and thus that is the quantity that should be conserved in an approximation of the hollow-

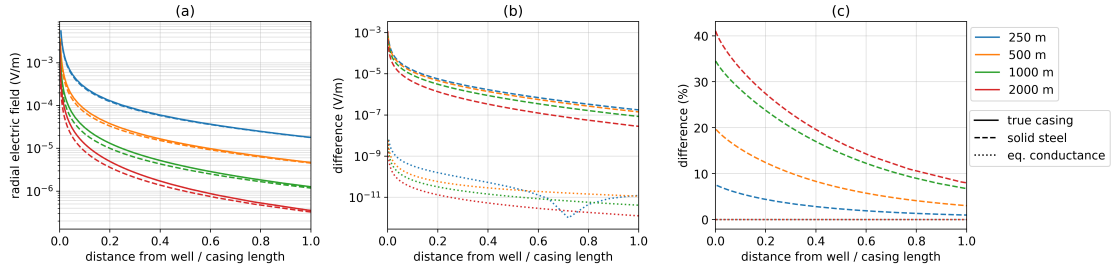


Figure 4.23: Radial electric field measured at the surface for a model of a hollow steel-cased well (solid lines), a solid cylinder with conductivity equal to that of the steel-cased well (dashed-lines), and a solid cylinder with a conductivity such that the product of the conductivity and the cross sectional area of the cylinder is equal to that of the hollow-pipe (dotted lines). Each of the line-colors corresponds to a different casing length, as indicated in the legend. In (a), we show the total radial electric field, (b) shows the difference in electric field from that due to the true, hollow-cased well, and (c) shows that difference as a percentage of the true electric fields. The x-axis on all plots is distance from the well normalized by the length of the casing.

cased well by a solid rod.

In order to confirm that this conclusion is valid for variable geology, I have included a simulation with a 2 km long casing in a layered background. Each layer is 50 m thick and the conductivity was assigned randomly; three instances are included, as shown in Figure 4.24. The mean of the background conductivity is 0.1 S/m for each of the models.

The currents and charges along the length of the well for the true model, and a model approximating the well as a solid cylinder with equal cross-sectional conductance, are shown in Figure 4.25. For all of the models shown, the difference in both the casing currents and the charges are 5 orders of magnitude less than the amplitude of the total currents and charges; thus I conclude that approximating a hollow cylindrical steel casing by a solid cylinder with a conductivity that preserves cross-sectional conductance is valid for models with variable geology.

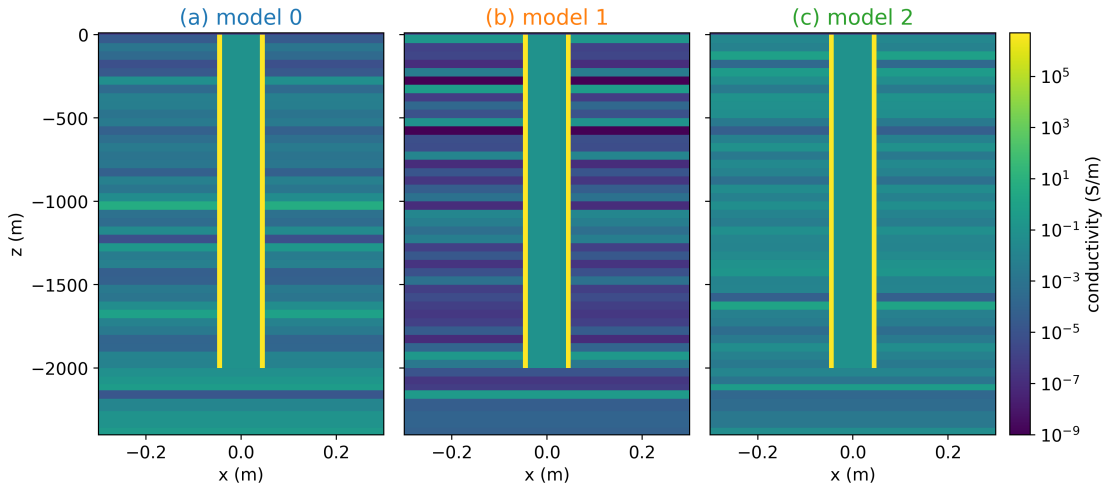


Figure 4.24: Three realizations of a 2 km long casing in a layered background, where the conductivity of the layers is assigned randomly. Each layer is 50 m thick, and the mean conductivity of the background is 0.1 S/m. The color of the title corresponds to the plots of the currents and charges in Figure 4.25

4.4.2 Cartesian grid

In the previous section, I showed that a hollow, cylindrical steel-cased well can be approximated by a solid cylinder with equal cross-sectional conductance. In this section, I move to a coarser, cartesian mesh, such as might be employed when solving a 3D inverse problem. I examine a simple approximation of a steel cased well on a cartesian grid. I employ 4 tensor meshes, each with progressively larger cell widths for the finest cells that capture the casing. On each of the cartesian meshes, I approximate the casing by preserving the product of the conductivity and the cross sectional area on the mesh. For comparison, I run a fine-scale simulation on a 3D cylindrical mesh that accurately discretizes the casing; it uses 4 cells across the casing-wall. The casing model is similar to that used in previous examples: it is 1 km long, has an outer diameter of 10 cm, a thickness of 1 cm, and is embedded in a 0.1 S/m half-space. The positive electrode is

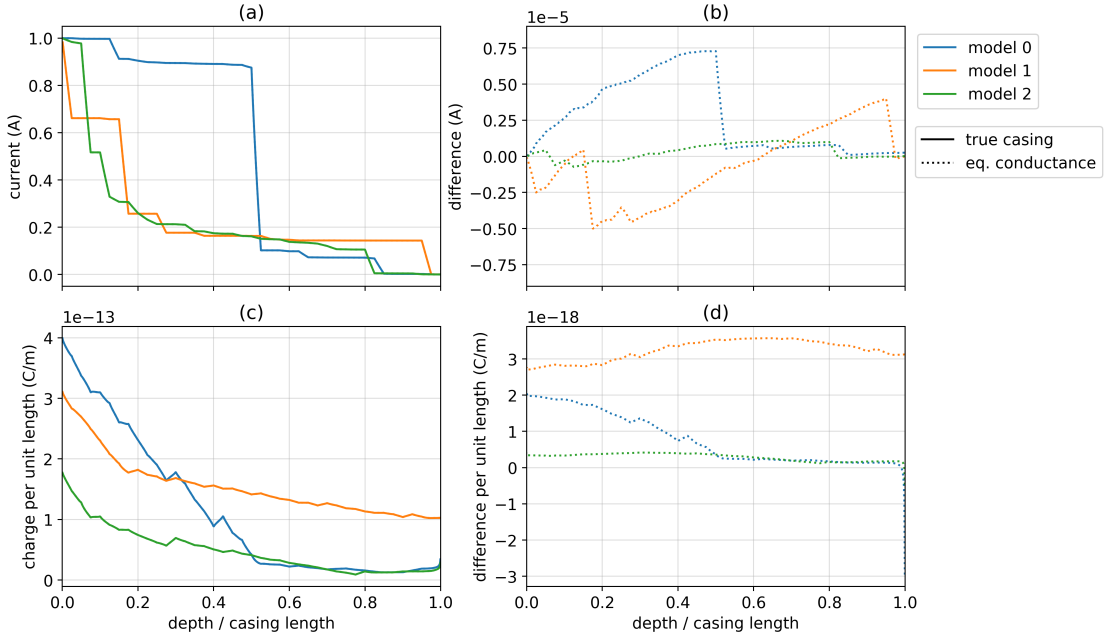


Figure 4.25: (a) Total vertical current through the casing for the three layered-earth models shown in Figure 4.24. The solid lines indicate the response of the true, hollow steel cased-well and the dotted lines indicate the response of a solid cylinder having the same cross-sectional conductance as the hollow well. (b) Difference between the currents along the casing in the solid well approximation and the true, hollow well. (c) Charge per unit length for each of the models. (d) Difference in charge per unit length between the true model of the casing and the approximation which preserves cross-sectional conductance.

connected to the top of the casing and a return electrode is positioned 1 km from the well-head.

The resultant currents and charge per unit length are shown in Figure 4.26. In the top row, panel (a) shows the total current in a region approximating the well, along with the total current in the “true” cylindrical well (black line), (b) shows the difference between the current through the cartesian cells and the true model, and (c) shows the difference as a percentage. Similarly, in the bottom row, I show (d) the charge per unit length along the cylindrical well (black line) and cartesian-prism approximations, (e) the difference

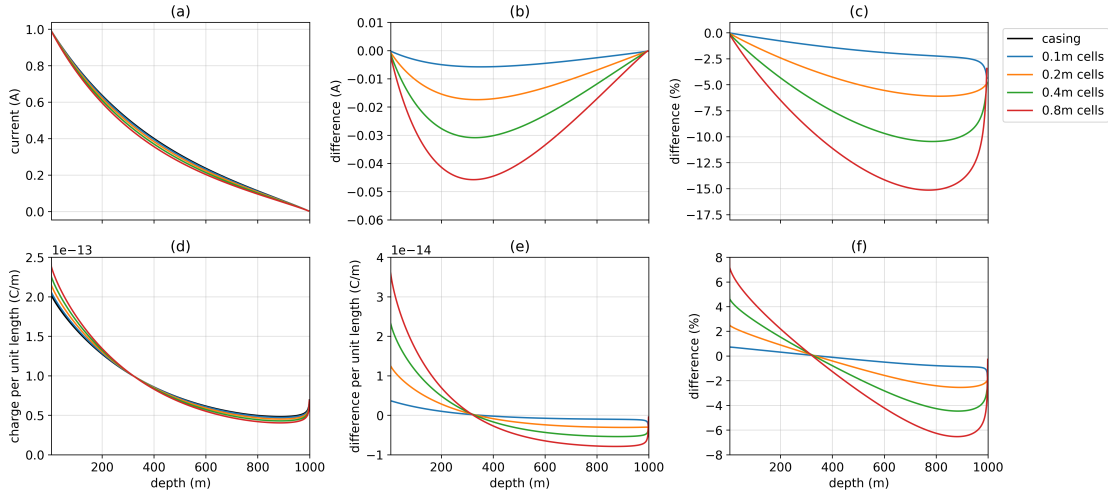


Figure 4.26: Currents (top row) and charges (bottom row) along the length of a steel cased well. The “true” hollow-cased well is simulated on a 3D cylindrical mesh and has 4 cells across the width of the casing thickness (black line). The colored lines correspond to the currents and charges computed along the well represented on a cartesian mesh with cell widths shown in the legend. The finest vertical discretization is 2.5 m in all simulations. To represent the hollow cased well on the cartesian mesh, the cells intersected by the casing are assigned a conductivity that preserves the product of the conductivity and cross-sectional area of the well. In (a), we show the vertical current in the casing, (b) shows the difference from the true, hollow-cased well in the vertical current within the casing, and (c) shows that difference as a percentage of the true currents. In (d), we show the charge per unit length along the casing, (e) shows the difference from the true, hollow-cased well and (e) shows that differences as a percentage of the true charge distribution.

in charge per unit length from the charge per unit length on the true cylindrical model, and (f) that difference as a percentage of the charge per unit length on the cylindrical well.

The approximation of the cylindrical well by a rectangular prism with width equal to the diameter of the casing introduces minimal error in the currents and charges computed using a finite volume approach, even though the casing is only captured by one cell

across its width. Comparing the current along the length of the well for the 3D cylindrical well and the cartesian simulation with 0.1 m cells, we see that the error introduced is $< 2.5\%$ (until the end of the well where the current approaches zero). Similarly, the difference in the charge per unit length is $< \pm 1.25\%$. As successively coarser discretizations are used, accuracy is gradually lost; by doubling the cell sizes to 0.2 m, the error in the currents is 6% at its maximum and $< \pm 3\%$ in the charge along the casing. A factor of 8 increase in cell size (0.8 m cells) results in a maximum error of 15% in the currents. It is important to note that the forward simulation is conducted using a finite volume approach; other approaches such as finite difference or integral equation approaches may have worse agreement if care is not taken to handle large physical property contrasts, captured by a single cell, in the simulation. Note that the behavior of the errors depends upon the properties of the casing (e.g. conductivity and length) as well as the conductivity of the background. This might be expected from the description of the casing conduction length (equation 4.1). If the conduction length is large relative to the length of the well, the currents decay linearly, and the geometry and conductivity of the well are less significant in the behavior of the currents. Alternatively, if the conduction length is comparable to the length of the well, the currents decay exponentially with a decay rate that depends on the geometry and conductivity of the well. For example, if the background is more resistive, increasing the contrast between the casing and background, the reduces the errors. Using a background conductivity of $100\Omega m$, the maximum error introduced in the current is $< 1\%$ with 0.1 m cells and $< 2\%$ with 0.8 m cells.

Depending on the level of accuracy required in a 3D simulation, there are several strategies that one might take to reduce this error. In some cases, local refinement can be achieved with a tetrahedral mesh, as is often employed when using finite element tech-

niques (e.g. Weiss et al. (2016)), or an OcTree mesh (Haber et al., 2007). Other, more advanced approaches including upscaling and multiscale could also be considered. In an upscaling approach, one inverts for a conductivity model, which might be anisotropic, that replicates the physical behavior of interest (Caudillo-Mata et al., 2017a). Multiscale techniques translate conductivity information from a fine-scale mesh to a coarse-scale mesh, on which the full simulation is to be solved, using a coarse-to-fine interpolation that is found by solving Maxwell’s equations on the fine mesh locally for each coarse grid cell (Haber, 2014a; Caudillo-Mata et al., 2017b). The 3D cylindrical forward simulation code described in Chapter 3 and used in this example can serve a tool for validating and refining an approach to achieve the desired level of accuracy.

4.5 Conclusion

The work in this chapter is motivated by the increasing use of steel cased wells in geoscience problems, including monitoring applications such as carbon capture and storage and hydraulic fracturing. For geophysical imaging of targets at depth, the wells are beneficial as they can be used to channel currents to depth and enhance signals at the surface for targets that otherwise would be undetectable from a surface-based survey. Additionally, there is interest in considering the casing itself as the geophysical target in casing integrity experiments; here the aim is to detect flaws or breaks in the casing. These applications, coupled with advances in modeling capabilities, open up the potential for advancing the utility of electrical and electromagnetic imaging in settings with metallic-cased wells.

Despite this potential, the reality is that electric field fields, especially if measured at the Earth’s surface, are small. Secondary fields might only be a few percent of the primary field, and thus too insignificant to reliably detect the target of interest. The

success of using a DC or EM survey then depends upon many details that pertain to understanding the basic physics, the effects of parameters of the casing, the background conductivity, location of the current electrodes, and discerning which fields should be measured. DC resistivity is the starting point, as it allows us to examine the currents, charges, and electric fields in the electrostatic limit, prior to introducing inductive effects and the influence of magnetic permeability in an EM signal, and as such, was the focus of this paper. Regarding the physics, a DC survey involves attaching a current generator to a conductive medium. This establishes a steady state current; the signal to which we are sensitive is the electric field that arises from charges that accumulate at interfaces separating regions of different conductivity. For this reason, most of our results are first presented as currents and charges.

The large contrasts in physical properties and significant variation in length scales due to long, thin, cylindrical, steel-cased wells prompt a number of questions about how the EM fields behave. In many cases, the finer details about the physical responses has challenged my intuition. With respect to the casing integrity application there were basic questions: how does a flaw in the pipe affect the currents and electric fields measured at the surface? Does the extent of the flaw change our ability to detect it (e.g. if it has a vertical extent of several meters versus a vertical extent of centimeters)? What happens if the flaw only comprises a part of the well, leaving some connectedness in the casing? When considering a geophysical experiment for imaging a target: is there a significant difference in the currents at depth between scenarios where a source electrode is connected to the well-head at the surface and one where the source electrode is offset from the well by a few meters? The surface signals are small; are there preferential geometries for the source and receiver electrodes that maximize signal/noise? A major goal of the DC survey will be to excite and detect target bodies. For problems, such

as CO₂ sequestration, enhanced oil recovery, or hydraulic fracturing, the target may or may not be in contact with the well; how significant is an electrical contact between a target and the well in the data we measure at the surface?

Looking towards solving inverse problems in settings with steel-cased wells, it is advantageous to reduce the computational cost of the forward simulation because an inversion requires many forward simulations. There are several approaches that can be taken to achieve this; one common approach is to approximate the finely-discretized well with an approximation on a coarse-scale mesh. Currently, there is disagreement within the literature as to how this should be done. Some authors have advocated that the conductivity contrast between the casing and the background should be preserved and thus replace a hollow steel-cased well with a solid rod that has a conductivity equal to that of the casing. Other authors have opted to preserve the product of the conductivity and cross-sectional area of the casing, following the conclusions of the transmission-line solution shown in Kaufman (1990). What is the correct conductivity needed for substitution?

Some of the above questions have been addressed in theoretical papers extending back a few decades but numerical verification was often limited or carried out with simplifying assumptions. Other questions require the ability to carry out numerical modeling in 2D or 3D environments – these tools are just now becoming available. My goal with this chapter has been to examine the scientific questions above and to promote insight about the solution by plotting the currents, charges, and electric fields.

Chapter 5

Electromagnetics with steel cased wells

5.1 Introduction

In the previous chapter, I focussed on the physics of direct current (DC) resistivity experiments in settings with steel cased wells. This provided a fundamental understanding in terms of the charges, currents and electric fields. In this chapter, I shift attention to the electromagnetic (EM) problem where the fields and fluxes vary in time. EM can be advantageous in that for a given survey geometry, the response can be sampled at multiple frequencies or times, providing richer information than is available by only the electrostatic response in a DC experiment. The richness in information comes both from the additional physics introduced as inductive processes become relevant, as well as potentially multiple excitation directions as the formation currents change through time.

In addition to time-variation of fields and fluxes in an EM experiment, the physics in settings with steel casing is further complicated by the significant magnetic permeability of the steel. Typically, magnetic permeability is often neglected in EM simulations and inversions as the variations in permeability are typically much less significant than the

role of conductivity in the data. However, steel has a permeability of $\geq 100 \mu_0$ (Wu and Habashy, 1994).

The role of permeable casings has been explored for inductive sources and receivers, primarily in the context of cross-well EM surveys (Augustin et al., 1989a; Wu and Habashy, 1994; Wilt et al., 1996; Becker et al., 1997; Lee et al., 1998, 2005; Kim and Lee, 2006). For grounded sources, the influence of permeability is much less explored. More recently, some authors have included magnetic permeability in simulations with casings, (e.g. (Kong et al., 2009)), but most of the published EM simulations of metallic cased wells neglect to include magnetic permeability (e.g. (Swidinsky et al., 2013; Commer et al., 2015; Um et al., 2015; Fang et al., 2017; Puzyrev et al., 2017)). Within the publications that include permeability in grounded-source simulations, there is minimal analysis on how permeability alters the behavior of the currents in the earth or how it affects data measured at the surface. A notable exception is the work in Wait and Williams (1985); Williams and Wait (1985). They developed an analytical model for a dipole-dipole frequency domain electromagnetic experiment over a halfspace with a conductive, permeable, and polarizable casing. Their simulations showed that if the casing is permeable, the apparent resistivity and phase measurements made at the surface data can be biased upwards as compared to only a conductive casing. Expanding on our understanding of how the permeability impacts the subsurface currents and the resultant measured data in a grounded-source experiment with a steel cased well is a prime goal of this chapter.

For numerical modelling, particularly when considering the inverse problem, it is advantageous to reduce the size of the mesh to reduce the computational cost. In Chapter 4, I showed that for a DC resistivity experiment, preserving the product of the conductivity and the cross-sectional area of the casing is a viable strategy if the cells which

encapsulate the casing are approximately equal in size to the diameter of the casing. It is questionable if this same approximation holds for EM experiments. Furthermore, it is unclear how to approximate the magnetic permeability on a coarse scale. Schwarzbach and Haber (2018) suggests an upscaling strategy based upon that presented in Caudillo-Mata et al. (2017a), where one inverts for the conductivity and the permeability of the casing. By analyzing the behavior of the fields and fluxes, we may be able to calibrate our expectations of upscaling strategies for permeability.

We have the choice to focus our analysis in the time-domain or the frequency-domain. Here, I choose to conduct the analysis in the time-domain. The physics of EM are arguably more intuitive in the time-domain, as all fields are real and we can step through changes with time. The frequency-domain requires that we consider the partitioning of electromagnetic energy into real and quadrature components; this additional step can be a hurdle to building intuition.

The chapter is organized as follows. In section 5.2, I consider the time-domain EM (TDEM) response of a conductive well in a “top-casing” experiment where one electrode is connected to the top of the well and a return electrode is positioned some distance away on the surface. I examine the currents within the casing and in the surrounding geologic formation through time; this provides the foundation for understanding the EM casing response. Following from this, I introduce magnetic permeability in Section 5.3 and demonstrate how it alters the current and the impact this has on data collected at the surface. Finally, in section 5.4, I examine the problem of approximating a conductive, permeable, steel-cased well and discuss some of the challenges that are unique to EM as compared to DC.

Source code for all of the examples shown in this chapter are available as Jupyter notebooks as outlined in Appendix A.

5.2 EM response of a conductive casing

As a starting point for this discussion, I first perform a simple numerical experiment to demonstrate the behavior of the currents in a time-domain EM experiment over a half-space. For this simulation, a positive electrode is positioned at the origin (where the casing will be) and a return electrode is positioned 1 km away (at $x = 1000$ m). The conductivity of the background is 10^{-2} S/m, and the conductivity of the air is set to 1×10^{-4} S/m. When we come to simulations with the casing, I have observed that contrasts near or larger than $\sim 10^{12}$ S/m leads to erroneous numerical solutions, and thus it is preferable to set the air to be more conductive than what it typically employed in EM simulations (often $\sim 10^{-8}$ S/m). A step-off waveform is used and the currents within the formation are plotted through time in Figure 5.1. Panel (a) shows a vertical cross section along the line of the wire, (b) shows a horizontal depth slice at 50 m depth and (c) shows a depth slice at 800 m depth. The images in panels (a), (b) and (c) are on the same color scale.

At time $t=0$ s, the currents behave according to the DC solution. In panel (a), we see the flow of current from the current is shut-off, an image current develops in the formation; this image current acts to preserve the magnetic up by the source current. The image current flows in the same direction as the original current in the wire. This is opposite point between the two current electrodes) which propagates downward through time. Similarly, in the depth

Having established the background response, I now consider a model with a steel-cased well. The well has a conductivity of 5×10^6 S/m and is 1 km long; it has an outer diameter of 10 cm and a 1 cm thick casing wall. The mud which infills the well has the same conductivity as the background, 10^{-2} S/m. At this point, I focus on electrical conductivity only and set the permeability of the well to μ_0 . I will introduce variable magnetic permeability in the following section. The source electrode is connected to the top of the casing, and the return electrode is in the same position as the previous

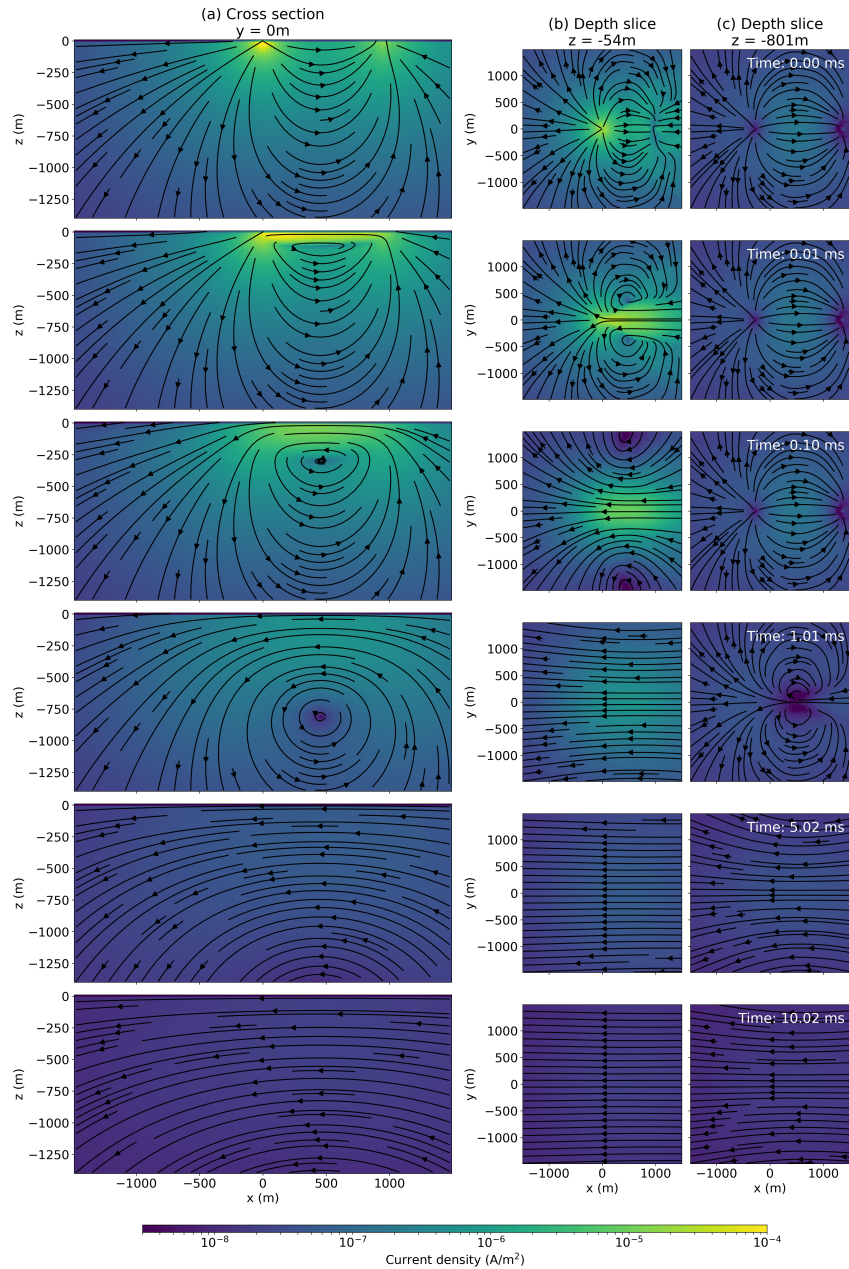


Figure 5.1: Current density for a time domain experiment over a 10^{-2} S/m half-space. The positive electrode is on the surface where the well-head will be and the return electrode is at $x = 1000\text{ m}$. Each row corresponds to different time, as indicated in the plots in panel (c). Panel (a) shows a cross section through the half-space along the same line as the source-wire. Panels (c) and (d) show depth-slices of the currents at 54 m and 801 m depth.

example ($x = 1000$ m). The same step-off experiment is run and the currents plotted in Figure 5.2. I have added a fourth panel (a) which zooms in to the wellbore. Panels (b), (c) and (d) again show a cross-section of the currents in the formation and depth slices at 50 m and 800 m depth, respectively.

At time, $t=0$ s, we can see the increased current density along the length of the well, which correspondingly increases off, which can be seen in Figure 5.2(b). There is again a circulation of current, however the geometry of this circulation is different. At $t=0.1$ ms it is at 225m and by $t=1$ ms, the zero crossing approaches the mid-way point in the casing and is at 470m. This crossing slows as the image currents are channeled into the highly conductive casing.

Further out in the formation, we similarly see the interaction of the diffusing formation currents set up at DC and the image currents. Rather than being centered at the midway point between the positive and negative electrodes as in the half-space example (Figure 5.1), the center of the circulating currents shifts with time. At early times, it is closer to the well, while at later times, it is closer to the mid-way point. By 10 ms, the impact of the well is much less evident and the currents are very similar in character to those obtained in the half-space experiment.

On the side of the well opposite to the wire, we also see a null develop; it is visible in the cross sections in panel (a). To help understand this, we examine the depth slices in panel (c). Behind the well, we see that as the image currents diffuse downwards and outwards, some of those currents are channeled back towards the well; this is visible in the depth slice at 10^{-4} s. These channeled currents are opposite in direction to those the formation currents set up at $t = 0$ s, which also are diffusing downwards and outwards; where these two processes intersect, there is a current shadow.

We can isolate the “casing response” by taking the difference between the currents generated when the casing is present (Figure 5.2) and those generated in the half-space model (Figure 5.1). This is plotted in Figure 5.3. Within the casing and the surround-

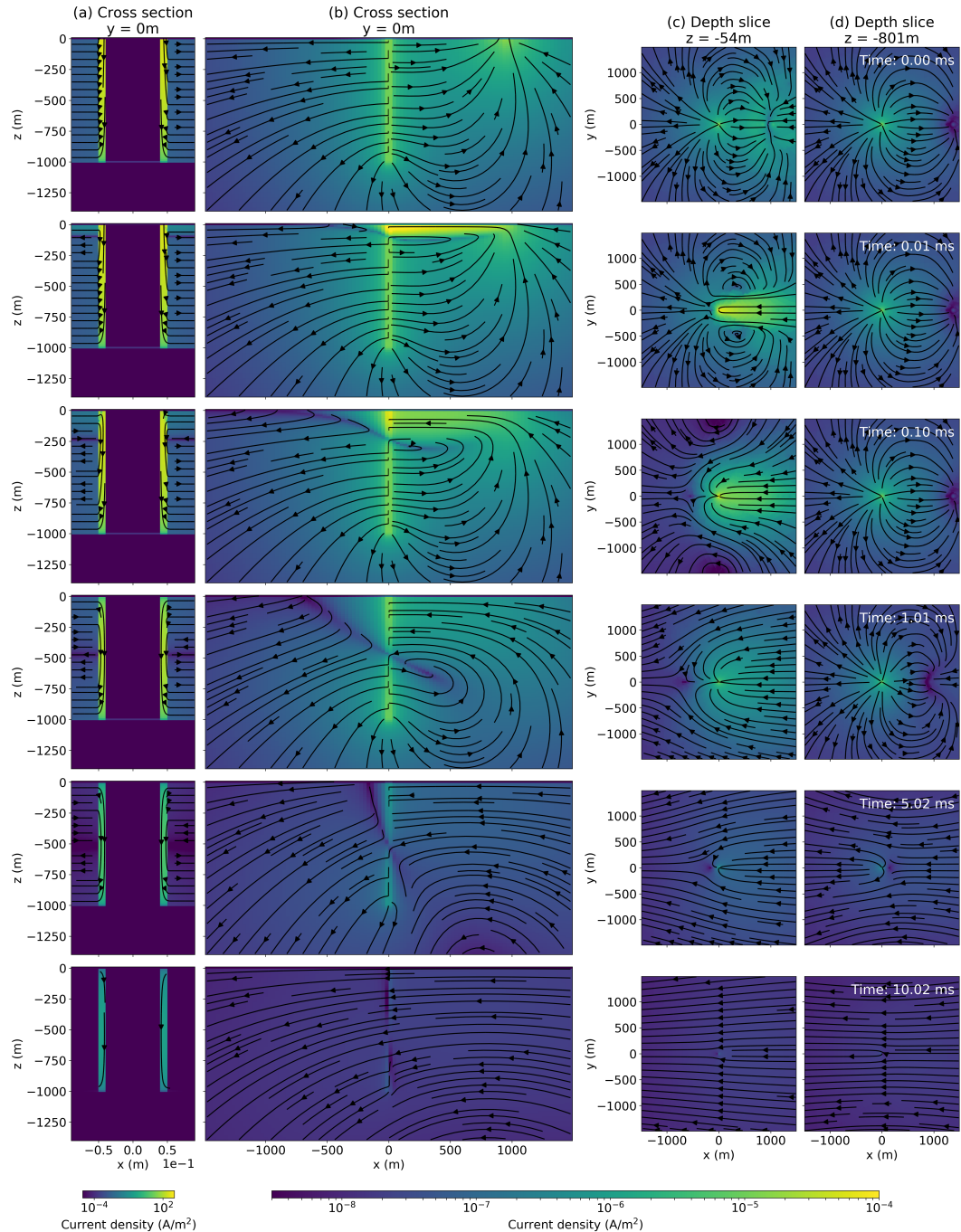


Figure 5.2: Current density for a top-casing time domain EM experiment with a conductive well (5×10^6 S/m). (a) Cross section in the immediate vicinity of the well. (b) Cross section through the formation. (c – d) depth-slices.

ing formation, these secondary currents are cylindrically symmetric. This might not be immediately intuitive given the complexity of the behavior observed in Figure 5.2, however, it is a highly conductive, cylindrically symmetric target, and the main impact it has on the physical behavior is that it channels currents along its length. At all times, there is a downward-going secondary current within the casing. This results in dipolar-like currents within the surrounding formation.

5.2.1 Data

On the surface, we can measure electric field data and/or the time-rate of change of the magnetic field (db/dt) as a function of time. Due to the cylindrical symmetry of the currents in Figure 5.3, we can expect that the radial electric field and the tangential db/dt will be most impacted by the presence of the casing.

Electric field

In Figure 5.4, I show surface electric field data for 2 times, an early time (0.01 ms) and a later time (5 ms). The top row shows data from the background model. The two panels on the left show the electric field at the surface at (a) 0.01 ms and (b) 5 ms. On the right, (c) shows the radial electric field measured along the $x = 0$ m line (indicated by the white-dashed lines in (a) and (b)), and (d) shows a time-decay for a receiver positioned 300 m from the well (indicated by the red dot in (a) and (b)). Data that are positive are plotted with the solid lines and data that are negative are plotted with dashed lines. The red dots in panel (c) correspond to the 300 m offset location where the data in (d) are taken from. Similarly, the blue and green dots in (d) correspond to the time-channels shown in (c). The middle row shows the same information but for the simulation with the conductive well, and the bottom row shows the difference between the casing and background data (casing minus background).

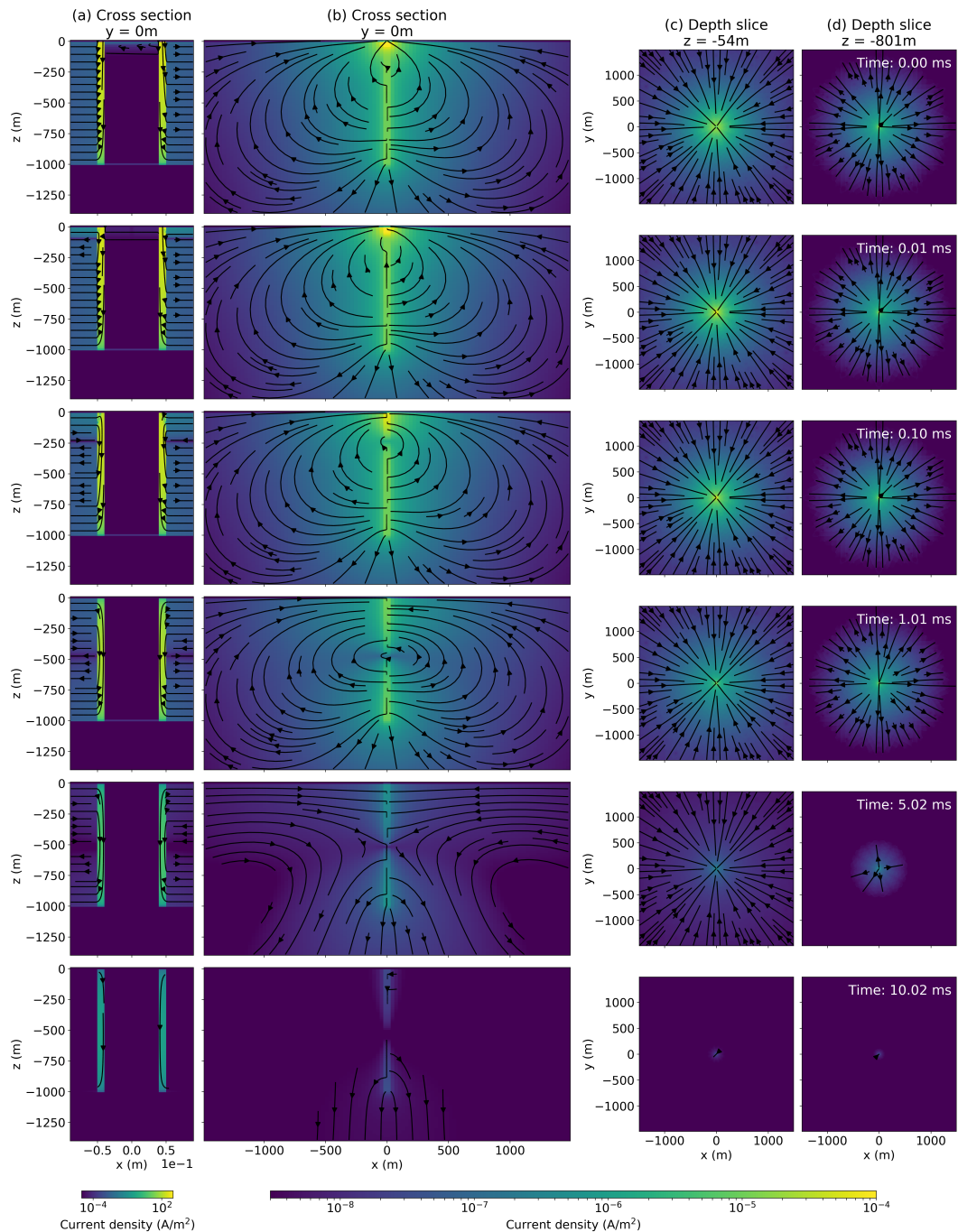


Figure 5.3: Difference in current density for a time domain experiment which includes a conductive steel-cased well (as in Figure 5.2) and an experiment over a halfspace (as in Figure 5.1).

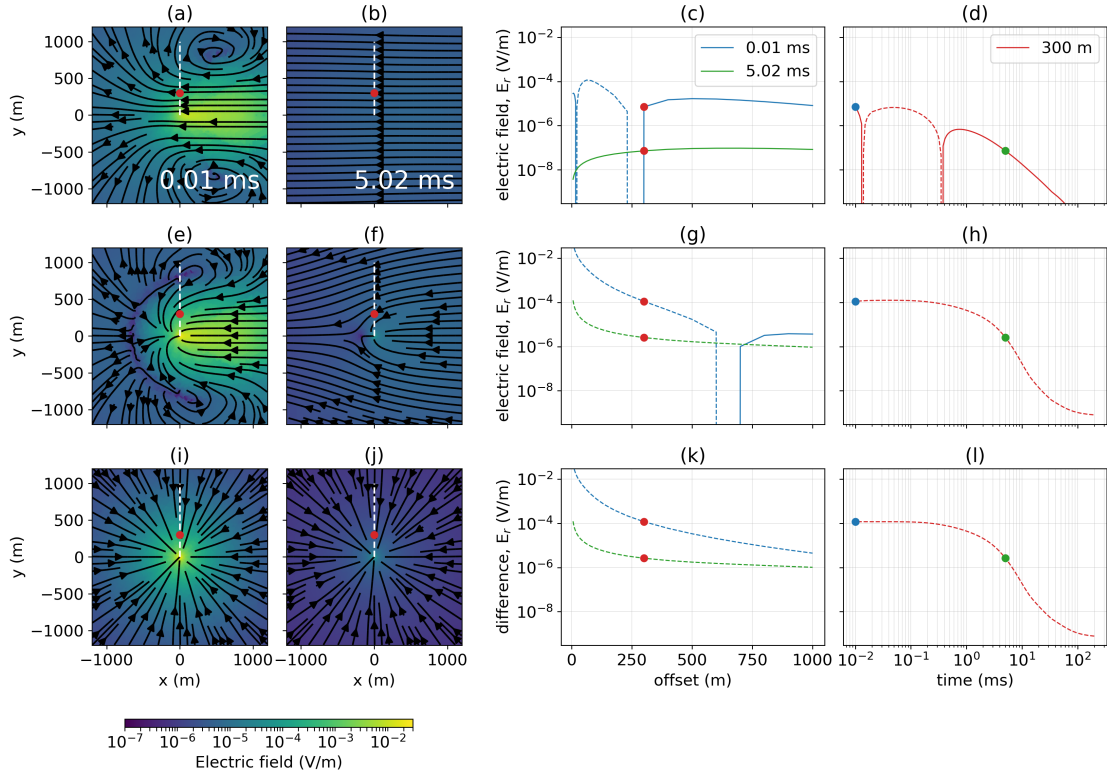


Figure 5.4: Simulated electric field at the surface of the earth at (a) 0.01 ms and (b) 5 ms after shut-off for the halfspace model. (c) Radial electric field data measured along the survey line shown in white in (a) and (b) at 0.01 ms (blue) and 5 ms (green). (d) Radial electric field as a function of time at 300 m along the survey line (shown in the red dot in (a)). The red dots in (c) correspond to the data observed at 300 m offset and the blue and green dots in (d) correspond to the 0.01 ms and 5 ms data. Similar information is shown in (e), (f), (g) and (h) for the model with the conductive casing. The difference in the radial electric field data (casing minus halfspace) is shown in (i), (j), (k) and (l).

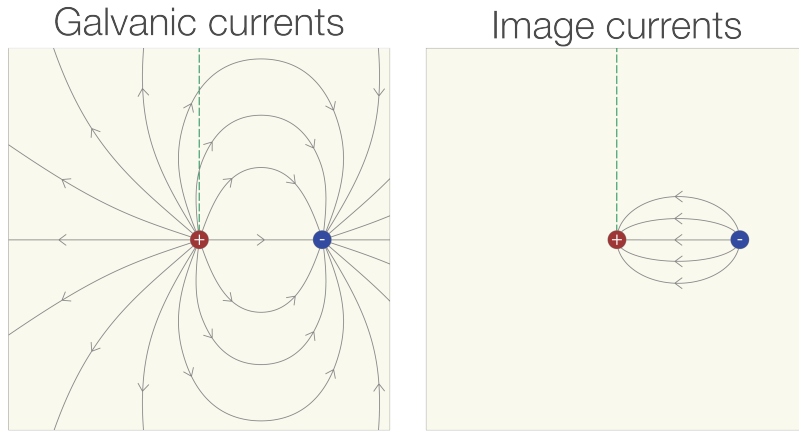


Figure 5.5: Sketch of the plan-view geometry of the early-time galvanic currents (left) and image currents (right) in a time-domain EM experiment over a half-space. Through time, both current systems diffuse downwards and outwards as they decay. The wire follows a straight line between the negative and positive electrodes. The green dashed line shows where we are measuring the radial electric field data. Prior to shut-off, current in the wire flows from the negative to the positive electrode. In the earth, the galvanic currents are dipolar in nature and flow from the positive to the negative electrode. Along the survey-line, the radial component of the galvanic currents always points outwards. Immediately after shut-off, image currents are induced in the earth. They are oriented in the same direction as the original current in the wire and are directed away from the negative electrode towards the positive. Along the survey-line, the radial component of the image currents is always pointed inwards.

At early times (0.01ms), the behavior of the geometry of the electric field is fairly complex (panel a). The electric field we observe results from a combination of the diffusing galvanic and image currents. The galvanic currents, set up at DC, are dipolar in nature, with field lines directed radially outward from the positive electrode located at $x = 0$ m. The image current is directed in the negative x-direction and causes some inward deflection of the fields (this can also be observed at 0.01 ms in Figure 5.1). A sketch of both current systems is shown in Figure 5.5

The radial electric field data at offsets less than 300 m are primarily influenced by the geometry of the image currents, while beyond 300 m, the data are primarily influenced by the dipolar galvanic currents. Diffusion of both current systems continues through time. By 5 ms the image current has passed and the geometry of the fields reflects that of the diffusing galvanic currents. This means that the electric fields are a diffuse dipolar shape that is centered at the midpoint of the wire (e.g. as in Figure 5.1b at 1 and 5 ms). Along our survey line, the electric field is oriented mainly in the negative y-direction, but with a slight outward deflection due to the dipolar nature of the fields, and are therefore positive. Through time, we can similarly see the impact of the passing image current. At very early times, the data are positive, as the galvanic currents and associate electric field are the main contributor to the response. When the image current arrives, just past 0.01 ms, the electric field is deflected inwards, reversing the sign of the radial electric field data. The second sign-reversal occurs at ~ 0.3 ms; at this point, the image current has diffused considerably, and we again return to a geometry that is mainly influenced by the diffusing galvanic currents.

I now consider the data when a casing is present. The casing introduces further complexity as it channels both galvanic and image currents. We can see the impact in the geometry of the fields in (e). The channeled currents are directed inwards, towards the well, giving the large negative radial electric field response observed at short offsets in (g). In panel (g), we see that this additional current-channeling pushes the sign reversal that we observed in the early time in (c) for the background model to a further offset. At later times, we continue to see the impact of the casing as the diffusing currents are deflected inwards (panel f). The result is that the radial electric field data remain negative through time as can be seen in (g) and (h).

The story simplifies if we examine the difference between the data from the model

with the casing and those simulated with the background. Essentially, by subtracting the background data from the casing data, we remove the 3D survey geometry from the behavior of the fields, and are left with the current-channeling behavior. The well is a highly conductive feature and once the source current is shut off, the diffusing image current and galvanic currents are channeled towards it. The result is the cylindrically symmetric fields shown in (g) and (h). The electric field is directed radially inwards, and thus the secondary “casing-response” in (k) and (l) is always negative through time.

Time rate-of-change of the magnetic flux

We can examine the db/dt data at the surface. Figure 5.6, shows the db/dt data for the background (top row), casing model (second row), and difference between them (third row). Additionally, I include plots of the db/dt data difference as a percentage of the background response in (m) and (n). The data plotted in the rightmost column (plots (c), (d) and below) are the azimuthal component of db/dt along the white-dashed lines shown in panels (a) and (b).

The db/dt response is quite 3-dimensional in its geometry. At early times (panel (a), 0.01 ms), we have a rotational component that arises from the downward-directed current density at the positive electrode, located at the origin. We also have a contribution from the horizontal image currents and galvanic currents, which complicates the behavior between $x = 0$ m and $x = 1000$ m. Near the surface, there is a y-directed component from these current systems. Later in time (5 ms) the db/dt data in (b) are primarily influenced by the diffusing horizontal currents and thus db/dt is oriented in the y-direction along the wirepath. The difference between the data from the simulation with the casing and without is much less dramatic than we observed in the electric field data. It is really only the late times at short offsets that are significantly impacted; be-

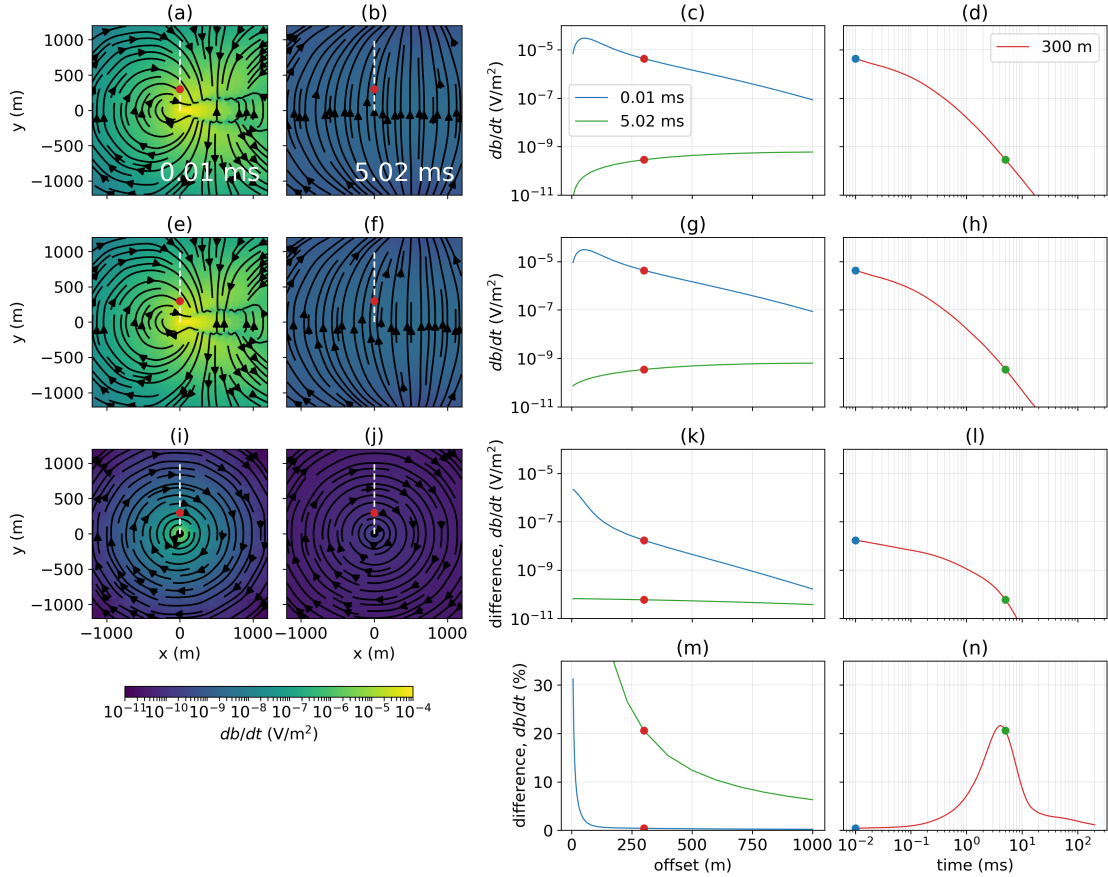


Figure 5.6: Simulated db/dt at (a) 0.01 ms and (b) 5 ms after shut-off for the halfspace model. (c) Tangential db/dt measured along the white line in (a) and (b) at 0.01 ms (blue) and 5 ms (green). (d) Tangential db/dt as a function of time at 300 m along the survey line (shown in the red dot in (a)). Similar information is shown in (e), (f), (g) and (h) for the model with the conductive casing. The difference in the db/dt data (casing minus halfspace) is shown in (i), (j), (k) and (l). The difference is also shown as a percentage of the halfspace solution at 0.01 ms and 5 ms in (m) and through time at 300 m offset in (n).

yond 400 m offset from the well, the difference between the db/dt data with the casing (f) and without (c) is less than 10% for the 1 ms data. In contrast, the electric field data in Figure 5.4 differed by several orders of magnitude different at all offsets shown.

To summarize the above results, we see that each data-type is sensitive to different aspects of the physics. The radial electric field data are influenced by radial currents, which, as seen in the Figure 5.3, are significantly altered near the surface over a large range of offsets when the casing is present. The tangential db/dt data, however, are primarily influenced by vertical currents, which are most altered near the wellbore.

5.2.2 Discussion

There are a number of points to highlight in these examples. The first, which has been noted by several authors (e.g. Schenkel and Morrison (1994); Hoversten et al. (2015)), is that the casing helps increase sensitivity to targets at depth. This occurs by two mechanisms: (1) at DC, prior to shut-off, the casing acts as an “extended electrode” leaking current into the formation along its length; (2) after shut-off, it channels the image currents and increases the current density within the vicinity of the casing. The second point to note is that there are several survey design considerations raised by examining the currents: targets that are positioned where there is significant current will be most illuminated. If the target is near the surface and offset from the well, a survey where the source wire runs along the same line as the target will have the added benefits of the excitation due to the image currents. These benefits are twofold: (1) the passing image current increases the current density for a period of time, and (2) the changing amplitude and direction of the currents with time generate different excitations of the target. This should provide enhanced information in an inversion, as compared to a single excitation that is available from a DC survey. For deeper targets in this experiment, the passing

image current has diffused significantly, and thus it appears that the wire location has less impact on the magnitude of the current density with location. However, it is possible that increasing the wire length could be beneficial. This extension is straightforward and could be examined with the provided script. Often, little attention is paid to the wirepath in an EM survey, and only the electrode positions are considered as a part of the survey design. These examples show that the image currents, whose geometry is dictated by the geometry of the wirepath, have a significant influence on the behavior of the currents and the resultant data. Thus, these examples also provide motivation for thinking of the wirepath as a component of the EM survey design.

5.3 EM response of permeable casings

The previous section demonstrated the behavior of the currents in a TDEM experiment with a conductive casing; in this section, I am interested in building an understanding of how the magnetic permeability of the pipe affects the currents the EM response. Using the same survey setup and casing geometry as in Figure 5.2, I now include magnetic permeability in the simulation. The permeability of the casing is set to $\mu = 100\mu_0$ and the resultant currents are shown in Figure 5.7.

The early-time behavior of the currents is very similar to what we observed in the case of a conductive well (Figure 5.7). As we move to later times, however, we can see that the permeability of the steel introduces further complexity into the behavior of the currents. Notably, in Figure 5.7(a) at 5ms and 10ms, there is a vertical circulation of currents within the well-casing; near the inner wall of the casing, the currents are moving downwards, while near the outer wall, the currents are moving upwards. This is particularly noticeable near 750m depth in the 5ms image. The behavior of the currents within the formation is also more complex. By 10ms, the impact of the conductive

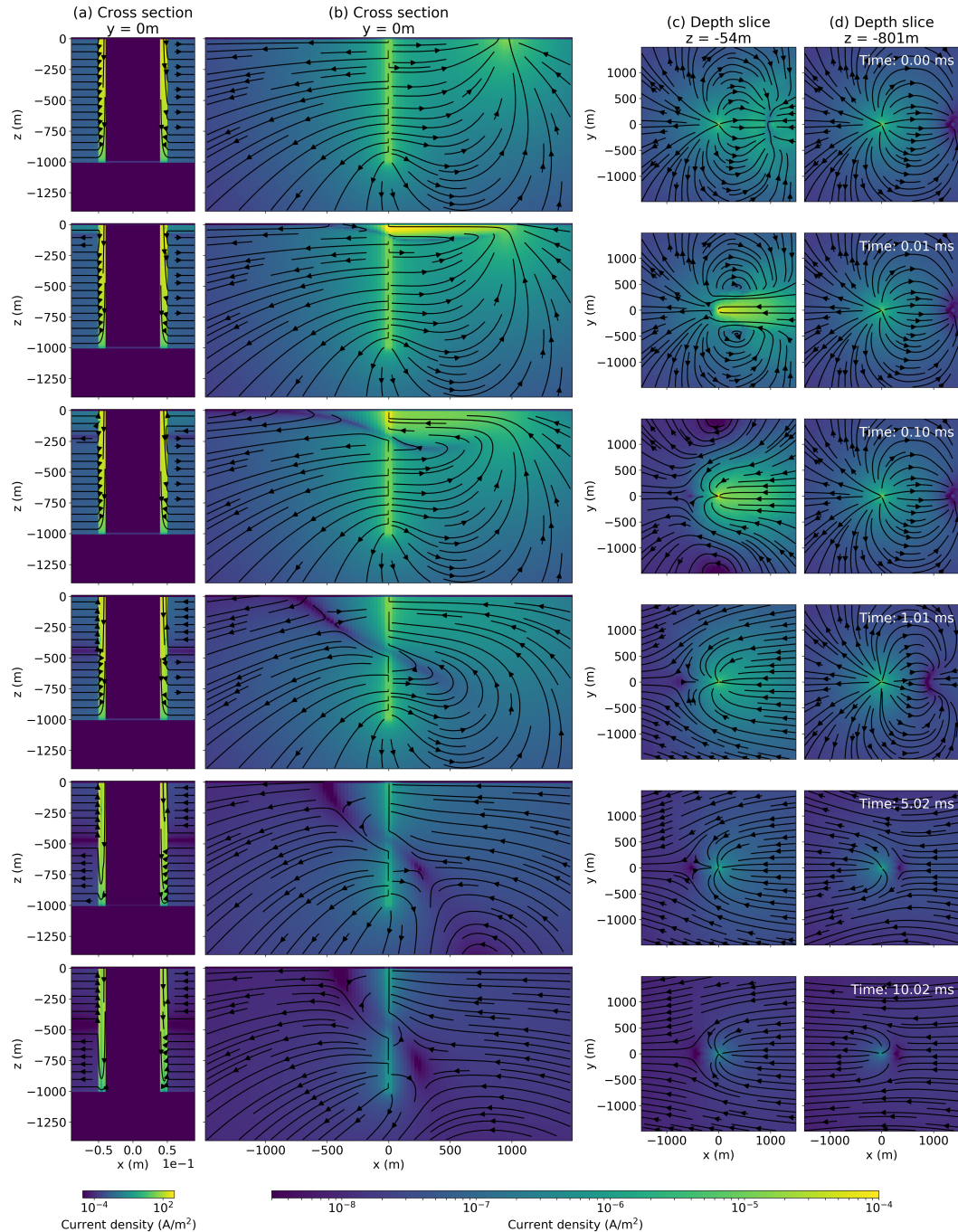


Figure 5.7: Current density for a top-casing time domain EM experiment over a 10^{-2} S/m half-space and a 1 km-long, conductive, permeable steel-cased well (5×10^6 S/m, $100\mu_0$).

casing was minimal on the behavior of the formation currents, whereas here, we see that the permeable and conductive casing still significantly alters the formation currents (as compared to Figure 5.1b).

To isolate the influence of magnetic permeability, I take the difference between the currents observed in the example with the conductive, permeable well (Figure 5.7) and those observed in the conductive well (Figure 5.2). The result is shown in Figure 5.8.

At the DC limit, magnetic permeability has no influence on the behavior of the currents. However, as we move to later times, EM effects become relevant and we begin to see the impact that permeability has on the behavior of the currents. The generation of poloidal currents within the casing wall is not an effect that can be caused by conductivity alone. Often in EM problems the magnetic field, \vec{h} and the magnetic flux density \vec{b} are treated interchangeably, which is sensible when $\mu = \mu_0$ everywhere in the domain. However, when variable permeability is introduced, the distinction is important. Figure 5.9 demonstrates how the vertical circulation of current can arise due to the interplay between the currents and corresponding rotational magnetic fields and fluxes. The downward directed current density within the casing (a) generates a toroidal magnetic field everywhere in space (b) according to Ampere's law. The magnetic flux is related to the magnetic field through the constitutive relation, and since the pipe is much more permeable than the background, the magnetic flux density is concentrated within the pipe. Once the transmitter is shut-off, the magnetic flux decreases, and the time variation of the magnetic flux generates rotating electric fields (d) according to Faraday's law. Finally, the electric field is related to the current density through Ohm's law, and therefore the rotating current density is concentrated within the pipe (e). If the pipe is only conductive and not permeable, then there is no concentration of the magnetic flux, as in (c). Instead, the magnetic flux has identical geometry to the magnetic field, and by

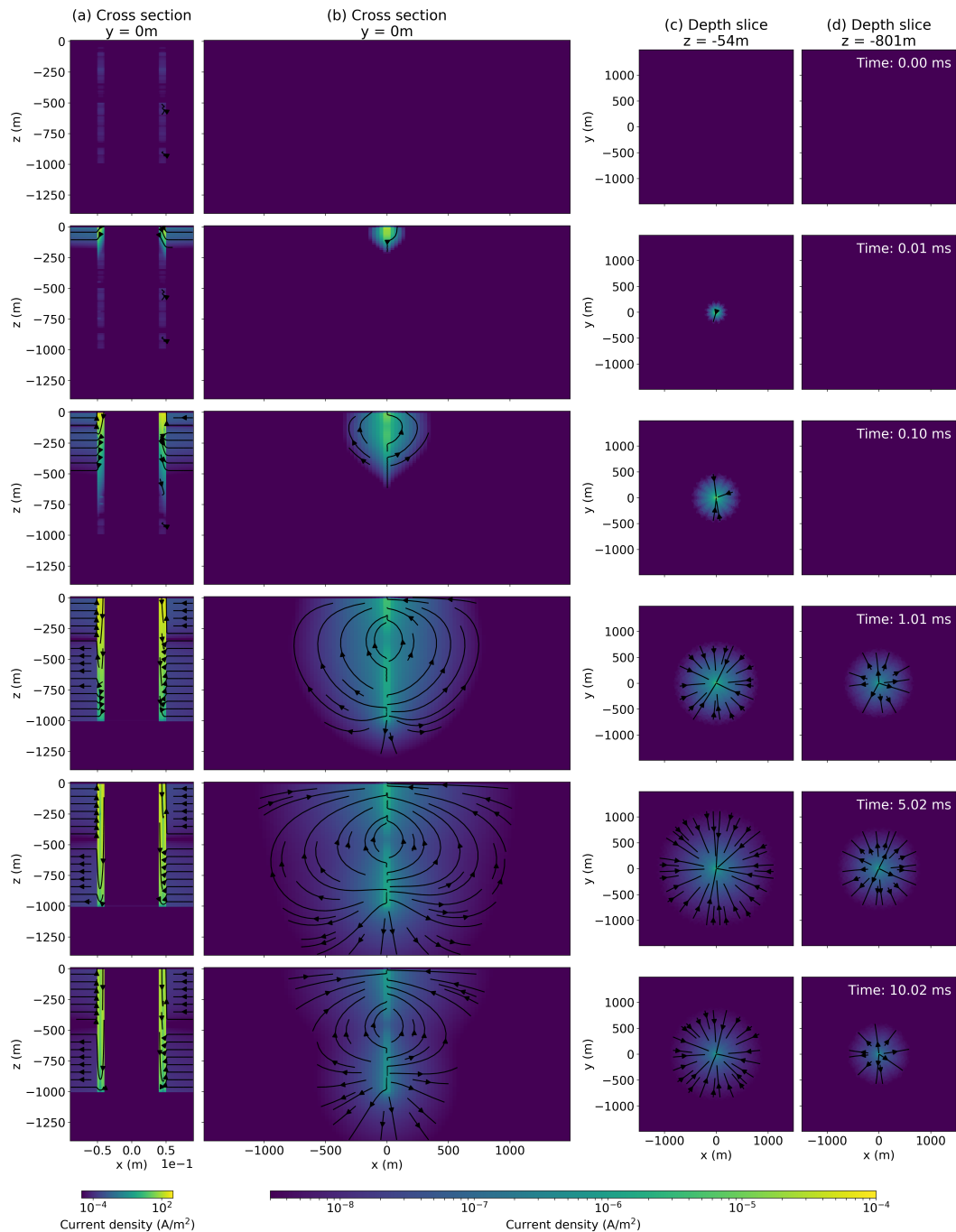


Figure 5.8: Difference in current density for a time domain experiment which includes a conductive, permeable steel-cased well (as in Figure 5.7) and an experiment over a conductive well (as in Figure 5.2).

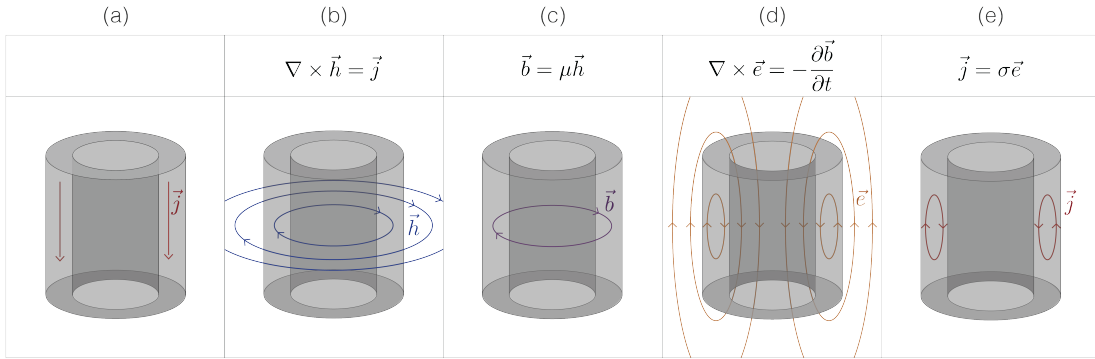


Figure 5.9: Sketch demonstrating how a vertical circulation of current can arise inside of a permeable casing in a top-casing TDEM experiment. A source current is applied and (a) currents flow downwards through the pipe. (b) Currents generate rotational magnetic fields according to Ampere's law. (c) Magnetic flux is concentrated in the permeable pipe according to the constitutive relation between \vec{b} and \vec{h} . (d) The magnetic flux varies with time after shut-off, and the time-varying magnetic flux creates rotational electric fields according to Faraday's law. (e) Currents associated with those electric fields are concentrated in conductive regions of the model in accordance with Ohm's law.

symmetry, the rotation of the electric field cancels, leaving only a vertical component.

5.3.1 Data

As in Figure 5.3, the secondary currents due to the permeability of the well are cylindrically symmetric. In the data, we then expect that the radial electric field will be minimally impacted at early times, but at later times, we will see the influence of permeability. Figure 5.10 shows the radial electric field data for the conductive casing (top row), and permeable casing (second row). As well as the difference (permeable minus conductive) and difference as a percentage of the data simulated with the conductive well in the third and fourth rows, respectively. At early times, the impact of permeability is minimal. For example, at 0.01 ms, it is only the data very near the wellbore (less

than 100m offset) that are marginally impacted. At the later time-channel, however, the difference is significant. At 5 ms the difference between including permeability and not is over 40% for all offsets shown (panel m). Through time, at the 300 m offset, we can see that the response decays more slowly, particularly in the time window between 2 ms and 100 ms. The maximum difference is $> 4000\%$ at 20 ms; in the conductive well-case (d), the response has decayed to $\sim 10^{-8}$ V/m, while in the permeable well (h), the value of the electric field is nearly two orders of magnitude larger.

Although one might typically associate magnetic permeability with a large impact on the magnetic fields and fluxes, the difference in the db_θ/dt data is much less significant and localized to short-offsets, as can be seen in Figure 5.11.

5.3.2 Down-hole source

The impact of the magnetic permeability of the casing is much more significant if we consider an experiment in which one electrode is positioned within the borehole. In this case, the wire path is through the borehole, and the vertical current through it generates a azimuthal magnetic field that is essentially perfectly coupled to the permeable casing. I demonstrate this with an experiment where the positive electrode is attached to the permeable casing at 950m depth. The currents through time are shown in Figures 5.12 and 5.13 which show the total currents and the difference between an experiment with the permeable pipe and one with a conductive pipe whose permeability is μ_0 , respectively.

Shortly after shut-off, currents along the entire length of the pipe contribute to the difference in the response between the permeable pipe and a conductive pipe. This is reflected in the radial electric field data shown in Figure 5.14

In the radial electric field data, shown in Figure 5.14m, this corresponds to a difference of over 60% at 1000 m offset in the 5 ms data.

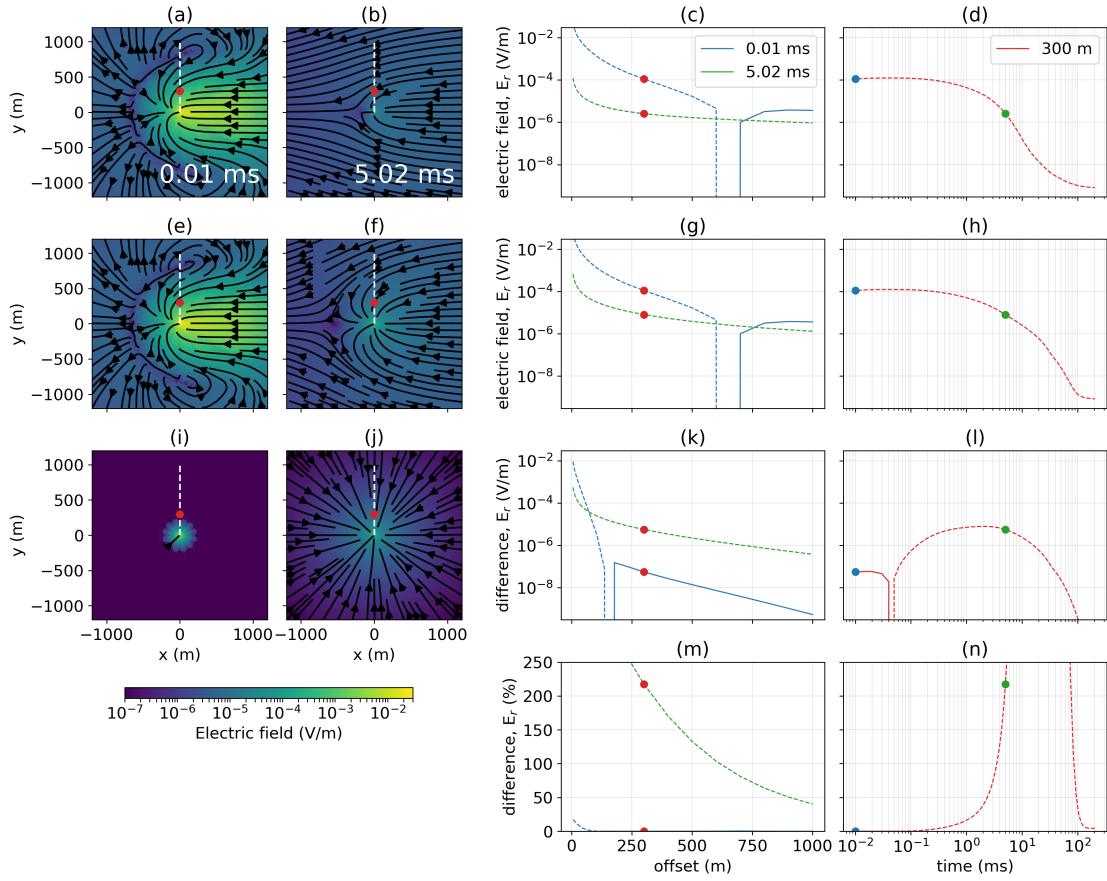


Figure 5.10: Simulated electric field at the surface of the earth, as was presented in 5.4. The top row (a – d) are the data simulated with the conductive casing. The second rows (e – h) are the data simulated with the conductive, permeable casing. The third row (i – l) is the difference (permeable and conductive minus conductive only), and the fourth row (m and n) show the difference as a percentage of the conductive solution.

5.3.3 Discussion

Magnetic permeability introduces yet another complication into the physics of EM in settings with steel-cased wells. In the top-casing experiment, we saw that by introducing permeability, a circulation of current in which current travelled downwards near the inner wall of the well-casing and upwards along the outer wall of the well casing,

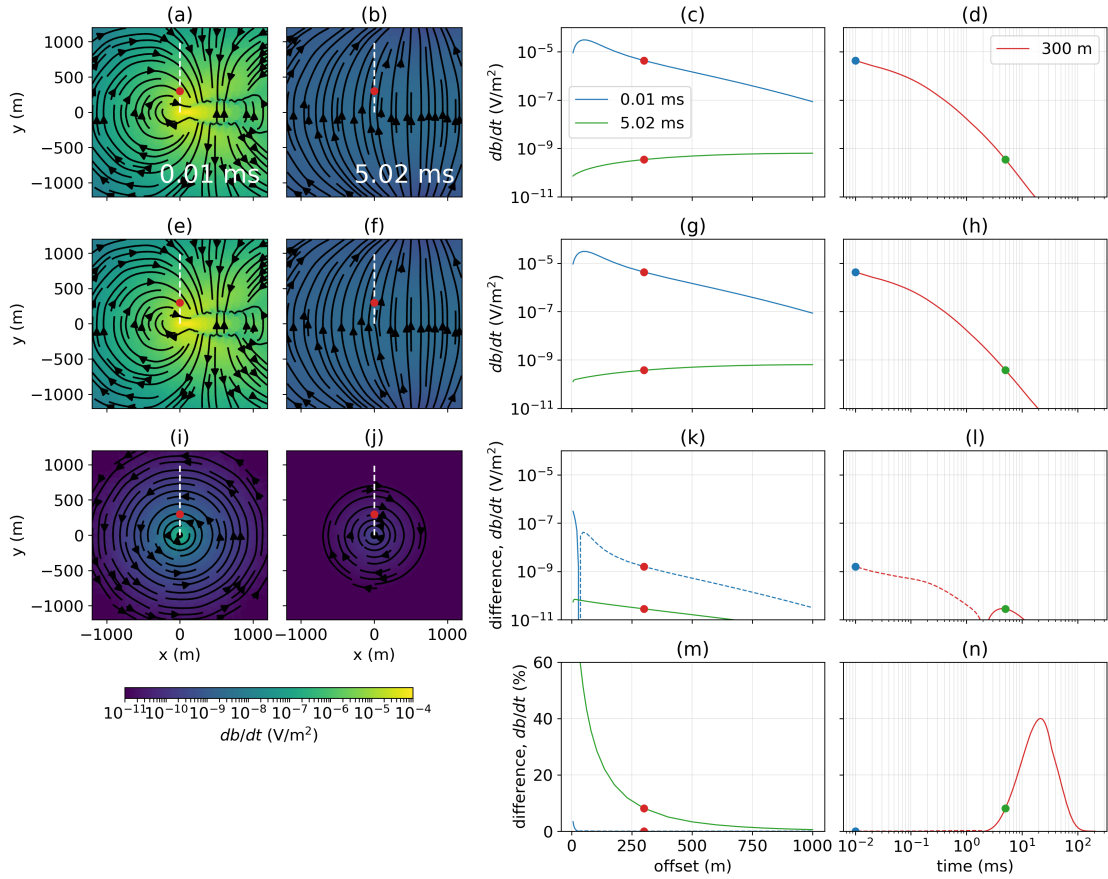


Figure 5.11: Simulated db/dt at the surface of the earth, as was presented in 5.6.

The top row (a – d) are the data simulated with the conductive casing. The second rows (e – h) are the data simulated with the conductive, permeable casing. The third row (i – l) is the difference (permeable and conductive minus conductive only), and the fourth row (m and n) show the difference as a percentage of the conductive solution.

was generated. Such an effect is not observed if the casing is only conductive. This indicates that it is important to model both permeability and conductivity in numerical simulations to capture the physics; this is not commonly done in geophysical electromagnetic simulations. Furthermore, even low-frequency or late-time data, which are sometimes treated as DC, may be impacted by magnetic permeability. Typically one might associate magnetic permeability with most significantly impacting magnetic field

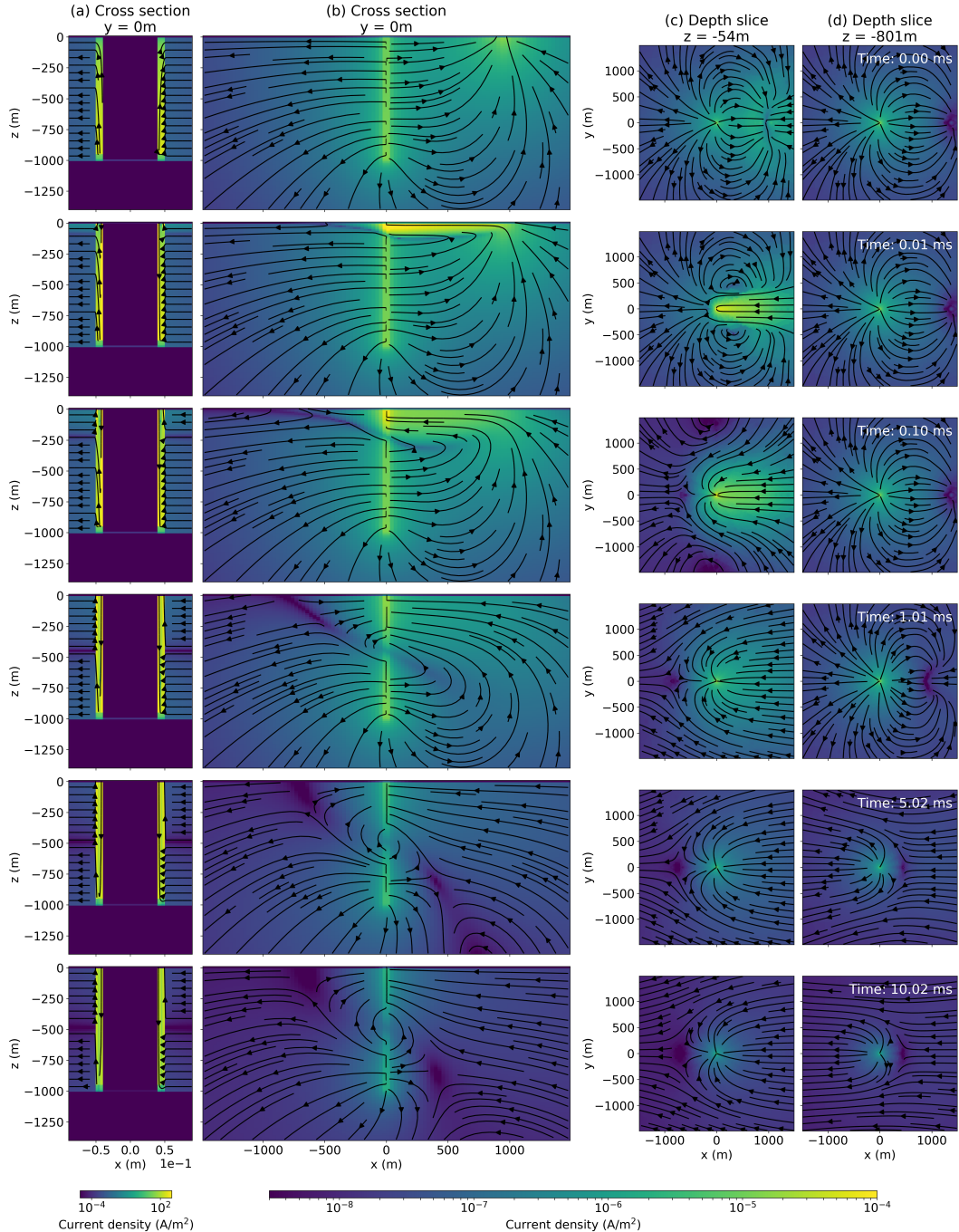


Figure 5.12: Current density for a down-hole time domain experiment with a conductive, permeable steel-cased well ($5 \times 10^6 \text{ S/m}$, $100\mu_0$). The positive electrode is connected to the casing at 950 m depth and the return electrode is on the surface at $x = 1000 \text{ m}$.

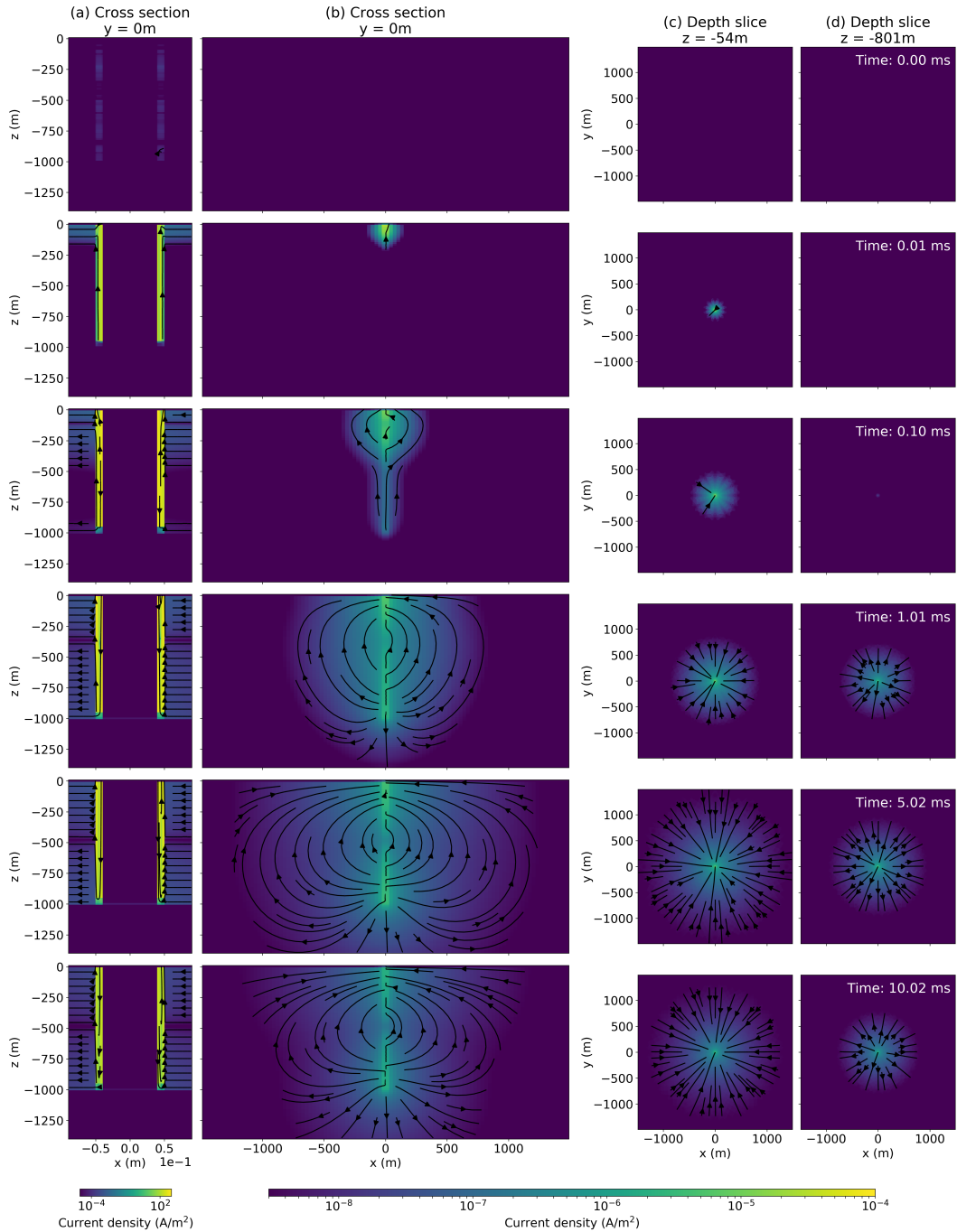


Figure 5.13: Difference in current density for a down-hole time domain experiment with a conductive, permeable steel-cased well (as in Figure 5.12) and a similar experiment with a conductive well.

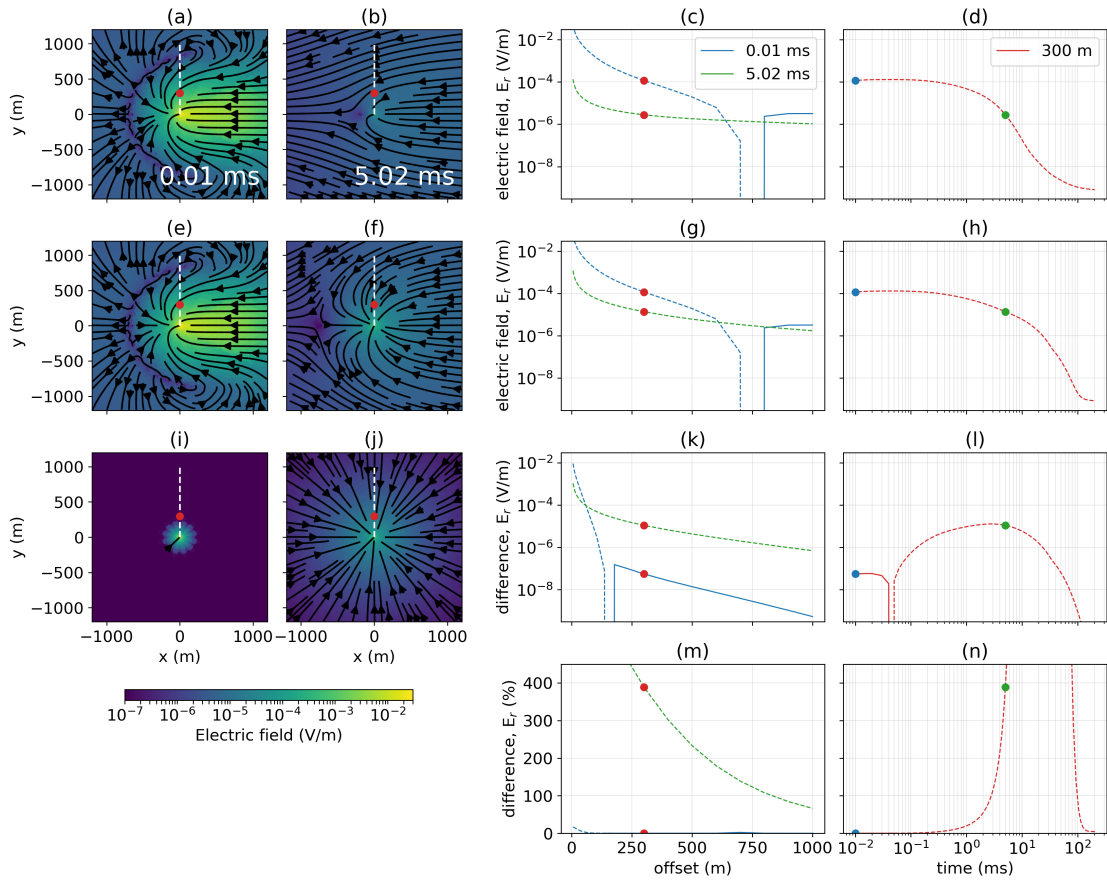


Figure 5.14: Simulated electric field at the surface of the earth, as was presented in 5.10 for a TDEM experiment in which the positive electrode is coupled to the casing at a depth of 950m.

data, however these results show that the electric field in a top-casing experiment can be off by >40% at late times, even 1000 m from the well if permeability is not considered in the simulation. On the positive side however, one benefit that the permeability of the steel may have in time-domain EM imaging experiments is that it increases the current density within the formation at later times. As a result, there is a long time-window over which a target may be excited.

5.4 Approximations to a steel cased well

The above simulations accurately discretize the casing, with 4 cells across the thickness of the casing wall. This is suitable for simulations in which the aim is to examine the physics. When considering an inversion, which requires many forward simulations and in which it is often preferable to use a cartesian grid to capture the geologic structures of interest, it may not be feasible to use such a highly-refined mesh to capture the finer details of the physics.

In the previous chapter, I showed that if we treat the well as a solid cylinder with a conductivity that preserves the product of the conductivity and cross-sectional area of the casing, we achieved an identical solution (within numerical error) at DC for the total current and charge-per-unit-length along the casing (see Section 4.4). This raises the question about whether, or not, this same approximation can be used for an electromagnetic experiment. Also, is there a straight-forward approximation that can be used to estimate the magnetic permeability for a coarse-scale representation of the well? In this section, I examine these two questions, first by considering a conductive well, and then introducing permeability.

5.4.1 Electrical conductivity

We consider the same model of a 1 km long, conductive well (5×10^6 S/m) in a 10^{-2} S/m half-space as used in Section 5.2 and perform a similar TDEM experiment in which one electrode is connected to the top of the casing and a return electrode is positioned 1 km away. The approximate model I use is a solid cylinder which has a conductivity of 1.8×10^6 S/m, so that both the true and approximate models have equal cross-sectional conductances. Both simulations are performed on identical meshes; this minimizes numerical differences that might otherwise occur from employing different discretizations.

To compare the responses, I first consider the total current along the length of the well. If the approximation is valid, we should expect that the total current density in the hollow-cased well is equal to the total current density in the cylinder approximating the well through time. Figure 5.15 shows (a) the current at two times (0.01 ms and 5 ms) along the length of the well, and (b) current at 500 m depth through time for the true solution. Similarly, (c) and (d) show the current for the approximation to the well, (e) and (f) show the difference (approximation minus true), and (g) and (h) show that difference as a percentage of the true solution. At early times, there is good agreement between the two solutions; at 0.01 ms, the percent-error in (g) is negligible and beyond 200 m depth in (e), the error is 5 orders of magnitude smaller than the true current. Above 200 m depth, we do see some coherent error that reaches a maximum of $\sim 10^{-3}$ A near the surface. However, this is still several orders of magnitude smaller than the true current at 0.01 ms. At later times the approximate solution underestimates the true current. At 5 ms, the current is underestimated by 8% along the entire length of the well, as can be seen in (g). Through time, the error shown in (h) reaches a maximum of nearly 10% at 8 ms. There is a large increase in percent difference beyond 30 ms, this is simply because we are dividing the difference by the very small current at the late times.

In electric field data measured at the surface, similar errors are observed. Figure 5.16 shows the electric field data for the true model (top row), approximate model (second row), difference between the approximate and true models (third row) and difference as a percentage (fourth row). At early times (0.01 ms), there is minimal difference, but at 5 ms, there is an 8% difference between the data generated with the true model and those generated with the approximate model. At 300 m offset, the time-period between 1 and 10 ms is when we observe the largest error (panel n).

Errors of 8-10% are not as egregious as neglecting magnetic permeability, but the

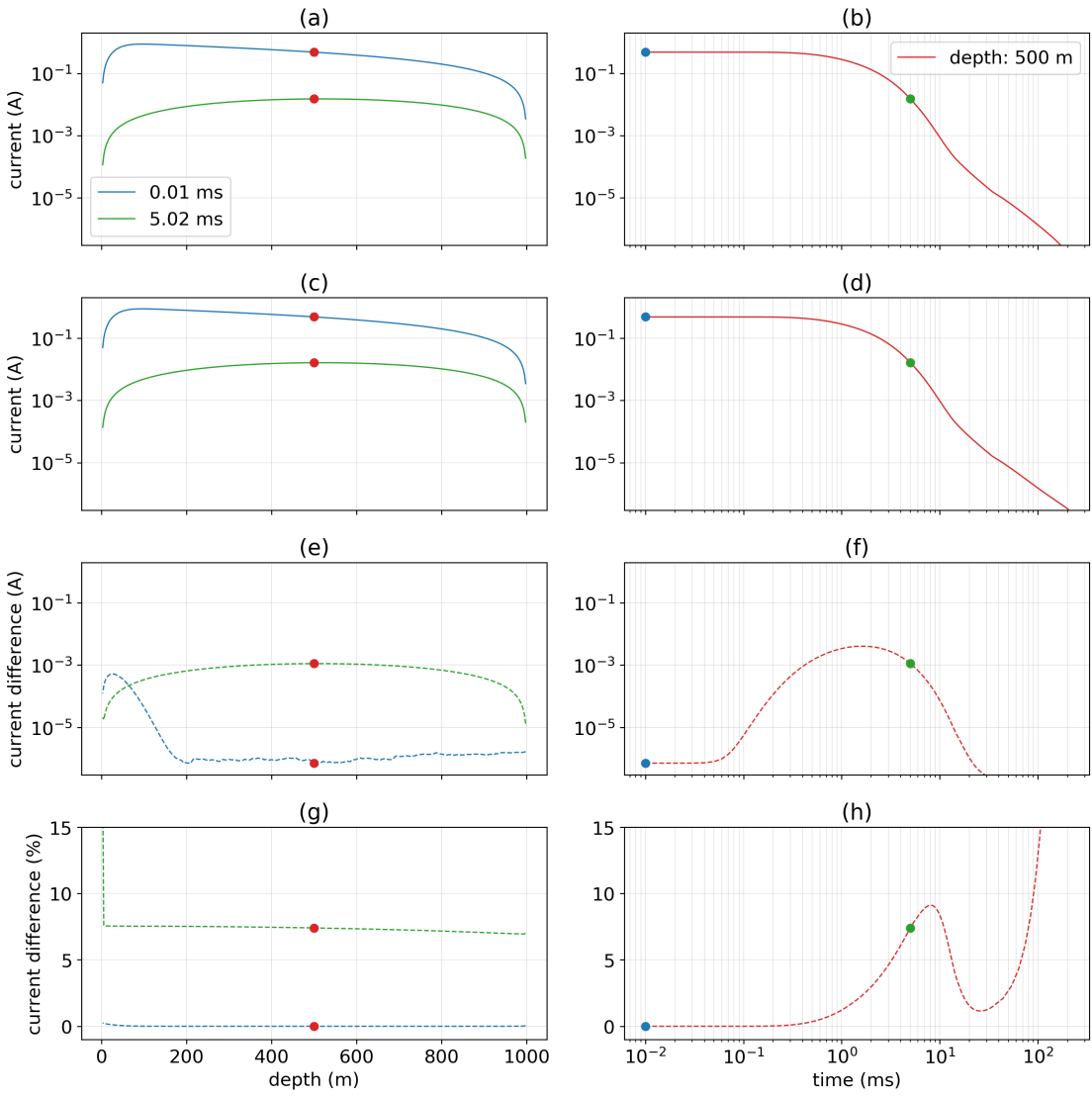


Figure 5.15: (a) Downward-directed current (a) within the casing at 0.01 ms (blue) and 5 ms (green) and (b) as a function of time at 500 m depth for the true, hollow-cased well. (c), (d) Current in the approximate model which treats the casing as a solid cylinder. The conductivity of the cylinder approximating the well is chosen so that both models have equal products of the conductivity and the cross sectional area. (e), (f) Difference between the current in the approximate model and the true model (approximate minus true). (g), (h) Difference as a percentage of the true solution.

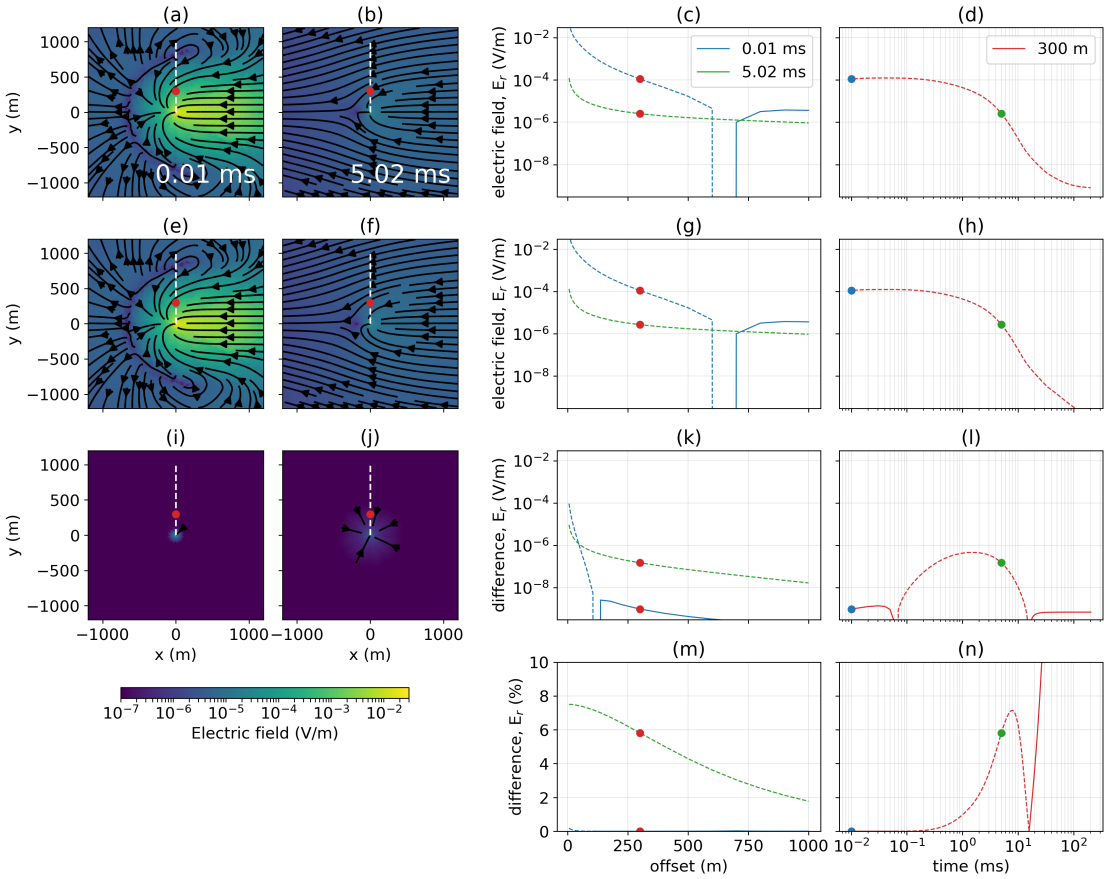


Figure 5.16: Simulated electric field at the surface of the earth, as was presented in 5.4. The top row (a – d) are the data simulated with the true, conductive casing. The second rows (e – h) are the data simulated with the solid cylinder approximating the well. The third row (i – l) is the difference (approximate minus true), and the fourth row (m and n) show the difference as a percentage of the true solution.

anomalies that we will be looking for when considering subsurface injections are small and may only comprise 10% to 20% of the background signal, so an error of 10% is certainly not negligible.

In order to provide more context for where this approximation is breaking down, I have plotted the current density, charge density and electric fields through time in Figure 5.17. Panel (a) shows the true current density, (b) shows the secondary current density

(the difference between the simulation using the approximation of the casing and that using the true casing), (c) shows the true charge density (d) shows the secondary charge density, (e) shows the true electric field, and (f) shows the secondary electric field. Note that (a) and (b) are on the same logarithmic color scales as are (e) and (f). Panels (c) and (d) are each have their own associated linear colormap. Panels (b), (c) and (e) are effectively looking at “what physics are we introducing by making by making this approximation?”

At the DC limit, the solutions are in agreement, with the exception that the current distribution between the true casing and the approximate casing are different inside of the well, as expected. There is also a small secondary electric field at the bottom of the pipe – this is because by treating the pipe as a solid cylinder, we have introduced a conductivity contrast, and thus small secondary charge at that bottom interface. This however has minimal impact on the currents in the formation or data measured at the surface.

Shortly after shut-off, however, the approximation begins to break down. There is a dipolar charge introduced on the casing with a concentrated negative charge density near the top and a positive charge density beneath that. Corresponding to the positive charges, there are similarly outward-directed currents and electric fields. As time progresses, the secondary dipolar charge and associated currents and electric fields spread out along the length of the well.

The passing image current changes the geometry of the currents and distribution of charges. At DC, the well has a positive charge along its length and all currents are outward from the well. The incoming image current is a source of the negative charges; the currents enter the conductive casing from the resistive background, thus negative charges build up at the interface. This indicates that the conductivity contrast between

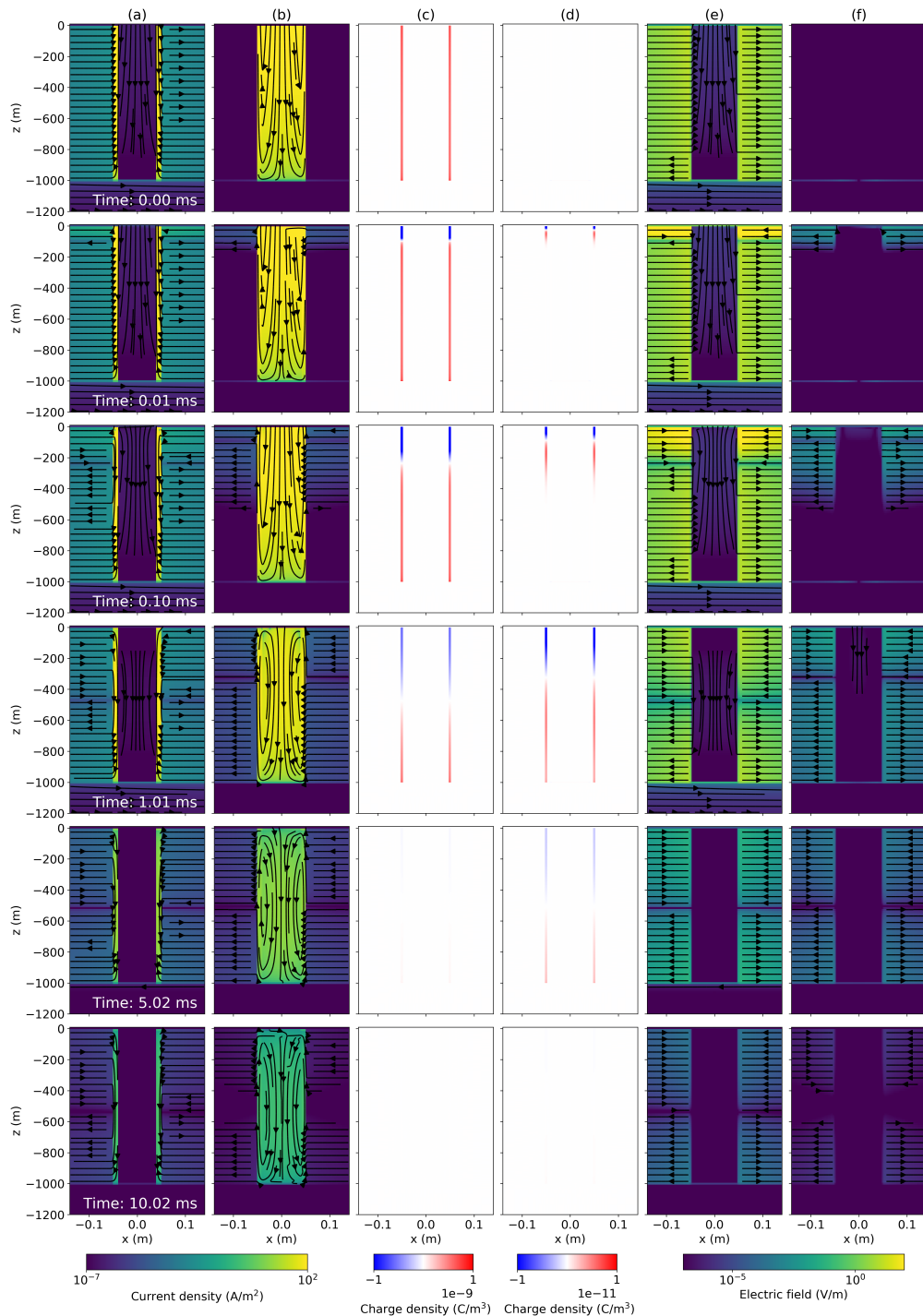


Figure 5.17: (a) True current density (b) difference between the currents in the simulation with the approximation to the conductive well and the true solution (secondary currents), (c) True charge density, (d) secondary charge density, (e) true electric field, (f) secondary electric field.

the background and the casing is important when considering EM effects. At DC, the approximation of the well by a cylinder with equal product of the conductivity and the cross sectional area is correct. Any alteration of the conductivity would introduce errors in the initial condition. However, the approximation does not hold through time as the geometry of the current-systems changes. This suggests that perhaps a conductivity which varies with time, and possibly along the length of the casing, may be necessary in order to accurately approximate the casing on a coarse scale.

5.4.2 Magnetic permeability

Clearly, if we do not have a suitable approach for estimating a coarse-scale conductivity of a well in an EM experiment, we cannot expect to build up a strategy for a conductive, permeable pipe. If the currents are incorrect, then the magnetic fields and fluxes are incorrect, and the interplay between the currents and magnetic permeability that I demonstrated in Section 5.3 (Figure 5.12, in particular) will not be captured. Therefore, the purpose of this section is to introduce some of the additional challenges that are raised when permeability is considered and see if, by examining the physics, there are any insights to be gleaned about this problem.

Simply based on the geometry of the currents and magnetic fields, one reasonable approach to estimating the permeability of a solid cylinder which approximates the hollow-cased well is to preserve the product of the permeability and the casing thickness. The magnetic fields and fluxes are rotational within the casing, so the thickness of the casing is a primary control on the magnetic flux within the casing.

To introduce a first-order approximation for a conductive, permeable well, I preserve the product of the conductivity and cross-sectional area, as in the previous section, and preserve the product of the permeability ($100 \mu_0$ for the true well) and the thickness of

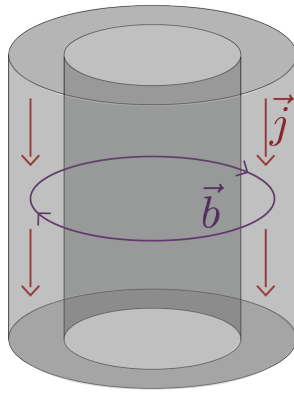


Figure 5.18: Sketch of the geometry of the dominant geometry of the current density, \vec{j} and magnetic flux density, \vec{b} , within the casing. Most of the current flows vertically while most of the magnetic flux density is rotational.

the casing (1 cm), giving a permeability of $20\mu_0$. The experiment is again a top-casing simulation, as in Section 5.3. The resultant current within the pipe and data from the true and approximate simulation are shown in Figures 5.19 and 5.20, respectively (note that the y-limits on this plot are different than those shown in the conductive-well example, Figures 5.15 5.16). As might be expected, the discrepancy, in terms of percentage of the true solution, at late times is nearly twice what we observed in the conductive well approximation. The direction of the difference is opposite to the conductive case. Here, the currents within the casing are overestimated, creating an outward-directed secondary electric field which reduces the magnitude of the radial electric field data relative to the true solution.

To see where the solution is breaking down, I plot the currents, charges, and electric fields in Figure 5.21. Note that the colorbar for the secondary charges in panel (d) has a range that is an order of magnitude larger than that shown in Figure 5.17. The behavior of the secondary currents charges and electric fields due to the approximation is opposite to what we observed in Figure 5.17. Here, there is a positive secondary charge at the

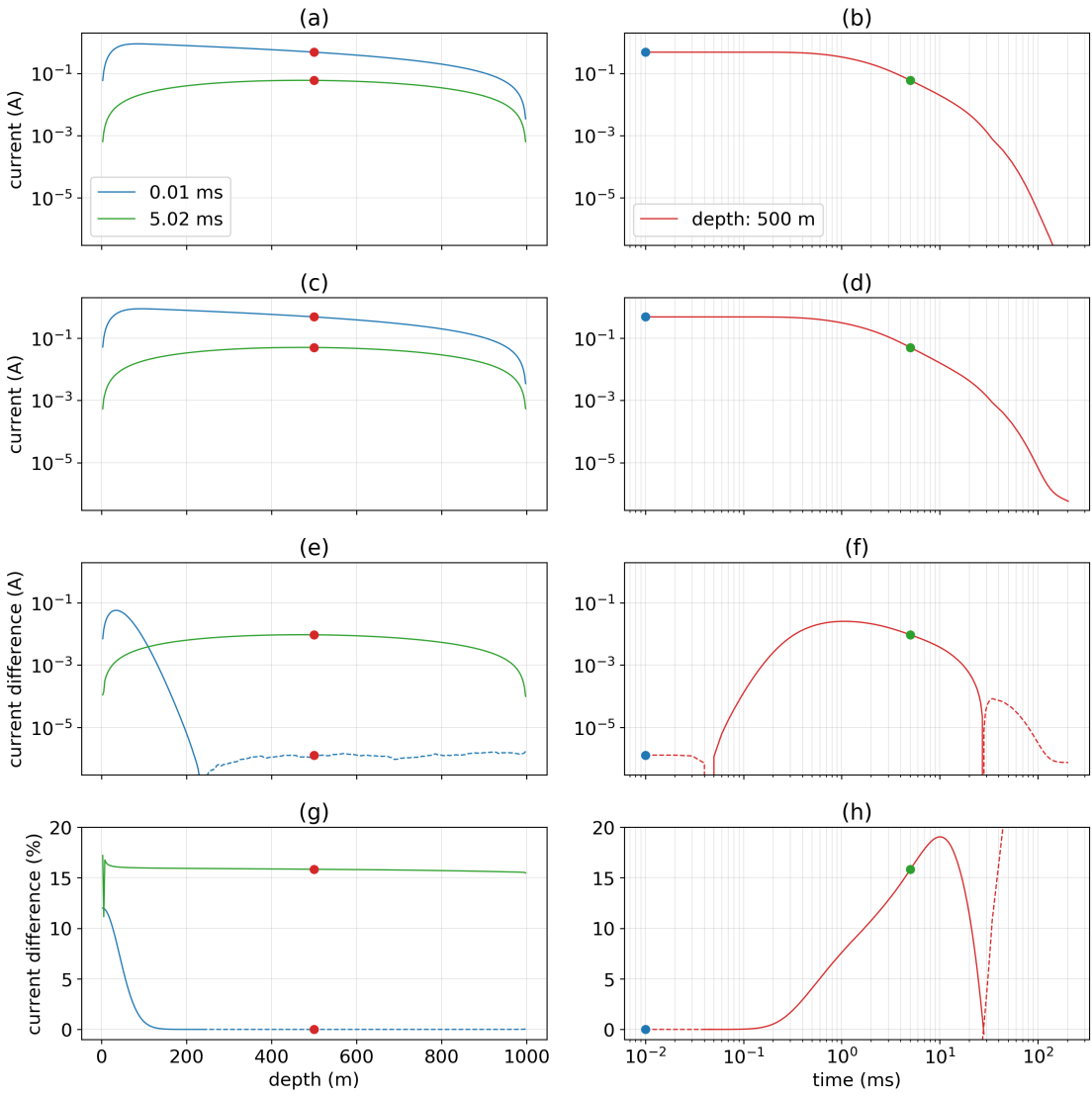


Figure 5.19: (a) Downward-directed current (a) within the casing at 0.01 ms (blue) and 5 ms (green) and (b) as a function of time at 500 m depth for the true, permeable, hollow-cased well. (c), (d) Current in the approximate model which treats the casing as a solid cylinder. The conductivity of the cylinder approximating the well is chosen so that both models have equal products of the conductivity and the cross sectional area. The permeability of the cylinder is chosen so that both models have equal products of the permeability and the thickness. (e), (f) Difference between the current in the approximate model and the true model (approximate minus true). (g), (h) Difference as a percentage of the true solution.

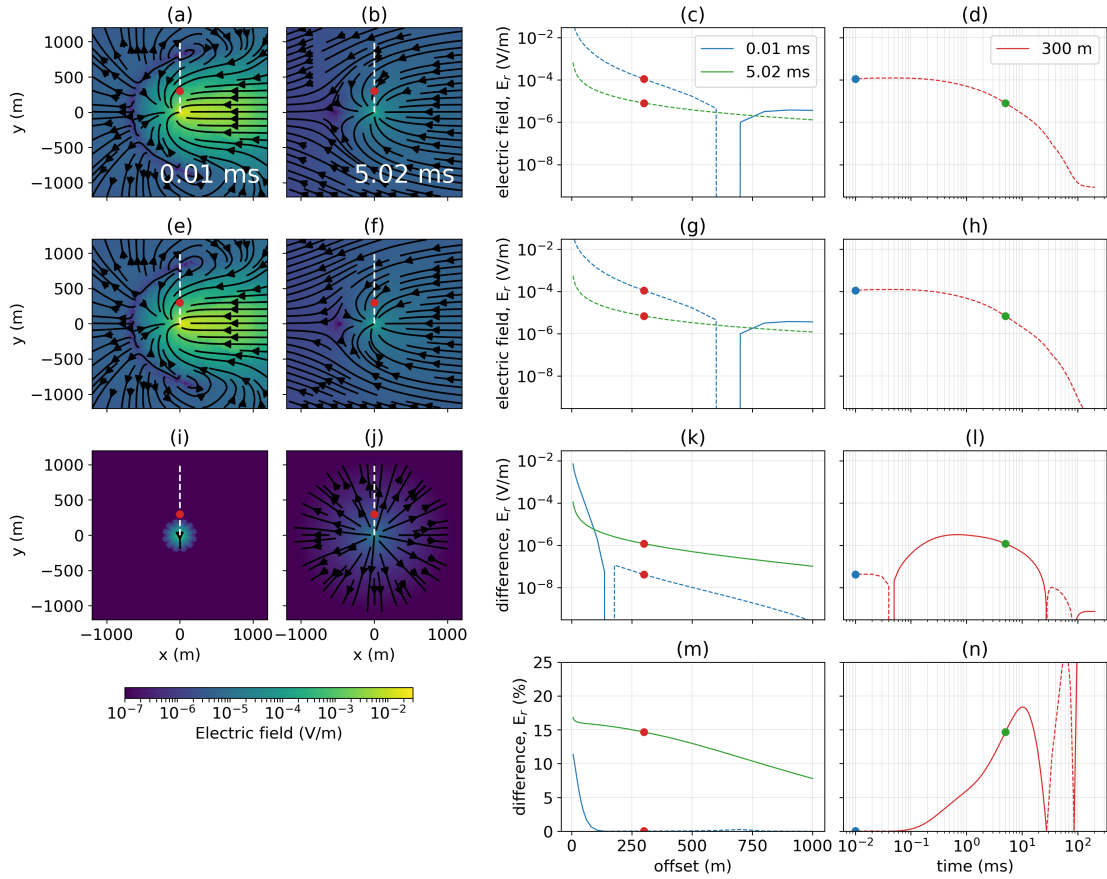


Figure 5.20: Simulated electric field at the surface of the earth, as was presented in 5.4. The top row (a – d) are the data simulated with the true, conductive, permeable casing. The second rows (e – h) are the data simulated with the solid cylinder approximating the well. The third row (i – l) is the difference (approximate minus true), and the fourth row (m and n) show the difference as a percentage of the true solution.

top of the casing and a negative secondary charge beneath it, and as the image current passes, we evolve to a state where there are outward-directed secondary currents and electric fields in the top portion of the casing and inward-directed secondary currents and electric fields in the bottom portion of the casing.

The interplay between currents, magnetic flux and magnetic permeability is clearly complex. Before developing a strategy for upscaling conductive, permeable wells, there

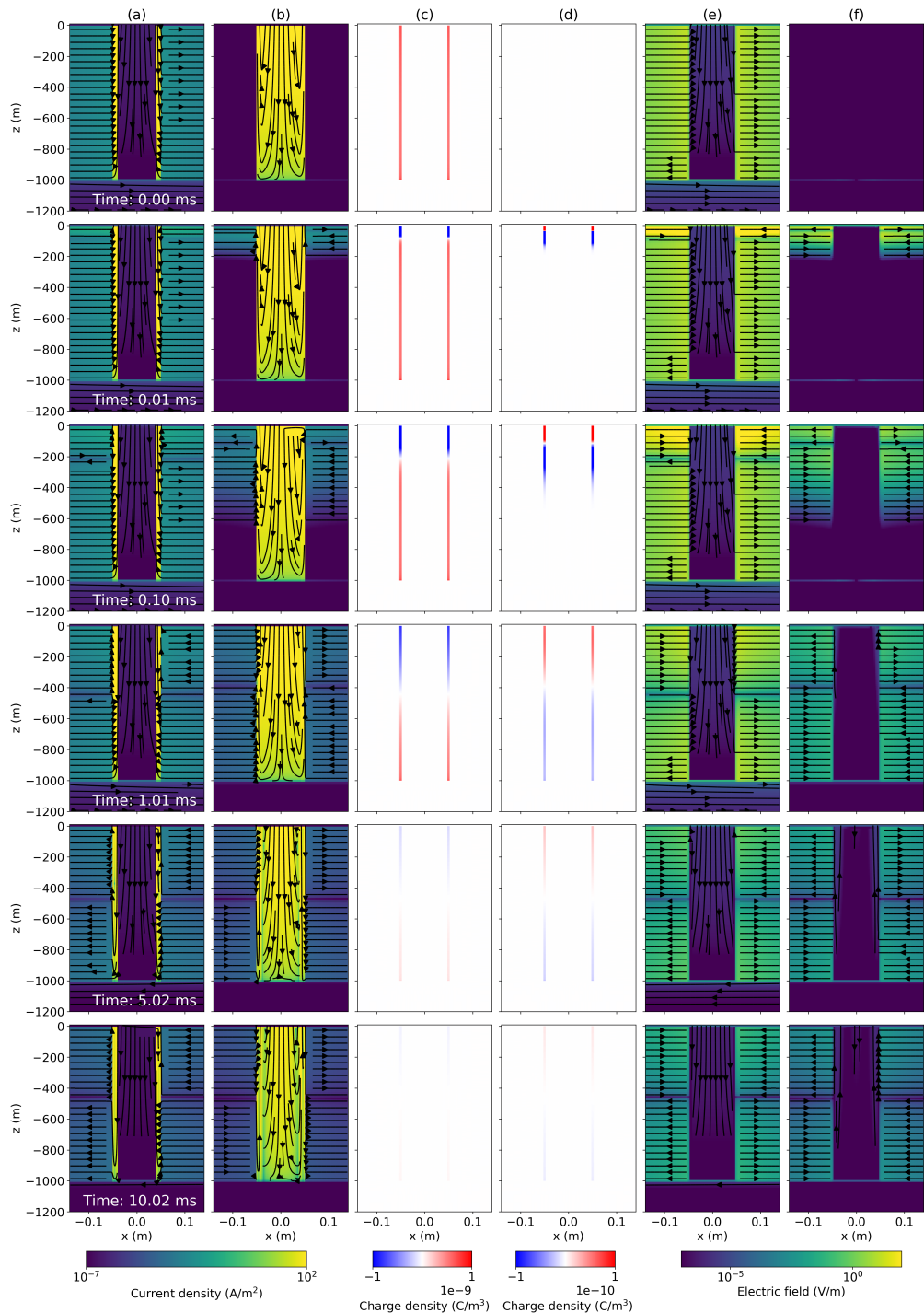


Figure 5.21: (a) True current density, (b) difference between the currents in the simulation with the approximation to the conductive, permeable well and the true solution (secondary currents), (c) true charge density, (d) secondary charge density, (e) true electric field, (f) secondary electric field.

are a host of questions that will need to be addressed: Can a conductivity which varies vertically along its length and through time be used to approximate a casing? Does this approximation still hold if the conductivity of the background, and thus distribution of the currents within the formation is variable? If an appropriate description of the conductivity is found, is there a simple description of the permeability that can be adopted (e.g. is capturing the complexity of the currents the main item of concern)?

5.5 Conclusions

This chapter poses more questions than answers. Even for the (seemingly) simple model of a conductive casing in a half-space, there are subtleties to the behavior of the currents in an EM experiment. The interaction of the diffusing formation currents (set up at DC, before shut-off), the image current generated when the source current is shut-off, and the highly conductive well produce a “shadow-zone” along a line 180° from the wire. The geometric complexities are slightly simplified if we subtract-off the background response of a grounded source over a half-space; the resulting “casing-response” is cylindrically symmetric through time.

Steel has a significant permeability, and the simulations in this chapter demonstrate that including permeability significantly alters the currents, particularly at later times. Within the well, a vertical circulation of current develops; this cannot be explained by conductivity. Within the formation, the currents do not diffuse as rapidly as they did when the well was only conductive. By 10 ms, in a 10^{-2} S/m half-space with a conductive well, there was very little distortion of the currents due to the presence of the well. However, in the simulation with a conductive, permeable well – the currents within the formation were still significantly altered at 10 ms. Correspondingly, the late-time data are much more significantly affected by permeability than the early-time data (upwards

of 40% difference at 5 ms for a top-casing experiment and 60% for a down-hole experiment). Many of the publications considering EM in settings with steel cased wells neglect permeability. These results show that it is essential to consider. Furthermore, late-time or low frequency data that are simulated and inverted as DC data could be contaminated with permeability-effects.

Using sufficient spatial discretization to accurately simulate data on cartesian meshes is costly, and can render the inversions, which require many forward simulations, infeasible. As a result, it is advantageous to reduce the size of the mesh and approximate the casing. The simple rule-of-thumb of preserving the product of the conductivity and the cross-sectional area of the casing was suitable for DC resistivity problems, but this breaks down when we consider EM problems. The incoming image current changes the geometry of the fields and their interaction with the pipe through time. An effective replacement conductivity for a simulation on a coarse mesh may need to vary with time and with distance along the pipe. Matters are more complicated when permeability is introduced, as there is an interplay between the currents, magnetic field, and magnetic flux through time. Using a geometrically-motivated approximation for the permeability and preserving the product of the permeability and the thickness of the casing introduce errors in the opposite direction to those observed when only conductivity was considered. I showed that secondary positive charges were introduced due to the approximation of a conductive well, but negative charges were introduced as a result of the approximation to the conductive, permeable well. How to approximate the permeability is unclear at this point, and will first require that a suitable strategy be developed for electrical conductivity.

There is much yet to be investigated and understood about electromagnetics in settings with conductive, permeable, steel cased wells. Central to this work is the ability to

simulate, visualize, and interact with aspects of the physics. This chapter provides some glimpses into the behavior of the currents, fields and fluxes, and includes source code and Jupyter notebooks (see Appendix A) that can be used to continue the exploration.

Chapter 6

An inversion approach for subsurface injections

6.1 Introduction

The previous three chapters have focussed on understanding the physics of electromagnetics over conductive, permeable, steel-cased wells. In this chapter, we return to the goal of imaging subsurface injections through geophysical inversion. We view this as a time-lapse problem, in which one data set is obtained prior to the injection and second data set is obtained after the injection. The aim of the inversion, then, is to characterize the changes in the earth model due to the injection.

Time-lapse direct current (DC) resistivity, and in some cases electromagnetics (EM), is commonly used in the groundwater hydrology community. In particular, DC resistivity has been used, in salt-tracer experiments aimed at understanding groundwater flow (e.g. Slater et al. (2002); Kemna et al. (2002); Singha and Gorelick (2005); Doetsch et al. (2012)) and for characterizing time-lapse vadose zone processes (e.g. Daily et al.

(1992); Park (1998); Binley et al. (2002)). Within the context of hydrogeophysics, typically multiple time-lapse surveys are conducted. A range of interpretation techniques have been applied. In terms of algorithmic complexity, the most straightforward approach is to invert each time-snapshot independently. The recovered models can then be differenced and the difference interpreted (Cassiani et al., 2006), or an intermediate interpretation, for example estimating the center of mass of a plume (Singha and Gorelick, 2006; Doetsch et al., 2012), can serve as an indicator that is tracked through time. Daily et al. (1992) presented an approach for inverting ratios between initial and subsequent datasets, and (LaBrecque and Yang, 2000) proposed an inversion for the resistivity difference between two subsequent data sets by inverting the difference between the two data sets. A common approach is to use the inversion result from an initial timestep as a reference and starting model for the following datasets (Loke, 2001; Oldenborger et al., 2007), this is sometimes referred to as a “cascaded inversion” (Miller et al., 2008). More advanced techniques simultaneously invert all of the time-snapshots and apply both spatial and temporal regularization (Kim et al., 2009; Loke et al., 2014). Hayley et al. (2011) provides an overview and comparison of common time-lapse inversion approaches and demonstrates a comparison of several approaches for a synthetic example of the remediation of a saline plume.

In the context of reservoir imaging applications, the “time-lapse” aspect of the problem is somewhat simpler than that typically encountered in hydrogeophysics. Very few temporally dense DC or EM data sets have been collected for reservoir imaging. Notable exceptions include the cross-well DC resistivity surveys described in Carrigan et al. (2013) and Tøndel et al. (2014), for monitoring of a deep CO₂ injection in a gas field and monitoring steam chamber growth in a steam-assisted gravity drainage operation in the Athabasca Oil sands, respectively. Much more common are time-lapse data sets

consisting of only two times: pre-injection and post-injection. Cross-well EM has been applied for such surveys in to monitor water-floods (Wilt et al., 2005, 2012) and steam injections (Wilt et al., 1996, 1997; Marion et al., 2011). By far, the most common inversion approach involves inverting for a background model with the initial data set, typically including constraints from well-logs and potentially interfaces from seismic data and using this as the starting model for the inversion, typically in 2D (e.g. Wilt et al. (2012)).

Although the “time-lapse” aspect of injection-monitoring applications is generally simpler than applications in hydrogeophysics, the large depths considered in reservoir applications means that we are usually working with small signals. Furthermore, the presence of steel cased wells complicates signals. Efforts to reduce the impact of steel cased wells on DC surveys include using a coating on the casing which the electrodes are connected to and thus insulate the casing from the survey (Tøndel et al., 2014). For cross-well EM applications, fibreglass casings may sometimes be used (Wilt et al., 2012), or when a single well is cased, a “casing-correction” is applied to the data collected at a fixed frequency (Augustin et al., 1989b; Becker et al., 1997).

For the emerging application of grounded-source DC or EM in the monitoring of subsurface injections, very few inversions of synthetic or field studies have been published, leaving many open questions. How does the casing affect our sensitivities in the inversion? In particular, Rucker (2012), have shown that in near surface studies where the casings are used as long electrodes, depth information is lost in the inversion. Additionally, forward modelling shows that the currents spread out along the length of the well. These prompt the question: can we expect to resolve the location of the target along the well? Specific to subsurface injections, there is also further a-priori information that may be included, for example the conductivity of the injected material and

the volume of material injected should be known. What is the best way to include this information in the inversion?

For DC data, Weiss et al. (2015) works with the scattered potential due to the fracture and suggests an approach which approximates the well as a line-charge distribution and the fracture as a point charge. The information content of a DC survey with only a few sources is quite limited, so reducing the number of free parameters, as in Weiss et al. (2015), is appropriate for obtaining meaningful information from the data. Here, I wish to work towards the use of electromagnetic data. In addition to providing information at the electrostatic limit provided by DC data, EM data include the role of inductive processes and are therefore richer in their information content. As such, I am interested in using an inversion approach which enables us to interpret geometric and physical property information from the result.

To focus discussion, we will consider synthetic examples related to hydraulic fracturing. The goal of the inversion in this case is to delineate the extent and geometry of the propped region of the fractured reservoir. Changes in electrical conductivity are viewed as a proxy for estimating the concentration of propped fractures. I will consider voxel-based and parametric inversions, as well as alternate parameterizations using effective medium theory. Using this range of approaches, I aim to develop an understanding of the non-uniqueness we face for grounded-source surveys in settings with steel cased wells. The analysis conducted in this chapter builds on the SimPEG framework and all of the examples shown are available in the form of Jupyter notebooks (see Appendix A).

6.2 Choosing an inversion model

Background material on the general inversion approach I follow was provided in the introduction (Section 1.5) with further details included in Cockett et al. (2015) and Ap-

pendix D. The overview I provided laid out a general strategy for solving for the inversion model \mathbf{m} , but I have not yet specified how \mathbf{m} is chosen. This chapter will explore several different approaches for defining an inversion model including parametric models and using effective medium theory to invert for fracture concentration. This section provides mathematical background on how these different model parameterizations are treated in the inversion.

The physical property which we aim to characterize in an electromagnetic inversion is electrical conductivity σ (or equivalently, its inverse, resistivity ρ). In a DC or an EM inversion, however, it is common to invert for log-conductivity on the forward simulation mesh, that is

$$\sigma = \mathcal{M}(\mathbf{m}) \quad (6.1)$$

where $\mathcal{M}(\mathbf{m}) = \exp \mathbf{m}$. We refer to $\mathcal{M}(\cdot)$ as a mapping. Mappings have two implications in the inversion. One implication is in the model regularization: we have changed the space in which we are applying the regularization, for this example, we regularize on log-conductivity values rather than linear conductivity. As the conductivity of common earth materials varies over several orders of magnitude, it is preferable to penalize jumps in orders of magnitude between voxels rather than penalizing linear values. The second implication is in the computation of the sensitivity. The forward simulation in an EM or DC problem depends upon electrical conductivity, thus the mapping modifies the sensitivity via the chain rule

$$\mathbf{J}[\mathbf{m}] = \frac{dF[\mathcal{M}(\mathbf{m})]}{d\mathcal{M}(\mathbf{m})} \frac{d\mathcal{M}(\mathbf{m})}{d\mathbf{m}} = \frac{dF[\sigma(\mathbf{m})]}{d\sigma} \frac{d\sigma}{d\mathbf{m}} \quad (6.2)$$

Mappings can be composed, for example if inactive cells are included in the modelling domain, such as air cells or cells capturing known structures such as a steel-cased

well, then

$$\sigma = \mathcal{M}_2(\mathcal{M}_1(\mathbf{m})) \quad (6.3)$$

where \mathcal{M}_1 injects in the log-conductivity values of the inactive cells and \mathcal{M}_2 takes the exponential. The sensitivity is appropriately modified by adding another step to the chain rule.

In addition to mappings routinely employed in electromagnetic inversions, such as those used for working with log-conductivity values and handling inactive cells in the modelling domain, there are two mapping which we will make use of in this chapter: an effective medium theory mapping, based on the homogenization technique for propped, fractured reservoirs discussed in Chapter 2 and parametric mappings.

Parametric mappings

The other type of mapping will make extensive use of in this chapter are parametric maps. I consider model parameterizations of blocks and ellipsoids, similar to that described in McMillan et al. (2015a); McMillan (2017). For example, using a simple parametrization of a block, the model is

$$\mathbf{m} = [m_{\text{back}}, m_{\text{block}}, x_0, \Delta x, y_0, \Delta y, z_0, \Delta z]^\top \quad (6.4)$$

where m_{back} is the model value of the background, m_{block} , (x_0, y_0, z_0) is the center of the block and $(\Delta x, \Delta y, \Delta z)$ are the widths of the block in each dimension. The mapping is then

$$\mathcal{M}(\mathbf{m}) = m_{\text{back}} + (m_{\text{block}} - m_{\text{back}}) s(\tau(\mathbf{m})) \quad (6.5)$$

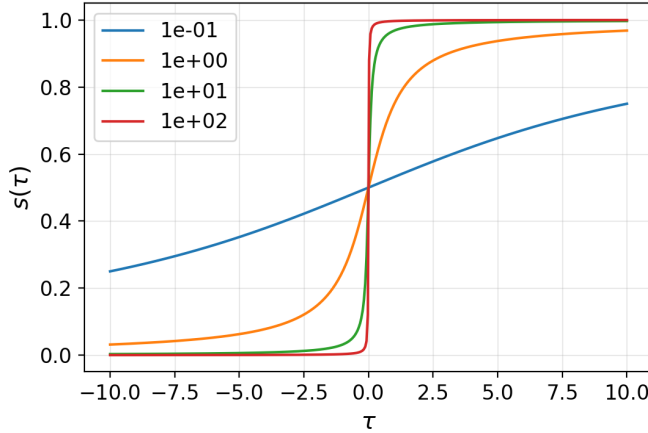


Figure 6.1: Approximation to a step function using an arctangent, as described in equation 6.6. The values in the legend indicate the value of the slope, a . Smaller values have a more gradual transition between zero and one, while larger values have a more rapid transition.

where $s(\cdot)$ is a differentiable approximation to a step-function and τ is a level set function of the block. To approximate a step function, I use the arctangent function,

$$s(\tau) = \frac{1}{\pi} \tan^{-1}(a\tau) + \frac{1}{2} \quad (6.6)$$

where a controls the slope of the transition between 0 and 1. Small values of a result in a gradual transition while larger values give a sharper transition, as shown in Figure 6.1. For more robust performance of the Gauss-Newton inversion, I choose a such that the transition happens over a multiple cells in the simulation mesh (McMillan, 2017).

To define a level set function for a block, I need to define a function, τ , which evaluates to $\tau < 0$ when outside the target and $\tau > 0$ inside the target. To define a block, I could, for example use

$$\tau = 1 - \left(\left\| \frac{x - x_0}{\Delta x/2} \right\|_{\infty}^2 + \left\| \frac{y - y_0}{\Delta y/2} \right\|_{\infty}^2 + \left\| \frac{z - z_0}{\Delta z/2} \right\|_{\infty}^2 \right) \quad (6.7)$$

however, the infinity norm is not differentiable. Thus, I approximate the infinity norm using an Ekblom norm (Ekblom, 1973),

$$\tau = 1 - \left(\left[\left(\frac{x-x_0}{\Delta x/2} \right)^2 + \varepsilon^2 \right]^{p/2} + \left[\left(\frac{y-y_0}{\Delta y/2} \right)^2 + \varepsilon^2 \right]^{p/2} + \left[\left(\frac{z-z_0}{\Delta z/2} \right)^2 + \varepsilon^2 \right]^{p/2} \right) \quad (6.8)$$

where ε is a small constant and p is a constant describing the approximate norm, for example, if $p = 2$, then equation 6.8 describes an ellipsoid. To represent a block, I choose a p that is sufficiently large. For the length scales I consider, a value of $p = 4$ is appropriate. The value of ε is chosen to be large enough, and the value of p small enough so that the derivatives of the mapping are stable and second-order for the length scales of the problem. In addition, rotations can be included in the model, as described in McMillan (2017)¹.

When employing parametric mappings, there are two important implications to note in the setup of the inversion. Since the mathematical statement of the inverse problem is, in principle, overdetermined (there are more data than model parameters), I fix the value of β at zero and do not employ a regularization. The second point is that for a starting model, it is important to start with the block and background having different conductivities. This was similarly discussed in McMillan (2017).

Effective medium theory mapping

In Chapter 2, I introduced a two-step process for estimating the electrical conductivity of a propped, fractured volume of rock. The first step involved estimating the effective conductivity of a mixture of electrically conductive proppant and fluid, and in the second step, I estimated the effective conductivity of a volume of rock which has fractures filled

¹McMillan (2017) also employs a weighting scheme to scale the model parameters. I have not found this to be necessary for the examples I consider and thus do not use any weights or scaling

with the proppant-fluid composite.

Assuming the electrical conductivity of the fluid and proppant are known, then rather than inverting for electrical conductivity, we can invert for the concentration of conductive fractures. To avoid introducing additional non-uniqueness into the problem, I use a fixed ratio of proppant and fluid within the propped region of the reservoir and treat the fracture concentration φ as the inversion model (e.g. $\mathbf{m} = \varphi$). In a voxel-based inversion, φ is a vector with a value for the concentration in each cell. For simplicity, I assume that the fractures are randomly oriented and work only with isotropic conductivities. In this case, the mapping requires that we solve the two-phase effective medium theory approximation,

$$(1 - \varphi)(\sigma^* - \sigma_0)R^{(0,*)} + \varphi(\sigma^* - \sigma_1)R^{(1,*)} = 0 \quad (6.9)$$

for the effective conductivity, σ^* . The background has conductivity σ_0 and the conductive, proppant-filled cracks have conductivity σ_1 . Note that σ_0 , the conductivity of the background, does not need to be a scalar, it can be a vector with a background conductivity value for each voxel in the mesh. These values can be obtained by first inverting the pre-fracture data. The electric field concentration tensor $R^{(i,*)}$ captures the geometry of the particles that compose each phase. Note that for randomly oriented fractures $R^{(i,*)}$ is a scalar ($1/3\text{trace}\mathbf{R}^{(i,*)}$), where $\mathbf{R}^{(i,*)}$ is given in equation 2.3:

$$R^{(j,*)} = \frac{1}{3}\text{trace}\left(\left[\mathbf{I} + \mathbf{A}\sigma^{*-1}(\sigma_j - \sigma^*)\right]^{-1}\right) \quad (6.10)$$

For the background, I use an aspect ratio of 1, assuming a spherical geometry for the particles that compose it, and for the fractures, I use a small aspect ratio ($\sim 10^{-4} - 10^{-3}$) and treat them as ellipsoidal cracks. In Section 2.2.3, I demonstrated that for sufficiently

thin fractures, the exact aspect ratio is not significant. For a gradient based inversion, we also require the derivative of the effective conductivity, σ^* , with respect to our model, which is the fracture concentration, e.g.

$$\frac{\partial \sigma}{\partial \mathbf{m}} = \frac{\partial \sigma^*}{\partial \phi} \quad (6.11)$$

This derivation is outlined in Appendix C.

The general time-lapse inversion workflow using effective medium theory is two steps:

- Construct a background conductivity model, σ_0 , by inverting pre-fracture data.
This inversion is a voxel-inversion for log-conductivity.
- Invert the post-fracture data for fracture concentration, ϕ . Note that using a starting model and reference model of $\mathbf{m}_0 = \mathbf{0}$ is equivalent to starting the post-fracture inversion with the pre-fracture model.

Self-consistent effective medium theory is the method I adopt to connect the concentration of fractures with the effective conductivity of a fractured volume of rock, however, other relationships, such as an empirical relationship estimated from a lab study, could equally be employed. One interesting implication of relating the concentration of the fractures to the change in conductivity is that this provides a conduit for bringing in a-priori information about the volume of proppant injected into the reservoir. The predicted volume is

$$V_{\text{pred}} = \int \phi \, dV \quad (6.12)$$

I can then define a volume data misfit term,

$$\phi_V = \frac{1}{2} \left\| \frac{1}{\varepsilon_V} (V_{\text{pred}} - V_{\text{obs}}) \right\|^2 \quad (6.13)$$

where V_{obs} is the known volume terms which accounts for the estimated ratio of proppant and fluid and ε_V is an uncertainty term. I note that I am assuming a fixed ratio of proppant and fluid within the cracks. In reality, this will be variable, thus I use a sufficiently large ε_V so as not to over-fit this assumption.

In the implementation, the inclusion of an additional data misfit term is handled by a combo-objective function which enables joint inversions in the SimPEG framework.

6.3 Inversions with steel-cased wells

In the Chapter 4, we saw that the current spreads out along the length of the casing, decaying as we move away from the source. In the inversion, this raises questions about our ability to resolve the depth and vertical extent of the target. In this section, I start from a simple model of a vertical well with a conductive target and examine our ability to recover that target. Although most fracture operations are conducted in horizontal wells, I start by considering a vertical well as this reduces computational cost and allows us to explore aspects of the behavior of inversion prior to moving to the more fully 3D, more computationally intensive scenario.

I start by considering a DC experiment with a simple cylindrically symmetric model, shown in Figure 6.2. A 1 km long casing is embedded in a background that has a resistivity of $100 \Omega\text{m}$. The casing has an outer diameter of 10 cm, a thickness of 1 cm and a conductivity of $5 \times 10^6 \text{ S/m}$. For modelling, I approximate the hollow-cased well as solid cylinder with a conductivity of $1.4 \times 10^4 \text{ S/m}$, which preserves the product of the

conductivity and the cross sectional area. This was shown to be a valid approximation for DC problems in Section 4.4 and allows us to reduce the number of cells in the mesh, thus speeding up the computation of the forward simulation and sensitivities. Similar to the model used in 2, I assume a moderately-sized fracture operation which uses an 800 m³ slurry comprised of 15% proppant by volume. I assume leak-off of some of the fluid, leaving a mixture of 50% fluid and 50% proppant, by volume, in the fractures. This gives a total fracture volume of 240 m³ which I distribute among 10 each with 3 mm width are positioned within a 10 m interval along the well. Conserving volume gives a 50 m radius for the fractures. Using a fluid conductivity of 3 S/m and a proppant conductivity of 10⁵ S/m, the conductivity of the 50/50 proppant-fluid mixture found using self-consistent effective medium theory (equation 2.1) is 2500 S/m. Using a fracture aspect ratio of 3×10^{-5} and assuming randomly-oriented fractures, I obtain a conductivity of 3 S/m for the propped region of the reservoir.

The survey I use employs a downhole electrode and a distant return electrode. There are 10 down-hole source locations from 900 m depth to 1000 m depth, as shown by the red dots in Figure 6.2b. Radial electric field data are collected at the surface; there are 40 receiver locations from 25 m to 1000 m along a radial line extending from the well. In total, the survey consists of 400 data. Figure 6.3 shows (a) the simulated data for both the background (prior to the fracture) and the fracture, (b) the difference between the data with and without the fracture, and (c) the difference as a percentage of the background response. The color of each line indicates the depth of the positive electrode, as indicated by the colorbar at the bottom of the plot. The difference between the data simulated over is significant both in magnitude and in percentage and thus we can expect that the inversion will introduce structure in order to fit the fracture data. In the following sections, I will explore several approaches to the inverse problem for

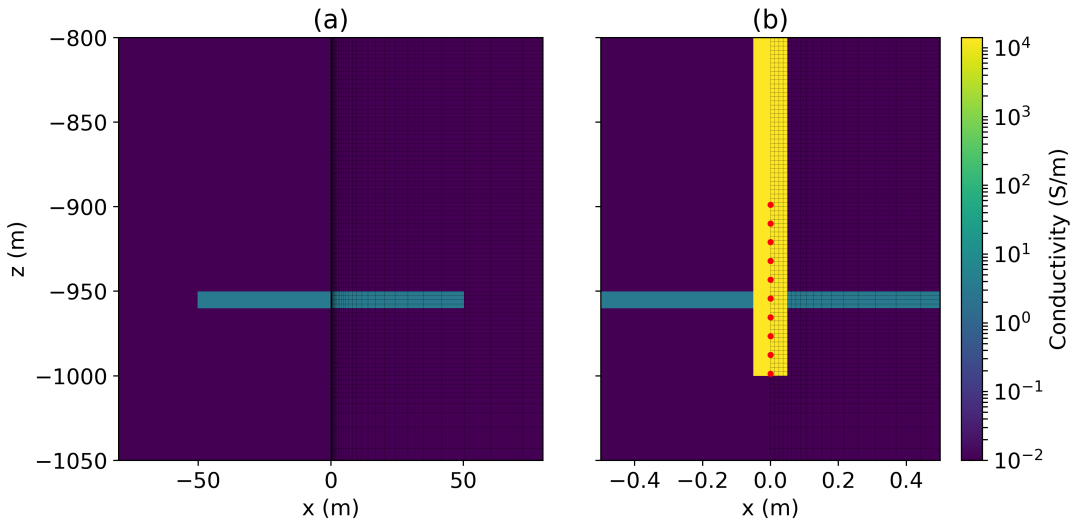


Figure 6.2: Model of an electrically conductive propped fracture zone (3 S/m) in a halfspace ($100 \Omega \text{ m}$) with a steel-cased well. The well is modelled as a solid cylinder with a conductivity of $1.4 \times 10^4 \text{ S/m}$. The mesh has 4 cells across the radius of the casing. The fractured region extends vertically from 950 to 960 m depth and has a radius of 50 m. Panel (a) has a radial extent of 80 m to show the fractured zone and panel (b) has a radius of 0.4 m to show the casing. The a-electrode locations are shown in panel (b).

obtaining meaningful information from the data.

6.3.1 Voxel inversion for conductivity

I begin by applying standard inversion techniques and perform a voxel inversion using a Tikhonov regularization. As the simulation is cylindrically symmetric, I invert for a 2D model which varies radially and vertically. Our aim in this inversion and the ones that follow is to examine, under ideal circumstances, what information we can obtain from the data using a given inversion approach. I therefore do not add noise to the data and assign low uncertainties: 1% with a 10^{-9} V/m floor.

The choice of parameters is quite standard, similar to how one would approach a

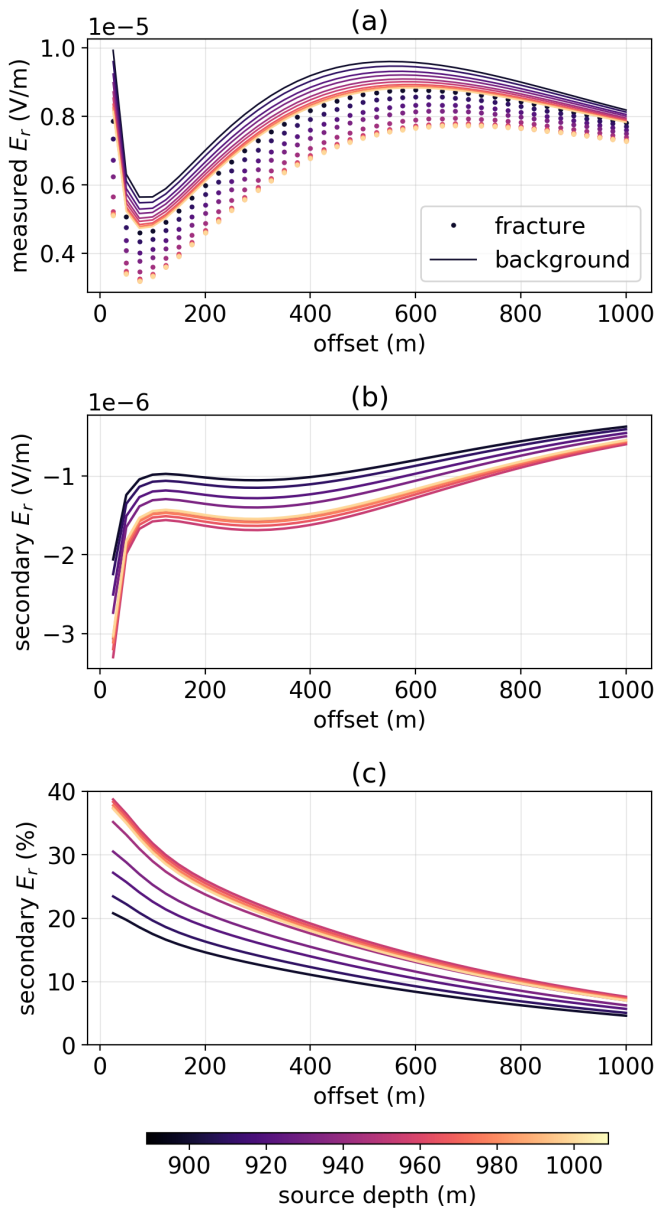


Figure 6.3: (a) Synthetic data for the down-hole casing experiment for the background, prior to the fracture (solid lines), and after the fracture (dots), (b) secondary electric field (fracture - background), and (c) secondary electric field as a percentage of the primary (background). The color of the lines or dots indicates the depth of the source.

blind inversion. In the regularization, I use $\alpha_s = 10^{-3}$, $\alpha_x = \alpha_z = 1$. I start the inversion with a large value of β , so that the regularization term initially dominates the objective function, and reduce its value over the course of the inversion. The initial and reference model are equal to the half-space resistivity of $100 \Omega\text{m}$.

The results of the first inversion I run are shown in Figure 6.4. This inversion reached a global χ -factor of < 0.1 and fits all data points within 5% (Figure 6.4c). It converged in two iterations. Because of the regularization function being used, the recovered model is smooth and diffuse. Perhaps unexpected is the location of the center of the recovered target; its depth is shifted below the true location, closer to the end of the well. Typically, we might expect that if the inversion were to shift the location of a target, it would be shifted up, closer to the receivers, where we have greater sensitivity. However, the presence of the casing alters the sensitivity. In Chapter 3, I demonstrated that there is an increase in charge near the ends of the well (see Figure 3.6, in particular), for the DC problem, this translates to an increase in sensitivity near the end of the well. This can also be seen by plotting the sensitivity. In Figure 6.5, I plot the sensitivity function for the starting model of the casing in a $100 \Omega\text{m}$ half-space (a) and (b), as well as for the true model, with the conductive target in (c) and (d). In panels (a) and (b), we see that throughout the region where the source electrodes are positioned, the sensitivity is relatively uniform. The exception is near the end of the well, where the region of large sensitivity broadens. When the target is included, the sensitivity is increased in that region. However, we still see a broadened region of high sensitivity near the bottom of the well. The increase in high sensitivity near the end of the well has a tendency to promote structure near the end of the well in the inversion.

If I push the inversion harder, the depth of the target is better-resolved, as shown in Figure 6.6. In practice, this requires very high data quality; here I fit all data points

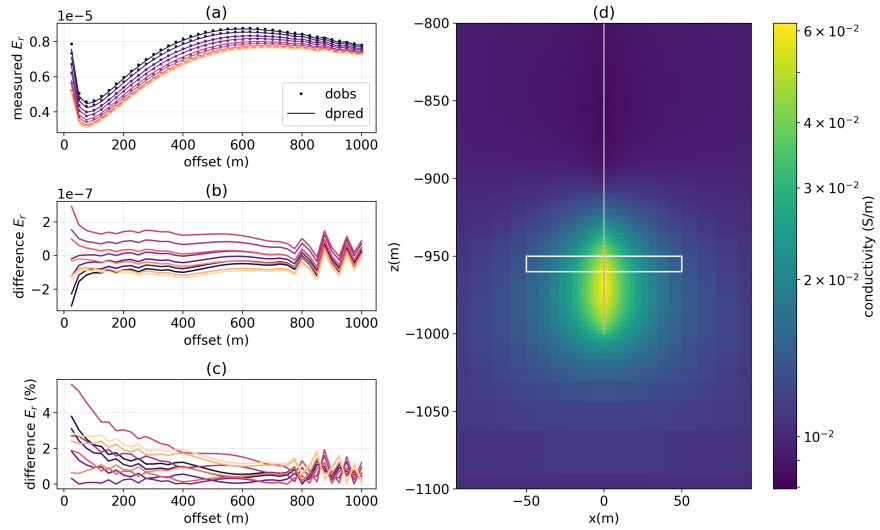


Figure 6.4: (a) Observed and predicted radial electric field data, (b) difference between the observed and predicted data (V/m), (c) difference between the observed and predicted data as a percentage of the observed data, and (d) conductivity model recovered in the inversion. The colors in (a), (b), and (c) indicate the source location as shown in Figure 6.3. The white outline in (d) outlines the true geometry of the fracture zone and the grey line shows the location of the wellbore. The data are fit to a global χ -factor < 0.1 and the inversion took 3 iterations.

within $\sim 2\%$ and reach a global χ -factor < 0.05. The geometry of the target that I recover is elongated vertically; this is consistent with having larger sensitivity near the well. We also notice that the conductivity of the region above the target drops beneath that of the background – this is a common effect in smooth inversions when conductive targets are present. In this case, we know that the changes due to the conductive proppant and fluid should only increase the conductivity with respect to the background. I could impose a lower-bound on the conductivity of the inversion model, however, experimentation shows that this tends to push the center of the conductive anomaly beneath the true target depth.

More horizontally elongated structure can be promoted by altering the regulariza-

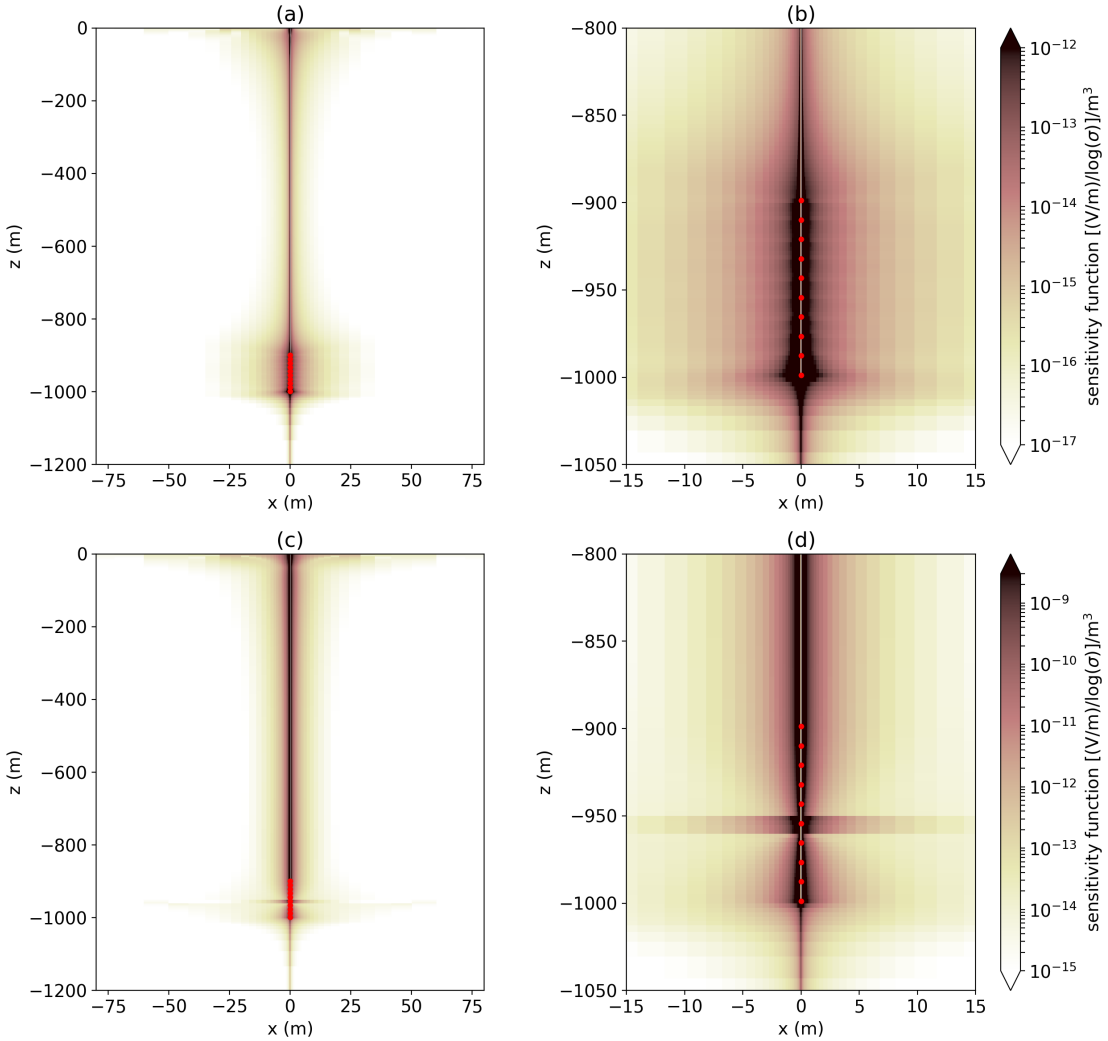


Figure 6.5: Integrated sensitivity for (a, b) a survey conducted in a $100 \Omega\text{m}$ half-space and (c, d) the true model with the conductive target, shown in Figure 6.2. The inversion model is log-conductivity. The casing is shown by the grey line, and the source locations are shown by the red dots. The integrated sensitivity is computed by squaring the elements of the sensitivity matrix, summing along the rows of the sensitivity matrix and then taking the square-root. This gives a vector whose length is the number of model parameters.

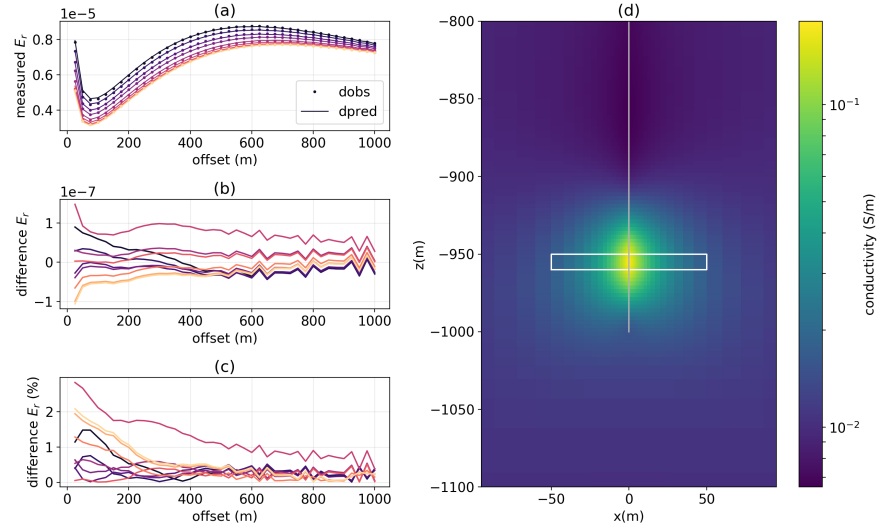


Figure 6.6: Tikhonov inversion result, similar to that shown in 6.4 that fits the data to a global χ -factor < 0.05 . The inversion took 5 iterations.

tion. Figure 6.7 demonstrates an inversion using $\alpha_x = 100$ and fitting the data to a χ -factor < 0.05 . Using a large α_x smears out the target horizontally and also reduces the maximum conductivity as compared to Figure 6.6.

In summary, by using a standard voxel inversion, we can recover a target at the correct location, and by adapting the α values, we can recover a general geometry reflective of the true target. However, these are not particularly insightful images for delineating the extent of the fractured region of the reservoir. With the aim of using the inversion to obtain parameters indicative of the injection, I next examine an approach using a parametric inversion.

6.3.2 Parametric Inversion

In a parametric approach to the inversion, the fractured volume of rock is represented as a simple geometric structure, and we invert for a handful of parameters that describe the properties of the background, target and the position and geometry of the target.

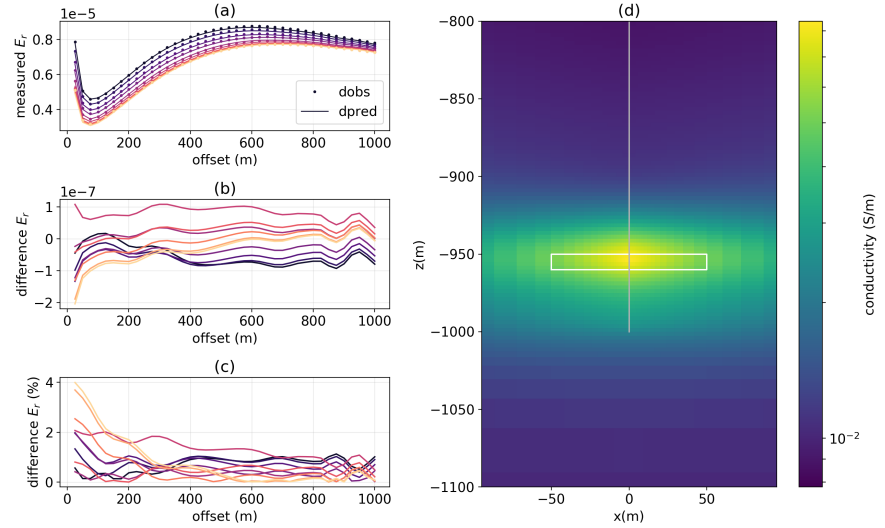


Figure 6.7: Tikhonov inversion result, similar to that shown in 6.6 that uses $\alpha_x = 100$. The inversion took 5 iterations.

For the following examples, I treat the fractured volume of rock as a cylinder. I fix $x_0 = 0\text{m}$ and invert for the log-conductivity of the background and the target, as well as the depth, radius and thickness of the target. I again push the inversion quite hard, fitting the following results to a global χ -factor < 0.05 , meaning that most of the data are fit within $\sim 2\%$.

For the parametric inversion to find an initial step, it is important that we start with a model where target has physical properties distinct from the background. In this example, I build a starting model based on the first voxel inversion result, shown in Figure 6.4. The center of the target is at 980 m depth, its radius is 5 m and it thickness is 5 m. The conductivity of the background is 10^{-2} S/m and the conductivity of the target is set to 3×10^{-2} S/m. Figure 6.8 shows the recovered model; the true geometry is outlined by the solid white line and the starting model geometry is shown by the dashed white line. The radius is underestimated (25 m) and the conductivity significantly overestimated

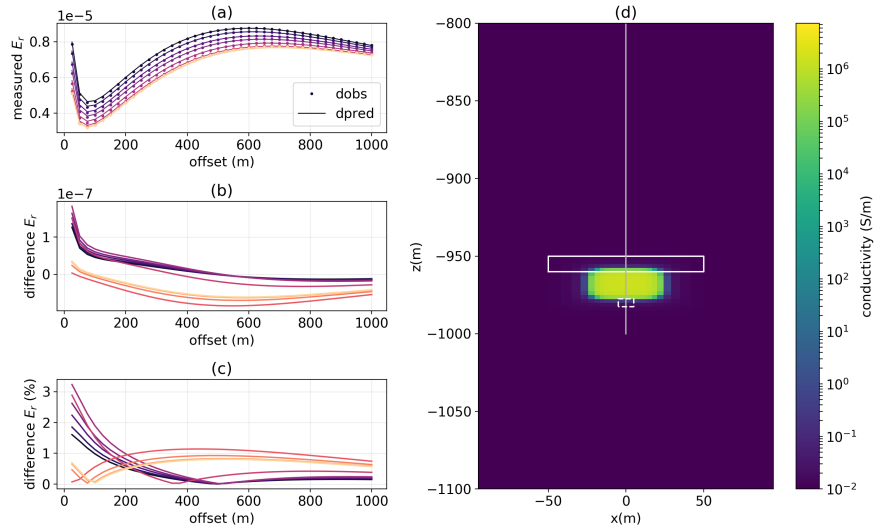


Figure 6.8: Parametric inversion result for a starting model centered at 980 m depth with a thickness of 5 m and a radius of 5 m. The initial background conductivity is 10^{-2} S/m and the initial conductivity of the target is 3×10^{-2} S/m. The geometry of the starting model is shown by the white dashed-lines and the true model is shown by the solid white outline. The inversion reached a χ -factor < 0.05 and took 8 iterations.

$(7 \times 10^6$ S/m).

If instead, I use the true depth-center of the target, informed by the inversion result in Figure 6.6, I obtain the model shown in Figure 6.9. The starting conductivities, radius and thickness were the same used in the previous inversion. In this inversion, the target is still shifted beneath the true location. The thickness, 12 m, is much closer to the true thickness (10 m). However, the recovered conductivity, 10^{10} S/m is even more severely overestimated than the previous inversion. Typically, one might expect that there is a saturation in the conductivity effects for a DC experiment. For example, if I consider the solution for a conductive sphere in a half-space subject to a uniform inducing electric field, the conductivity-dependence of the magnitude of the electric field external to the sphere is through the term: $(\sigma_2 - \sigma_1)/(\sigma_2 - 2\sigma_1)$, where σ_2 is the conductivity of the

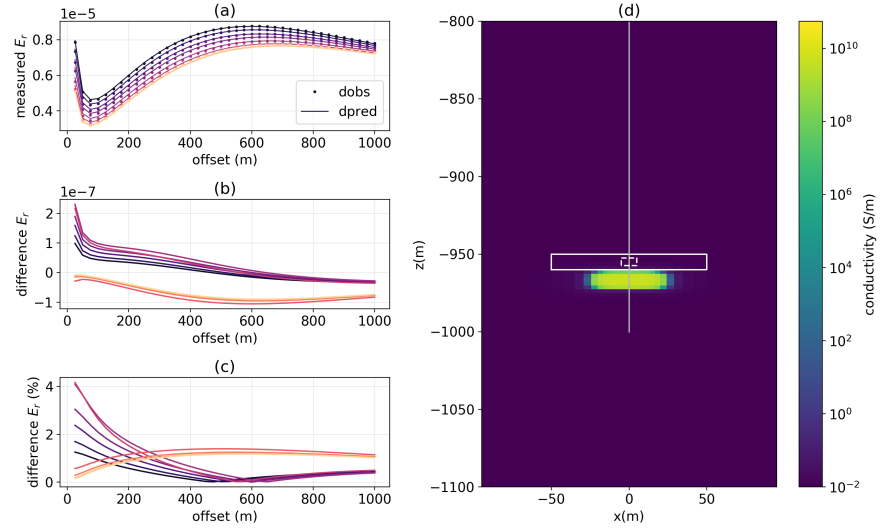


Figure 6.9: Parametric inversion result for a starting model centered at 955 m depth with a thickness of 5 m and a radius of 5 m. The initial background conductivity is 10^{-2} S/m and the initial conductivity of the target is 3×10^{-2} S/m. The geometry of the starting model is shown by the white dashed-lines and the true model is shown by the solid white outline. The inversion reached a χ -factor < 0.05 and took 8 iterations.

sphere and σ_1 is the conductivity of the background (see equation 6.67 in Ward and Hohmann (1988)). For a fixed background conductivity, whether the conductivity of the target is 2 or 3 orders of magnitude larger than the background, makes little difference in the external electric field. However, in this example, the conductive target is directly coupled to the casing, which has a conductivity of 10^4 S/m. I suspect that this survey geometry is sensitive to a larger dynamic range of conductivity values and this might contribute to the large updates in the electrical conductivity of the target.

The casing spreads out the source currents along its length, this may reduce sensitivity to the depth and thickness of the target. If that is the case, perhaps starting with the correct depth-center and thickness will improve the result. Figure 6.10 shows the recovered model when the correct depth and vertical extent of the target are used for the

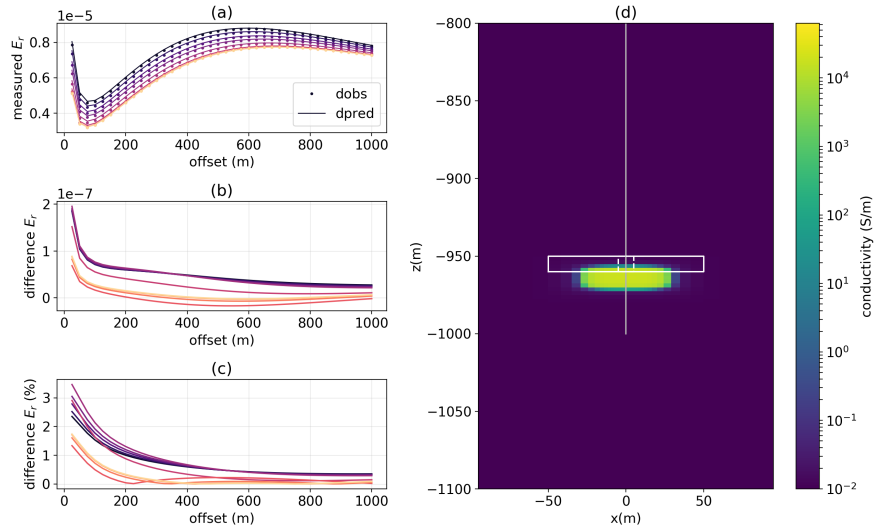


Figure 6.10: Parametric inversion result for a starting model centered at 955 m depth with a thickness of 10 m and a radius of 5 m. The initial background conductivity is 10^{-2} S/m and the initial conductivity of the target is 3×10^{-2} S/m. The geometry of the starting model is shown by the white dashed-lines and the true model is shown by the solid white outline. The inversion reached a χ -factor < 0.05 and took 12 iterations.

starting model. The thickness of the target is closer to the true thickness. However, the conductivity is still overestimated (960 S/m), but not nearly as severely as the previous inversion. The depth has been shifted down beneath the target, and the radius (23 m) is underestimated.

If I start the inversion closer to the true solution, for example a radius of 75 m and a thickness of 5 m, then, not surprisingly, I obtain a solution closer to the true solution. The recovered radius is 76 m, thickness is 7 m and the conductivity 2 S/m. This inversion result is shown in Figure 6.11.

These inversion results provide some insights into the non-uniqueness of the problem. In particular, depending on the starting model, the recovered conductivity of the target can vary by many orders of magnitude. I suspect that the large conductivity of the

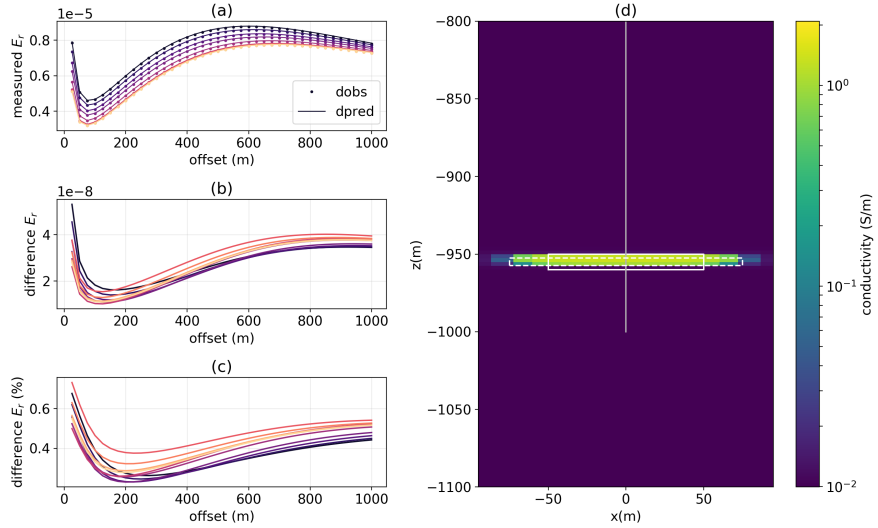


Figure 6.11: Parametric inversion result where the center of the target is fixed at a depth of 955 m. The starting model has a thickness of 5 m and a radius of 75 m. The initial background conductivity is 10^{-2} S/m and the initial conductivity of the target is 3×10^{-2} S/m. The geometry of the starting model is shown by the white dashed-lines and the true model is shown by the solid white outline. The inversion reached a χ -factor < 0.05 and took 6 iterations.

casing is a major contributor to the difficulty of this inverse problem. The conductive casing tends to spread out the source currents, which consequently spreads out the sensitivity as compared to a point electrode. Furthermore, the currents along the casing are altered due to the presence of a conductive target – this is a more complex interaction than typically encountered in a DC experiment.

The geometry of the parametric inversion results provides a more intuitive geometry for interpretation, but, on its own, the inversion is not particularly robust. Thus we require more a-priori information or assumptions be imposed in the inversion. There are several approaches that could be taken to try and tame the inversion: the electrical conductivity could be bounded, for example by using hard-constraints in the optimiza-

tion, or a weighting scheme could be adopted to try to compensate for the sensitivities. This level of “tuning” in the inversion is something I wish to avoid. Instead, I will consider changing the model-space by using effective medium theory to map a volume-concentration of fractures to electrical conductivity.

6.3.3 Inversion for fracture concentration

Effective medium theory provides a mapping from a volume-concentration of fractures, φ , to electrical conductivity given known values for the conductivity of the background and the conductivity of the material filling the fractures. Instead of inverting for electrical conductivity (or log-conductivity), we can invert for a concentration of fractures. This has several important implications in the inversion. First of all, it changes the parameter space which we are working in; this affects both the regularization and the computation of the sensitivities. In addition, it provides natural bounds for the conductivity, as $0 \leq \varphi \leq 1$. Figure 6.12 shows the effective conductivity as a function of fracture concentration for the model considered here. Panels (a) and (b) show the effective conductivity on a linear scale, while panels (c) and (d) show the effective conductivity on a log-scale. The panels on the right (b) and (d) zoom in to lower concentrations ($0 < \varphi < 0.005$). The mapping between concentration and effective conductivity is approximately linear over the range of concentrations we expect to encounter for a fractured volume of rock. Recall that the true concentration is 0.003. In comparison, the bottom two plots, Figure 6.12 (c) and (d) show the log-conductivity, which is the parameter I was inverting for in previous examples. It is quite non-linear, particularly at low concentrations. Consider, for example how this manifests in the regularization. If I regularize on log-conductivity, the difference between 10^{-2} S/m (the background) and 1 S/m is penalized much more significantly than the difference between 1 S/m and

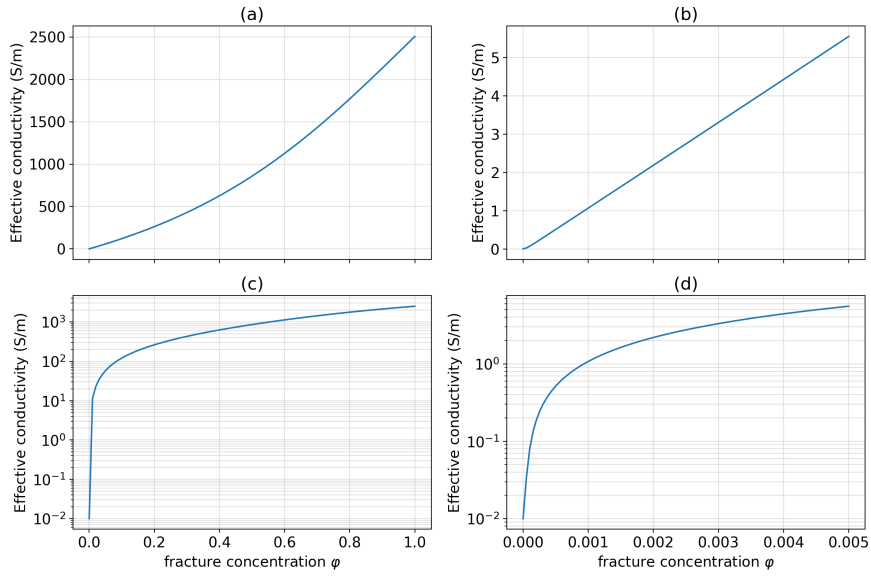


Figure 6.12: Self-consistent effective medium theory estimation of electrical conductivity as a function of fracture concentration. The conductivity of the background is 10^{-2} S/m and the conductivity of the material filling the fractures is 2500 S/m. We use an aspect ratio of 3×10^{-5} , and the fractures are assumed to be randomly oriented. Panels (a) and (b) show the conductivity on a linear scale while panels (c) and (d) show the conductivity on a logarithmic scale. Panels (a) and (c) show the full range of possible ϕ values from 0 to 1, and panels (b) and (d) zoom into a smaller range, $0 \leq \phi \leq 0.005$.

2 S/m. If instead, I regularize on concentration, then the difference between 10^{-2} S/m and 1 S/m is treated nearly the same as the difference between 1 S/m and 2 S/m as each corresponds to an increase in concentration by 0.001 S/m. The associated sensitivity function is shown in Figure 6.13. As compared to the log-conductivity inversion (Figure 6.5), the sensitivity is much more uniform over the length of the well for both (a, b) the halfspace and (c, d) the true models.

To examine how using an effective medium theory model parameterization impacts the inversion, I run a standard voxel inversion, as in Section 6.3.1, but now using ϕ

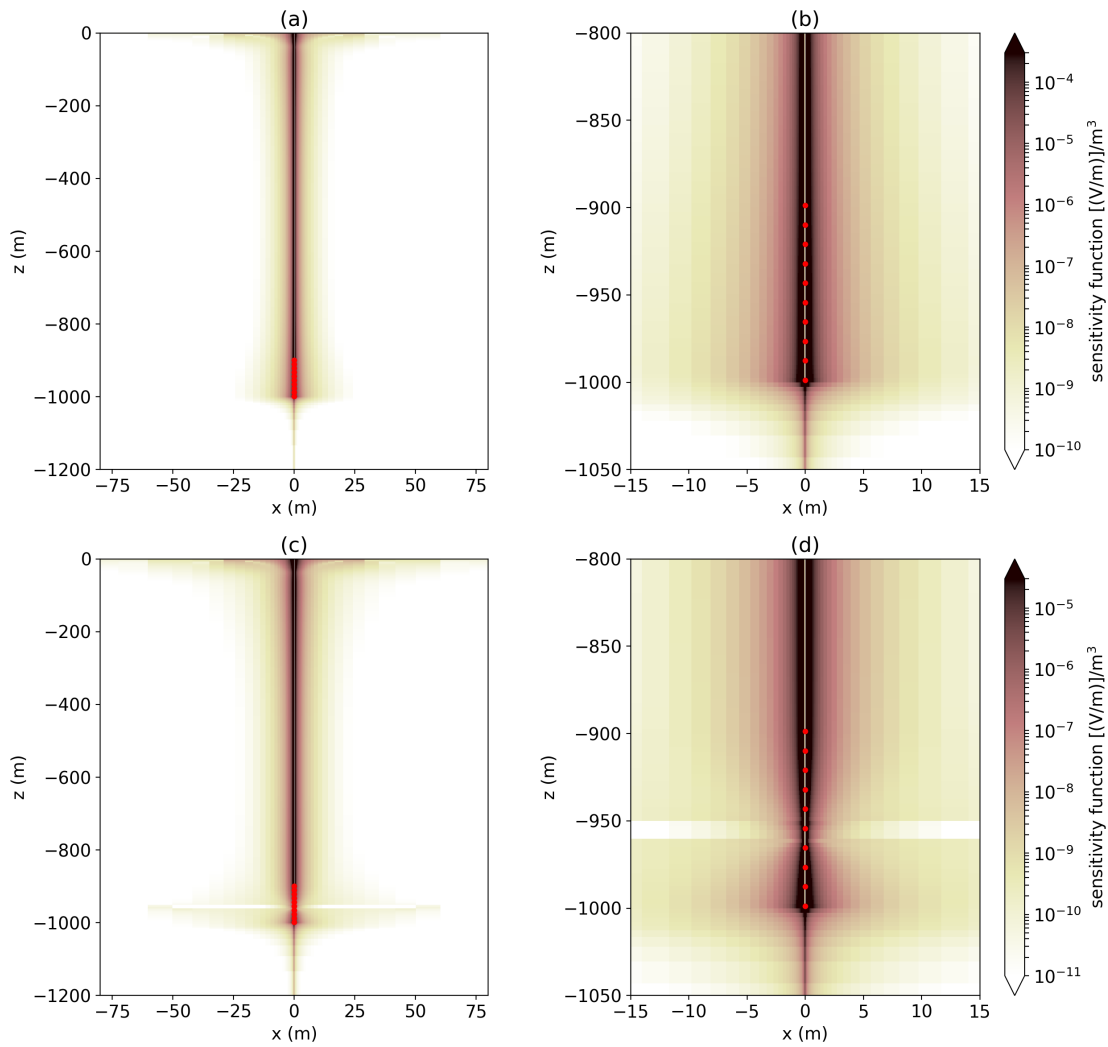


Figure 6.13: Integrated sensitivity, similar to that shown in 6.5, except here, the inversion model is fracture concentration. Panels (a, b) are the sensitivity for a $\varphi = 0$ half-space and (c, d) show the sensitivity calculated using the true model which includes the fracture.

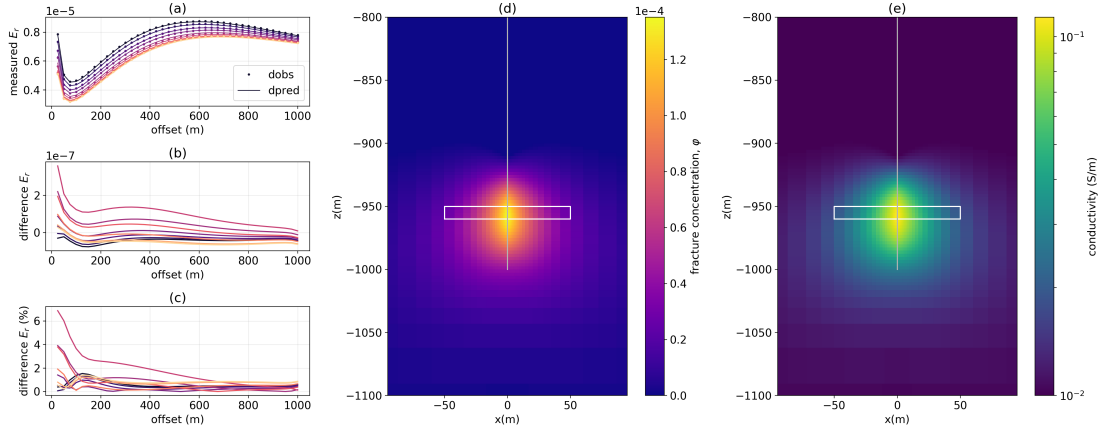


Figure 6.14: (a) Observed and predicted radial electric field data, (b) difference between the observed and predicted data (V/m), (c) difference between the observed and predicted data as a percentage of the observed data, (d) fracture concentration model, φ , recovered in the inversion, and (e) electrical conductivity model obtained by converting φ to electrical conductivity using equation 6.9. The colors in (a), (b), and (c) indicate the source location as shown in Figure 6.3. The white outline in (d) outlines the true geometry of the fracture zone and the grey line shows the location of the wellbore. The data are fit to a global χ -factor < 0.05 and the inversion took 5 iterations.

as the inversion model. For σ_0 , I use the scalar value for the background, 10^{-2} S/m in all cells. The initial model was set slightly above zero (10^{-10}) S/m so that not all model cells were starting on the lower bound of $\varphi = 0$. The reference model is set to zero. Pushing the inversion to a χ -factor < 0.05 gives the result shown in Figure 6.14. I have added an additional panel and now show both the recovered concentration model (d) and the corresponding conductivity model (e). The inversion result is quite comparable to the model obtained through a log-conductivity inversion shown in Figure 6.6. The main notable difference is that there is no region in which the conductivity of the background is underestimated; by bounding the concentration between 0 and 1, there is no mechanism for the inversion to reduce the conductivity.

Next, I consider combining the effective medium theory map with the parametric

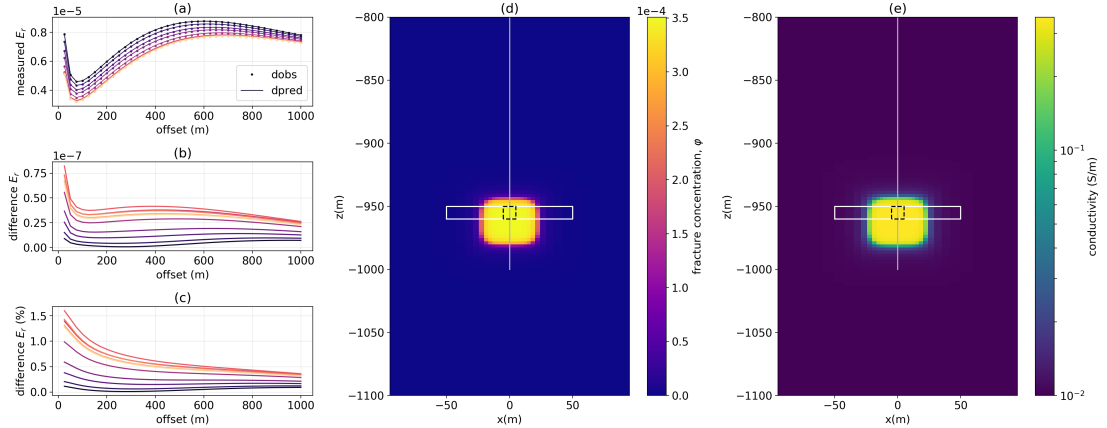


Figure 6.15: Inversion result using a parametric model of the fracture concentration. The black dashed line outlines the geometry of the starting model. The initial fracture concentration is 10^{-10} in the background and 10^{-4} in the target. The data are fit to a global χ -factor < 0.05 and the inversion took 11 iterations.

map. I invert for the volume concentration of fractures in the background and within the target as well as the depth, vertical extent and radius of the target. Similar to the starting model used to obtain the inversion result in Figure 6.10, I start with a target at the correct depth and with the correct thickness; its radius is 10 m. For a starting φ -values, I use 10^{-10} in the background and 10^{-4} in the target. In comparison to the parametric inversions for log-conductivity, the fracture concentration, and thus electrical conductivity are much closer to the range we are expecting. The recovered concentration within the target is 4×10^{-4} and its conductivity is 0.3 S/m. The vertical extent is 37 m which is an overestimate, and its radial extent is 22 m, which is an underestimate. This result closely resembles the voxel model shown in 6.14 and thus provides some evidence that using effective medium theory may be a more robust approach to the parametric inversion.

Experimentation shows that using effective medium theory in combination with the

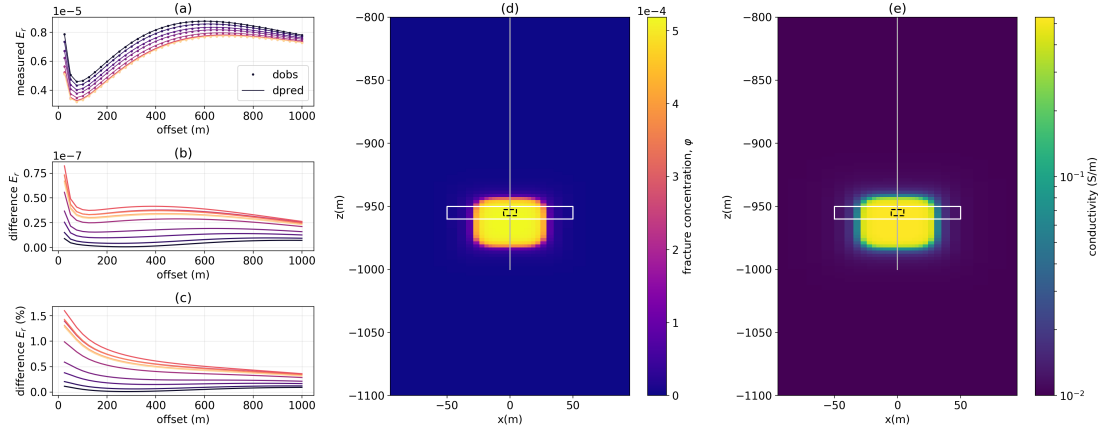


Figure 6.16: Inversion result using a parametric model of the fracture concentration. The concentration is converted to electrical conductivity using the effective medium theory mapping shown in equation 6.9. The black dashed line outlines the geometry of the starting model. The initial fracture concentration is 10^{-10} in the background and 10^{-4} in the target. The data are fit to a global χ -factor < 0.05 and the inversion took 12 iterations.

parametric inversion is less sensitive to the starting model. For example, starting with a thin target as in Figure 6.9 (which resulted in a conductivity of 10^{10} S/m for the target), I obtain the inversion result shown in Figure 6.16. The recovered concentration is 5×10^{-4} S/m, which corresponds to a conductivity of 0.5 S/m. Its vertical extent is 39 m, and its radial extent is 29 m. Although there are some differences between the results obtained in Figures 6.15 and 6.16, these are quite minor, and are not nearly as dramatic as the models obtained by inverting for log-conductivity. Note that no regularization is used here, the difference that the effective medium theory mapping makes in the parametric inversion is in its impact on the sensitivities as well as the bounds it imposes on the conductivity. In particular, the modification of the sensitivity seems to be the main contributing factor. As the inversion progressed, the fracture concentration within the target never reached the upper bound.

For the DC problem, it seems that there is an element of non-uniqueness between

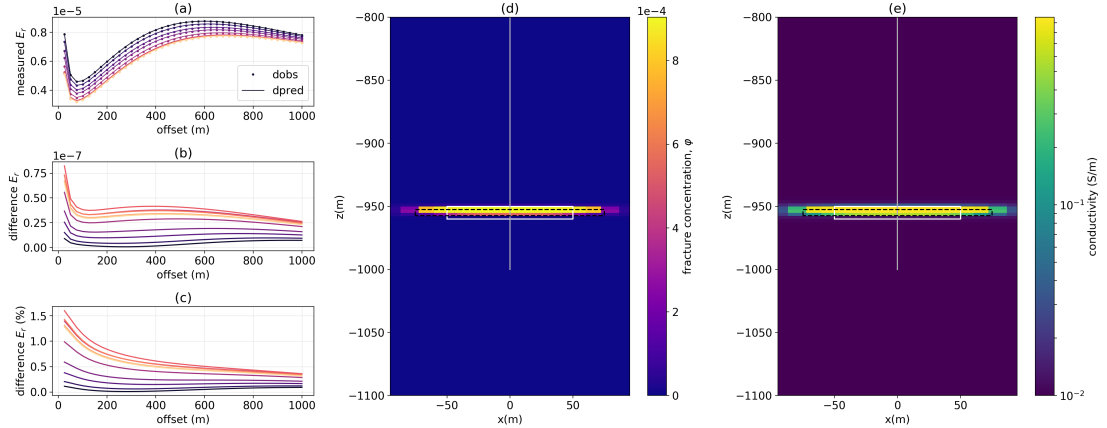


Figure 6.17: Parametric inversion result where the center of the target is fixed at a depth of 955 m. The concentration is converted to electrical conductivity using the effective medium theory mapping shown in equation 6.9. The black dashed line outlines the geometry of the starting model. The initial fracture concentration is 10^{-10} in the background and 10^{-4} in the target. The data are fit to a global χ -factor < 0.05 and the inversion took 6 iterations.

the vertical thickness of the target and its radial extent. Starting the inversion with a geometry closer to the true solution, as in Figure 6.11, results in the model shown in Figure 6.17. The recovered concentration is 10^{-3} , which corresponds to a conductivity of 1 S/m. The recovered radius is 75 m and thickness is 7 m. This indicates that in order to obtain meaningful inversion results, we will need to start in the correct proximity to the solution. For example, if the fracture was monitored with microseismic, then the volume interpreted with microseismic, which is likely an overestimate of the extent of the propped volume, could be used as a starting model.

These inversions did not take advantage of the known volume of proppant and fluid (235 m^3). The inversion result in Figure 6.15 underestimates the volume at 88 m^3 . Coincidentally, the inversion result in Figure 6.16 comes quite close to the true volume, 226 m^3 . The inversion which we might expect the best performance of, as its geometry

is closest to the true fracture, is that in Figure 6.17; this inversion overestimates the volume by a factor of two: 471 m^3 . In the next section, I examine if the inversion results can be improved by including a-priori knowledge of the volume of injected material.

6.3.4 Adding a-priori volume information

Provided that we have an estimate of the total volume of injected material (which accounts for leak-off of fluid), as well as an estimate of the relationship between the concentration of the injected material and the electrical conductivity, then the total volume can be treated as a datum in the inversion, as described in Section 6.2. In the following inversions, I include the volume data-misfit term (equation 6.13 in the statement of the inverse problem:

$$\phi_d = \phi_{DC} + \phi_V \quad (6.14)$$

When combining two quantities into a single misfit function there is a need to balance the two terms so that they each are effective. This could be done by introducing an additional weighting parameter or by increasing or decreasing the uncertainty assigned to the volume datum. I have chosen the latter route.

The volume term can be incorporated into both the voxel and the parametric inversions. For a voxel inversion, the “forward simulation” which computes the volume is simply the sum over all cells in the forward modelling mesh of the product of the fracture concentration, φ , and the volume of each cell. In practice, the addition of the volume datum in a voxel inversion makes little difference on the result. Over the large domain, the concentration values in each cell can be updated by an amount that is negligible to the electrical conductivity in order to fit the volume datum. Thus, I focus my attention on the parametric inversion. To perform the “forward simulation” for the volume datum with the parametric model, I simply use the recovered radius, thickness and

concentration of fractures within the target. An alternative approach would be to map the parametric concentration model to the simulation mesh and integrate over the entire mesh. In practice, this can lead to a very large contribution from the background. For example, a background concentration of 6×10^{-7} was obtained for the inversion shown in Figure 6.15. This value is insignificant in its impact on the electrical conductivity model, however, when integrated over the entire modelling domain, including padding cells, it translates to a large volume.

It is important to note that the “forward simulation” for volume has no spatial sensitivity; the location of the target is irrelevant to the volume calculation, and there is a clear non-uniqueness between the radius and the thickness of the target. Therefore, we cannot expect that the addition of volume information to the inversions shown in Figures 6.15 or 6.16 provides much improvement to the estimate of the geometry of the target. However, where I hypothesize some improvement is for inversions where the geometry is a reasonable estimate of the true geometry, as in the inversion result obtained in Figure 6.17.

Using the same thin-sheet starting model as in Figure 6.17, I perform a “joint inversion” for the DC data and the volume. The uncertainty on the volume was set to 5%. The recovered model is shown in Figure 6.18. The inversion result is quite similar to that shown in Figure 6.17. The main differences are that in the inversion considering a volume term, the sheet was made thinner, 3 m, as compared to the 7 m thickness recovered in the inversion not considering volume.

6.4 Conclusions

The inversions shown in this section provide a glimpse into the nonuniqueness of the inverse problem, particularly when steel-cased wells are present. Pushing the voxel inver-

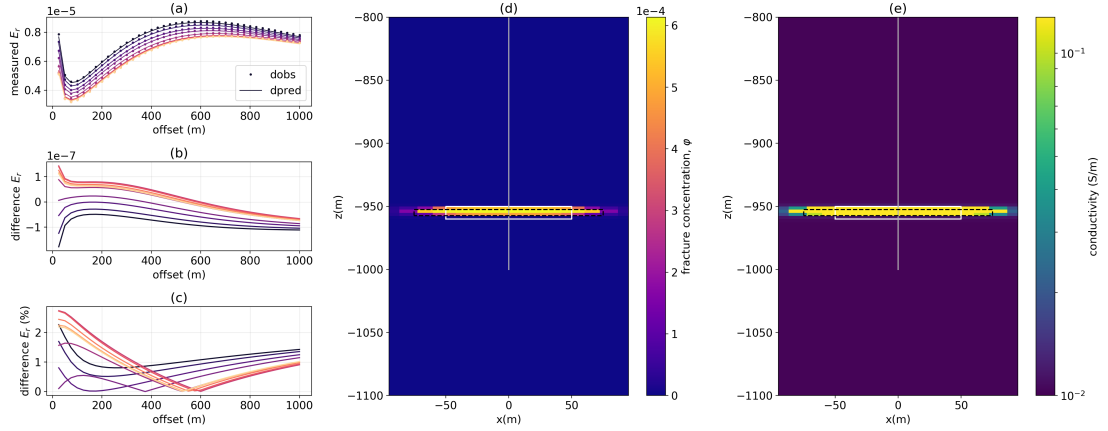


Figure 6.18: Parametric inversion using effective medium theory and a volume data-misfit in the statement of the inverse problem. The uncertainty on the volume datum was 5%. The starting model was the same as used in Figure 6.17. The inversion reached a global χ -factor < 0.05 after 5 iterations.

sion allows us to estimate the depth-center of the fractures, however a smooth inversion provides diffuse structures by design and therefore are not particularly insightful for estimating the geometry of a compact target. Parametric inversions provide a strategy for obtaining a simple geometric structure from the inversion. A standard approach to the parametric inversion and inverting for log-conductivity of the target and the background proved to be quite unstable, and, in particular, the recovered conductivity varied by orders of magnitude depending on the starting model. I suspect that the high conductivity of the casing, which is electrically in contact with the target, plays a significant role in this instability. This could be further examined in a study which varies the conductivity of the casing. If the casing is indeed the main cause of the instability, then reducing the conductivity of the borehole should reduce the large fluctuations in the recovered conductivity of the target.

If instead of inverting for log-conductivity, we invert for fracture concentration using effective medium theory, the parametric inversion is much more stable. The effective

medium theory mapping is an approximately linear relationship between the fracture concentration and the electrical conductivity, and it provides natural bounds on the recovered conductivity. Additionally, it allows us to incorporate a volume data-misfit term in the statement of the inverse problem. With the presented inversion approach, the mathematical statement of the effective medium theory relationship between fracture concentration electrical conductivity could be replaced by an empirical relationship based upon lab-studies. Although I used examples with a constant background, this is not required. A variable background model, based upon an inversion of data collected before the fracture, can be used.

Framing the inverse problem as one for fracture concentration resulted in a more robust inversion scheme that was less sensitive to the starting model, but clearly, there is significant non-uniqueness in the DC problem and we do not have much sensitivity to the geometry of the target. Experimentation shows that even adding vertical electric field data from an offset borehole does not significantly improve the results. Here is where electromagnetics has significant potential to provide further insights. In addition to the static excitation at DC, the time-variation of the fields causes induction processes and variation in the direction and magnitude of the fields, resulting in a richer data set. Chapter 3 examined details of the physics of the induction process for conductive permeable wells. The next step, which is a topic of future research, is to combine those research results with the insight I have developed in this inversion chapter to quantify how much additional information can be obtained using the full EM data set.

Chapter 7

Conclusions and outlook

Resource extraction and the storage of materials, such as CO₂, in the subsurface are current realities in our relationship with the earth. Making the best use of resources, such as the water required to perform hydraulic fracturing, and minimizing potential hazards, such as leakage of CO₂ requires that we have access to data which can ground and inform decisions. Electromagnetic geophysics has a role to play. In many cases, injected materials have different electrical conductivity than the host rock and the change in physical properties can be targeted with a non-invasive electrical or electromagnetic survey. A variety of EM surveys can be considered. Sources can be grounded or inductive, they can be positioned on the surface or within a borehole, and the data can consist of electric and/or magnetic field measurements. Each combination results in a different excitation and sensing of the earth. The main objective in designing a survey is to collect high quality data that are sensitive to the target. These data can then be inverted to obtain information about the subsurface structures of interest.

Inversions are an important tool for working with EM data, particularly when the goal is to extract information from subtle time-lapse signals. To formulate a meaningful

inverse problem requires that: (a) we have data that are sensitive to the target of interest, (b) we have the ability to forward-simulate data and compute sensitivities, and (c) we can incorporate the necessary a-priori information and select a set of inversion parameters that allow the question-of-interest to be investigated. The success (or not) of the methods used to address each of these elements depends upon an understanding of the governing physics. In reservoir settings, the behavior of the currents, charges, fields and fluxes is significantly complicated by the presence of highly conductive, permeable steel-cased wells. As a result, much of my thesis focussed on developing a fundamental understanding of electrical and EM methods in the presence of steel-cased wells.

With respect to steel-cased wells, this thesis includes contributions in terms of numerical modelling as well as physical understanding of the behavior of electromagnetic fields and fluxes in settings with highly conductive, permeable wells. By discretizing Maxwell's equations on a 3D cylindrical mesh, I was able to design a mesh which finely discretizes the casing and captures 3D survey geometries without the number of cells in the mesh resulting in an intensive computation. I considered two forms of validation, both comparing values with published simulation results and comparing physical behaviors with that predicted in formative papers on DC and EM with steel cased wells. At DC, I demonstrated the transition between an approximately linear decay of currents away from the source along short wells to an exponential decay in longer wells. This behavior was predicted by both Schenkel (1991); Kaufman and Wightman (1993) and has important implications in terms of testing approximations to the steel cased well. If the test is performed on a short well, there is minimal change in the behavior of the currents with changing conductivity. However, in longer wells, the product of the conductivity and the cross-sectional area controls the nature of the decay, and thus is the important quantity to conserve when approximating a steel cased well by a coarser conductivity

structure. Related to the currents is the distribution of charges along the well. For short wells, the distribution is nearly constant while for longer wells, there is an exponential decay. There is also a significant charge increase near the end of the well. Although no closed-form solution exists for this behavior, Griffiths and Li (1997) similarly demonstrated this effect using an asymptotic analysis. When considering inverse problems in settings with steel-cased wells, this has the implication that the sensitivity is larger near the end of the well and as a result causes the inversion to shift structure closer to the end of the well.

The DC resistivity experiment is the starting point for building an understanding of the behavior of currents, charges, and electric fields when steel-cased wells are present. Using the application of casing integrity, I demonstrated that the location of the return electrode can be an important parameter in terms of survey design: the source and receiver lines can be oriented such that the coupling of the primary-field with the receivers is reduced as compared to a survey with a very distant return electrode. Reducing the coupling means that the secondary signals of interest comprise a larger percentage of the data, and therefore provide greater opportunity to extract meaningful information in an inversion. Our ability to detect a target of interest depends on many factors: the conductivity of the background, casing, and target, the location of the target, the position of the source electrodes electrode, as well as the position and sensitivity of the receivers. The examples I demonstrated in Chapter 4 provide some indication of the relative importance of these parameters. Naturally, these details are site-specific and forward modelling is a critical tool for assessing the feasibility of a successful DC or EM survey in a given setting. The Jupyter Notebooks associated with this thesis can contribute to this task.

Electromagnetic problems introduce challenges both with respect to the time-variation

of the fields and fluxes as well as the additional complexity caused by the significant magnetic permeability of the pipe. In a “simple” grounded-source time-domain EM experiment with one electrode connected to the top of the pipe and an offset return electrode, a shadow zone develops along the azimuth opposite to the source wire. This is caused by the image currents being channeled into the pipe. When permeability is included in the simulation, we saw that a poloidal current develops within the pipe. Along the inner wall, the current flows downwards, while along the outer wall, it flows upwards. The effects of permeability onset at later times and can alter radial electric field data measured at the surface by > 100% as compared to a pipe which is only conductive. This shows that in order to accurately simulate EM data collected in settings with steel-cased wells, it is critical that permeability be modelled. Depending on the survey and site parameters (e.g. base frequency, background conductivity, etc.), it may even influence data that are classically treated as DC; EM forward modelling can be used to assess if this is a concern.

To reduce computational load, particularly when considering the inverse problem where many forward simulations are required, it is of interest to represent the casing on a coarse mesh. At DC, we could achieve this by approximating the hollow-cased well by a solid cylinder that preserves the product of the conductivity and the cross sectional area of the pipe. However, in an EM experiment, the image current, which diffuses through time complicates the geometry of the currents and their interaction with the well. As a result, it appears that to design an appropriate approximation to the well, we may need to use a conductivity that varies through time and as a function of distance along the well. In the upscaling work I contributed to in Caudillo-Mata et al. (2017a), we showed that the values we estimated for a coarse-scale approximation to a fine-scale conductivity structure depended upon sensitivity. For example a different conductivity value might be

obtained if we favored a value that replicated the behavior of the current density than if we favored a value that replicated the magnetic flux. Similarly, when approximating the casing in an EM experiment, the galvanic source currents provide a different excitation on the casing than the image current. Therefore, to capture each behavior on a coarse scale may require a more sophisticated approach than simply replacing the well with a constant conductivity. When permeability is included in the model, the behavior of the currents and magnetic flux are intertwined. It may be the case that a single scalar value can be used for the permeability, or it may be as complicated as conductivity and require that both a spatially and temporally varying model is necessary to accurately model the EM behavior. Designing a coarse-scale appropriate approximation to a steel-cased well is an avenue for future research. The development of the 3D cylindrical mesh simulation is an important contribution for this continuing work, as it provides a means for accurately discretizing the casing and performing simulations which include both permeability and conductivity.

The application of imaging hydraulic fractures was a primary motivator for the thesis. To create a sufficient contrast in electrical conductivity between the host rock and the fractures, I considered fracture operations conducted with an electrically conductive proppant and fluid. In order to estimate the electrical conductivity of a fractured volume of rock, I used a two-step homogenization process based on effective medium theory. In the first step, I estimate the conductivity of the proppant-fluid slurry and in the second, I estimate the conductivity of a volume of rock containing conductive cracks that are filled with the slurry. This approach provides a mathematical relationship between the concentration of conductive fractures and the coarse-scale conductivity. This relationship can be incorporated into an inversion, so that rather than inverting for log-conductivity, as is traditionally done in a DC or EM inversion, we can invert for a fracture concen-

tration given a background conductivity model. Furthermore, it provides a mechanism for incorporating a-priori knowledge of the volume of injected proppant and fluid into the statement of the inverse problem. Although the workflow I adopted in this thesis uses effective medium theory to connect the concentration of proppant and fluid to the coarse-scale conductivity, the same methodology could be applied using an empirical relationship found in a lab-study.

The features of interest in an imaging problem for fractures are primarily geometric. For example, from an engineering standpoint, it is of interest to delineate the height and lateral extent of the propped volume of the reservoir. A smooth voxel inversion is then not necessarily an ideal approach as diffuse structures are recovered. Adopting a parametric representation of the fractured volume of rock is one trajectory for estimating its shape. I performed several parametric inversions for a DC resistivity experiment. In particular, the inversion results demonstrated some of the complications that arise due to the presence of the highly conductive steel casing. The parametric inversions in which log-conductivity was used to describe the properties of the target were highly sensitive to the starting model; the recovered conductivities varied by several orders of magnitude with small changes in the starting model parameters. If instead of using log-conductivity, we use effective-medium theory and invert for the fracture concentration in a parametric inversion, the results were more robust. Minor variations in the starting model did not drastically change the recovered model. The effective medium theory mapping is an approximately linear mapping between the fracture concentration and the conductivity, whereas the mapping from log-conductivity to conductivity is highly non-linear. This changes the sensitivities, and in a setting with such significant physical property contrasts, the non-linear log-conductivity mapping is not particularly stable. The combination of a parametric description of the fractured volume of rock and the

effective-medium-theory mapping for the properties of the target resulted in reasonable model recoveries from the inversion. This was particularly true if the geometry of the starting model was somewhat representative of the true model.

Although parameterizing the model in terms of fracture concentration improved the stability of the inversion, there is still significant non-uniqueness. EM methods have significant potential to reduce some of this non-uniqueness because they provide richer information that comes with the variable excitation of the target through time. Exploring the use of EM inversions to image the propped-volume of a fracture is another avenue for future research. The software tools used to perform the DC inversions are implemented within the SimPEG framework. As such, the DC forward simulation component can readily be interchanged with an EM forward simulation and the same inversion machinery employed, which should reduce the overhead for future research along this trajectory.

The research conducted in this thesis required a significant amount of software to be developed. I needed to be able to forward-simulate Maxwell's equations at DC and in both the frequency and time-domains and view the results in terms of fields, fluxes and charges. For the EM simulations, permeability was included, and multiple formulations (E-B vs. H-J) were necessary for simulating inductive and grounded sources. For the inversion, I performed both voxel and parametric inversions in terms of log-conductivity and in terms of fracture-concentration through effective medium theory. This requires optimization machinery, computation of the sensitivities, and flexibility in how the inversion model is defined. Taken together, the composite of these tasks is an enormous effort and would be intractable if tackled in isolation. Further, much of the potential contribution to the broader community would be lost if the software had been written with the aim of “getting the job done” rather than written with the aim of re-use and

adaptation by others. Working within the open-source ecosystem provides opportunities for researchers to leverage existing tools and to contribute new components into a larger framework where their value can be realized by a broader community. The work in this thesis has greatly benefited from work conducted by the SimPEG community and more broadly by the Jupyter and scientific Python communities. I in turn hope that the contributions I have made to the SimPEG ecosystem add long-term value to the geophysics community.

Bibliography

- Aghasi, A., Kilmer, M., Miller, E., 2011. Parametric level set methods for inverse problems. *SIAM J. Imaging Sci.* 4 (2), 618–650. → pages 316
- Aldridge, D. F., Weiss, C. J., Knox, H. A., Schramm, K. A., Bartel, L. C., 2015. Is a Steel-Cased Borehole an Electrical Transmission Line? *SEG Technical Program Expanded Abstracts 2015*, 736–741.
URL <http://library.seg.org/doi/10.1190/segam2015-5927874.1> → pages 80
- Amestoy, P. R., Duff, I. S., L'Excellent, J.-Y., Koster, J., jan 2001. A Fully Asynchronous Multifrontal Solver Using Distributed Dynamic Scheduling. *SIAM Journal on Matrix Analysis and Applications* 23 (1), 15–41. → pages 295
- Amestoy, P. R., Guermouche, A., L'Excellent, J.-Y., Pralet, S., feb 2006. Hybrid scheduling for the parallel solution of linear systems. *Parallel Computing* 32 (2), 136–156. → pages 295
- Archie, G., 1942. The Electrical Resistivity Log as an Aid in Determining Some Reservoir Characteristics. *Transactions of the AIME* 146 (01), 54–62. → pages 36
- Ascher, U. M., jan 2008. Numerical Methods for Evolutionary Differential Equations. Society for Industrial and Applied Mathematics. → pages vii, 295
- Astropy Collaboration, Robitaille, T. P., Tollerud, E. J., Greenfield, P., Droettboom, M., Bray, E., Aldcroft, T., Davis, M., Ginsburg, A., Price-Whelan, A. M., Kerzendorf, W. E., Conley, A., Crighton, N., Barbary, K., Muna, D., Ferguson, H., Groffier, F., Parikh, M. M., Nair, P. H., Günther, H. M., Deil, C., Woillez, J., Conseil, S., Kramer, R., Turner, J. E. H., Singer, L., Fox, R., Weaver, B. A., Zabalza, V., Edwards, Z. I., Azalee Bostroem, K., Burke, D. J., Casey, A. R., Crawford, S. M., Dencheva, N., Ely, J., Jenness, T., Labrie, K., Lim, P. L., Pierfederici, F., Pontzen, A., Ptak, A., Refsdal, B., Servillat, M., Streicher, O., oct 2013. Astropy: A community Python package for astronomy. *Astronomy & Astrophysics* 558, A33. → pages 334
- Augustin, A. M., Kennedy, W. D., Morrison, H. F., Lee, K. H., jan 1989a. A theoretical study of surfacetoborehole electromagnetic logging in cased holes. *Geophysics* 54 (1), 90–99.
URL <http://library.seg.org/doi/10.1190/1.1442581> → pages 8, 15, 64, 66, 76, 83, 84, 86, 88, 90, 154
- Augustin, A. M., Kennedy, W. D., Morrison, H. F., Lee, K. H., 1989b. A theoretical study of surfacetoborehole electromagnetic logging in cased holes. *Geophysics* 54 (1), 90–99. → pages 195
- Bartel, L., McCann, R., Keck, L., apr 1976. Use of Potential Gradients in Massive Hydraulic Fracture Mapping and Characterization. In: *SPE Annual Fall Technical Conference and Exhibition*. Society of Petroleum Engineers. → pages 5
- Becker, A., Wang, B., Lee, K. H., Wilt, M., jan 1997. Subsurface electromagnetic measurement through steel casing. In: *SEG Technical Program Expanded Abstracts 1997*. Society of Exploration Geophysicists, pp. 1965–1968. → pages 154, 195
- Berryman, J. G., Hoversten, G. M., mar 2013. Modelling electrical conductivity for earth media with macroscopic fluid-filled fractures. *Geophysical Prospecting* 61 (2), 471–493. → pages 13, 35, 36, 37, 39, 41
- Bevc, D., Morrison, H. F., jun 1991. Boreholetosurface electrical resistivity monitoring of a salt water injection experiment. *Geophysics* 56 (6), 769–777. → pages 5
- Binley, A., Cassiani, G., Middleton, R., Winship, P., 2002. Vadose zone flow model parameterisation using cross-borehole radar and resistivity imaging. *Journal of Hydrology* 267 (3-4), 147–159. → pages 194

- Börner, J. H., Wang, F., Weißflog, J., Bär, M., Görz, I., Spitzer, K., 2015. Multi-method virtual electromagnetic experiments for developing suitable monitoring designs: A fictitious CO₂ sequestration scenario in Northern Germany. *Geophysical Prospecting* 63 (6), 1430–1449. → pages 64
- Brandl, G., 2010. Sphinx documentation. URL <http://sphinx-doc.org/sphinx.pdf>. → pages 278
- Brannon, H. D., Starks, T. R., apr 2008. The Impact of Effective Fracture Area and Conductivity on Fracture Deliverability and Stimulation Value. In: SPE Annual Technical Conference and Exhibition. Society of Petroleum Engineers. → pages 3
- Brill, T. M., Le Calvez, J. L., Demichel, C., Nichols, E., Zapata Bermudez, F., 2012. Electromagnetic casing inspection tool for corrosion evaluation. Society of Petroleum Engineers - International Petroleum Technology Conference 2012, IPTC 2012 3 (February), 2109–2122. → pages 7, 277
- Bruggeman, D. A. G., 1935. The calculation of various physical constants of heterogeneous substances. I. The dielectric constants and conductivities of mixtures composed of isotropic substances. *Annalen der Physik* 416 (7), 636–664. → pages 13, 37
- Byerlee, J. D., Johnston, M. J., 1976. A magnetic method for determining the geometry of hydraulic fractures. *Pure and Applied Geophysics PAGEOPH* 114 (3), 425–433. → pages 5
- Cannan, C., Bartel, L., Palisch, T., Aldridge, D., 2014. Electrically conductive proppant and methods for detecting, locating and characterizing the electrically conductive proppant. → pages 5
- Carrigan, C. R., Yang, X., LaBrecque, D. J., Larsen, D., Freeman, D., Ramirez, A. L., Daily, W., Aines, R., Newmark, R., Friedmann, J., Hovorka, S., oct 2013. Electrical resistance tomographic monitoring of CO₂ movement in deep geologic reservoirs. *International Journal of Greenhouse Gas Control* 18, 401–408. → pages 194
- Cassiani, G., Bruno, V., Villa, A., Fusi, N., Binley, A. M., 2006. A saline trace test monitored via time-lapse surface electrical resistivity tomography. *Journal of Applied Geophysics* 59 (3), 244–259. → pages 194
- Caudillo-Mata, L., Haber, E., Heagy, L., Schwarzbach, C., 2017a. A framework for the upscaling of the electrical conductivity in the quasi-static Maxwell's equations. *Journal of Computational and Applied Mathematics* 317. → pages 150, 155, 230
- Caudillo-Mata, L. A., Haber, E., Heagy, L. J., Oldenburg, D. W., aug 2014. Numerical upscaling of electrical conductivity: A problem specific approach to generate coarse-scale models. In: SEG Technical Program Expanded Abstracts 2014. No. 4. Society of Exploration Geophysicists, pp. 680–684. → pages 34, 277
- Caudillo-mata, L. A., Haber, E., Heagy, L. J., Schwarzbach, C., 2016. A Framework for the Upscaling of the Electrical Conductivity in the Quasi-static Maxwell 's Equations. (in review), 1–29. → pages 34
- Caudillo-Mata, L. A., Haber, E., Schwarzbach, C., 2017b. An oversampling technique for the multiscale finite volume method to simulate electromagnetic responses in the frequency domain. *Computational Geosciences* 21 (5-6), 963–980. → pages 150
- Cipolla, C., Wallace, J., feb 2014. Stimulated Reservoir Volume: A Misapplied Concept? In: SPE Hydraulic Fracturing Technology Conference. Society of Petroleum Engineers. → pages 3
- Cipolla, C., Warpinski, N., Mayerhofer, M., apr 2008a. Hydraulic Fracture Complexity: Diagnosis Remediation And Exploitation. SPE Asia Pacific Oil and ... (October), 20–22. → pages xviii, 34
- Cipolla, C. L., Lolom, E., Mayerhofer, M. J., Warpinski, N. R., apr 2009. The Effect of Proppant Distribution and Un-Propped Fracture Conductivity on Well Performance in Unconventional Gas Reservoirs. In: SPE Hydraulic Fracturing Technology Conference. Society of Petroleum Engineers. → pages 3
- Cipolla, C. L., Warpinski, N. R., Mayerhofer, M. J., Lolom, E., Vincent, M. C., apr 2008b. The Relationship Between Fracture Complexity, Reservoir Properties, and Fracture Treatment Design. In: SPE Annual Technical Conference and Exhibition. Society of Petroleum Engineers, pp. 1–25. → pages 34
- Claerbout, J. F., Karrenbach, M., jan 1992. Electronic documents give reproducible research a new meaning. In: SEG Technical Program Expanded Abstracts 1992. Society of Exploration Geophysicists, pp. 601–604. → pages 329
- Cockett, A. R. B., 2017. A framework for geophysical inversions with application to vadose zone parameter estimation. Ph.D. thesis, University of British Columbia. → pages 17

- Cockett, R., Heagy, L. J., Oldenburg, D. W., aug 2016a. Pixels and their neighbors : Finite volume. *The Leading Edge* (August), 703–706. → pages 286, 293
- Cockett, R., Heagy, L. J., Oldenburg, D. W., aug 2016b. Pixels and their neighbors: Finite volume. *The Leading Edge* 35 (8), 703–706.
 URL <http://library.seg.org/doi/10.1190/tle35080703.1> → pages 70
- Cockett, R., Kang, S., Heagy, L. J., Pidlisecky, A., Oldenburg, D. W., dec 2015. SimPEG: An open source framework for simulation and gradient based parameter estimation in geophysical applications. *Computers & Geosciences* 85, 142–154. → pages viii, xviii, xlvi, 17, 24, 25, 30, 65, 72, 196, 278, 279, 280, 282, 284, 286, 287, 293
- Coggon, J. H., 1971. Electromagnetic and electrical modeling by the finite element method. *GEOPHYSICS* 36 (1), 132–155. → pages 290, 297, 299
- Commer, M., Hoversten, G. M., Um, E. S., mar 2015. Transient-electromagnetic finite-difference time-domain earth modeling over steel infrastructure. *Geophysics* 80 (2), E147–E162. → pages xxii, 10, 14, 66, 73, 74, 75, 76, 98, 154, 277, 312
- Constable, S. C., Parker, R. L., Constable, C. G., 1987. Models From Electromagnetic Sounding Data. *Geophysics* 52 (3), 289–300. → pages 276
- Cosmin, G., Schenk, O., Lubin, M., Gärtner, K., 2016. An Augmented Incomplete Factorization Approach for Computing the Schur Complement in Stochastic Optimization The MIT Faculty has made this article openly available . Please share how this access benefits you . Your story matters . Citation An Augmented . → pages 74
- Cuevas, N., 2014a. Energizing a Bipole Casing Electromagnetic Source - Sensitivity Analysis. In: 76th EAGE Conference and Exhibition 2014. No. June 2014. pp. 16–19. → pages 312
- Cuevas, N. H., sep 2014b. Analytical solutions of EM fields due to a dipolar source inside an infinite casing. *Geophysics* 79 (5), E231–E241. → pages 10, 277
- Daily, W., Ramirez, A., LaBrecque, D., Nitao, J., may 1992. Electrical resistivity tomography of vadose water movement. *Water Resources Research* 28 (5), 1429–1442. → pages 193, 194
- Devriese, S. G. R., Oldenburg, D. W., 2016. Feasibility of electromagnetic methods to detect and image steam-assisted gravity drainage steam chambers. *Geophysics* 81 (4), E227–E241. → pages 277
- Doetsch, J., Linde, N., Vogt, T., Binley, A., Green, A. G., 2012. Imaging and quantifying salt-tracer transport in a riparian groundwater system by means of 3D ERT monitoring. *Geophysics* 77 (5), B207–B218. → pages 193, 194
- Doll, H., 1949. Introduction to Induction Logging and Application to Logging of Wells Drilled With Oil Base Mud. *Journal of Petroleum Technology* 1 (6). → pages 83
- Durlofsky, L. J., 2003. Upscaling of Geocellular Models for Reservoir Flow Simulation : A Review of Recent Progress. Paper presented at the 7th International Forum on Reservoir Simulation Buhl/Baden-Baden, Germany, June 23-27. → pages 34
- Ekblom, H., sep 1973. Calculation of linear bestL p -approximations. *BIT* 13 (3), 292–300. → pages 200
- Fang, Y., Dai, J., Yu, Z., Zhou, J., Liu, Q. H., 2017. Through-Casing Hydraulic Fracture Evaluation by Induction Logging I: An Efficient em Solver for Fracture Detection. *IEEE Transactions on Geoscience and Remote Sensing* 55 (2), 1179–1188. → pages 154
- GeoSci.xyz, 2018. em.geosci.xyz, 0th Edition. → pages 18
- Griffiths, D. J., 2007. An Introduction to Electrodynamics. Vol. 110. → pages 298
- Griffiths, D. J., Li, Y., 1997. Charge density on a conducting needle.
 URL <http://aapt.scitation.org/doi/10.1119/1.18671> → pages 82, 103, 229
- Haber, E., 2014a. Computational Methods in Geophysical Electromagnetics.
 URL <http://pubs.siam.org/doi/book/10.1137/1.9781611973808> → pages vii, 18, 34, 68, 69, 71, 72, 150

- Haber, E., dec 2014b. Computational Methods in Geophysical Electromagnetics. Society for Industrial and Applied Mathematics, Philadelphia, PA. → pages 24, 276, 282, 286, 288, 290, 294, 297, 298, 299, 316, 318
- Haber, E., Ascher, U. M., 2001. Fast Finite Volume Simulation of 3D Electromagnetic Problems With Highly Discontinuous Coefficients 22 (6), 1943–1961. → pages 276
- Haber, E., Ascher, U. M., Oldenburg, D. W., 2004. Inversion of 3D electromagnetic data in frequency and time domain using an inexact allatonce approach. *Geophysics* 69 (5), 1216–1228.
URL <http://library.seg.org/doi/10.1190/1.1801938> → pages 69
- Haber, E., Heldmann, S., Ascher, U., 2007. Adaptive finite volume method for distributed non-smooth parameter identification. *Inverse Problems* 23 (4), 1659–1676. → pages 14, 66, 73, 150
- Haber, E., Oldenburg, D., 1998. Joint Inversion: A Structural Approach. Unknown 63. → pages 276
- Haber, E., Schwarzbach, C., Shekhtman, R., 2016. Modeling electromagnetic fields in the presence of casing. *SEG Technical Program Expanded Abstracts 2016* (1988), 959–964. → pages 10
- Hashin, Z., Shtrikman, S., 1962. A Variational approach to the theory of the effective magnetic permeability of multiphase materials. *Journal of Applied Physics* 33 (10), 3125–3131. → pages 50
- Hayley, K., Pidlisecky, A., Bentley, L. R., 2011. Simultaneous time-lapse electrical resistivity inversion. *Journal of Applied Geophysics* 75 (2), 401–411. → pages 194
- Heagy, L., Oldenburg, D., Chen, J., 2014a. Where does the proppant go? Examining the application of electromagnetic methods for hydraulic fracture characterization. *Geoconvention.Com*, 1–7. → pages vi
- Heagy, L. J., Cockett, A. R., Oldenburg, D. W., aug 2014b. Parametrized Inversion Framework for Proppant Volume in a Hydraulically Fractured Reservoir. → pages vii, 292
- Heagy, L. J., Cockett, R., Kang, S., Rosenkjaer, G. K., Oldenburg, D. W., 2017a. A framework for simulation and inversion in electromagnetics. *Computers and Geosciences* 107 (July), 1–19.
URL <http://dx.doi.org/10.1016/j.cageo.2017.06.018> → pages viii, 17, 30
- Heagy, L. J., Cockett, R., Oldenburg, D. W., 2017b. Modular electromagnetic simulations with applications to steel cased wells. *Proceedings of the Sixth International Symposium in Three-Dimensional Electromagnetics*, 125–129. → pages vii
- Heagy, L. J., Cockett, R., Oldenburg, D. W., Wilt, M., aug 2015. Modelling electromagnetic problems in the presence of cased wells. In: *SEG Technical Program Expanded Abstracts 2015*. Society of Exploration Geophysicists, pp. 699–703. → pages vii, xlvi, 10, 277, 287, 290, 294, 297, 299, 312, 313
- Heagy, L. J., Oldenburg, D. W., sep 2013. Investigating the potential of using conductive or permeable proppant particles for hydraulic fracture characterization. In: *SEG Technical Program Expanded Abstracts 2013*. Vol. i. Society of Exploration Geophysicists, pp. 576–580. → pages vi
- Heagy, L. J., Oldenburg, D. W., apr 2018. Modeling electromagnetics on cylindrical meshes with applications to steel-cased wells. → pages vii
- Holladay, J. S., West, G. F., 1984. Effect of well casings on surface electrical surveys. *Geophysics* 49 (2), 177–188.
URL <http://library.seg.org/doi/10.1190/1.1441649> → pages 8, 97
- Horesh, L., Haber, E., jan 2011. A Second Order Discretization of Maxwell's Equations in the Quasi-Static Regime on OcTree Grids. *SIAM Journal on Scientific Computing* 33 (5), 2805–2822.
URL <http://epubs.siam.org/doi/10.1137/100798508> → pages 68
- Hoversten, G., Commer, M., Haber, E., Schwarzbach, C., 2014. Hydro-frac Monitoring Using Ground Time-domain EM. In: *76th EAGE Conference and Exhibition*. No. June 2014. pp. 76–78. → pages 277, 312
- Hoversten, G. M., Commer, M., Haber, E., Schwarzbach, C., nov 2015. Hydro-frac monitoring using ground time-domain electromagnetics. *Geophysical Prospecting* 63 (6), 1508–1526. → pages 3, 33, 43, 55, 167, 277, 312

- Hoversten, G. M., Schwarzbach, C., Belliveau, P., Haber, E., Shekhtman, R., 2017. Borehole to Surface Electromagnetic Monitoring of Hydraulic Fractures. In: 79th EAGE Conference and Exhibition 2017. → pages 9, 64, 80, 98
- Hu, Y., Fang, Y., LaBrecque, D., Ahmadian, M., Liu, Q. H., 2018. Reconstruction of high-contrast proppant in hydraulic fractures with galvanic measurements. *IEEE Transactions on Geoscience and Remote Sensing* 56 (4), 2066–2073. → pages 33
- Hunter, J. D., 2007. Matplotlib: A 2D graphics environment. *Computing In Science & Engineering* 9 (3), 90–95. → pages ix, 278
- Hyman, J., Morel, J., Shashkov, M., Steinberg, S., 2002. Mimetic finite difference methods for diffusion equations , 333–352. → pages 286
- Hyman, J. M., Shashkov, M., 1999. Mimetic Discretizations for Maxwell ' s Equations 909, 881–909. → pages 68, 286
- Ingraffea, A. R., Wells, M. T., Santoro, R. L., Shonkoff, S. B. C., 2014. Assessment and risk analysis of casing and cement impairment in oil and gas wells in Pennsylvania, 2000-2012. *Proceedings of the National Academy of Sciences* 111 (30), 10955–10960.
URL <http://www.pnas.org/cgi/doi/10.1073/pnas.1323422111> → pages 100
- Jackson, R. B., Vengosh, A., Darrah, T. H., Warner, N. R., Down, A., Poreda, R. J., Oshborn, S. G., Zhao, K., Karr, J. D., 2013. Increased stray gas abundance in a subset of drkng water wells. *Proceedings of the National Academy of Sciences of the United States of America* 110 (28), 11250–11255. → pages 100
- Jahandari, H., Farquharson, C. G., 2014. A finite-volume solution to the geophysical electromagnetic forward problem using unstructured grids. *Geophysics* 79 (6), E287–E302.
URL <http://library.seg.org/doi/10.1190/geo2013-0312.1> → pages 68
- Johnston, R., Trofimenkoff, F., Haslett, J., jul 1987. Resistivity Response of a Homogeneous Earth with a Finite-Length Contained Vertical Conductor. *IEEE Transactions on Geoscience and Remote Sensing* GE-25 (4), 414–421.
URL <http://ieeexplore.ieee.org/document/4072660/> → pages 8, 97
- Johnston, R. H., Trofimenkoff, F. N., Haslett, J. W., 1992. The Complex Resistivity Response of a Homogeneous Earth with a Finite-Length Contained Vertical Conductor. *IEEE Transactions on Geoscience and Remote Sensing* 30 (1), 46–54. → pages 8
- Jones, E., Oliphant, T., Peterson, P., Others, 2001. {SciPy}: Open source scientific tools for {Python}. → pages ix
- Kalderimis, J., Meyer, M., 2011. Travis CI GmbH. → pages 278, 301
- Kang, S., Cockett, R., Heagy, L. J., Oldenburg, D. W., Facility, G. I., 2015. Moving between dimensions in electromagnetic inversions (2), 5000–5004. → pages 276, 287, 291, 292
- Kaufman, A. A., jan 1990. The electrical field in a borehole with a casing. *Geophysics* 55 (1), 29–38. → pages 8, 15, 64, 66, 76, 77, 79, 80, 95, 99, 123, 141, 152
- Kaufman, A. A., Wightman, E. W., 1993. A transmission-line model for electrical logging through casing. *Geophysics* 58 (12), 1739. → pages xxii, 8, 15, 64, 66, 76, 77, 80, 81, 99, 142, 143, 144, 228
- Kelbert, A., Meqbel, N., Egbert, G. D., Tandon, K., 2014. ModEM: A modular system for inversion of electromagnetic geophysical data. *Computers and Geosciences* 66, 40–53. → pages 276
- Kemna, A., Kulessa, B., Vereecken, H., 2002. Imaging and characterisation of subsurface solute transport using electrical resistivity tomography (ERT) and equivalent transport models. *Journal of Hydrology* 267 (3-4), 125–146. → pages 193
- Kim, H. J., Lee, K. H., 2006. Electromagnetic fields in a non-uniform steel-cased borehole. *Geophysical Prospecting* 54 (4), 433–439. → pages 154
- Kim, J. H., Yi, M. J., Park, S. G., Kim, J. G., 2009. 4-D inversion of DC resistivity monitoring data acquired over a dynamically changing earth model. *Journal of Applied Geophysics* 68 (4), 522–532. → pages 194
- King, G. E., apr 2010. Thirty Years of Gas Shale Fracturing: What Have We Learned? In: SPE Annual Technical Conference and Exhibition. Society of Petroleum Engineers. → pages 5

- Kohnke, C., Liu, L., Streich, R., Swidinsky, A., 2017. A method of moments approach to modeling the electromagnetic response of multiple steel casings in a layered earth. *Geophysics*, 1–72.
 URL <https://library.seg.org/doi/10.1190/geo2017-0303.1> → pages 10, 141
- Kong, F. N., Roth, F., Olsen, P. A., Stalheim, S. O., 2009. Casing effects in the sea-to-borehole electromagnetic method. *Geophysics* 74 (5), F77–F87.
 URL <http://library.seg.org/doi/10.1190/1.3173807> → pages 64, 80, 154
- Labrecque, D., Brigham, R., Liu, Q. H., Fang, Y., Dai, J., Hu, Y., Yu, Z., Kleinhammes, A., Doyle, P., Wu, Y., 2016. SPE-179170-MS Remote Imaging of Proppants in Hydraulic Fracture Networks Using Electromagnetic Methods: Results of Small-Scale Field Experiments, 9–11. → pages 33
- LaBrecque, D. J., Yang, X., 2000. Difference Inversion of ERT Data : A Fast Inversion Method For 3-D IN-Situ Monitoring. *Eegs* 0 (m), 907–914. → pages 194
- Landauer, R., 1952. The electrical resistance of binary metallic mixtures. *Journal of Applied Physics* 23 (7), 779–784. → pages 37
- Landauer, R., 1978. Electrical conductivity in inhomogeneous media. *AIP Conference Proceedings* 40 (1978), 2–45. → pages 37
- Lee, K. H., Kim, H. J., Song, Y., 1998. Electromagnetic Method for Analyzing the Property of steel casing. Lawrence Berkeley National Laboratory. → pages 154
- Lee, K. H., Kim, H. J., Uchida, T., 2005. Electromagnetic fields in a steel-cased borehole. *Geophysical Prospecting* 53 (1), 13–21. → pages 154
- Li, M., Abubakar, A., Habashy, T. M., 2010. Application of a two-and-a-half dimensional model-based algorithm to crosswell electromagnetic data inversion. *Inverse Problems* 26 (7), 074013.
 URL <http://stacks.iop.org/0266-5611/26/i=7/a=074013> → pages 291
- Li, Y., Key, K., 2007. 2D marine controlled-source electromagnetic modeling: Part 1 An adaptive finite-element algorithm. *GEOPHYSICS* 72 (2), WA51–WA62. → pages 276
- Loke, M. H., jan 2001. Constrained TimeLapse Resistivity Imaging Inversion. In: *Symposium on the Application of Geophysics to Engineering and Environmental Problems 2001*. Environment and Engineering Geophysical Society, pp. EEM7–EEM7. → pages 194
- Loke, M. H., Dahlin, T., Rucker, D. F., 2014. Smoothness-constrained time-lapse inversion of data from 3D resistivity surveys. *Near Surface Geophysics* 12 (1), 5–24. → pages 194
- Marion, B. P., Zhang, P., Safdar, M., Wilt, M., Loh, F. F. H., Nalonnal, A., 2011. Crosswell Technologies: New Solutions for Enhanced Reservoir Surveillance. *SPE Enhanced Oil Recovery Conference SPE 144271*, 1–9. → pages 195
- Marsala, A. F., Al-Buali, M., Zaki Ali, Ma, S. M., He, Z., Biyan, T., Guo, Z., He, T., apr 2011. First Borehole to Surface Electromagnetic Survey in KSA: Reservoir Mapping and Monitoring at a New Scale. In: *SPE Annual Technical Conference and Exhibition*. Society of Petroleum Engineers, p. SPE 146348. → pages 5
- Marsala, A. F., Al-Ruwaili, S. B., Shouxiang, M. M., Al-Ali, Z. A., Al-Buali, M. H., Donadille, J.-M., Crary, S. F., Wilt, M., apr 2008. Crosswell Electromagnetic Tomography: from Resistivity Mapping to Interwell Fluid Distribution. In: *International Petroleum Technology Conference*. International Petroleum Technology Conference, pp. 1–6. → pages 5
- Marsala, A. F., Hibbs, A. D., Morrison, H. F., dec 2014. Evaluation of Borehole Casing Sources for Electromagnetic Imaging of Deep Formations. In: *International Petroleum Technology Conference*. International Petroleum Technology Conference. → pages 5
- Marsala, A. F., Lyngra, S., Aramco, S., Safdar, M., Zhang, P., Wilt, M., 2015. Crosswell electromagnetic induction between two widely spaced horizontal wells : Coiled-tubing conveyed data collection and 3D inversion from a carbonate reservoir in Saudi Arabia, 2848–2852. → pages 55, 277, 312
- Marsala*, A. F., Lyngra, S., Safdar, M., Zhang, P., Wilt, M., aug 2015. Crosswell electromagnetic induction between two widely spaced horizontal wells: Coiled-tubing conveyed data collection and 3D inversion from a carbonate reservoir in Saudi Arabia. In: *SEG Technical Program Expanded Abstracts 2015*. Society of Exploration Geophysicists, pp. 2848–2852. → pages 55, 57

- Maxwell, J. C., 1873. A Treatise on Electricity and Magnetism, Vol.1. Clarendon Press (Oxford). → pages 36
- Maxwell, S., 2014. Microseismic Imaging of Hydraulic Fracturing : Improved Engineering of Unconventional Shale Reservoirs. No. 17. → pages 2
- Maxwell, S., Urbancic, T., Steinsberger, N., Zinno, R., sep 2002. Microseismic Imaging of Hydraulic Fracture Complexity in the Barnett Shale. In: Proceedings of SPE Annual Technical Conference and Exhibition. Society of Petroleum Engineers, pp. 1–9. → pages 3
- Mayerhofer, M. J., Lolom, E., Warpinski, N. R., Cipolla, C. L., Walser, D. W., Rightmire, C. M., 2010. What Is Stimulated Reservoir Volume? SPE Production & Operations 25 (01), 89–98. → pages 3
- McMillan, M. S., Oldenburg, D. W., Haber, E., Christoph, 2015a. Parametric 3D inversion of airborne time domain electromagnetics. 24th International Geophysical Conference and Exhibition, 1–5. → pages 198, 276
- McMillan, M. S., Schwarzbach, C., Haber, E., Oldenburg, D. W., 2015b. 3D parametric hybrid inversion of time-domain airborne electromagnetic data. Geophysics 80 (6), K25–K36. → pages 276, 291, 316
- McMillan, M. S. G., 2017. Cooperative and parametric strategies for 3D airborne electromagnetic inversion (April). → pages 198, 199, 200
- Merwin, N., Donahoe, L., Mcangus, E., 2015. Coveralls. → pages 278
- Miller, C. R., Routh, P. S., Brosten, T. R., McNamara, J. P., may 2008. Application of time-lapse ERT imaging to watershed characterization. GEOPHYSICS 73 (3), G7–G17. → pages 194
- Milton, G. W., 1985. The coherent potential approximation is a realizable effective medium scheme. Communications in Mathematical Physics 99 (4), 463–500. → pages 37
- Milton, G. W., 2002. The Theory of Composites. Cambridge University Press, Cambridge. → pages 35, 36
- Moran, J. H., Kunz, K. S., dec 1962. Basic theory of induction logging and application to study of two-coil sondes. GEOPHYSICS 27 (6), 829–858.
URL <http://library.seg.org/doi/10.1190/1.1439108> → pages 83
- Munday, T. J., Doble, R., Berens, V., Fitzpatrick, A., 2006. The Application of Air, Ground and In River' Electromagnetics in the Definition of Spatial Patterns of Groundwater Induced Salt Accumulation in a Salinising Floodplain, Lower River Murray, South Australia. Symposium on the Application of Geophysics to Engineering and Environmental Problems, 886–891. → pages 306, 311
- Nekut, A. G., 1995. Crosswell electromagnetic tomography in steelcased wells. Geophysics 60 (3), 912–920.
URL <http://library.seg.org/doi/10.1190/1.1443826> → pages 9
- Newman, G. A., Alumbaugh, D. L., jan 1999. 20. Electromagnetic Modeling and Inversion on Massively Parallel Computers. Society of Exploration Geophysicists, Ch. 20, pp. 299–321. → pages 276
- Nocedal, J., Wright, S. J., 1999. Numerical Optimization, 2nd Edition. Springer, New York. → pages 28
- Novotny, E., 1977. Proppant Transport. SPE Annual Fall Technical Conference and Exhibition. → pages 43, 55
- Oldenborger, G. a., Knoll, M. D., Routh, P. S., LaBrecque, D. J., 2007. Time-lapse ERT monitoring of an injection/withdrawal experiment in a shallow unconfined aquifer. Geophysics 72 (4), F177–F187. → pages 194
- Oldenburg, D. D. W., Li, Y., jan 2005a. Inversion for applied geophysics: A tutorial. Investigations in geophysics 13, 1–85. → pages 276, 281, 282
- Oldenburg, D. W., Haber, E., Shekhtman, R., 2013. Three dimensional inversion of multisource time domain electromagnetic data. Geophysics 78 (1), E47–E57. → pages 288
- Oldenburg, D. W., Heagy, L. J., Kang, S., 2017. Geophysical Electromagnetics: Fundamentals and Applications. SEG Distinguished Instructor Short Course.
URL <https://seg.org/Education/Courses/DISC/2017-DISC-Doug-Oldenburg> → pages 63

- Oldenburg, D. W., Li, Y., jan 2005b. 5. Inversion for Applied Geophysics: A Tutorial. In: Butler, D. K. (Ed.), Near-Surface Geophysics. Vol. 13. Society of Exploration Geophysicists, pp. 89–150. → pages 24, 25, 27
- Oliphant, T. E., may 2007. Python for Scientific Computing. Computing in Science Engineering 9 (3), 10–20. → pages 278, 295, 334
- Osborn, S. G., Vengosh, A., Warner, N. R., Jackson, R. B., 2011. Methane contamination of drinking water accompanying gas-well drilling and hydraulic fracturing. Proceedings of the National Academy of Sciences 108 (37), E665–E666. → pages 100
- Overton, I. C., Jolly, I. D., Slavich, P. G., Lewis, M. M., Walker, G. R., 2004. Modelling vegetation health from the interaction of saline groundwater and flooding on the Chowilla floodplain, South Australia. Australian Journal of Botany 54 (2), 207–220. → pages 306
- Palisch, T., Al-Tailji, W., Bartel, L., Cannan, C., Czapski, M., Lynch, K., 2016. Recent Advancements in Far-Field Proppant Detection. SPE Hydraulic Fracturing Technology Conference. → pages 3
- Pardo, D., Torres-Verdin, C., 2013. Sensitivity analysis for the appraisal of hydrofractures in horizontal wells with borehole resistivity measurements. Geophysics 78 (4), D209–D222. → pages 10, 33, 42, 64, 277
- Park, S., 1998. Fluid migration in the vadose zone from 3-D inversion of resistivity monitoring data. Geophysics 63 (1), 41–51. → pages 194
- Parker, R. L., aug 1980. The inverse problem of electromagnetic induction: Existence and construction of solutions based on incomplete data. Journal of Geophysical Research: Solid Earth 85 (B8), 4421–4428. → pages 276
- Parker, R. L., 1994a. Geophysical inverse theory. Princeton university press. → pages 26, 28
- Parker, R. L., 1994b. Geophysical inverse theory. Princeton university press. → pages 281
- Perez, F., Berkeley, L., Granger, B. E., 2015. Project Jupyter : Computational Narratives as the Engine of Collaborative Data Science (April), 1–24. → pages ix, 65, 326, 331
- Petra, C. G., Schenk, O., Anitescu, M., 2014. Real-time stochastic optimization of complex energy systems on high-performance computers. Computing in Science and Engineering 16 (5), 32–42. → pages 74
- Pidlisecky, A., Singha, K., Day-Lewis, F. D., 2011. A distribution-based parametrization for improved tomographic imaging of solute plumes. Geophysical Journal International 187 (1), 214–224. → pages 276, 291
- Project Jupyter, Bussonnier, M., Forde, J., Freeman, J., Granger, B., Head, T., Holdgraf, C., Kelley, K., Nalvarate, G., Osheroff, A., Pacer, M., Panda, Y., Perez, F., Ragan-Kelley, B., Willing, C., 2018. Binder 2.0 - Reproducible, interactive, sharable environments for science at scale (Scipy), 113–120. → pages 326, 332
- Puzyrev, V., Vilamajo, E., Queralt, P., Ledo, J., Marcuello, A., 2017. Three-Dimensional Modeling of the Casing Effect in Onshore Controlled-Source Electromagnetic Surveys. Surveys in Geophysics 38 (2), 527–545. → pages 10, 141, 154
- Rahmani, A. R., Athey, A. E., Chen, J., Wilt, M. J., 2014. Sensitivity of dipole magnetic tomography to magnetic nanoparticle injectates. Journal of Applied Geophysics 103, 199–214. → pages 33
- Ramirez, A., Daily, W., Binley, A., LaBrecque, D., Roelant, D., 1996. Detection of Leaks in Underground Storage Tanks Using Electrical Resistance Methods. Journal of Environmental and Engineering Geophysics 1 (3), 189–203.
URL <http://library.seg.org/doi/abs/10.4133/JEEG1.3.189> → pages 9, 98
- Rivera Rios, A., 2014. Multi-order Vector Finite Element Modelling of 3D Magnetotelluric Data including complex geometry and anisotropic earth. Ph.D. thesis, The University of Adelaide. → pages 294
- Rocroi, J. P., Koulakov, A. V., feb 1985. The use of vertical line sources in electrical prospecting for hydrocarbon. Geophysical Prospecting 33 (1), 138–152.
URL <http://doi.wiley.com/10.1111/j.1365-2478.1985.tb00426.x> → pages 9
- Ronczka, M., Rücker, C., Günther, T., 2015. Numerical study of long-electrode electric resistivity tomography Accuracy, sensitivity, and resolution. Geophysics 80 (6), E317–E328. → pages 9, 98

- Rucker, D. F., 2012. Enhanced resolution for long electrode ERT. *Geophysical Journal International* 191 (1), 101–111. → pages 9, 98, 195
- Rucker, D. F., Loke, M. H., Levitt, M. T., Noonan, G. E., 2010. Electrical-resistivity characterization of an industrial site using long electrodes. *Geophysics* 75 (4), WA95. → pages 9, 98
- Rule, A., Tabard, A., Hollan, J. D., 2018. Exploration and Explanation in Computational Notebooks. Proceedings of the 2018 CHI Conference on Human Factors in Computing Systems - CHI '18, 1–12. → pages 332
- Schenkel, C., 1991. The Electrical Resistivity Method in Cased Boreholes. PhD Thesis, Lawrence Berkeley National Laboratory LBL-31139. → pages 99, 114, 121, 143, 228
- Schenkel, C. J., Morrison, H. F., aug 1990. Effects of well casing on potential field measurements using downhole current sources. *Geophysical Prospecting* 38 (6), 663–686. → pages 8, 99, 124
- Schenkel, C. J., Morrison, H. F., 1994. Electrical resistivity measurement through metal casing. *Geophysics* 59 (7), 1072–1082. → pages 8, 80, 81, 98, 99, 125, 139, 167
- Schwarzbach, C., Haber, E., 2018. Improved upscaling of steel-cased wells through inversion. SEG Technical Program Expanded Abstracts 2018, 888–892. → pages 155
- Singha, K., Gorelick, S. M., 2005. Saline tracer visualized with three-dimensional electrical resistivity tomography: Field-scale spatial moment analysis. *Water Resources Research* 41 (5), 1–17. → pages 193
- Singha, K., Gorelick, S. M., 2006. Effects of spatially variable resolution on field-scale estimates of tracer concentration from electrical inversions using Archie's law. *Geophysics* 71 (3), G83–G91. → pages 194
- Slater, L., Binley, A., Versteeg, R., Cassiani, G., Birken, R., Sandberg, S., 2002. A 3D ERT study of solute transport in a large experimental tank. *Journal of Applied Geophysics* 49 (4), 211–229. → pages 193
- Smith, M., Holman, G., Fast, C., Covlin, R., 1978. The Azimuth of Deep, Penetrating Fractures in The Wattenberg Field. *Journal of Petroleum Technology* 30, 185–193. → pages 6
- Sørensen, K. I., Auken, E., 2004. SkyTEM-a new high-resolution helicopter transient electromagnetic system. *Exploration Geophysics* 35 (3), 191–199. → pages 307
- Swidinsky, A., Edwards, R. N., Jegen, M., 2013. The marine controlled source electromagnetic response of a steel borehole casing: Applications for the NEPTUNE Canada gas hydrate observatory. *Geophysical Prospecting* 61 (4), 842–856. → pages 10, 16, 64, 141, 154
- Telford, W. M., Geldart, L. P., Sheriff, R. E., 1990a. *Applied geophysics*. Vol. 1. Cambridge university press. → pages 19, 33, 101
- Telford, W. M., Geldart, L. P., Sheriff, R. E., 1990b. *Applied geophysics*. Vol. 1. Cambridge university press. → pages 282
- Tietze, K., Ritter, O., Veeken, P., 2015. Controlled-source electromagnetic monitoring of reservoir oil saturation using a novel borehole-to-surface configuration. *Geophysical Prospecting* 63 (6), 1468–1490. → pages 64
- Tikhonov, A. N., Arsenin, V. Y., 1977. Solutions of Ill-Posed Problems. *SIAM Review* 32, 1320–1322. → pages 276
- Tøndel, R., Schütt, H., Dümmong, S., Ducrocq, A., Godfrey, R., Labrecque, D., Nutt, L., Campbell, A., Rufino, R., 2014. Reservoir monitoring of steam-assisted gravity drainage using borehole measurements. *Geophysical Prospecting* 62 (4), 760–778. → pages 194, 195
- Torquato, S., 2002. *Random Heterogeneous Materials: Microstructure and Macroscopic Properties*. Vol. 16. Springer. → pages 35, 36, 37, 39, 49, 50
- Uchida, T., Lee, K. H., Wilt, M. J., 1991. Effect of a steel casing on crosshole EM measurement. SEG Technical Program Expanded Abstracts 1991, 442–445.
URL <http://library.seg.org/doi/abs/10.1190/1.1889151> → pages 8
- Um, E. S., Commer, M., Newman, G. A., Hoversten, G. M., jun 2015. Finite element modelling of transient electromagnetic fields near steel-cased wells. *Geophysical Journal International* 202 (2), 901–913. → pages 10, 15, 64, 80, 82, 98, 141, 144, 154, 277, 312

- van der Walt, S., Colbert, S. C., Varoquaux, G., mar 2011. The NumPy Array: A Structure for Efficient Numerical Computation. Computing in Science Engineering 13 (2), 22–30. → pages ix, 278
- Van Rossum, G., Drake Jr, F. L., 1995. Python reference manual. Centrum voor Wiskunde en Informatica Amsterdam. → pages 65
- Vengosh, A., Jackson, R. B., Warner, N., Darrah, T. H., Kondash, A., aug 2014. A Critical Review of the Risks to Water Resources from Unconventional Shale Gas Development and Hydraulic Fracturing in the United States. Environmental Science & Technology 48 (15), 8334–8348. → pages 5
- Viezzoli, A., Auken, E., Munday, T., 2009. Spatially constrained inversion for quasi 3D modeling of airborne electromagnetic data - an application for environmental assessment in the Lower Murray Region of South Australia. Exploration Geophysics 40 (2008), 173–183. → pages 307
- Viezzoli, A., Munday, T., Auken, E., Christiansen, A. V., 2010. Accurate quasi 3D versus practical full 3D inversion of AEM data {‐} the Bookpurnong case study. Preview 2010 (149), 23–31. → pages 307, 311
- Wait, J., Hill, D., apr 1977. Electromagnetic Shielding of Sources within a Metal-Cased Bore Hole. IEEE Transactions on Geoscience Electronics 15 (2), 108–112.
URL <http://ieeexplore.ieee.org/lpdocs/epic03/wrapper.htm?arnumber=4071844> → pages 83
- Wait, J. R., 1983. Resistivity Response of a Homogeneous Earth with a Contained Vertical Conductor (1). → pages 8, 97
- Wait, J. R., Williams, J. T., aug 1985. EM AND IP RESPONSE OF A STEEL WELL CASING FOR A FOURELECTRODE SURFACE ARRAY. PART I: THEORY. Geophysical Prospecting 33 (5), 723–735.
URL <http://doi.wiley.com/10.1111/j.1365-2478.1985.tb00775.x> → pages 8, 154
- Ward, S. H., Hohmann, G. W., 1988. Electromagnetic Theory for Geophysical Applications. In: Electromagnetic Methods in Applied Geophysics, 1st Edition. Society of Exploration Geophysicists, Ch. 4, pp. 130–311. → pages 18, 213, 282
- Warpinski, N. R., oct 1996. Hydraulic Fracture Diagnostics. Journal of Petroleum Technology 48 (10), 907–910. → pages 3
- Weiss, C. J., 2017. Finite-element analysis for model parameters distributed on a hierarchy of geometric simplices. Geophysics 82 (4), E155–E167. → pages 10
- Weiss, C. J., Aldridge, D. F., Knox, H. A., Schramm, K. A., Bartel, L. C., aug 2015. The DC response of electrically conducting fractures excited by a grounded current source. SEG Technical Program Expanded Abstracts 2015 81 (3), 930–936. → pages 33, 42, 196, 312
- Weiss, C. J., Aldridge, D. F., Knox, H. A., Schramm, K. A., Bartel, L. C., 2016. The direct-current response of electrically conducting fractures excited by a grounded current source. Geophysics 81 (3), E201–E210.
URL <http://library.seg.org/doi/10.1190/geo2015-0262.1> → pages 9, 10, 64, 80, 82, 98, 141, 150
- Wiener, O., 1912. Die Theorie des Mischkörpers für das Feld der stationären Stromung. Abhandlungen der Sachsischen Gesellschaft der Akademischen Wissenschaften in Mathematik und Physik 32, 507—604. → pages 49
- Williams, J. T., Wait, J. R., aug 1985. EM and IP response of a steel well casing for a four-electrode surface array. Part II: Numerical results. Geophysical Prospecting 33 (5), 736–745.
URL <http://doi.wiley.com/10.1111/j.1365-2478.1985.tb00776.x> → pages 8, 154
- Wilson, G. A., Cox, L. H., Zhdanov, M. S., 2010. Practical 3D inversion of entire airborne electromagnetic surveys. Preview (146), 29–33. → pages 307
- Wilt, M., 2003. Oil Reservoir Characterization and CO₂ injection monitoring in the Permeable Basing with crosswell electromagnetic imaging. Tech. rep. → pages 57
- Wilt, M., Cuevas, N., Heagy, L., 2015. Determining Proppant and Fluid Distribution, US 2015/0083404 A1. → pages vi
- Wilt, M., Heagy, L., Chen, J., 2014. Hydrofracture mapping and monitoring with borehole electromagnetic (EM) methods. In: 76th European Association of Geoscientists and Engineers Conference and Exhibition 2014: Experience the Energy - Incorporating SPE EUROPEC 2014. → pages vi

- Wilt, M., Lee, K. H., Becker, A., Spies, B., Wang, S., jan 1996. Crosshole EM in steelcased boreholes. In: SEG Technical Program Expanded Abstracts 1996. Society of Exploration Geophysicists, pp. 230–233.
 URL <http://library.seg.org/doi/abs/10.1190/1.1826605> → pages 8, 154, 195
- Wilt, M., Little, J., Zhang, P., Chen, J., Morea, M., jan 2005. Using crosswell EM to track waterflooding at the Lost Hills oil field. In: SEG Technical Program Expanded Abstracts 2005. Society of Exploration Geophysicists, pp. 1269–1272. → pages 195
- Wilt, M., Nieuwenhuis, G., MacLennan, K., Um, E., 2018a. Casing-integrity mapping using top-casing electrodes and surface-based EM fields. pp. 858–862. → pages 9
- Wilt, M., Schenkel, C., Daley, T., Peterson, J., Majer, E., Murer, A. S., Johnston, R. M., Klonsky, L., 1997. Mapping Steam and Water Flow in Petroleum Reservoirs. SPE Reservoir Engineering 12 (November), 284–287. → pages 55, 195
- Wilt, M., Um, E., Weiss, C., Vasco, D., Petrov, P., Newman, G., Wu, Y., 2018b. Wellbore Integrity Assessment with Casing-Based Advanced Sensing (Figure 1), 1–7. → pages 9, 15
- Wilt, M., Zhang, P., Maeki, J., Netto, P., Queiroz, J. L. S., Santos, J. B., Oliveira, V., 2012. Monitoring a Water Flood of Moderate Saturation Changes with Crosswell Electromagnetics (EM): A Case Study from Dom Joao Brazil. SEG Technical Program Expanded Abstracts 2012, 1–5. → pages 55, 195
- Wilt, M. J., Alumbaugh, D. L., Morrison, H. F., Becker, A., Lee, K. H., DeszczPan, M., may 1995. Crosswell electromagnetic tomography: System design considerations and field results. Geophysics 60 (3), 871–885. → pages 5, 21, 54, 57
- Wright, C., Davis, E., Weijers, L., Golich, G., Ward, J., Demetrius, S., Minner, W., apr 1998. Downhole Tiltmeter Fracture Mapping: A New Tool for Directly Measuring Hydraulic Fracture Dimensions. In: SPE Annual Technical Conference and Exhibition. Society of Petroleum Engineers, pp. 585–597. → pages 3
- Wu, X., Habashy, T. M., mar 1994. Influence of steel casings on electromagnetic signals. Geophysics 59 (3), 378–390. → pages 7, 12, 64, 154, 277, 312
- Yang, D., 2017. Airborne electromagnetic data inversion for floodplain salinization investigation at Bookpurnong, South Australia. → pages 307, 311
- Yang, D., Oldenburg, D. W., 2016. Survey decomposition : A scalable framework for 3D controlled-source electromagnetic inversion. Geophysics 81 (2), E69–E87. → pages 10, 14, 73, 114, 139, 141
- Yang, D., Oldenburg, D. W., Haber, E., 2014. 3-D inversion of airborne electromagnetic data parallelized and accelerated by local mesh and adaptive soundings. Geophysical Journal International 196 (3), 1492–1507. → pages 96, 276
- Yang, D., Oldenburg, D. W., Heagy, L. J., sep 2016. 3D DC resistivity modeling of steel casing for reservoir monitoring using equivalent resistor network. SEG Technical Program Expanded Abstracts 2016, 932–936. → pages 312
- Yee, K., may 1966. Numerical solution of initial boundary value problems involving maxwell's equations in isotropic media. IEEE Transactions on Antennas and Propagation 14 (3), 302–307. → pages 68, 276, 286
- Zawadzki, J., Bogacki, J., 2016. Smart magnetic markers use in hydraulic fracturing. Chemosphere 162, 23–30. → pages 32, 33
- Zhang, P., Brick, Y., Sharma, M. M., 2018. Numerical study of an electrode-based resistivity tool for fracture diagnostics in steel-cased wellbores 83 (2). → pages 9, 64
- Zhang, P., Shiriyev, J., Torres-Verdín, C., Sharma, M. M., Brick, Y., Massey, J. W., Yilmaz, A. E., 2016. Fracture diagnostics using a low-frequency electromagnetic induction method. 50th ARMA US Rock Mechanics/Geomechanics Symp., 1–10.
 URL <https://www.onepetro.org/conference-paper/ARMA-2016-862> → pages 48, 61

Appendix A

Source code

The source-code for each chapter is available as a stand-alone repository on GitHub and has additionally been archived with digital-object-identifier (DOI). Here, we provide a summary of where each code can be accessed and where the archive is:

- **Chapter 2:**

- GitHub: <https://github.com/simpeg-research/heagy-2018-fracture-physprops>
- DOI: 10.5281/zenodo.1434456

- **Chapter 3:**

- GitHub: <https://github.com/simpeg-research/heagy-2018-emcyl>
- DOI: 10.5281/zenodo.1220427

- **Chapter 4:**

- GitHub: <https://github.com/simpeg-research/heagy-2018-dc-casing>
- DOI: 10.5281/zenodo.1324543

- **Chapter 5:**

- GitHub: <https://github.com/simpeg-research/heagy-2018-em-casing>
- DOI: 10.5281/zenodo.1434454

- **Chapter 6:**

- GitHub: <https://github.com/simpeg-research/heagy-2018-injection-inversions>
- DOI: 10.5281/zenodo.1434458

- **Appendix D:**

- GitHub: <https://github.com/simpeg-research/heagyetal-2017-simpegem>
- DOI: 10.5281/zenodo.1434469

Appendix B

Concentric spheres in a uniform electrostatic field

Coating proppant particles with a conductive material is one potential strategy for generating an electrically conductive proppant pack. In this appendix, we work through a derivation of the electric potential outside of two concentric spheres in the presence of a uniform electrostatic field. Using this solution, we estimate an effective electrical conductivity of a composite particle.

B.1 Setup

The set-up is shown in Figure B.1

- primary electric field $\mathbf{E}_0 = E_0 \hat{x}$
- background conductivity σ_0 ,
- outer shell conductivity σ_1 and radius R_1
- inner sphere conductivity σ_2 and radius R_2

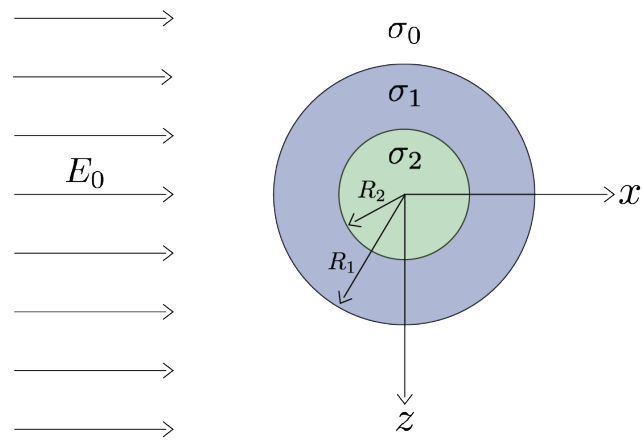


Figure B.1: Problem setup. Concentric spheres in a uniform electric field.

The basic equations are

$$\nabla \times \mathbf{E} = 0 \quad (\text{B.1})$$

$$\nabla \times \mathbf{H} = \mathbf{J} \quad (\text{B.2})$$

$$\mathbf{J} = \sigma \mathbf{E} \quad (\text{B.3})$$

By equation B.1, we can express \mathbf{E} as a gradient of a potential

$$\mathbf{E} = -\nabla V \quad (\text{B.4})$$

and combining equations B.1, B.2 and B.3, we see

$$\nabla \times \mathbf{H} = -\sigma \nabla V$$

Taking the divergence gives

$$0 = -\nabla \cdot \sigma \nabla V$$

and in a region with constant σ

$$\nabla^2 V = 0 \quad (\text{B.5})$$

At each of the conductivity interfaces, we have continuity of the normal component of the current density, and continuity of the electric potential. Continuity of the normal current density gives

$$\sigma_0 \frac{\partial V_0}{\partial r} = \sigma_1 \frac{\partial V_1}{\partial r} \quad \text{at } r = R_1 \quad (\text{B.6})$$

$$\sigma_1 \frac{\partial V_1}{\partial r} = \sigma_2 \frac{\partial V_2}{\partial r} \quad \text{at } r = R_2 \quad (\text{B.7})$$

Continuity of the potential gives

$$V_0 = V_1 \quad \text{at } r = R_1 \quad (\text{B.8})$$

$$V_1 = V_2 \quad \text{at } r = R_2 \quad (\text{B.9})$$

B.2 Solving for the Potential

The primary potential is given by

$$E_0 \hat{x} = -\frac{\partial V^P}{\partial x} \hat{x} \Rightarrow E_0 = -\frac{\partial V^P}{\partial x}$$

By integrating in x and setting the reference point to $V^P(r = 0) = 0$, we see

$$\begin{aligned} \int_0^x E_0 dx &= - \int_0^x \frac{\partial V^P}{\partial x} dx \\ E_0 x &= -V^P \end{aligned}$$

which gives a primary potential of

$$V^P = E_0 x = E_0 r \cos \theta \quad (\text{B.10})$$

In spherical coordinates, the Laplace equation, equation B.5, is given by

$$\left(\frac{\partial}{\partial r} \left(r^2 \frac{\partial}{\partial r} \right) + \frac{1}{\sin \theta} \frac{\partial}{\partial \theta} \left(\sin \theta \frac{\partial}{\partial \theta} \right) + \frac{1}{\sin^2 \theta} \frac{\partial^2}{\partial \phi^2} \right) V(r, \theta, \phi) = 0$$

by symmetry, $V = V(r, \theta)$, so the above equation simplifies to:

$$\left(\frac{\partial}{\partial r} \left(r^2 \frac{\partial}{\partial r} \right) + \frac{1}{\sin \theta} \frac{\partial}{\partial \theta} \left(\sin \theta \frac{\partial}{\partial \theta} \right) \right) V(r, \theta) = 0 \quad (\text{B.11})$$

which has general solution

$$V = \sum_{n=0}^{\infty} \left(A_n r^n + \frac{B_n}{r^{n+1}} \right) P_n(\cos \theta) \quad (\text{B.12})$$

B.2.1 Solving for the coefficients

Regarding notation, on the coefficients A, B the subscript denotes the order of the Legendre polynomial and the superscript denotes the region where that coefficient is applicable (i.e. 0: outside the sphere, 1: in the shell, 2: in the inner sphere). On the radius, R , the subscript denotes the region (1: outer shell, 2: inner sphere), while the superscript is an exponent.

Outside the sphere

Outside the spheres ($r > R_1$), we require that $V \Rightarrow V^P$ for $r \gg R_1$

$$V_0 = A_0^0 + A_1^0 r \cos \theta + \sum_{n=2}^{\infty} A_n^0 r^n P_n(\cos \theta) + \sum_{n=0}^{\infty} \frac{B_n^0}{r^{n+1}} P_n(\cos \theta)$$

for $r \gg R_1$

$$V_0 \Rightarrow A_0^0 + A_1^0 r \cos \theta + \sum_{n=2}^{\infty} A_n^0 r^n P_n(\cos \theta) + \sum_{n=0}^{\infty}$$

Since the Legendre polynomials, $P_n(\cos \theta)$, are orthogonal, then $A_0^0, A_n^0 = 0 \ \forall n$, and

$A_1^0 = -E_0$. So

$$V_0 = -E_0 r \cos \theta + \sum_{n=0}^{\infty} \frac{B_n^0}{r^{n+1}} P_n(\cos \theta) \quad (\text{B.13})$$

In the outer shell

In the outer shell ($R_2 < r < R_1$)

$$V_1 = \sum_{n=0}^{\infty} \left(A_n^1 r^n + \frac{B_n^1}{r^{n+1}} \right) P_n(\cos \theta) \quad (\text{B.14})$$

Using the interface condition in equation B.8, we have

$$\begin{aligned} -E_0 R_1 \cos \theta + \sum_{n=0}^{\infty} \left(\frac{B_n^0}{R_1^{n+1}} \right) P_n(\cos \theta) &= \sum_{n=0}^{\infty} \left(A_n^1 R_1^n + \frac{B_n^1}{R_1^{n+1}} \right) P_n(\cos \theta) \\ -E_0 R_1 \cos \theta + \frac{B_0^0}{R_1} + \frac{B_1^0}{R_1^2} \cos \theta + \sum_{n=2}^{\infty} \left(\frac{B_n^0}{R_1^{n+1}} \right) P_n(\cos \theta) &= A_0^1 + A_1^1 R_1 \cos \theta + \frac{B_0^1}{R_1} + \frac{B_1^1}{R_1^2} \cos \theta + \sum_{n=2}^{\infty} \left(A_n^1 R_1^n + \frac{B_n^1}{R_1^{n+1}} \right) P_n(\cos \theta) \end{aligned}$$

which must hold for all θ . Thus, we can break this up in to a series of smaller equations.

For the $n = 0$ polynomials, we have

$$\begin{aligned} \frac{B_0^0}{R_1} &= A_0^1 + \frac{B_0^1}{R_1} \\ \Rightarrow B_0^0 &= R_1 A_0^1 + B_0^1 \end{aligned} \tag{B.15}$$

For the $n = 1$ polynomials, we have

$$\begin{aligned} -E_0 R_1 + \frac{B_1^0}{R_1^2} &= A_1^1 R_1 + \frac{B_1^1}{R_1^2} \\ \Rightarrow -E_0 R_1^3 + B_1^0 &= A_1^1 R_1^3 + B_1^1 \end{aligned} \tag{B.16}$$

and for $n \geq 2$ (using orthogonality of $P_n(\cos \theta)$)

$$\begin{aligned} \frac{B_n^0}{R_1^{n+1}} &= A_n^1 R_1^n + \frac{B_n^1}{R_1^{n+1}} \\ \Rightarrow B_n^0 &= A_n^1 R_1^{2n+1} + B_n^1 \end{aligned} \tag{B.17}$$

Next, we look to the interface conditions on the derivative of the potential, as described in equation B.6. We first find the derivatives of V_0 , V_1 with respect to r :

$$\frac{\partial V_0}{\partial r} = -E_0 \cos \theta + \sum_{n=0}^{\infty} -(n+1) \frac{B_n^0}{r^{n+2}} P_n(\cos \theta) \tag{B.18}$$

$$\frac{\partial V_1}{\partial r} = \sum_{n=1}^{\infty} n A_n^1 r^{n-1} P_n(\cos \theta) + \sum_{n=0}^{\infty} -(n+1) \frac{B_n^1}{r^{n+2}} P_n(\cos \theta) \tag{B.19}$$

Imposing the interface in equation B.6, we have,

$$\begin{aligned} -\sigma_0 E_0 \cos \theta + \sigma_0 \sum_{n=0}^{\infty} -(n+1) \frac{B_n^0}{R_1^{n+2}} P_n(\cos \theta) \\ = \sigma_1 \sum_{n=1}^{\infty} n A_n^1 R_1^{n-1} P_n(\cos \theta) + \sigma_1 \sum_{n=0}^{\infty} -(n+1) \frac{B_n^1}{R_1^{n+2}} P_n(\cos \theta) \end{aligned}$$

Breaking out coefficients up to $n = 2$ gives

$$\begin{aligned} -\sigma_0 E_0 \cos \theta - \sigma_0 \frac{B_0^0}{R_1^2} - 2\sigma_0 \frac{B_1^0}{R_1^3} \cos \theta - \sigma_0 \sum_{n=2}^{\infty} (n+1) \frac{B_n^0}{R_1^{n+2}} P_n(\cos \theta) \\ = \sigma_1 A_1^1 \cos \theta - \sigma_1 \frac{B_0^1}{R_1^2} - 2\sigma_1 \frac{B_1^1}{R_1^3} \cos \theta + \sigma_1 \sum_{n=2}^{\infty} \left(n A_n^1 R_1^{n-1} - (n+1) \frac{B_n^1}{R_1^{n+2}} \right) P_n(\cos \theta) \end{aligned}$$

Again, this must hold for all θ , so we can break this up into a series of smaller equations.

For the $n = 0$ polynomials, we have

$$\begin{aligned} -\sigma_0 \frac{B_0^0}{R_1^2} &= -\sigma_1 \frac{B_0^1}{R_1^2} \\ \Rightarrow \quad \sigma_0 B_0^0 &= \sigma_1 B_0^1 \end{aligned} \tag{B.20}$$

For the $n = 1$ polynomials, we have

$$\begin{aligned} -\sigma_0 E_0 - 2\sigma_0 \frac{B_1^0}{R_1^3} &= \sigma_1 A_1^1 - 2\sigma_1 \frac{B_1^1}{R_1^3} \\ \Rightarrow \quad -\sigma_0 E_0 R_1^3 - 2\sigma_0 B_1^0 &= \sigma_1 A_1^1 R_1^3 - 2\sigma_1 B_1^1 \end{aligned} \tag{B.21}$$

and for the polynomials where $n \geq 2$, we have

$$\begin{aligned} -\sigma_0 (n+1) \frac{B_n^0}{R_1^{n+2}} &= \sigma_1 n A_n^1 R_1^{n-1} - \sigma_1 (n+1) \frac{B_n^1}{R_1^{n+2}} \\ \Rightarrow \quad -\sigma_0 (n+1) B_n^0 &= \sigma_1 n A_n^1 R_1^{2n+1} - \sigma_1 (n+1) B_n^1 \end{aligned} \tag{B.22}$$

Inner sphere

In the inner-most sphere ($r < R_2$), we have that

$$V_2 = \sum_{n=0}^{\infty} \left(A_n^2 r^n + \frac{B_n^2}{r^{n+1}} \right) P_n(\cos \theta)$$

as $r \Rightarrow 0$, $V_2 \Rightarrow 0$ by choice of our ref. point. This implies $B_n^2 = 0 \forall n$, and $A_0^2 = 0$, so we have

$$V_2 = \sum_{n=1}^{\infty} A_n^2 r^n P_n(\cos \theta) \quad (\text{B.23})$$

Now we use the interface conditions at $r = R_2$, given by equations B.7 and B.9. Starting with the continuity of the potential V (equation B.9), we see

$$\sum_{n=0}^{\infty} \left(A_n^1 r^n + \frac{B_n^1}{r^{n+1}} \right) P_n(\cos \theta) = \sum_{n=1}^{\infty} A_n^2 r^n P_n(\cos \theta)$$

which must hold for all θ , giving

$$\begin{aligned} A_0^1 + \frac{B_0^1}{R_2} &= 0 \\ \Rightarrow A_0^1 R_2 + B_0^1 &= 0 \end{aligned} \quad (\text{B.24})$$

and for $n \geq 1$,

$$\begin{aligned} A_n^1 R_2^n + \frac{B_n^1}{R_2^{n+1}} &= A_n^2 R_2^n \\ \Rightarrow A_n^1 R_2^{2n+1} + B_n^1 &= A_n^2 R_2^{2n+1} \end{aligned} \quad (\text{B.25})$$

For the continuity of the current density (equation B.7), we have

$$\sigma_1 \sum_{n=1}^{\infty} n A_n^1 R_2^{n-1} P_n(\cos \theta) - \sigma_1 \sum_{n=0}^{\infty} (n+1) \frac{B_n^1}{R_2^{n+2}} P_n(\cos \theta) = \sigma_2 \sum_{n=1}^{\infty} n A_n^2 R_2^{n-1} P_n(\cos \theta)$$

which must hold for all θ , giving

$$-\sigma_1 \frac{B_0^1}{R_2} = 0$$

and since both σ_1 and R_2 are non-zero,

$$B_0^1 = 0 \quad (\text{B.26})$$

and for $n \geq 1$

$$\begin{aligned} \sigma_1 n A_n^1 R_2^{n-1} - \sigma_1 (n+1) \frac{B_n^1}{R_2^{n+2}} &= \sigma_2 n A_n^2 R_2^{n-1} \\ \Rightarrow \quad \sigma_1 n A_n^1 R_2^{2n+1} - \sigma_1 (n+1) B_n^1 &= \sigma_2 n A_n^2 R_2^{2n+1} \end{aligned} \quad (\text{B.27})$$

Now that we have equations B.15, B.16, B.17, B.20, B.21, B.22, B.24, B.25, B.26 and B.27, we have 10 equations and 10 unknowns. Therefore, we can proceed to solve for each of the coefficients.

By combining B.24 and B.26, we see

$$A_0^1 = 0. \quad (\text{B.28})$$

Combining this with equation B.15, we see

$$B_0^0 = 0 \quad (\text{B.29})$$

From equation B.16, we know $B_1^1 = -E_0 R_1^3 + B_1^0 - A_1^1 R_1^3$, which we put into equation

B.21 to give

$$-\sigma_0 E_0 R_1^3 - 2\sigma_0 B_1^0 = \sigma_1 A_1^1 R_1^3 - 2\sigma_1 (-E_0 R_1^3 + B_1^0 - A_1^1 R_1^3)$$

giving us an equation in A_1^1 and B_1^0 , which we can simplify to

$$-E_0 R_1^3 (\sigma_0 + 2\sigma_1) = 3\sigma_1 A_1^1 R_1^3 + 2(\sigma_0 - \sigma_1) B_1^0 \quad (\text{B.30})$$

From equation B.25, we know $A_n^2 R_2^{2n+1} = A_n^1 R_2^{2n+1} + B_n^1$. Putting this in to eqn B.27, we see

$$\sigma_1 n A_n^1 R_2^{2n+1} - \sigma_1 (n+1) B_n^1 = \sigma_2 n (A_n^1 R_2^{2n+1} + B_n^1) \quad n \geq 1$$

which simplifies to

$$n(\sigma_1 - \sigma_2) A_n^1 R_2^{2n+1} = ((n+1)\sigma_1 + n\sigma_2) B_n^1 R_2^{2n+1} \quad n \geq 1 \quad (\text{B.31})$$

In the case where $n = 1$, we have that

$$\begin{aligned} (\sigma_1 - \sigma_2) A_1^1 R_2^3 &= (2\sigma_1 + \sigma_2) B_1^1 \\ \Rightarrow A_1^1 &= \left(\frac{2\sigma_1 + \sigma_2}{\sigma_1 - \sigma_2} \right) \frac{B_1^1}{R_2^3} \end{aligned} \quad (\text{B.32})$$

which we can put into equation B.30 giving

$$-(\sigma_0 + 2\sigma_1) E_0 R_1^3 = 3\sigma_1 \left(\frac{2\sigma_1 + \sigma_2}{\sigma_1 - \sigma_2} \right) \left(\frac{R_1}{R_2} \right)^3 B_1^1 + 2(\sigma_0 - \sigma_1) B_1^0 \quad (\text{B.33})$$

To get another equation in B_1^0 and B_1^1 , we use equations B.16 and B.32 to get

$$\begin{aligned} B_1^1 &= -E_0 R_1^3 + B_1^0 - \left(\frac{2\sigma_1 + \sigma_2}{\sigma_1 - \sigma_2} \right) \left(\frac{R_1}{R_2} \right)^3 B_1^1 \\ \Rightarrow \quad &\left(1 + \left(\frac{2\sigma_1 + \sigma_2}{\sigma_1 - \sigma_2} \right) \left(\frac{R_1}{R_2} \right)^3 \right) B_1^1 = -E_0 R_1^3 + B_1^0 \end{aligned}$$

to ease notation, define

$$\alpha = \left(\frac{R_1}{R_2} \right)^3 \quad (\text{B.34})$$

which lets us simplify the above to

$$\begin{aligned} B_1^1 &= (-E_0 R_1^3 + B_1^0) \left(1 + \left(\frac{2\sigma_1 + \sigma_2}{\sigma_1 - \sigma_2} \right) \alpha \right)^{-1} \\ &= (-E_0 R_1^3 + B_1^0) \left(\frac{(\sigma_1 - \sigma_2) + (2\sigma_1 + \sigma_2) \alpha}{\sigma_1 - \sigma_2} \right)^{-1} \\ &= (-E_0 R_1^3 + B_1^0) \left(\frac{\sigma_1 - \sigma_2}{(\sigma_1 - \sigma_2) + (2\sigma_1 + \sigma_2) \alpha} \right) \end{aligned} \quad (\text{B.35})$$

With equations B.33 and B.35, we finally have arrived at a set of two equations with two unknowns (B_1^1 and (B_1^0) . Putting equation B.35 into equation B.33 and using the

definition of α as given in equation B.34, we see

$$\begin{aligned}
& -(\sigma_0 + 2\sigma_1)E_0R_1^3 \\
& = 3\sigma_1\alpha \left(\frac{2\sigma_1 + \sigma_2}{\sigma_1 - \sigma_2} \right) \left(\frac{\sigma_1 - \sigma_2}{(\sigma_1 - \sigma_2) + (2\sigma_1 + \sigma_2)\alpha} \right) (-E_0R_1^3 + B_1^0) + 2(\sigma_0 - \sigma_1)B_1^0 \\
\Rightarrow & -(\sigma_0 + 2\sigma_1)E_0R_1^3 \\
& = 3\sigma_1\alpha \left(\frac{2\sigma_1 + \sigma_2}{(\sigma_1 - \sigma_2) + (2\sigma_1 + \sigma_2)\alpha} \right) (-E_0R_1^3 + B_1^0) + 2(\sigma_0 - \sigma_1)B_1^0 \\
\Rightarrow & -(\sigma_0 + 2\sigma_1)E_0R_1^3 \\
& = \left(\frac{3\sigma_1(2\sigma_1 + \sigma_2)\alpha}{(\sigma_1 - \sigma_2) + (2\sigma_1 + \sigma_2)\alpha} \right) (-E_0R_1^3 + B_1^0) + 2(\sigma_0 - \sigma_1)B_1^0 \\
\Rightarrow & - \left((\sigma_0 + 2\sigma_1) - \frac{3\sigma_1(2\sigma_1 + \sigma_2)\alpha}{(\sigma_1 - \sigma_2) + (2\sigma_1 + \sigma_2)\alpha} \right) E_0R_1^3 \\
& = \left(\frac{3\sigma_1(2\sigma_1 + \sigma_2)\alpha}{(\sigma_1 - \sigma_2) + (2\sigma_1 + \sigma_2)\alpha} + 2(\sigma_0 - \sigma_1) \right) B_1^0 \\
\Rightarrow & - \left(\frac{(\sigma_0 + 2\sigma_1)(\sigma_1 - \sigma_2) + (\sigma_0 + 2\sigma_1)(2\sigma_1 + \sigma_2)\alpha - 3\sigma_1(2\sigma_1 + \sigma_2)\alpha}{(\sigma_1 - \sigma_2) + (2\sigma_1 + \sigma_2)\alpha} \right) E_0R_1^3 \\
& = \left(\frac{3\sigma_1(2\sigma_1 + \sigma_2)\alpha + 2(\sigma_0 - \sigma_1)(\sigma_1 - \sigma_2) + 2(\sigma_0 - \sigma_1)(2\sigma_1 + \sigma_2)\alpha}{(\sigma_1 - \sigma_2) + (2\sigma_1 + \sigma_2)\alpha} \right) B_1^0 \\
\Rightarrow & -((\sigma_0 + 2\sigma_1)(\sigma_1 - \sigma_2) + (\sigma_0 - \sigma_1)(2\sigma_1 + \sigma_2)\alpha)E_0R_1^3 \\
& = (2(\sigma_0 - \sigma_1)(\sigma_1 - \sigma_2) + (2\sigma_0 + \sigma_1)(2\sigma_1 + \sigma_2)\alpha)B_1^0
\end{aligned}$$

So the coefficient B_1^0 is given by

$$B_1^0 = -E_0R_1^3 \left(\frac{(\sigma_0 + 2\sigma_1)(\sigma_1 - \sigma_2) + (\sigma_0 - \sigma_1)(2\sigma_1 + \sigma_2)\alpha}{2(\sigma_0 - \sigma_1)(\sigma_1 - \sigma_2) + (2\sigma_0 + \sigma_1)(2\sigma_1 + \sigma_2)\alpha} \right) \quad (\text{B.36})$$

Putting this into equation B.35, we can solve for B_1^1

$$\begin{aligned} B_1^1 &= -E_0 R_1^3 \left(1 + \frac{(\sigma_0 + 2\sigma_1)(\sigma_1 - \sigma_2) + (\sigma_0 - \sigma_1)(2\sigma_1 + \sigma_2)\alpha}{2(\sigma_0 - \sigma_1)(\sigma_1 - \sigma_2) + (2\sigma_0 + \sigma_1)(2\sigma_1 + \sigma_2)\alpha} \right) \\ &\quad \left(\frac{\sigma_1 - \sigma_2}{(\sigma_1 - \sigma_2) + (2\sigma_1 + \sigma_2)\alpha} \right) \\ \Rightarrow B_1^1 &= -E_0 R_1^3 \left(\frac{3\sigma_0(\sigma_1 - \sigma_2) + 3\sigma_0(2\sigma_1 + \sigma_2)\alpha}{2(\sigma_0 - \sigma_1)(\sigma_1 - \sigma_2) + (2\sigma_0 + \sigma_1)(2\sigma_1 + \sigma_2)\alpha} \right) \\ &\quad \left(\frac{\sigma_1 - \sigma_2}{(\sigma_1 - \sigma_2) + (2\sigma_1 + \sigma_2)\alpha} \right) \end{aligned}$$

$$B_1^1 = -E_0 R_1^3 \left(\frac{3\sigma_0(\sigma_1 - \sigma_2)}{2(\sigma_0 - \sigma_1)(\sigma_1 - \sigma_2) + (2\sigma_0 + \sigma_1)(2\sigma_1 + \sigma_2)\alpha} \right) \quad (\text{B.37})$$

Next, we solve for A_1^1 using equation B.32.

$$A_1^1 = \left(\frac{2\sigma_1 + \sigma_2}{\sigma_1 - \sigma_2} \right) \frac{1}{R_2^3} \left(-E_0 R_1^3 \left(\frac{3\sigma_0(\sigma_1 - \sigma_2)}{2(\sigma_0 - \sigma_1)(\sigma_1 - \sigma_2) + (2\sigma_0 + \sigma_1)(2\sigma_1 + \sigma_2)\alpha} \right) \right)$$

which simplifies to

$$A_1^1 = -E_0 \alpha \left(\frac{3\sigma_0(2\sigma_1 + \sigma_2)}{2(\sigma_0 - \sigma_1)(\sigma_1 - \sigma_2) + (2\sigma_0 + \sigma_1)(2\sigma_1 + \sigma_2)\alpha} \right) \quad (\text{B.38})$$

Now, using equation B.27 for $n = 1$, we can solve for A_1^2

$$\begin{aligned} \sigma_2 A_1^2 R_2^3 &= \sigma_1 A_1^1 R_2^3 - 2\sigma_1 B_1^1 \\ A_1^2 &= \frac{\sigma_1}{\sigma_2} \left(A_1^1 - \frac{2}{R_2^3} B_1^1 \right) \\ &= -E_0 \alpha \frac{\sigma_1}{\sigma_2} \left(\frac{3\sigma_0(2\sigma_1 + \sigma_2) - 2(3\sigma_0(\sigma_1 - \sigma_2))}{2(\sigma_0 - \sigma_1)(\sigma_1 - \sigma_2) + (2\sigma_0 + \sigma_1)(2\sigma_1 + \sigma_2)\alpha} \right) \\ &= -E_0 \alpha \frac{\sigma_1}{\sigma_2} \left(\frac{3\sigma_0(3\sigma_2)}{2(\sigma_0 - \sigma_1)(\sigma_1 - \sigma_2) + (2\sigma_0 + \sigma_1)(2\sigma_1 + \sigma_2)\alpha} \right) \end{aligned}$$

$$A_1^2 = -E_0 \alpha \left(\frac{3\sigma_0(3\sigma_1)}{2(\sigma_0 - \sigma_1)(\sigma_1 - \sigma_2) + (2\sigma_0 + \sigma_1)(2\sigma_1 + \sigma_2)\alpha} \right) \quad (\text{B.39})$$

At this point, the remaining coefficients to be found are B_n^0 , A_n^1 and B_n^1 and A_n^2 for $n \geq 2$, and four remaining equations B.17, B.22, B.25 and B.27 for each n . These can be written more concisely as a matrix equation, namely

$$\begin{pmatrix} 0 \\ 0 \\ 0 \\ 0 \end{pmatrix} = \begin{pmatrix} 1 & 0 & -1 & 1 \\ n\sigma_1 & 0 & (n+1)\sigma_0 & -(n+1)\sigma_1 \\ 1 & -1 & 0 & 1 \\ n\sigma_1 & -n\sigma_2 & 0 & -(n+1)\sigma_1 \end{pmatrix} \begin{pmatrix} A_n^1 R_1^{2n+1} \\ B_n^0 \\ A_n^2 R_2^{2n+1} \\ B_n^1 \end{pmatrix} \quad (\text{B.40})$$

The solution to equation B.40 requires the matrix inverse. If the matrix is invertible, than the unique solution is $(0, 0, 0, 0)$. To test if this is invertible, we perform Gaussian elimination to try and reduce it to the identity:

$$\begin{pmatrix} 1 & 0 & -1 & 1 \\ 1 & -1 & 0 & 1 \\ n\sigma_1 & -n\sigma_2 & 0 & -(n+1)\sigma_1 \\ n\sigma_1 & 0 & (n+1)\sigma_0 & -(n+1)\sigma_1 \end{pmatrix} \sim \begin{pmatrix} 1 & 0 & -1 & 1 \\ 0 & -1 & 0 & 1 \\ 0 & 0 & (n+1)\sigma_0 + n\sigma_1 & -(2n+1)\sigma_1 \\ 0 & -n\sigma_2 & n\sigma_1 & -(2n+1)\sigma_1 \end{pmatrix}$$

$$\begin{aligned}
&\sim \begin{pmatrix} 1 & 0 & -1 & 1 \\ 0 & 1 & 0 & -1 \\ 0 & 0 & (n+1)\sigma_0 + n\sigma_1 & -(2n+1)\sigma_1 \\ 0 & 0 & n\sigma_1 & -(2n+1)\sigma_1 - n\sigma_2 \end{pmatrix} \\
&\sim \begin{pmatrix} 1 & 0 & -1 & 1 \\ 0 & 1 & 0 & -1 \\ 0 & 0 & 1 & \frac{-(2n+1)\sigma_1}{(n+1)\sigma_0 + n\sigma_1} \\ 0 & 0 & 0 & -(2n+1)\sigma_1 - n\sigma_2 - n\sigma_1 \frac{-(2n+1)\sigma_1}{(n+1)\sigma_0 + n\sigma_1} \end{pmatrix} \\
&\sim \begin{pmatrix} 1 & 0 & -1 & 1 \\ 0 & 1 & 0 & -1 \\ 0 & 0 & 1 & \frac{-(2n+1)\sigma_1}{(n+1)\sigma_0 + n\sigma_1} \\ 0 & 0 & 0 & 1 \end{pmatrix} \\
&\sim \begin{pmatrix} 1 & 0 & 0 & 0 \\ 0 & 1 & 0 & 0 \\ 0 & 0 & 1 & 0 \\ 0 & 0 & 0 & 1 \end{pmatrix}
\end{aligned}$$

Therefore,

$$A_n^1 = 0 \quad \forall n \geq 2 \quad (\text{B.41})$$

$$B_n^0 = 0 \quad \forall n \geq 2 \quad (\text{B.42})$$

$$A_n^2 = 0 \quad \forall n \geq 2 \quad (\text{B.43})$$

$$B_n^1 = 0 \quad \forall n \geq 2 \quad (\text{B.44})$$

Now we have everything we need to express the potentials in each region. Outside the sphere ($r > R_2$)

$$V_0 = -E_0 r \cos \theta \left(1 + \frac{R_1^3}{r^3} \left(\frac{(\sigma_0 + 2\sigma_1)(\sigma_1 - \sigma_2) + (\sigma_0 - \sigma_1)(2\sigma_1 + \sigma_2)\alpha}{2(\sigma_0 - \sigma_1)(\sigma_1 - \sigma_2) + (2\sigma_0 + \sigma_1)(2\sigma_1 + \sigma_2)\alpha} \right) \right) \quad (\text{B.45})$$

In the outer shell ($R_1 < r < R_2$)

$$V_1 = -E_0 r \cos \theta \frac{3\sigma_0}{2(\sigma_0 - \sigma_1)(\sigma_1 - \sigma_2) + (2\sigma_0 + \sigma_1)(2\sigma_1 + \sigma_2)\alpha} \left((2\sigma_1 + \sigma_2)\alpha + (\sigma_1 - \sigma_2) \frac{R_1^3}{r^3} \right) \quad (\text{B.46})$$

In the inner sphere ($r < R_2$)

$$V_2 = -E_0 r \cos \theta \left(\frac{(3\sigma_0)(3\sigma_1)\alpha}{2(\sigma_0 - \sigma_1)(\sigma_1 - \sigma_2) + (2\sigma_0 + \sigma_1)(2\sigma_1 + \sigma_2)\alpha} \right) \quad (\text{B.47})$$

B.2.2 Sanity Checks

Before moving any further, there are a few end-member cases we can use to validate our solution.

For a number of checks, it is useful to compare to the solution of a single sphere. From Ward and Hohmann (pg. 282-285), we have that the potential exterior to the sphere ($r > R$) is

$$V_e = -E_0 r \cos \theta \left(1 + \frac{R^3}{r^3} \left(\frac{\sigma_e - \sigma_i}{2\sigma_e + \sigma_i} \right) \right) \quad (\text{B.48})$$

where σ_e is the conductivity of the background, σ_i is the conductivity of the sphere, and R is the radius of the sphere. The potential inside the sphere ($r < R$) is given by

$$V_i = -E_0 r \cos \theta \left(\frac{3\sigma_e}{2\sigma_e + \sigma_i} \right) \quad (\text{B.49})$$

Check 1: Equal conductivity of the inner sphere and outer shell

First, if $\sigma_2 = \sigma_1$, then $R = R_1$, and we expect $V_0 = V_e$ and $V_1 = V_2 = V_i$. Starting with V_0 , we see

$$\begin{aligned} V_0 &= -E_0 r \cos \theta \left(1 + \frac{R_1^3}{r^3} \left(\frac{(\sigma_0 + 2\sigma_1)(\sigma_1 - \sigma_0) + (\sigma_0 - \sigma_1)(2\sigma_1 + \sigma_0)\alpha}{2(\sigma_0 - \sigma_1)(\sigma_1 - \sigma_0) + (2\sigma_0 + \sigma_1)(2\sigma_1 + \sigma_0)\alpha} \right) \right) \\ &= -E_0 r \cos \theta \left(1 + \frac{R_1^3}{r^3} \left(\frac{(\sigma_0 - \sigma_1)(3\sigma_1)\alpha}{(2\sigma_0 + \sigma_1)(3\sigma_1)\alpha} \right) \right) \\ &= -E_0 r \cos \theta \left(1 + \frac{R_1^3}{r^3} \left(\frac{\sigma_0 - \sigma_1}{2\sigma_0 + \sigma_1} \right) \right) \\ &= V_e \checkmark \end{aligned}$$

For V_1 , we have

$$\begin{aligned} V_1 &= -E_0 r \cos \theta \frac{3\sigma_0}{2(\sigma_0 - \sigma_1)(\sigma_1 - \sigma_0) + (2\sigma_0 + \sigma_1)(2\sigma_1 + \sigma_0)\alpha} \\ &\quad \left((2\sigma_1 + \sigma_0)\alpha + (\sigma_1 - \sigma_0)\frac{R_1^3}{r^3} \right) \\ &= -E_0 r \cos \theta \frac{3\sigma_0}{(2\sigma_0 + \sigma_1)(3\sigma_1)\alpha} ((3\sigma_1)\alpha) \\ &= -E_0 r \cos \theta \frac{3\sigma_0}{(2\sigma_0 + \sigma_1)} \\ &= V_i \checkmark \end{aligned}$$

For V_2 , we have

$$\begin{aligned}
V_2 &= -E_0 r \cos \theta \left(\frac{(3\sigma_0)(3\sigma_1)\alpha}{2(\sigma_0 - \sigma_1)(\sigma_1 - \sigma_1) + (2\sigma_0 + \sigma_1)(2\sigma_1 + \sigma_1)\alpha} \right) \\
&= -E_0 r \cos \theta \left(\frac{(3\sigma_0)(3\sigma_1)\alpha}{(2\sigma_0 + \sigma_1)(3\sigma_1)\alpha} \right) \\
&= -E_0 r \cos \theta \left(\frac{3\sigma_0}{2\sigma_0 + \sigma_1} \right) \\
&= V_i \checkmark
\end{aligned}$$

Check 2: Conductivity of the outer shell equals that of the background

If $\sigma_1 = \sigma_0$, then $R = R_2$, and we expect $V_0 = V_1 = V_e$ and $V_2 = V_i$. For V_0 , we have

$$\begin{aligned}
V_0 &= -E_0 r \cos \theta \left(1 + \frac{R_1^3}{r^3} \left(\frac{(\sigma_0 + 2\sigma_0)(\sigma_0 - \sigma_2) + (\sigma_0 - \sigma_0)(2\sigma_0 + \sigma_2)\alpha}{2(\sigma_0 - \sigma_0)(\sigma_0 - \sigma_2) + (2\sigma_0 + \sigma_0)(2\sigma_0 + \sigma_2)\alpha} \right) \right) \\
&= -E_0 r \cos \theta \left(1 + \frac{R_1^3}{r^3} \left(\frac{(3\sigma_0)(\sigma_0 - \sigma_2)}{(3\sigma_0)(2\sigma_0 + \sigma_2)\alpha} \right) \right) \\
&= -E_0 r \cos \theta \left(1 + \frac{R_1^3}{r^3} \left(\frac{(\sigma_0 - \sigma_2)}{(2\sigma_0 + \sigma_2)\alpha} \right) \right) \\
&= -E_0 r \cos \theta \left(1 + \frac{R_1^3}{r^3} \left(\frac{\sigma_0 - \sigma_2}{2\sigma_0 + \sigma_2} \right) \frac{R_2^3}{R_1^3} \right) \\
&= -E_0 r \cos \theta \left(1 + \frac{R_2^3}{r^3} \left(\frac{\sigma_0 - \sigma_2}{2\sigma_0 + \sigma_2} \right) \right) \\
&= V_e \checkmark
\end{aligned}$$

For V_1 , we have

$$\begin{aligned}
V_1 &= -E_0 r \cos \theta \frac{3\sigma_0}{2(\sigma_0 - \sigma_0)(\sigma_0 - \sigma_2) + (2\sigma_0 + \sigma_0)(2\sigma_0 + \sigma_2)\alpha} \\
&\quad \left((2\sigma_0 + \sigma_2)\alpha + (\sigma_0 - \sigma_2)\frac{R_1^3}{r^3} \right) \\
&= -E_0 r \cos \theta \frac{3\sigma_0}{(3\sigma_0)(2\sigma_0 + \sigma_2)\alpha} \left((2\sigma_0 + \sigma_2)\alpha + (\sigma_0 - \sigma_2)\frac{R_1^3}{r^3} \right) \\
&= -E_0 r \cos \theta \frac{1}{(2\sigma_0 + \sigma_2)\alpha} \left((2\sigma_0 + \sigma_2)\alpha + (\sigma_0 - \sigma_2)\frac{R_1^3}{r^3} \right) \\
&= -E_0 r \cos \theta \left(1 + \left(\frac{\sigma_0 - \sigma_2}{(2\sigma_0 + \sigma_2)\alpha} \right) \frac{R_1^3}{r^3} \right) \\
&= -E_0 r \cos \theta \left(1 + \left(\frac{\sigma_0 - \sigma_2}{2\sigma_0 + \sigma_2} \right) \frac{R_2^3 R_1^3}{R_1^3 r^3} \right) \\
&= -E_0 r \cos \theta \left(1 + \left(\frac{\sigma_0 - \sigma_2}{2\sigma_0 + \sigma_2} \right) \frac{R_2^3}{r^3} \right) \\
&= V_e \checkmark
\end{aligned}$$

and for V_2 ,

$$\begin{aligned}
V_2 &= -E_0 r \cos \theta \left(\frac{(3\sigma_0)(3\sigma_0)\alpha}{2(\sigma_0 - \sigma_0)(\sigma_0 - \sigma_2) + (2\sigma_0 + \sigma_0)(2\sigma_0 + \sigma_2)\alpha} \right) \\
&= -E_0 r \cos \theta \left(\frac{(3\sigma_0)(3\sigma_0)\alpha}{(3\sigma_0)(2\sigma_0 + \sigma_2)\alpha} \right) \\
&= -E_0 r \cos \theta \left(\frac{3\sigma_0}{2\sigma_0 + \sigma_2} \right) \\
&= V_i \checkmark
\end{aligned}$$

Check 3: Equal radius of the inner sphere and outer shell

If $\alpha = 1$ (i.e. $R_1 = R_2$), we expect $V_0 = V_e$, and $V_2 = V_i$. For V_0 , we have

$$\begin{aligned}
 V_0 &= -E_0 r \cos \theta \left(1 + \frac{R_1^3}{r^3} \left(\frac{(\sigma_0 + 2\sigma_1)(\sigma_1 - \sigma_2) + (\sigma_0 - \sigma_1)(2\sigma_1 + \sigma_2)}{2(\sigma_0 - \sigma_1)(\sigma_1 - \sigma_2) + (2\sigma_0 + \sigma_1)(2\sigma_1 + \sigma_2)} \right) \right) \\
 &= -E_0 r \cos \theta \left(1 + \frac{R_1^3}{r^3} \left(\frac{\sigma_0(\sigma_1 - \sigma_2 + 2\sigma_1 + \sigma_2) + \sigma_1(2\sigma_1 - 2\sigma_2 - 2\sigma_1 - \sigma_2)}{2\sigma_0(\sigma_1 - \sigma_2 + 2\sigma_1 + \sigma_2) + \sigma_1(-2\sigma_1 + 2\sigma_2 + 2\sigma_1 + \sigma_2)} \right) \right) \\
 &= -E_0 r \cos \theta \left(1 + \frac{R_1^3}{r^3} \left(\frac{\sigma_0(3\sigma_1) + \sigma_1(-3\sigma_2)}{2\sigma_0(3\sigma_1) + \sigma_1(3\sigma_2)} \right) \right) \\
 &= -E_0 r \cos \theta \left(1 + \frac{R_1^3}{r^3} \left(\frac{\sigma_0 - \sigma_2}{2\sigma_0 + \sigma_2} \right) \right) \\
 &= V_e \checkmark
 \end{aligned}$$

For V_2 , we have

$$\begin{aligned}
 V_2 &= -E_0 r \cos \theta \left(\frac{(3\sigma_0)(3\sigma_1)}{2(\sigma_0 - \sigma_1)(\sigma_1 - \sigma_2) + (2\sigma_0 + \sigma_1)(2\sigma_1 + \sigma_2)} \right) \\
 &= -E_0 r \cos \theta \left(\frac{(3\sigma_0)(3\sigma_1)}{2\sigma_0(\sigma_1 - \sigma_2 + 2\sigma_1 + \sigma_2) + \sigma_1(-2\sigma_1 + 2\sigma_2 + 2\sigma_1 + \sigma_2)} \right) \\
 &= -E_0 r \cos \theta \left(\frac{(3\sigma_0)(3\sigma_1)}{2\sigma_0(3\sigma_1) + \sigma_1(3\sigma_2)} \right) \\
 &= -E_0 r \cos \theta \left(\frac{3\sigma_0}{2\sigma_0 + \sigma_2} \right) \\
 &= V_i \checkmark
 \end{aligned}$$

Check 4: $\lim R_2 \rightarrow 0$

If we take $R_2 \rightarrow 0$ (i.e. $\alpha^{-1} \rightarrow 0$), we expect $V_0 \rightarrow V_e$ and $V_1 \rightarrow V_i$. For V_0 , we have

$$\begin{aligned}\lim_{\alpha^{-1} \rightarrow 0} V_0 &= \lim_{\alpha^{-1} \rightarrow 0} -E_0 r \cos \theta \left(1 + \frac{R_1^3}{r^3} \left(\frac{(\sigma_0 + 2\sigma_1)(\sigma_1 - \sigma_2) + (\sigma_0 - \sigma_1)(2\sigma_1 + \sigma_2)\alpha}{2(\sigma_0 - \sigma_1)(\sigma_1 - \sigma_2) + (2\sigma_0 + \sigma_1)(2\sigma_1 + \sigma_2)\alpha} \right) \right) \\ &= \lim_{\alpha^{-1} \rightarrow 0} -E_0 r \cos \theta \left(1 + \frac{R_1^3}{r^3} \left(\frac{(\sigma_0 + 2\sigma_1)(\sigma_1 - \sigma_2)\alpha^{-1} + (\sigma_0 - \sigma_1)(2\sigma_1 + \sigma_2)}{2(\sigma_0 - \sigma_1)(\sigma_1 - \sigma_2)\alpha^{-1} + (2\sigma_0 + \sigma_1)(2\sigma_1 + \sigma_2)} \right) \right) \\ &= -E_0 r \cos \theta \left(1 + \frac{R_1^3}{r^3} \left(\frac{(\sigma_0 - \sigma_1)(2\sigma_1 + \sigma_2)}{(2\sigma_0 + \sigma_1)(2\sigma_1 + \sigma_2)} \right) \right) \\ &= -E_0 r \cos \theta \left(1 + \frac{R_1^3}{r^3} \left(\frac{\sigma_0 - \sigma_1}{2\sigma_0 + \sigma_1} \right) \right) \\ &= V_e \checkmark\end{aligned}$$

and for V_1 , we have

$$\begin{aligned}\lim_{\alpha^{-1} \rightarrow 0} V_1 &= \lim_{\alpha^{-1} \rightarrow 0} -E_0 r \cos \theta \frac{3\sigma_0}{2(\sigma_0 - \sigma_1)(\sigma_1 - \sigma_2) + (2\sigma_0 + \sigma_1)(2\sigma_1 + \sigma_2)\alpha} \\ &\quad \left((2\sigma_1 + \sigma_2)\alpha + (\sigma_1 - \sigma_2)\frac{R_1^3}{r^3} \right) \\ &= \lim_{\alpha^{-1} \rightarrow 0} -E_0 r \cos \theta \frac{3\sigma_0}{2(\sigma_0 - \sigma_1)(\sigma_1 - \sigma_2)\alpha^{-1} + (2\sigma_0 + \sigma_1)(2\sigma_1 + \sigma_2)} \\ &\quad \left((2\sigma_1 + \sigma_2) + (\sigma_1 - \sigma_2)\alpha^{-1}\frac{R_1^3}{r^3} \right) \\ &= -E_0 r \cos \theta \frac{3\sigma_0}{(2\sigma_0 + \sigma_1)(2\sigma_1 + \sigma_2)} (2\sigma_1 + \sigma_2) \\ &= -E_0 r \cos \theta \left(\frac{3\sigma_0}{2\sigma_0 + \sigma_1} \right) \\ &= V_i \checkmark\end{aligned}$$

B.3 Effective Conductivity Expression

After all of that, now we want an expression for the effective conductivity of a coated sphere. To clarify, I mean that we want to find a value σ^* such that the potential external to a sphere with radius R_1 and conductivity σ^* is equivalent to the potential due to the concentric spheres with inner radius R_2 and conductivity σ_2 , and outer radius R_1 and conductivity σ_1 .

To proceed, we equate V_0 as defined in equation B.45 with the V_e given by equation B.48 and specify that $\sigma_e = \sigma_0$, $\sigma_i = \sigma^*$ and $R = R_1$, giving

$$V_e = V_0$$

$$\begin{aligned} -E_0 r \cos \theta & \left(1 + \frac{R_1^3}{r^3} \left(\frac{\sigma_0 - \sigma^*}{2\sigma_0 + \sigma^*} \right) \right) \\ &= -E_0 r \cos \theta \left(1 + \frac{R_1^3}{r^3} \left(\frac{(\sigma_0 + 2\sigma_1)(\sigma_1 - \sigma_2) + (\sigma_0 - \sigma_1)(2\sigma_1 + \sigma_2)\alpha}{2(\sigma_0 - \sigma_1)(\sigma_1 - \sigma_2) + (2\sigma_0 + \sigma_1)(2\sigma_1 + \sigma_2)\alpha} \right) \right) \\ \frac{\sigma_0 - \sigma^*}{2\sigma_0 + \sigma^*} &= \frac{(\sigma_0 + 2\sigma_1)(\sigma_1 - \sigma_2) + (\sigma_0 - \sigma_1)(2\sigma_1 + \sigma_2)\alpha}{2(\sigma_0 - \sigma_1)(\sigma_1 - \sigma_2) + (2\sigma_0 + \sigma_1)(2\sigma_1 + \sigma_2)\alpha} \end{aligned}$$

From this, we can solve for σ^*

$$\begin{aligned}
& ((\sigma_0 + 2\sigma_1)(\sigma_1 - \sigma_2) + (\sigma_0 - \sigma_1)(2\sigma_1 + \sigma_2)\alpha)(2\sigma_0 + \sigma^*) \\
& = (2(\sigma_0 - \sigma_1)(\sigma_1 - \sigma_2) + (2\sigma_0 + \sigma_1)(2\sigma_1 + \sigma_2)\alpha)(\sigma_0 - \sigma^*) \\
& \sigma^*((\sigma_0 + 2\sigma_1)(\sigma_1 - \sigma_2) + (\sigma_0 - \sigma_1)(2\sigma_1 + \sigma_2)\alpha \\
& \quad + 2(\sigma_0 - \sigma_1)(\sigma_1 - \sigma_2) + (2\sigma_0 + \sigma_1)(2\sigma_1 + \sigma_2)\alpha) \\
& = \sigma_0(-2(\sigma_0 + 2\sigma_1)(\sigma_1 - \sigma_2) - 2(\sigma_0 - \sigma_1)(2\sigma_1 + \sigma_2)\alpha \\
& \quad + 2(\sigma_0 - \sigma_1)(\sigma_1 - \sigma_2) + (2\sigma_0 + \sigma_1)(2\sigma_1 + \sigma_2)\alpha) \\
& \sigma^*((\sigma_0 + 2\sigma_1 + 2\sigma_0 - 2\sigma_1)(\sigma_1 - \sigma_2) \\
& \quad + (\sigma_0 - \sigma_1 + 2\sigma_0 + \sigma_1)(2\sigma_1 + \sigma_2)\alpha) \\
& = \sigma_0(2(-\sigma_0 - 2\sigma_1 + \sigma_0 - \sigma_1)(\sigma_1 - \sigma_2) \\
& \quad + (-2\sigma_0 + 2\sigma_1 + 2\sigma_0 + \sigma_1)(2\sigma_1 + \sigma_2)\alpha) \\
& \sigma^*((3\sigma_0)(\sigma_1 - \sigma_2) + (3\sigma_0)(2\sigma_1 + \sigma_2)\alpha) \\
& = \sigma_0(2(-3\sigma_1)(\sigma_1 - \sigma_2) + (3\sigma_1)(2\sigma_1 + \sigma_2)\alpha)
\end{aligned}$$

We can cancel a factor of $3\sigma_0$ from each side, giving an expression independent of σ_0

$$\begin{aligned}
& \sigma^*((\sigma_1 - \sigma_2) + (2\sigma_1 + \sigma_2)\alpha) = (-2(\sigma_1)(\sigma_1 - \sigma_2) + (\sigma_1)(2\sigma_1 + \sigma_2)\alpha) \\
& \sigma^*((\sigma_1 - \sigma_2) + (2\sigma_1 + \sigma_2)\alpha) = \sigma_1(-2(\sigma_1 - \sigma_2) + (2\sigma_1 + \sigma_2)\alpha) \\
& \sigma^* = \sigma_1 \frac{-2(\sigma_1 - \sigma_2) + (2\sigma_1 + \sigma_2)\alpha}{(\sigma_1 - \sigma_2) + (2\sigma_1 + \sigma_2)\alpha}
\end{aligned}$$

With a slight re-arrangement and substituting in the definition of α , we see

$$\sigma^* = \sigma_1 \frac{(2\sigma_1 + \sigma_2)R_1^3 - 2(\sigma_1 - \sigma_2)R_2^3}{(2\sigma_1 + \sigma_2)R_1^3 + (\sigma_1 - \sigma_2)R_2^3} \quad (\text{B.50})$$

A few end-members can serve as checks. If $\sigma_1 = \sigma_2$, then $\sigma^* = \sigma_1$, as expected. If

$\alpha \rightarrow \infty$, (ie. $R_2 \rightarrow 0$), then $\sigma^* = \sigma_1$, as expected, and if $\alpha \rightarrow 1$ ($R_1 = R_2$), then $\sigma^* = \sigma_2$, as expected.

Appendix C

Self consistent effective medium theory derivatives

Here, I derive the sensitivity of the effective conductivity calculated via effective medium theory, σ^* with respect to the concentration of the included material ϕ for the inversions discussed in Chapter 6. The effective conductivity is found by solving 6.9, which I restate here:

$$(1 - \phi)(\sigma^* - \sigma_0)R^{(0,*)} + \phi(\sigma^* - \sigma_1)R^{(1,*)} = 0 \quad (\text{C.1})$$

where σ_0 is the conductivity of the background, σ_1 is the conductivity of the included phase, and $\mathbf{R}^{(i,*)}$ electric field concentration tensor for the i -th phase. For simplicity, I assume that both phases are randomly oriented and thus the effective conductivity is isotropic. For randomly oriented particles, $\mathbf{R}^{(i,*)}$ is given by (recalling that \mathbf{A} is given in

equation 2.4),

$$\begin{aligned}
R^{(j,*)} &= \frac{1}{3} \text{trace} \left(\left[\mathbf{I} + \mathbf{A} \boldsymbol{\sigma}^{*-1} (\boldsymbol{\sigma}_j \mathbf{I} - \boldsymbol{\sigma}^*) \right]^{-1} \right) \\
&= \frac{1}{3} \text{trace} \left(\left[\mathbf{I} + \frac{(\boldsymbol{\sigma}_j - \boldsymbol{\sigma}^*)}{\boldsymbol{\sigma}^*} \begin{bmatrix} Q & & \\ & Q & \\ & & 1-2Q \end{bmatrix} \right]^{-1} \right) \\
&= \frac{1}{3} \text{trace} \left(\boldsymbol{\sigma}^* \begin{bmatrix} \boldsymbol{\sigma}^* + Q(\boldsymbol{\sigma}_j - \boldsymbol{\sigma}^*) & & \\ & \boldsymbol{\sigma}^* + Q(\boldsymbol{\sigma}_j - \boldsymbol{\sigma}^*) & \\ & & \boldsymbol{\sigma}_j - 2Q(\boldsymbol{\sigma}_j - \boldsymbol{\sigma}^*) \end{bmatrix}^{-1} \right) \\
&= \frac{\boldsymbol{\sigma}^*}{3} \left(\frac{2}{\boldsymbol{\sigma}^* + Q(\boldsymbol{\sigma}_j - \boldsymbol{\sigma}^*)} + \frac{1}{\boldsymbol{\sigma}_j - 2Q(\boldsymbol{\sigma}_j - \boldsymbol{\sigma}^*)} \right)
\end{aligned} \tag{C.2}$$

where Q is a scalar that depends on the geometry of the particles composing each phase of material. For spherical particles, $Q = 1/3$, for ellipsoidal particles, the expression is given in equations 2.6, 2.5.

For the sensitivity calculation, we require the derivative of $\boldsymbol{\sigma}^*$ with respect to the concentration ϕ . I will solve for it implicitly. Starting from equation C.1, we have

$$\begin{aligned}
&-(\boldsymbol{\sigma}^* - \boldsymbol{\sigma}_0)R^{(0,*)} + (1-\varphi)R^{(0,*)}\frac{\partial \boldsymbol{\sigma}^*}{\partial \varphi} + (1-\varphi)(\boldsymbol{\sigma}^* - \boldsymbol{\sigma}_0)\frac{\partial R^{(0,*)}}{\partial \varphi} \\
&+ (\boldsymbol{\sigma}^* - \boldsymbol{\sigma}_1)R^{(1,*)} + \varphi R^{(1,*)}\frac{\partial \boldsymbol{\sigma}^*}{\partial \varphi} + \varphi(\boldsymbol{\sigma}^* - \boldsymbol{\sigma}_1)\frac{\partial R^{(1,*)}}{\partial \varphi} = 0
\end{aligned}$$

As the only dependence of $R^{(j,*)}$ on φ is through σ^* , we can use the chain rule, giving

$$\begin{aligned} & \left[(1 - \varphi) \left(R^{(0,*)} + (\sigma^* - \sigma_0) \frac{\partial R^{(0,*)}}{\partial \sigma^*} \right) + \varphi \left(R^{(1,*)} + (\sigma^* - \sigma_1) \frac{\partial R^{(1,*)}}{\partial \sigma^*} \right) \right] \frac{\partial \sigma^*}{\partial \varphi} \\ &= (\sigma^* - \sigma_0) R^{(0,*)} - (\sigma^* - \sigma_1) R^{(1,*)} \end{aligned}$$

Thus, the derivative of the effective conductivity with respect to the concentration of phase-1 material is

$$\begin{aligned} \frac{\partial \sigma^*}{\partial \varphi} &= \left[(1 - \varphi) R^{(0,*)} + \varphi R^{(1,*)} + (1 - \varphi)(\sigma^* - \sigma_0) \frac{\partial R^{(0,*)}}{\partial \sigma^*} + \varphi(\sigma^* - \sigma_1) \frac{\partial R^{(1,*)}}{\partial \sigma^*} \right]^{-1} \\ &\quad (\sigma^* - \sigma_0) R^{(0,*)} - (\sigma^* - \sigma_1) R^{(1,*)} \end{aligned} \tag{C.3}$$

The derivative of the electric field concentration tensor with respect to the effective conductivity is given by

$$\begin{aligned} \frac{\partial R^{(j,*)}}{\partial \sigma^*} &= \frac{1}{3} (2 [\sigma^* + Q(\sigma_j - \sigma^*)]^{-1} + [\sigma_j - 2Q(\sigma_j - \sigma^*)]^{-1}) \\ &\quad + \frac{\sigma^*}{3} \left(\frac{-2(1-Q)}{(\sigma^* + Q(\sigma_j - \sigma^*))^2} + \frac{-2Q}{(\sigma_j - 2Q(\sigma_j - \sigma^*))^2} \right) \end{aligned} \tag{C.4}$$

Appendix D

A framework for simulation and inversion in electromagnetics

D.1 Introduction

The field of electromagnetic (EM) geophysics encompasses a diverse suite of problems with applications across mineral and resource exploration, environmental studies and geotechnical engineering. EM problems can be formulated in the time or frequency domain. Sources can be grounded electric sources or inductive loops driven by time-harmonic or transient currents, or natural, plane wave sources, as in the case of the magnetotelluric method. The physical properties of relevance include electrical conductivity, magnetic permeability, and electric permittivity. These may be isotropic, anisotropic, and also frequency dependent. Working with electromagnetic data to discern information about subsurface physical properties requires that we have numerical tools for carrying out forward simulations and inversions that are capable of handling each of these permutations.

The goal of the forward simulation is to solve a specific set of Maxwell's equations and obtain a prediction the EM responses. Numerical simulations using a staggered grid discretization (Yee, 1966), have been extensively studied in their application for finite difference, finite volume and finite element approaches (c.f. Newman and Alumbaugh (1999); Haber (2014b)), with many such implementations being optimized for efficient computations for the context in which they are being applied (Haber and Ascher, 2001; Li and Key, 2007; Kelbert et al., 2014; Yang et al., 2014).

Finding a model of the earth that is consistent with the observed data and prior geologic knowledge is the 'inverse problem'. It presupposes that we have a means of solving the forward problem. The inverse problem is generally solved by minimizing an objective function that consists of a data misfit and regularization, with a trade-off parameter controlling their relative contributions. (Tikhonov and Arsenin, 1977; Parker, 1980; Constable et al., 1987). Deterministic, gradient-based approaches to the inverse problem are commonplace in EM inversions. Relevance of the recovered inversion model is increased by incorporating *a priori* geologic information and assumptions. This can be accomplished through, the regularization term (Oldenburg and Li, 2005a; Constable et al., 1987) or parameterizing the inversion model (Pidlisecky et al., 2011; McMillan et al., 2015a; Kang et al., 2015). Multiple data sets may be considered through cooperative or joint inversions (Haber and Oldenburg, 1998; McMillan et al., 2015b).

Each of these advances relies on a workflow and associated software implementation. Unfortunately, each software implementation is typically developed as a stand-alone solution. As a result, these advances are not readily interoperable with regard to concepts, terminology, notations *and* software.

The advancement of EM geophysical techniques and the expansion of their application requires a flexible set of concepts and tools that are organized in a framework so

that researchers can more readily experiment with, and explore, new ideas. For example, if we consider research questions within the growing application of EM for reservoir characterization and monitoring in settings with steel cased wells (cf. Hoversten et al. (2015); Um et al. (2015); Commer et al. (2015); Cuevas (2014b); Hoversten et al. (2014); Pardo and Torres-Verdin (2013)), the numerical tools employed must enable investigation into factors such as the impact of variable magnetic permeability (Wu and Habashy, 1994; Heagy et al., 2015) and casing integrity (Brill et al., 2012) on electromagnetic signals. Various modelling approaches in both time and frequency domain simulations are being explored, these include employing highly-refined meshes (Commer et al., 2015), using cylindrical symmetry (Heagy et al., 2015) or approximating the casing on a coarse-scale (Um et al., 2015), possibly 3D anisotropic approximations (Caudillo-Mata et al., 2014). Beyond forward simulations that predict EM responses, to enable the interpretation of field data with these tools requires that machinery to address the inverse problem and experiment with approaches for constrained and/or time lapse inversions be in place (Devriese and Oldenburg, 2016; Marsala et al., 2015). Typically, addressing each of these complexities would require a custom implementations, particularly for the frequency domain and time domain simulations, although aspects, such as physical properties, are common to both. Inconsistencies between implementations and the need to implement a custom solution for each type of EM method under consideration presents a significant barrier to a researcher's ability to experiment with and extend ideas.

Building from the body of work on EM geophysical simulations and inversions, the aim of our efforts is to identify a common, modular framework suitable across the suite of electromagnetic problems. This conceptual organization has been tested and developed through a numerical implementation. The implementation is modular in design

with the expressed goal of affording researchers the ability to rapidly adjust, interchange, and extend elements. By developing the software in the open, we also aim to promote an open dialog on approaches for solving forward and inverse problems in EM geophysics.

The implementation we describe for EM forward and inverse problems extends a general framework for geophysical simulation and gradient based inverse problems, called SIMPEG (Cockett et al., 2015). The implementation of SIMPEG is open-source, written in Python and has dependencies on the standard numerical computing packages NumPy, SciPy, and Matplotlib (van der Walt et al., 2011; Oliphant, 2007; Hunter, 2007). The contribution described in this chapter is the implementation of the physics engine for problems in electromagnetics, including the forward simulation and calculation of the sensitivities. Building within the SIMPEG ecosystem has expedited the development process and allowed developments to be made in tandem with other applications (<http://simpeg.xyz>). SIMPEGEM aspires to follow best practices in terms of documentation, testing, continuous integration using the publically available services Sphinx, Travis CI, and Coveralls (Brandl, 2010; Kalderimis and Meyer, 2011; Merwin et al., 2015). As of the writing of this chapter, when any line of code is changed in the open source repository, over 3 hours of testing is completed; documentation and examples are also tested and automatically updated (<http://docs.simpeg.xyz>). We hope these practices encourage the growth of a community and collaborative, reproducible software development in the field of EM geophysics.

The chapter is organized as follows. To provide context for the structure and implementation of SIMPEGEM, we begin with a brief overview of the SIMPEG inversion framework as well as the governing equations for electromagnetics in Section D.2. In Section D.3, we discuss the motivating factors for the EM framework, and in Section D.4, we discuss the framework and implementation of the forward simulation and

calculation of sensitivities in SIMPEGEM. We demonstrate the implementation with two synthetic examples and one field example in Section D.5. The first example shows the similarities between the time and frequency implementations for a 1D inversion. In the second example, we invert field data from the Bookpurnong Irrigation district in Australia. The final example demonstrates how the modular implementation is used to compute the sensitivity for a parametric model of a block in a layered space where a transmitter is positioned inside a steel cased well.

D.2 Background

We are focused on geophysical inverse problems in electromagnetics (EM), that is, given EM data, we want to find a model of the earth that explains those data and satisfies prior assumptions about the geologic setting. We follow the SIMPEG framework, shown in Figure D.1, which takes a gradient- based approach to the inverse problem (Cockett et al., 2015). Inputs to the inversion are the data and associated uncertainties, a description of the governing equations, as well as prior knowledge and assumptions about the model. With these defined, the SIMPEG framework accomplishes two main objectives:

1. the ability to forward simulate data and compute sensitivities (Forward Simulation - outlined in green in Figure D.1),
2. the ability to assess and update the model in an inversion (Inversion Elements and Inversion as Optimization - outlined in red in Figure D.1).

The implementation of the framework is organized into the self-contained modules shown in Figure D.1; each module is defined as a base- class within SIMPEG. The `Mesh` provides the discretization and numerical operators. These are leveraged by the `Problem`, which is the numerical physics engine; the `Problem` computes fields

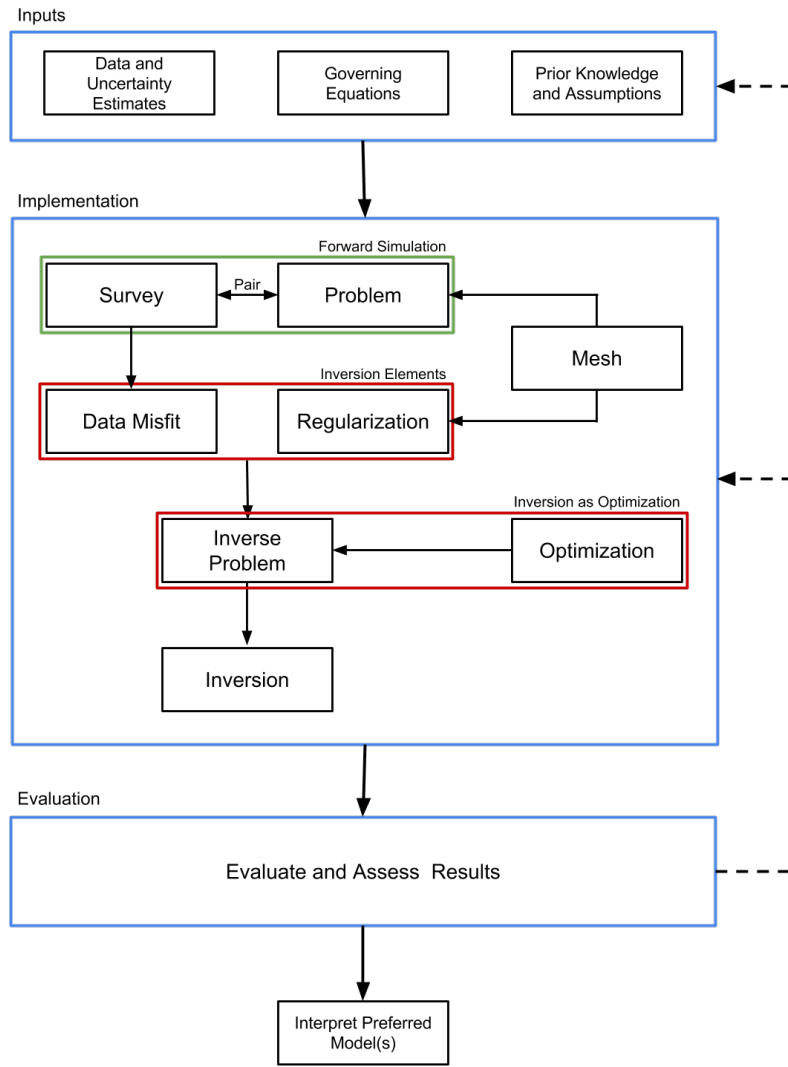


Figure D.1: Inversion approach using the SIMPEG framework. Adapted from Cockett et al. (2015)

and fluxes when provided a model and Sources. The Sources are specified in the Survey, as are the Receivers. The Receivers take the Fields computed by the Problem and evaluate them at the receiver locations to create predicted data. Each action taken to compute data, when provided a model, has an associated derivative with respect to the model; these components are assembled to create the sensitivity. Hav-

ing the ability to compute both predicted data and sensitivities accomplishes the first objective.

To accomplish the second objective of assessing and updating the model in the context of the data and our assumptions, we consider a gradient-based approach to the inversion. For this, we specify an objective function which generally consists of a `DataMisfit` and `Regularization`. The `DataMisfit` is a metric that evaluates the agreement between the observed and predicted data, while the `Regularization` is a metric constructed to assess the model's agreement with assumptions and prior knowledge. These are combined with a trade-off parameter to form a mathematical statement of the `InvProblem`, an optimization problem. The machinery to update the model is provided by the `Optimization`. An `Inversion` brings all of the elements together and dispatches `Directives` for solving the `InvProblem`. These `Directives` are instructions that capture the heuristics for solving the inverse problem; for example, specifying a target misfit that, once reached, terminates the inversion, or using a beta-cooling schedule that updates the value of the trade-off parameter between the `DataMisfit` and `Regularization` (cf. Parker (1994b); Oldenburg and Li (2005a) and references within).

The output of this process is a model that must be assessed and evaluated prior to interpretation; the entire process requires iteration by a human, where underlying assumptions and parameter choices are re-evaluated and challenged. Be it in resource exploration, characterization or development; environmental remediation or monitoring; or geotechnical applications – the goal of this model is to aid and inform a complex decision.

Here we note that the inversion framework described above is agnostic to the type of forward simulation employed, provided the machinery to solve the forward simulation

and compute sensitivities is implemented. Specific to the EM problem, we require this machinery for Maxwell’s equations. As such, we focus our attention on the Forward Simulation portion of the implementation for the EM problem and refer the reader to Cockett et al. (2015) and Oldenburg and Li (2005a) for a more complete discussion of inversions.

D.2.1 Governing Equations

Maxwell’s equations are the governing equations of electromagnetic problems. They are a set of coupled partial differential equations that connect electric and magnetic fields and fluxes. We consider the quasi-static regime, ignoring the contribution of displacement current (Ward and Hohmann, 1988; Telford et al., 1990b; Haber, 2014b)¹

We begin by considering the first order quasi-static EM problem in time,

$$\begin{aligned}\vec{\nabla} \times \vec{e} + \frac{\partial \vec{b}}{\partial t} &= \vec{s}_m \\ \vec{\nabla} \times \vec{h} - \vec{j} &= \vec{s}_e\end{aligned}\tag{D.1}$$

where \vec{e} , \vec{h} are the electric and magnetic fields, \vec{b} is the magnetic flux density, \vec{j} is the current density, and \vec{s}_m , \vec{s}_e are the magnetic and electric source terms. \vec{s}_e is a physical, electric current density, while \vec{s}_m is “magnetic current density”. Although \vec{s}_m is unphysical, as continuity of the magnetic current density would require magnetic monopoles, the definition of a magnetic source term can be a useful construct, as we will later demonstrate in Section D.4 (see also Ward and Hohmann (1988)).

By applying the Fourier Transform (using the $e^{i\omega t}$ convention), we can write Maxwell’s

¹In most geophysical electromagnetic surveys, low frequencies or late-time measurements are employed. In these scenarios $\sigma \gg \epsilon_0 \omega$ (eg. conductivities are typically less than 1S/m, $\epsilon_0 = 8.85 \times 10^{-12} F/m$ and frequencies considered are generally less than 10^5 Hz), so displacement current can safely be ignored.

equations in the frequency domain:

$$\begin{aligned}\vec{\nabla} \times \vec{E} + i\omega \vec{B} &= \vec{S}_m \\ \vec{\nabla} \times \vec{H} - \vec{J} &= \vec{S}_e\end{aligned}\tag{D.2}$$

where we use capital letters to denote frequency domain variables. The fields and fluxes are related through the physical properties: electrical conductivity σ , and magnetic permeability μ , as described by the constitutive relations

$$\begin{aligned}\vec{J} &= \sigma \vec{E} \\ \vec{B} &= \mu \vec{H}\end{aligned}\tag{D.3}$$

The physical properties, σ and μ are generally distributed and heterogeneous. For isotropic materials, σ and μ are scalars, while for anisotropic materials they are 3×3 symmetric positive definite tensors. The same constitutive relations can be applied in the time domain provided that the physical properties, σ, μ are not frequency-dependent.

In an EM geophysical survey, the sources provide the input energy to excite responses that depend on the physical property distribution in the earth. These responses, electric and magnetic fields and fluxes, are sampled by receivers to give the observed data. The simulation of Maxwell's equations may be conducted in either the time or frequency domain, depending on the nature of the source; harmonic waveforms are naturally represented in the frequency domain, while transient waveforms are better described in the time domain.

The aim of the inverse problem is to find a model, \mathbf{m} (which may be a voxel-based or a parametric representation) that is consistent with observed data and with prior knowledge and assumptions about the model. Addressing the inverse problem using

a gradient-based approach requires two abilities of the forward simulation: (1) the ability to compute predicted data given a model

$$\mathbf{d}_{\text{pred}} = \mathcal{F}[\mathbf{m}] \quad (\text{D.4})$$

and (2) the ability to compute or access the sensitivity, given by

$$\mathbf{J}[\mathbf{m}] = \frac{d\mathcal{F}[\mathbf{m}]}{d\mathbf{m}}. \quad (\text{D.5})$$

To employ second order optimization techniques, we also require the adjoint of the sensitivity, \mathbf{J}^\top . These two elements, when combined into the SIMPEG framework, enable data to be simulated and gradient-based inversions to be run. As such, this work benefits from other peoples' contributions to the underlying inversion machinery, including: discrete operators on a variety of meshes, model parameterizations, regularizations, optimizations, and inversion directives (Cockett et al., 2015).

D.3 Motivation

The motivation for the development of this framework is that it be a resource for researchers in the field of electromagnetic geophysics. To best serve this goal, we require a framework that is modular and extensible in order to enable exploration of ideas. An associated numerical implementation is essential for this work to be tested and acted upon. As such, we provide a tested, documented, fully open-source software implementation of the framework (under the permissive MIT license).

Specific to the EM problem, we require the implementation of Maxwell's equations in both the time domain and frequency domain. The implementation must allow for variable electrical conductivity and magnetic permeability, anisotropic physical

properties; various model parameterizations of the physical properties (e.g. voxel log-conductivity or parametric representations); a range of sources including wires, dipoles, natural sources; variable receiver types; variable formulations of Maxwell’s equations; solution approaches such as using a primary-secondary formulation; and the flexibility to work with and move between a variety of meshes such as tensor, cylindrically symmetric, curvilinear, and octree discretizations. Furthermore, the sensitivity computation must be flexible enough to be computed for any sensible combination of these approaches. In the following section, we will outline the framework we have used to organize and implement these ideas.

D.4 Simulation Framework

The aim of the forward simulation is to compute predicted data, \mathbf{d}_{pred} , when provided with an inversion model², \mathbf{m} and Sources. SIMPEGEM contains implementations for both time domain (TDEM) and frequency domain (FDEM) simulations, allowing data from commonly used EM methods to be simulated.

The framework we follow to perform the forward simulation is shown in Figure D.2; it consists of two overarching categories:

1. the Problem, which is the implementation of the governing equations,
2. the Survey, which provides the source(s) to excite the system as well as the receivers to sample the fields and produce predicted data at receiver locations.

Here, we provide a brief overview of each of the components, and discuss them in more detail in the sections that follow.

²We use the term *inversion model* to describe a parameterized representation of the earth (e.g. voxel-based or parametric), even if the model is solely used for forward modelling, its form sets the context for the inverse problem and the parameter-space that is to be explored.

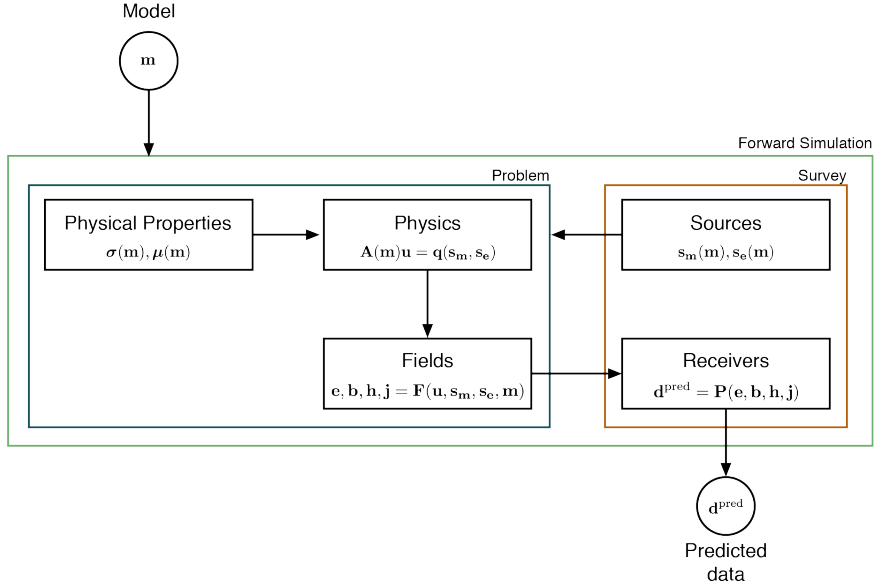


Figure D.2: Forward simulation framework.

The ‘engine’ of the forward simulation is the physics; it contains the machinery to solve the system of equations for EM fields and fluxes in the simulation domain when provided with a description of the physical properties and sources. In general, the physics engine may be an analytic or numeric implementation of Maxwell’s equations. Here, we focus our attention on the numerical implementation using a standard staggered-grid finite volume approach, requiring that the physical properties, fields, fluxes and sources be defined on a mesh (cf. Haber (2014b); Hyman et al. (2002); Hyman and Shashkov (1999); Yee (1966)). We discretize fields on edges, fluxes on faces and physical properties in cell centers, as shown in Figure D.3. To construct the necessary differential and averaging operators, we leverage the `Mesh` class within SIMPEG (Cockett et al., 2015, 2016a).

To compute electromagnetic responses, the forward simulation requires the definition of a physical property model describing the electrical conductivity (σ) and mag-

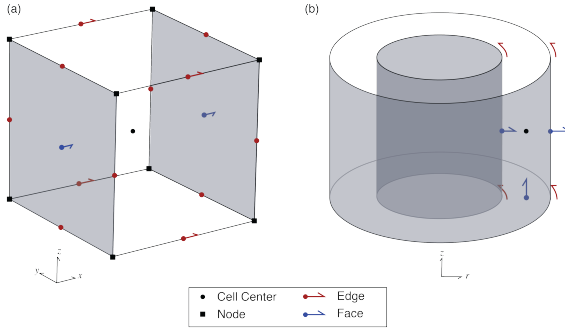


Figure D.3: Location of variables in the finite volume implementation for both a unit cell in (a) cartesian and (b) cylindrical coordinates (after Heagy et al. (2015))

netic permeability (μ) on the simulation mesh, as well as discrete representations of the sources used to excite EM responses (s_e, s_m). Often in solving an inverse problem, the model which one inverts for (the vector \mathbf{m}), is some discrete representation of the earth that is decoupled from the physical property model. This decoupling requires the definition of a Mapping capable of translating \mathbf{m} to physical properties on the simulation mesh. For instance, if the inversion model is chosen to be log-conductivity, an exponential mapping is required to obtain electrical conductivity (i.e. $\sigma = \mathcal{M}(\mathbf{m})$). To support this abstraction, SIMPEG provides a number of extensible Mapping classes (Cockett et al., 2015; Kang et al., 2015).

With both the physical property model and the source specified, we define and solve the physics, a Maxwell system of the form

$$\mathbf{A}(\mathbf{m})\mathbf{u} = \mathbf{q}(\mathbf{s}_m, \mathbf{s}_e), \quad (\text{D.6})$$

for an electric or magnetic field or flux. Here, \mathbf{A} is the system matrix that may eliminate a field or flux to obtain a system in a single field or flux, \mathbf{u} , the solution vector. Correspondingly, the vector \mathbf{q} is the second order right-hand-side. Note, if there are necessary

manipulations to make equation D.6 easier to solve numerically (e.g. symmetry) we can add these here; doing so has no effect on the derivative. The remaining fields and fluxes can be computed from \mathbf{u} anywhere in the simulation domain, through an operation of the form

$$\mathbf{f} = \mathbf{F}(\mathbf{u}(\mathbf{m}), \mathbf{s}_e(\mathbf{m}), \mathbf{s}_m(\mathbf{m}), \mathbf{m}) \quad (\text{D.7})$$

where \mathbf{f} is conceptually a vector of *all* of the fields and fluxes (i.e. \mathbf{e} , \mathbf{b} , \mathbf{h} and \mathbf{j}). This vector is never stored in the implementation, instead the fields are computed on demand through the subset of stored solution vectors (\mathbf{u}). From the computed fields (\mathbf{f}), predicted data are created by the Receivers through an operation of the form

$$\mathbf{d}_{\text{pred}} = \mathbf{P}(\mathbf{f}) \quad (\text{D.8})$$

In the simplest case, the action of \mathbf{P} selects the component of interest and interpolates the fields to the receiver locations, more involved cases could include the computation of ratios of fields, as is the case for impedance or tipper data. Obtaining predicted data from the framework concludes the forward simulation.

The same framework is employed for both time domain (TDEM) and frequency domain (FDEM) implementations within SIMPEGEM. In the case of the FDEM implementation, the matrix $\mathbf{A}(\mathbf{m})$ and the solution vector \mathbf{u} represent all frequencies. As these frequencies are independent (i.e. a block diagonal matrix, ), each frequency can be solved independently. In the TDEM code, the matrix $\mathbf{A}(\mathbf{m})$ and the solution vector \mathbf{u} represent all timesteps (Oldenburg et al., 2013; Haber, 2014b) and take the form of a lower triangular block matrix (bidiagonal in the case of Backward Euler, ), meaning the computation of each time-step depends on previous time-steps. The form of these matrices will be discussed further in the Physics section (Section D.4.2)

To perform a gradient-based inversion, we require the sensitivity of the data with respect to the inversion model, thus, each action taken to calculate data from the model must have an associated derivative. The full sensitivity is a dense matrix and is expensive to form and store, but when the optimization problem is solved using an iterative optimization approach, it does not need to be explicitly formed; all that is required are products and adjoint-products with a vector. We treat this using a modular approach so that individual elements of the framework can be rapidly interchanged or extended. The process we follow to compute matrix-vector products with the sensitivity is shown with red arrows in Figure D.4 (b). The sensitivity-vector product $\mathbf{J}\mathbf{v}$ is built in stages by taking matrix vector products with the relevant derivatives in each module, starting with the derivative of the physical property with respect to the model. The product with the adjoint is similarly shown in Figure D.4 (c) starting with the adjoint of the receiver operation.

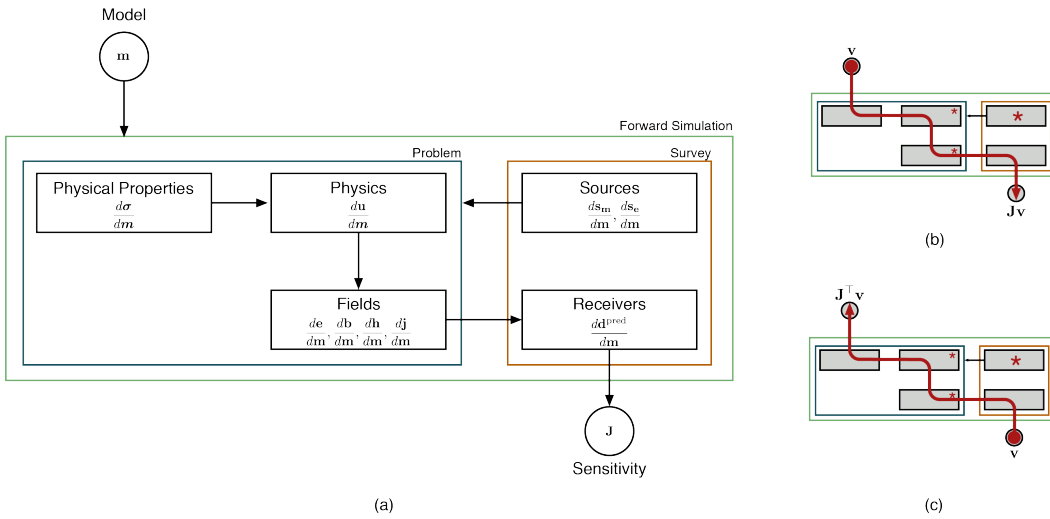


Figure D.4: (a) Contributions of each module to the sensitivity. (b) process for computing $\mathbf{J}\mathbf{v}$ and (c) $\mathbf{J}^\top \mathbf{v}$; stars indicate where the source derivatives are incorporated.

Using electrical conductivity, σ , as the only active property described by the inver-

sion model \mathbf{m} for brevity, the sensitivity takes the form

$$\mathbf{J}[\mathbf{m}] = \frac{d\mathbf{P}(\mathbf{f})}{d\mathbf{f}} \frac{d\mathbf{f}}{d\sigma} \frac{d\sigma}{d\mathbf{m}} = \underbrace{\frac{d\mathbf{P}(\mathbf{f})}{d\mathbf{f}}}_{\text{Receivers}} \left(\underbrace{\frac{\partial \mathbf{f}}{\partial \mathbf{u}} \frac{d\mathbf{u}}{d\sigma}}_{\text{Physics}} + \underbrace{\frac{\partial \mathbf{f}}{\partial \mathbf{s}_m} \frac{d\mathbf{s}_m}{d\sigma}}_{\text{Fields}} + \underbrace{\frac{\partial \mathbf{f}}{\partial \mathbf{s}_e} \frac{d\mathbf{s}_e}{d\sigma}}_{\text{Sources}} + \underbrace{\frac{\partial \mathbf{f}}{\partial \sigma}}_{\text{Sources}} \right) \underbrace{\frac{d\sigma}{d\mathbf{m}}}_{\text{Properties}} \quad (\text{D.9})$$

The annotations denote which of the elements shown in Figure D.4 are responsible for computing the respective contribution to the sensitivity. If the model provided is in terms of μ or a source/receiver location, this property replaces the role of σ . The flexibility to invoke distinct properties of interest (e.g. σ , μ , source location, etc.) in the inversion requires quite a bit of ‘wiring’ to keep track of which model parameters are associated with which properties; this is achieved through a property mapping or `PropMap` (physical properties, location properties, etc.) within SIMPEG.

Although typically the source terms do not have model dependence and thus their derivatives are zero, the derivatives of \mathbf{s}_e and \mathbf{s}_m must be considered in a general implementation. For example, if one wishes to use a primary-secondary approach, where source fields are constructed by solving a simplified problem, the source terms may have dependence on the model meaning their derivatives have a non-zero contribution to the sensitivity (c.f. Coggon (1971); Haber (2014b); Heagy et al. (2015)); this will be demonstrated in the Casing Example in Section D.5.3.

The derivative of the solution vector \mathbf{u} with respect to the model is found by implicitly taking the derivative of equation D.6 with respect to \mathbf{m} , giving

$$\frac{d\mathbf{u}}{d\mathbf{m}} = \mathbf{A}^{-1}(\mathbf{m}) \left(-\underbrace{\frac{\partial \mathbf{A}(\mathbf{m})\mathbf{u}^{\text{fix}}}{\partial \mathbf{m}}}_{\text{getADeriv}} + \underbrace{\frac{\partial \mathbf{q}}{\partial \mathbf{s}_m} \frac{d\mathbf{s}_m}{d\mathbf{m}} + \frac{\partial \mathbf{q}}{\partial \mathbf{s}_e} \frac{d\mathbf{s}_e}{d\mathbf{m}} + \frac{\partial \mathbf{q}}{\partial \mathbf{m}}}_{\text{getRHSDeriv}} \right) \quad (\text{D.10})$$

The annotations below the equation indicate the methods of the `Problem` class that are

responsible for calculating the respective derivatives. Typically the model dependence of the system matrix is through the physical properties (i.e. σ , μ). Thus, to compute derivatives with respect to \mathbf{m} , the derivatives are first taken with respect to σ and the dependence of σ on \mathbf{m} is treated using chain rule. The chain rule dependence is computed and tested automatically in SIMPEG using the composable Mapping classes.

In the following sections, we discuss the implementation of elements shown in Figure D.2 and highlight their contribution to the forward simulation and calculation of the sensitivity. We begin by discussing the inversion model and its relationship to the physical properties (Section D.4.1), move on to the core of the forward simulation, the Physics (Section D.4.2), and to how Sources which excite the system are defined (Section D.4.3). Following these, we then discuss how Fields are calculated everywhere in the domain (Section D.4.4) and how they are evaluated by the Receivers to create predicted data (Section D.4.5). We conclude this section with a Summary and discussion on testing (Section D.4.6).

D.4.1 Model and Physical Properties

For all EM problems, we require an inversion model that can be mapped to meaningful physical properties in the discretized Maxwell system. Typically, we consider the model to be a description of the electrical conductivity distribution in the earth. Often, the model is taken to be log-conductivity, in which case, an exponential mapping is required (`ExpMap`) to convert the model to electrical conductivity. The inversion model may be defined on a subset of a mesh and referred to as an ‘active cell’ model. For instance, air cells may be excluded and only the subsurface considered; in this case an `InjectActiveCells` map is used to inject the active model into the full simulation domain. In the case of a parametric inversion, the inversion model is defined on a domain that is independent of the forward modelling mesh and the mapping takes the parametric representation and defines a physical property on the forward modelling mesh (e.g. a gaussian ellipsoid defined geometrically) (Li et al., 2010; Pidlisecky et al., 2011; McMillan et al., 2015b; Kang et al., 2015). Maps can be composed, for instance, a layered, 1D log conductivity model defined only in the subsurface may be mapped to

a 2D cylindrical Mesh, as shown in Figure D.5.

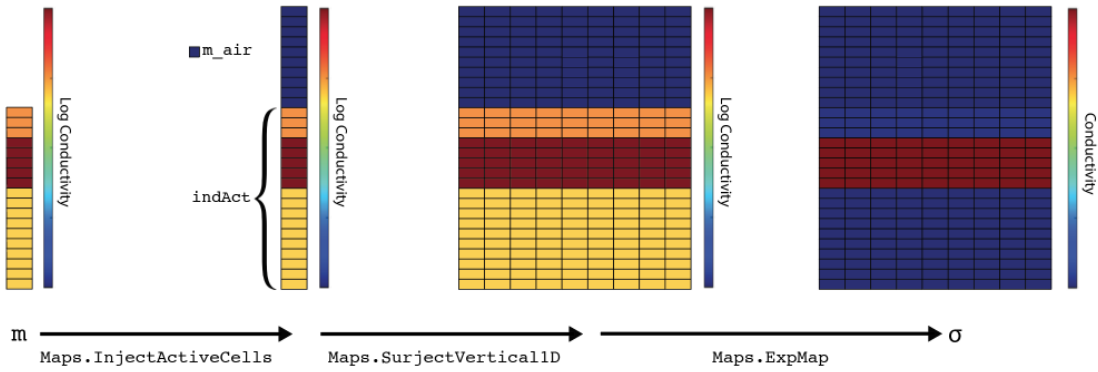


Figure D.5: Mapping an inversion model, a 1D layered, log conductivity model defined below the surface, to electrical conductivity defined in the full simulation domain.

```

import numpy as np
from SimPEG import Mesh, Maps
mesh = Mesh.CylMesh([20, 20])      # SimPEG cylindrically symmetric mesh
m_air = np.log(1e-8)                # value of the model in the air cells
indAct = mesh.vectorCCz < 0.0       # define active cells to be subsurface only
mapping = ( Maps.ExpMap(mesh) *
            Maps.SurjectVertical1D(mesh) *
            Maps.InjectActiveCells(mesh, indAct, m_air, nC=mesh.nCz) )

```

In the code above, the ‘multiplication’ performs the composition of the mappings. For the contribution of this action to the sensitivity, the derivative of the electrical conductivity with respect to the model is computed using the chain rule for the composed maps (cf. Kang et al. (2015); Heagy et al. (2014b)). During an inversion, the electrical conductivity on the simulation mesh associated with the current inversion model and its derivative are accessed through the `BaseEMProblem`, which is inherited by both the TDEM and FDEM problems. In some cases, variable magnetic permeability must be considered; this is accomplished through a property mapping (`PropMap`). The `PropMap` handles the organization and independent mappings of distinct physical properties (i.e.

σ, μ).

D.4.2 Physics

To formulate a system of equations from Maxwell's equations in time (equation D.1) or frequency (equation D.2) that can be solved numerically using a finite volume approach, we require a statement of the problem in terms of two equations with two unknowns, one of which is a field (discretized on edges), and the other a flux (discretized on faces). Thus, we can consider either the E-B formulation, or the H-J formulation. For the frequency-domain problem, we can discretize the electric field, \vec{e} , on edges, the magnetic flux, \vec{b} , on faces, physical properties σ and μ^{-1} at cell centers, and the source terms \vec{s}_m and \vec{s}_e on faces and edges, respectively (see Figure D.3). Doing so, we obtain the discrete system:

$$\begin{aligned} \mathbf{C}\mathbf{e} + i\omega\mathbf{b} &= \mathbf{s}_m \\ \mathbf{C}^\top \mathbf{M}_{\mu^{-1}}^f \mathbf{b} - \mathbf{M}_\sigma^e \mathbf{e} &= \mathbf{s}_e \end{aligned} \tag{D.11}$$

where \mathbf{C} is the discrete edge curl, $\mathbf{M}_{\mu^{-1}}^f$ is the face inner-product matrix for μ^{-1} , \mathbf{M}_σ^e is the edge inner-product matrix for σ ; these inner product matrices can be computed for isotropic, diagonally anisotropic or fully anisotropic physical properties using operators within SIMPEG's Mesh class (Cockett et al., 2015, 2016a).

Note that the source-term \mathbf{s}_e is an integrated quantity. Alternatively, the H-J formulation discretizes \vec{h} on edges, \vec{j} on faces, ρ and μ at cell centers, and the source terms \vec{s}_m, \vec{s}_e on edges and faces, respectively, giving

$$\begin{aligned} \mathbf{C}^\top \mathbf{M}_\rho^f \mathbf{j} + i\omega \mathbf{M}_\mu^e \mathbf{h} &= \mathbf{s}_m \\ \mathbf{Ch} - \mathbf{j} &= \mathbf{s}_e. \end{aligned} \tag{D.12}$$

Similarly, \mathbf{s}_m is an integrated quantity. In a full 3D simulation, the electric and magnetic contributions for the two formulations are merely staggered from one another. However, if using an assumption of cylindrically symmetry, the appropriate formulation must be used to simulate either rotational electric or magnetic contributions (Heagy et al., 2015). For both the basic FDEM and TDEM implementations, natural boundary conditions ($\mathbf{b} \times \hat{\mathbf{n}} = 0 \forall \vec{x} \in \partial\Omega$ in E-B formulation or $\mathbf{j} \times \hat{\mathbf{n}} = 0 \forall \vec{x} \in \partial\Omega$ in H-J formulation), in which the fields are assumed to have decayed to a negligible value at the boundary, are employed to construct the differential operators, the framework and implementation are however, extensible to consider other boundary conditions (cf. Haber (2014b); Rivera Rios (2014)).

In order to solve either equation D.11 or equation D.12, we eliminate one variable and solve the second order system. This elimination is performed by the FDEM problem classes. For instance, in FDEM Problem_e, we eliminate \mathbf{b} and obtain a second order system in \mathbf{e}

$$\underbrace{\left(\mathbf{C}^\top \mathbf{M}_{\mu^{-1}}^f \mathbf{C} + i\omega \mathbf{M}_\sigma^e \right)}_{\text{getA}} \underbrace{\mathbf{e}}_{\mathbf{u}} = \underbrace{\mathbf{C}^\top \mathbf{M}_{\mu^{-1}}^f \mathbf{s}_m - i\omega \mathbf{s}_e}_{\text{getRHS}} \quad (\text{D.13})$$

FDEM Problem_e has methods getA and getRHS to construct the system

```
def getA(self, freq):
    MfMui = self.MfMui
    MeSigma = self.MeSigma
    C = self.mesh.edgeCurl
    return C.T * MfMui * C + 1j * omega(freq) * MeSigma

def getRHS(self, freq):
    s_m, s_e = self.getSourceTerm(freq)
    MfMui = self.MfMui
    C = self.mesh.edgeCurl
    return C.T * (MfMui * s_m) - 1j * omega(freq) * s_e
```

and associated methods getADeriv and getRHSDeriv to construct the derivatives of each with respect to the inversion model. These function definitions are methods of the Problem class, where the `self` variable refers to the instance of the class, and is

standard Python (cf. Python documentation - <https://docs.python.org/3/tutorial/classes.html>).

For FDEM `Problem_e`, `getRHSDeriv` is zero unless one or both of the source terms have model dependence. However, if we eliminate \mathbf{e} and solve for \mathbf{b} (`Problem_b`), the right hand side contains the matrix \mathbf{M}_σ^e , and therefore will, in general, have a non-zero derivative. To solve this linear system of equations, SIMPEG interfaces to standard numerical solver packages (e.g. SciPy, Mumps (Oliphant, 2007; Amestoy et al., 2001, 2006), using for example `pymatsolver` <https://github.com/rowanc1/pymatsolver>). The components used to perform the forward simulation are assembled in the `fields` method of the `BaseFDEMProblem` class; the `fields` method solves the forward simulation for the solution vector \mathbf{u} (from equation D.13) at each frequency and source considered.

Similarly, for the time-domain problem, the semi-discretized E-B formulation is given by

$$\begin{aligned} \mathbf{C}\mathbf{e} + \frac{d\mathbf{b}}{dt} &= \mathbf{s}_m \\ \mathbf{C}^\top \mathbf{M}_{\mu^{-1}}^f \mathbf{b} - \mathbf{M}_\sigma^e \mathbf{e} &= \mathbf{s}_e \end{aligned} \tag{D.14}$$

and the semi-discretized H-J formulation is given by

$$\begin{aligned} \mathbf{C}^\top \mathbf{M}_\rho^f \mathbf{j} + \frac{d\mathbf{M}_\mu^e \mathbf{h}}{dt} &= \mathbf{s}_m \\ \mathbf{C}\mathbf{h} - \mathbf{j} &= \mathbf{s}_e. \end{aligned} \tag{D.15}$$

For the time discretization, we use Backward Euler (cf. Ascher (2008)). To form the TDEM `Problem_b`, we eliminate \mathbf{e} from equation D.14 and apply Backward Euler for

the time discretization. A single timestep takes the form

$$\underbrace{\left(\mathbf{C} \mathbf{M}_\sigma^e \mathbf{C}^\top \mathbf{M}_{\mu^{-1}}^f + \frac{1}{\Delta t^k} \right)}_{\mathbf{A}_0^{k+1}(\mathbf{m})} \underbrace{\mathbf{b}^{k+1}}_{\mathbf{u}^{k+1}} + \underbrace{\frac{-1}{\Delta t^k} \mathbf{I}}_{\mathbf{A}_{-1}^{k+1}(\mathbf{m})} \underbrace{\mathbf{b}^k}_{\mathbf{u}^k} = \underbrace{\mathbf{C} \mathbf{M}_\sigma^e \mathbf{s}_e^{k+1} + \mathbf{s}_m^{k+1}}_{\mathbf{q}^{k+1}(\mathbf{s}_m, \mathbf{s}_e)} \quad (\text{D.16})$$

where $\Delta t^k = t^{k+1} - t^k$ is the timestep and the superscripts $k, k+1$ indicate the time index. Each TDEM problem formulation (ie. `Problem_e`, `Problem_b`, `Problem_h`, `Problem_j`) has methods to create the matrices along the block-diagonals, $\mathbf{A}_0^{k+1}(\mathbf{m})$ and $\mathbf{A}_{-1}^{k+1}(\mathbf{m})$, as well as a method to construct the right hand side, $\mathbf{q}^{k+1}(\mathbf{s}_m, \mathbf{s}_e)$, at each timestep. When inverting for a model in electrical conductivity using `Problem_b`, the subdiagonal matrices are independent of \mathbf{m} , however, in other formulations, such as `Problem_e`, the subdiagonal matrices do have dependence on electrical conductivity, thus in general, the model dependence must be considered. Depending on the solver chosen, it can be advantageous to make the system symmetric; this is accomplished by multiplying both sides by $\mathbf{M}_{\mu^{-1}}^f$. To solve the full time-stepping problem, we assemble all timesteps in a lower block bidiagonal matrix, with on-diagonal matrices $\mathbf{A}_0^k(\mathbf{m})$ and sub-diagonal matrices $\mathbf{A}_{-1}^k(\mathbf{m})$, giving

$$\underbrace{\begin{pmatrix} \mathbf{A}_0^0(\mathbf{m}) & & & \\ \mathbf{A}_{-1}^1(\mathbf{m}) & \mathbf{A}_0^1(\mathbf{m}) & & \\ & \mathbf{A}_{-1}^2(\mathbf{m}) & \mathbf{A}_0^2(\mathbf{m}) & \\ & \ddots & \ddots & \\ & & \mathbf{A}_{-1}^{n-1}(\mathbf{m}) & \mathbf{A}_0^{n-1}(\mathbf{m}) \\ & & & \mathbf{A}_{-1}^n(\mathbf{m}) & \mathbf{A}_0^n(\mathbf{m}) \end{pmatrix}}_{\mathbf{A}(\mathbf{m})} \underbrace{\begin{pmatrix} \mathbf{u}^0 \\ \mathbf{u}^1 \\ \mathbf{u}^2 \\ \vdots \\ \mathbf{u}^{n-1} \\ \mathbf{u}^n \end{pmatrix}}_{\mathbf{u}} = \underbrace{\begin{pmatrix} \mathbf{q}^0 \\ \mathbf{q}^1 \\ \mathbf{q}^2 \\ \vdots \\ \mathbf{q}^{n-1} \\ \mathbf{q}^n \end{pmatrix}}_{\mathbf{q}(\mathbf{s}_m, \mathbf{s}_e)} \quad (\text{D.17})$$

When solving the forward simulation, the full time-stepping matrix, $\mathbf{A}(\mathbf{m})$, is not formed, instead the block system is solved using forward substitution with each block-row being computed when necessary. The initial condition, \mathbf{u}^0 , depends on the source type and waveform; it is computed numerically or specified using an analytic solution. For example, if using a grounded source and a step-off waveform, \mathbf{u}^0 is found by solving the direct current resistivity or the magnetometric resistivity problem, depending on which field we choose to solve for. When a general current waveform is considered, the initial condition will be $\mathbf{u}^0 = \mathbf{0}$, and either \mathbf{s}_m or \mathbf{s}_e , depending on type of the source used, will have non-zero values during the on-time.

Derivatives of the matrices along the block-diagonals of $\mathbf{A}(\mathbf{m})$ along with derivatives of the right-hand-side are stitched together in a forward time stepping approach to compute the contribution of $\frac{d\mathbf{u}}{d\mathbf{m}}$ to $\mathbf{J}\mathbf{v}$ and in a backwards time stepping approach for the contribution of $\frac{d\mathbf{u}}{d\mathbf{m}}^\top$ to $\mathbf{J}^\top\mathbf{v}$.

D.4.3 Sources

Sources input EM energy into the system. They can include grounded wires, loops, dipoles and natural sources. Controlled sources are implemented in the FDEM and TDEM modules of SIMPEGEM, and natural sources are implemented in the NSEM module. For simulations, we require that the sources be discretized onto the mesh so that a right-hand-side for the Maxwell system can be constructed (i.e. `getRHS`). This is addressed by the `eval` method of the source which returns both the magnetic and electric sources ($\mathbf{s}_m, \mathbf{s}_e$, shown in Figure D.2) on the simulation mesh.

In some cases, a primary-secondary approach can be advantageous for addressing the forward problem (cf. Coggon (1971); Haber (2014b); Heagy et al. (2015)). We split up the fields and fluxes into primary and secondary components ($\mathbf{e} = \mathbf{e}^P + \mathbf{e}^S$, $\mathbf{b} =$

$\mathbf{b}^{\mathcal{P}} + \mathbf{b}^{\mathcal{S}}$) and define a “Primary Problem”, a simple problem, often with an analytic solution, that is solved in order to construct a source term for a secondary problem. For instance, a point magnetic dipole source may be simulated by defining a zero-frequency primary which satisfies

$$\begin{aligned}\mathbf{e}^{\mathcal{P}} &= 0 \\ \mathbf{C}^{\top} \mathbf{M}_{\mu^{-1}}^f \mathbf{b}^{\mathcal{P}} &= \mathbf{s}_e^{\mathcal{P}}.\end{aligned}\tag{D.18}$$

If we define $\mu^{-1}{}^{\mathcal{P}}$ to be a constant, equation D.18 has an analytic solution for $\mathbf{b}^{\mathcal{P}}$ that may be expressed in terms of a curl of a vector potential (cf. Griffiths (2007)). When using a mimetic discretization, by defining the vector potential and taking a discrete curl, we maintain that the magnetic flux density is divergence free as the divergence operator is in the null space of the edge curl operator ($\nabla \cdot \nabla \times \vec{v} = 0$), so numerically we avoid creating magnetic monopoles (c.f. Haber (2014b)). The secondary problem is then

$$\begin{aligned}\mathbf{Ce}^{\mathcal{S}} + i\omega \mathbf{b}^{\mathcal{S}} &= -i\omega \mathbf{b}^{\mathcal{P}} \\ \mathbf{C}^{\top} \mathbf{M}_{\mu^{-1}}^f \mathbf{b}^{\mathcal{S}} - \mathbf{M}_{\sigma}^e \mathbf{e}^{\mathcal{S}} &= -\mathbf{C}^{\top} \left(\mathbf{M}_{\mu^{-1}}^f - \left(\mathbf{M}_{\mu^{-1}}^f \right)^{\mathcal{P}} \right) \mathbf{b}^{\mathcal{P}}\end{aligned}\tag{D.19}$$

The source terms for the secondary problem are $\mathbf{s}_m = -i\omega \mathbf{b}^{\mathcal{P}}$, and $\mathbf{s}_e = -\mathbf{C}^{\top} (\mathbf{M}_{\mu^{-1}}^f - \mathbf{M}_{\mu^{-1}}^f {}^{\mathcal{P}}) \mathbf{b}^{\mathcal{P}}$. In scenarios where magnetic permeability is homogeneous, the electric source contribution is zero.

The left hand side is the same discrete Maxwell system as in equation D.11; the distinction is that we are solving for secondary fields, and a primary problem was solved (analytically or numerically) in order to construct the source terms. To obtain the total fields, which we sample with the receivers, we must add the primary fields back to the solution. To keep track of the primary fields, they are assigned as properties of the

source class.

In most cases, source terms do not have a derivative with respect to the model. However, in a primary-secondary problem in electrical conductivity the source term depends on the electrical conductivity and derivatives must be considered (see Section D.5.3). This is similar to inverting for magnetic permeability using a primary-secondary approach described in equation D.19 (Coggon, 1971; Haber, 2014b; Heagy et al., 2015). It is also possible to consider your inversion model to be the location or waveform of the source, in which case the derivative is also non-zero and source derivatives can be included in the optimization procedure.

D.4.4 Fields

By solving the second-order linear system, as in equation D.13, we obtain a solution vector, \mathbf{u} , of one field or flux everywhere in the domain. In the case of a primary-secondary problem, this solution is a *secondary* field. To examine all of the fields, we require easy access to the total fields and total fluxes everywhere in the domain. This is achieved through the `Fields` object.

For efficient memory usage, only the solution vector is stored, all other fields and fluxes are calculated on demand through matrix vector multiplications. As such, each problem type (`e`, `b`, `h`, `j`) has an associated `Fields` object with methods to take the solution vector and translate it to the desired field or flux. For instance, `Fields_j` stores the solution vector from `Problem_j` and has methods to compute the total magnetic field in the simulation domain by first computing the secondary magnetic field from the solution vector (\mathbf{u} ; in this example, $\mathbf{u} = \mathbf{j}$) and adding back any contribution from the source

$$\mathbf{h} = \frac{1}{i\omega} \mathbf{M}_\mu^e -1 \left(-\mathbf{C}^\top \mathbf{M}_\rho^f \mathbf{u} + \mathbf{s}_m \right) \quad (\text{D.20})$$

For their contribution to the sensitivity (equation D.9), the fields have methods to compute derivatives when provided the vectors \mathbf{v} and $\frac{d\mathbf{u}}{d\mathbf{m}}\mathbf{v}$ (from the Physics). For instance, for \mathbf{h}

$$\frac{d\mathbf{h}}{d\mathbf{m}}\mathbf{v} = \frac{d\mathbf{h}}{d\mathbf{u}} \left(\frac{d\mathbf{u}}{d\mathbf{m}}\mathbf{v} \right) + \left(\frac{d\mathbf{h}}{ds_e} \frac{ds_e}{d\mathbf{m}} + \frac{d\mathbf{h}}{ds_m} \frac{ds_m}{d\mathbf{m}} + \frac{\partial \mathbf{h}}{\partial \mathbf{m}} \right) \mathbf{v} \quad (\text{D.21})$$

The derivatives for \mathbf{e} , \mathbf{b} , and \mathbf{j} take the same form. Conceptually, the product of the full derivative and a vector ($\frac{df}{d\mathbf{m}}\mathbf{v}$) can be thought of as a stacked vector of all of the contributions from all of the fields and fluxes, however, this is never formed in practice.

D.4.5 Receivers

The measured data consist of specific spatial components of the fields or fluxes sampled at the receiver locations at a certain time or frequency. Receivers have the method `eval` that interpolates the necessary components of the fields and fluxes to the receiver locations and evaluates the data required for the problem, such as the frequency domain fields or natural source impedance data. For the frequency domain problem, real and imaginary components are treated as separate data so that when inverting, we are always working with real values. The separation of the data evaluation from fields in receiver objects allows the derivative computation to be performed and tested in a modular fashion; this enables rapid development and implementation of new receiver types.

D.4.6 Summary

Having defined the role of each of the elements in the forward simulation framework outlined in Figure D.2, the necessary machinery to compute predicted data and sensitivities is at hand for both FDEM and TDEM problems. The modular nature of the framework allows us to make several abstractions which make the code more transpar-

ent and ensure consistency across implementations. For instance, the definition of the physical properties and associated inner product matrices is common to all formulations in both time and frequency domains. Thus, these are defined as properties of a `BaseEM` class which is inherited by both the `TDEM` and `FDEM` modules. Within each of the `TDEM` and `FDEM` modules, common methods for the calculation of the fields, sensitivities and adjoint are defined and shared across the approaches that solve for \mathbf{e} , \mathbf{b} , \mathbf{h} , or \mathbf{j} (see the documentation <http://docs.simpeg.xyz>).

Testing is conducted using comparisons with analytics, cross-comparisons between formulations, order tests on the sensitivity, adjoint tests, examples, tests on the finite volume operators, projections, interpolations, solvers, etc. Tests are run upon each update to the repository through the continuous integration service TravisCI (Kalderimis and Meyer, 2011). This ensures that we can trust the tools that we use and move faster in our research into new methods and implementations. This also supports new developers and researchers in contributing to the code base without fear of breaking assumptions and ideas laid out by previous development.

D.5 Examples

To demonstrate the application and structure of the framework, we explore three examples, one field example and two synthetic examples. The purpose of the first synthetic example is to show simple time and frequency domain electromagnetic inversions, and highlight the common framework. For this, we invert for a 1D layered Earth using a 2D cylindrically symmetric mesh for the forward simulation. In the second example, we show 1D inversions of field data (RESOLVE and SkyTEM) collected over the Bookpurnong Irrigation district in Australia. The final example is a 3D synthetic example that demonstrates a sensitivity analysis using a parametric model of a block in

a layered space for a reservoir characterization problem where the transmitter is positioned down-hole in a steel-cased well. We use this example to demonstrate how mappings, multiple physical properties (both electrical conductivity and magnetic permeability), and multiple meshes, a cylindrically symmetric and a 3D tensor mesh, can be composed in a primary-secondary approach for performing the forward simulation and computing the sensitivities. The scripts used to run these examples are available on <http://docs.simpeg.xyz>.

D.5.1 Cylindrically Symmetric Inversions

The purpose of this example is to demonstrate the implementation of the electromagnetic inversion in both time and frequency domains. We have chosen this example as it is computationally light, can be run on any modern laptop without installing complex dependencies, and yet it uses most of the elements and functionality needed to solve a large 3D EM problem. The script used to run this simulation is available at: <https://doi.org/10.6084/m9.figshare.5035175>.

We consider two 1D inversions for log-conductivity from an EM survey, one frequency domain experiment and one time domain experiment. Both surveys use a vertical magnetic dipole (VMD) source located on the surface. For simplicity, we consider a single receiver, measuring the vertical magnetic field, located 50m radially away from the source. The magnetic permeability is taken to be that of free space ($\mu = \mu_0$), and electrical conductivity is assumed to be frequency-independent.

Figure D.6 shows the setup used for: (a) the frequency domain simulation, (b) the time domain simulation, and (c) the common inversion implementation. In both, a cylindrical mesh is employed for the forward simulation and a 1D layered earth, described in terms of log-conductivity. To map the inversion model to electrical conductivity, a

composite mapping is used to inject the 1D subsurface model into one including air cells (`InjectActiveCells`), surject the 1D model onto the 2D simulation mesh (`SurjectVertical1D`) and take the exponential to obtain electrical conductivity (`ExpMap`), as described in the Model and Physical Properties section (Section D.4.1).

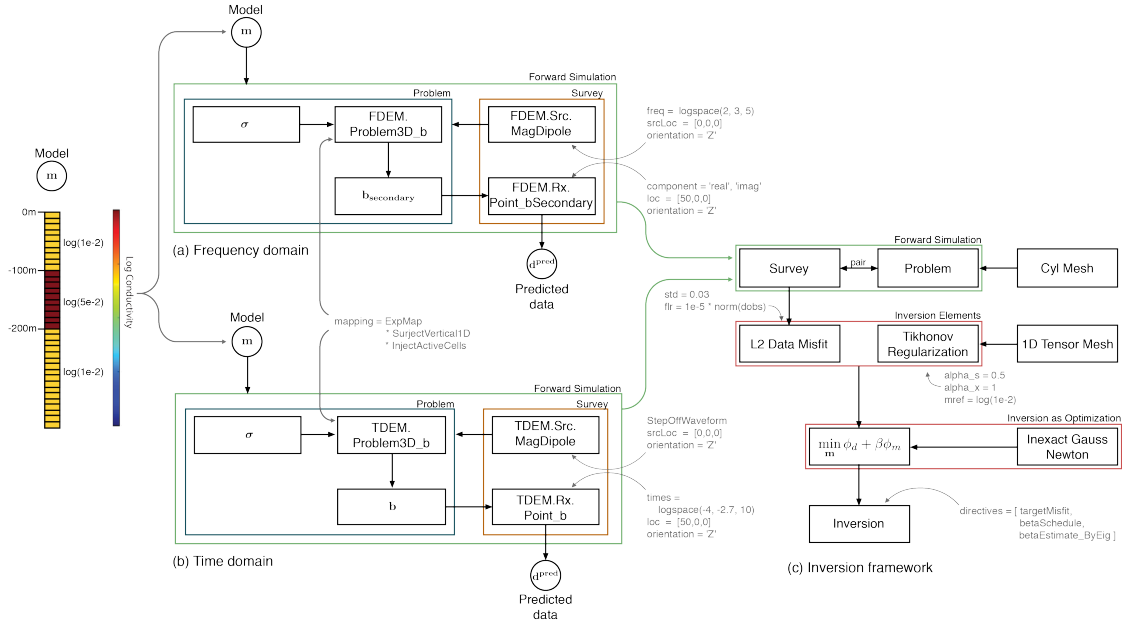


Figure D.6: Diagram showing the entire setup and organization of (a) the frequency domain simulation; (b) the time domain simulation; and (c) the common inversion framework used for each example. The muted text shows the programmatic inputs to each class instance.

The distinction between the frequency and time domain inversions comes in the setup of the forward simulations. Each employs the appropriate description of the physics (FDEM or TDEM) in the problem, and the definition of the survey, consisting of both sources and receivers, must be tailored to the physics chosen. For the FDEM survey, a vertical harmonic magnetic dipole located at the origin transmits at five frequencies logarithmically spaced between 100 Hz and 1000 Hz. The receiver is located at (50 m, 0 m, 0 m) and measures the secondary magnetic flux (with the primary being the free-space response of a harmonic magnetic dipole). The observed response is

complex- valued, having both real and imaginary components. We consider these as separate data, giving a total of ten data points for this example. For the time domain survey, we again use a vertical magnetic dipole at the origin, however, we now use a step-off waveform. The observed responses are defined through time, and thus are all real-valued. For this example, we sample 10 time channels, logarithmically spaced between 10^{-4} s and 2×10^{-3} s . These time channels were selected to be sensitive to depths similar to the FDEM simulation.

With the forward simulation parameters defined in both the time and frequency domain simulations, we can generate synthetic data. The model used consists of a 100m thick conductive layer (0.05 S/m) whose top boundary is 100 m-below from the surface, as shown in Figure D.6. The conductivity of the half-space earth is 0.01 S/m. In both cases, 3% gaussian noise is added to the simulated data, and these are treated as the observed data (\mathbf{d}^{obs}) for the inversion.

For the inversions, we specify the inversion elements: a data misfit and a regularization. We use an L2 data misfit of the form

$$\phi_d = \frac{1}{2} \|\mathbf{W}_d(\mathbf{d}^{\text{pred}} - \mathbf{d}^{\text{obs}})\|_2^2 \quad (\text{D.22})$$

where $\mathbf{W}_{d_{ii}} = 1/\varepsilon_i$ and we define $\varepsilon_i = 3\%|d_i^{\text{obs}}| + \text{floor}$. For both simulations the floor is set to $10^{-5}\|\mathbf{d}^{\text{obs}}\|$. The regularization is chosen to be a Tikhonov regularization on the 1D model

$$\phi_m = \frac{1}{2} (\alpha_s \|\mathbf{m} - \mathbf{m}_{\text{ref}}\|_2^2 + \alpha_x \|\mathbf{D}_x \mathbf{m}\|_2^2) \quad (\text{D.23})$$

where \mathbf{m}_{ref} is the reference model which is set to be a half- space of $\log(10^{-2})$. The matrix \mathbf{D}_x is a 1D gradient operator. For both examples $\alpha_s = 0.5$ and $\alpha_x = 1$. The data misfit and regularization are combined with a trade-off parameter, β , in the statement

of the inverse problem. To optimize, we use the second-order Inexact Gauss Newton scheme. In this inversion, we use a beta-cooling approach, where β is reduced by a factor of 4 every 3 Gauss Newton iterations.

The initial β is chosen to relatively weight the influence of the data misfit and regularization terms. We do this by estimating the largest eigenvalue of $\mathbf{J}^\top \mathbf{J}$ and $\mathbf{W}_m^\top \mathbf{W}_m$ using one iteration of the power method. We then take their ratio and multiply by a scalar to weight their relative contributions. For this example, we used a factor of 10. For a stopping criteria, we use the discrepancy principle, stopping the inversion when $\phi_d \leq \chi \phi_d^*$, with $\chi = 1$ and $\phi_d^* = 0.5N_{data}$ (with ϕ_d as defined in equation D.22.)

The FDEM inversion reaches the target misfit after 9 iterations, and the TDEM inversion reaches the target misfit after 6 iterations. Figure D.7 shows the recovered models (a), predicted and observed data for the FDEM inversion (b) and predicted and observed data for the TDEM inversion (c). In both the FDEM and TDEM inversions, the data are fit well. The recovered models are smooth, as is expected when employing an L2, Tikhonov regularization and both the location and amplitude of the conductive layer. The structure of both models are comparable, demonstrating that the information content in both the FDEM and TDEM data are similar. The recovered model can be improved by many additional techniques that are not explored here (e.g. using compact norms in the regularization). The SIMPEG package provides a number of additional directives and regularization modules which can be useful for this purpose.

D.5.2 Bookpurnong Field Example

The purpose of this example is to demonstrate the use of the framework for inverting field data and provide an inversion that can be compared with other results in the literature. In particular, we invert frequency and time domain data collected over the

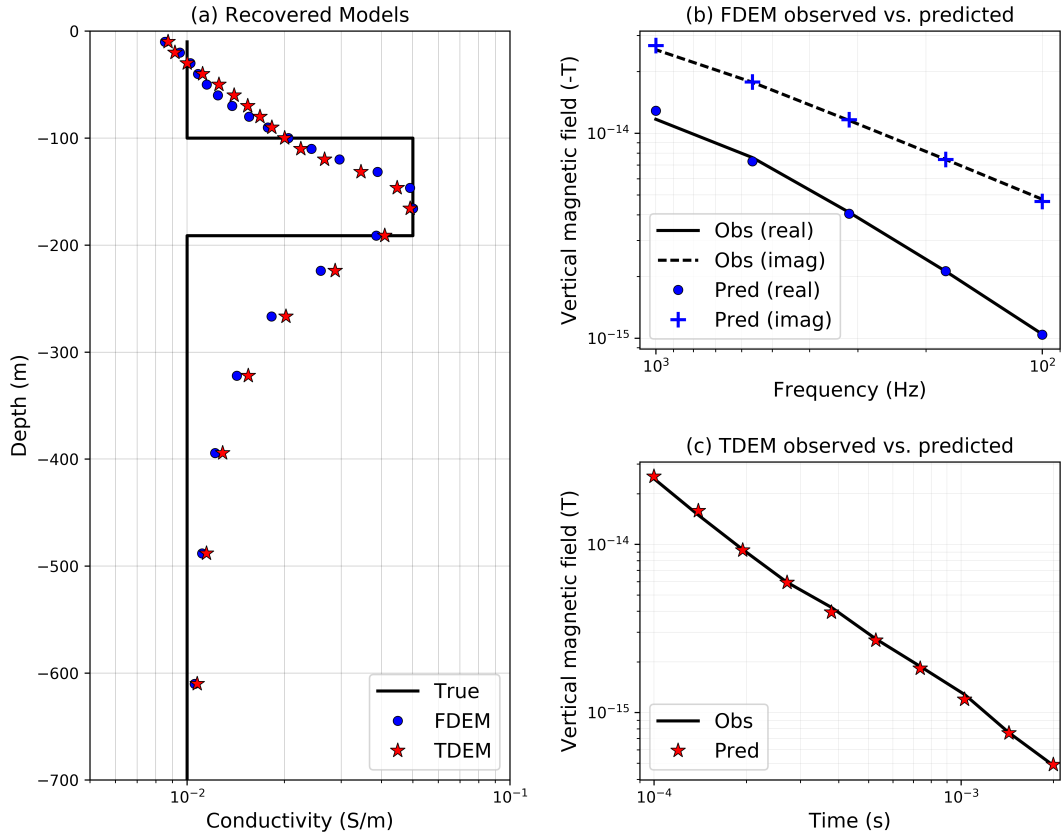


Figure D.7: (a) True and recovered models for the FDEM and TDEM inversions; predicted and observed data for (b) the FDEM example, and (c) the TDEM example. In (b) the magnetic field data are in the negative z-direction.

Bookpurnong Irrigation District in Southern Australia. The Murray River and adjacent floodplain in the Bookpurnong region have become extensively salinized, resulting in vegetation die-back (Munday et al., 2006; Overton et al., 2004). Multiple electrical and electromagnetic data sets have been collected with the aim of characterizing the near-surface hydrologic model of the area (Munday et al., 2006). For a more complete background on the geology and hydrogeology of the Bookpurnong region, we refer the reader to Munday et al. (2006).

Here, we will focus our attention to the RESOLVE frequency-domain data collected

in 2008 and the SkyTEM time-domain data collected in 2006. These data are shown in Figure D.8. The RESOLVE system consists of 5 pairs of horizontal coplanar coils, with nominal frequencies of 400 Hz, 1800 Hz, 8200 Hz, 40 000 Hz, and 130 000 Hz as well as a vertical coaxial coil pair of coils which operates at 3200Hz. For the Bookpurnong survey, the bird was flown at \sim 50m altitude (Viezzoli et al., 2010). The SkyTEM time-domain system operates in two transmitter modes that can be run sequentially. The high moment mode has high current and operates at a low base frequency (25 Hz and can be lowered to 12.5 Hz), and the low moment operates at a lower current and higher base frequency (222.5 Hz) (Sørensen and Auken, 2004). The Bookpurnong SkyTEM survey was flown at an altitude of \sim 60m (Viezzoli et al., 2010).

Multiple authors have inverted these data sets; 1D spatially constrained inversions of the SkyTEM and RESOLVE data were performed by (Viezzoli et al., 2009, 2010). Yang (2017) independently inverted these data in 1D and provides a discussion at <http://em.geosci.xyz/content/case>. The SkyTEM data (high moment) were inverted in 3D by (Wilson et al., 2010). In the example that follows, we select a location where both the RESOLVE and SkyTEM datasets have soundings and invert them in 1D, we then proceed to perform a stitched 1D inversion of the RESOLVE data. The data have been made available with the permission of CSIRO and are accessible, along with the script used to run the inversions at <https://doi.org/10.6084/m9.figshare.5107711>.

1D Inversion of RESOLVE and SkyTEM soundings

We have selected a sounding location (462100m, 6196500m) at which to perform 1D inversions of the RESOLVE and SkyTEM (High Moment) data. The observed data at this location are shown in Figure D.9 (b) and (c). For the RESOLVE inversion, we consider the horizontal co-planar data collected at 400 Hz, 1800 Hz, 8200 Hz, 40 000

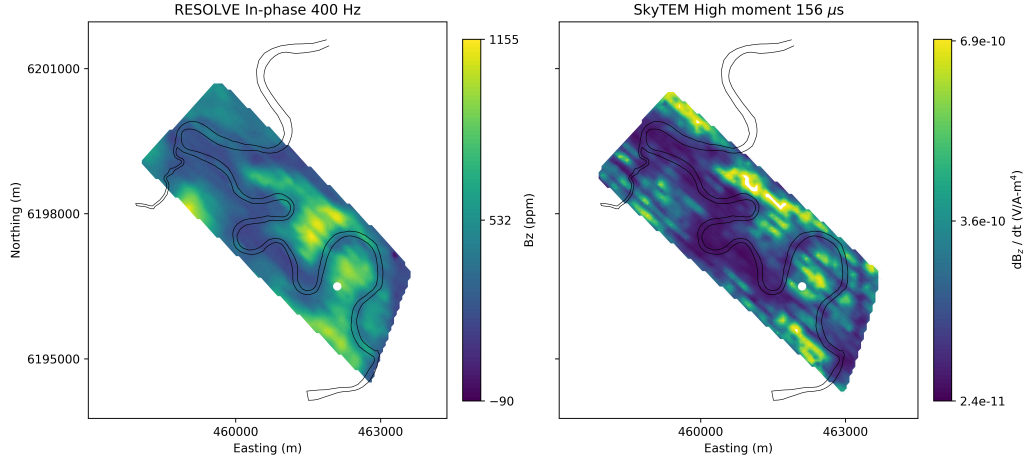


Figure D.8: 400 Hz In-phase RESOLVE data at (left) and High Moment SkyTEM data at $156 \mu\text{s}$. The white dot at (462100m, 6196500m) on both images is the location of the stations chosen to demonstrate the 1D inversions in frequency and time.

Hz, and 130 000 Hz. For the noise model, we assign 10% error for the three lowest frequencies and 15% error for the two highest; a noise floor of 20 ppm is assigned to all data. The inversion mesh uses cells that expand logarithmically with depth, starting at the surface with a finest cell size of 1 m. The forward simulation is carried out on the cylindrically symmetric mesh, similar to the previous example. In the inversion, we employ a Tikhonov regularization in which length scales have been omitted in the regularization function. A fixed trade-off parameter of $\beta = 2$ is used, α_z is set to be 1, and α_s is 10^{-3} . A half-space reference model with conductivity 0.1 S/m is used, this also served as the starting model for the inversion. The inversion reached target misfit after 2 iterations. The resulting model and data fits are shown in Figure D.9. Very close to the surface, we recover a resistor, while below that, we recover a conductive unit (~ 2 S/m). Examining the data (Figure D.9b), we see that the real components are larger in magnitude than the imaginary, and that with increasing frequency, the magnitude of the

imaginary component decreases while the real component increases; such behaviour is consistent with an inductive- limit response, and we thus expect to recover conductive structures in the model.

For the time domain inversion, we consider the SkyTEM high moment data. We use the source waveform shown in the inset plot in Figure D.9 (c). For data, we use 21 time channels from $47 \mu\text{s}$ to 4.4 ms; the latest three time channels (5.6ms, 7ms and 8.8 ms) are not included. For data errors, we assign a 12% uncertainty and a floor of $2.4 \times 10^{-14} \text{ V/Am}^4$. We again use a Tikhonov regularization, here with $\alpha_z = 1$ and $\alpha_s = 10^{-1}$. The trade-off parameter is $\beta = 20$. A half-space starting model of 0.1 S/m is again employed. For the reference model, we use the model recovered from the RESOLVE 1D inversion. As we are using the high-moment data, we do not expect the SkyTEM data to be as sensitive to the near surface structures as the RESOLVE data. By using the model recovered in the RESOLVE inversion as the starting model for the SkyTEM inversion, we can assess agreement between the two and isolate structures that are introduced by the SkyTEM inversion. The inversion reached the target misfit after 3 iteration and the results are shown in Figure D.9. At this location, there is good agreement in the models recovered from the RESOLVE and SkyTEM data, with both supporting a near-surface resistor and showing a deeper conductive structure.

Stitched 1D inversion of RESOLVE data

Next, we perform a stitched 1D inversion of the RESOLVE data set. With this example, we aim to demonstrate a practical inversion workflow that will run on modest computational resources. As such, we have heavily downsampled the data set, taking 1021 stations of the 40 825 collected. A 1D stitched inversion is a relatively straight-forward approach for creating a conductivity model - each sounding is inverted independently

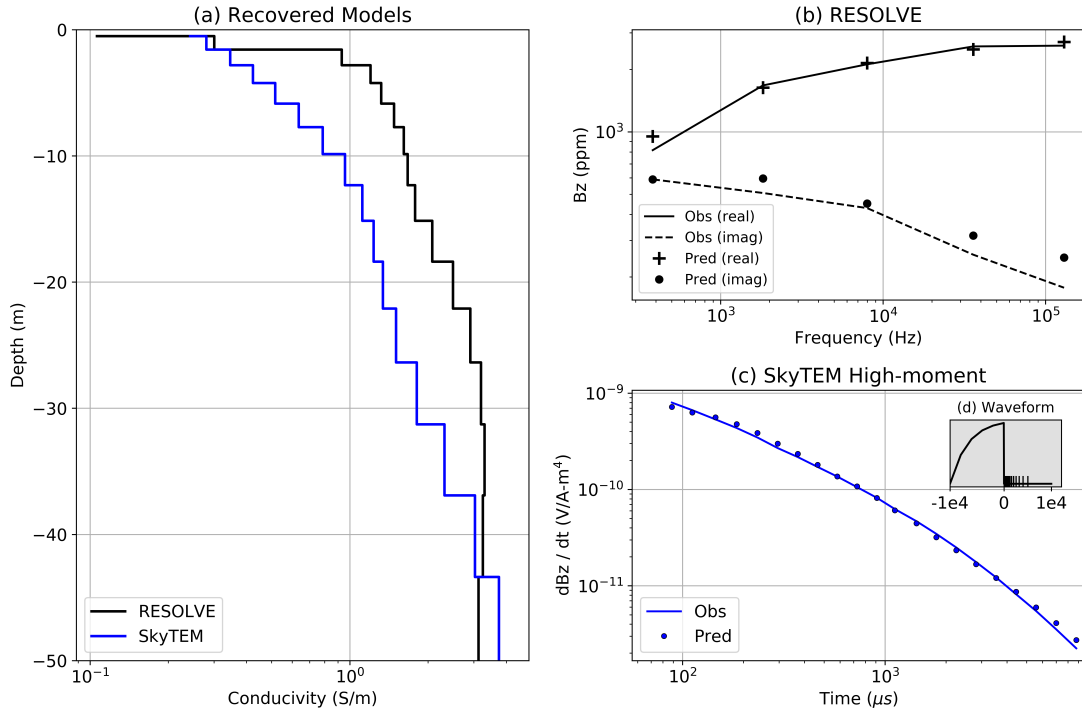


Figure D.9: (a) Models recovered from the 1D inversion of RESOLVE (back) and SkyTEM (blue) data at the location (462100m, 6196500m). (b) Observed (lines) and predicted (points) frequency domain data. (c) Observed and predicted time domain data. (d) Source waveform used in for the SkyTEM inversion, the x-axis is time (μ s) on a linear scale.

and the inversion results are then assembled to create a 3D model. This can be a valuable quality-control step prior to adopting more advanced techniques such as including lateral or 3D regularization across soundings or even performing a 3D inversion. In cases where the geology is relatively simple, a stitched 1D inversion may be sufficient. The inversion parameters are the same as those used in the inversion of the RESOLVE sounding discussed in the previous section. A plan- view of the recovered model 9.9m below the surface is shown in Figure D.10a. A global χ - factor of 0.74 was reached, and plots comparing the real component of the observed and predicted data at 400Hz are shown in Figures D.10 (b) & (c).

The recovered model (Figure D.10a), bears similar features to the models found by Viezzoli et al. (2010) (Figure 4 of Viezzoli et al. (2010)) and by Yang (2017). In general, the northwestern portion of the Murray river is more resistive, in particular near (459 000m, 6 200 000m) and (460 000m, 6 198 000m) while the southeastern portion of the river is more conductive. Two mechanisms of river salinization have been discussed in Munday et al. (2006); Viezzoli et al. (2010): the resistive regions are attributed to a “losing” groundwater system, in which freshwater from the Murray River discharges to adjacent banks, while the conductive regions are attributed to a “gaining” system, in which regional saline groundwater seeps into the river.

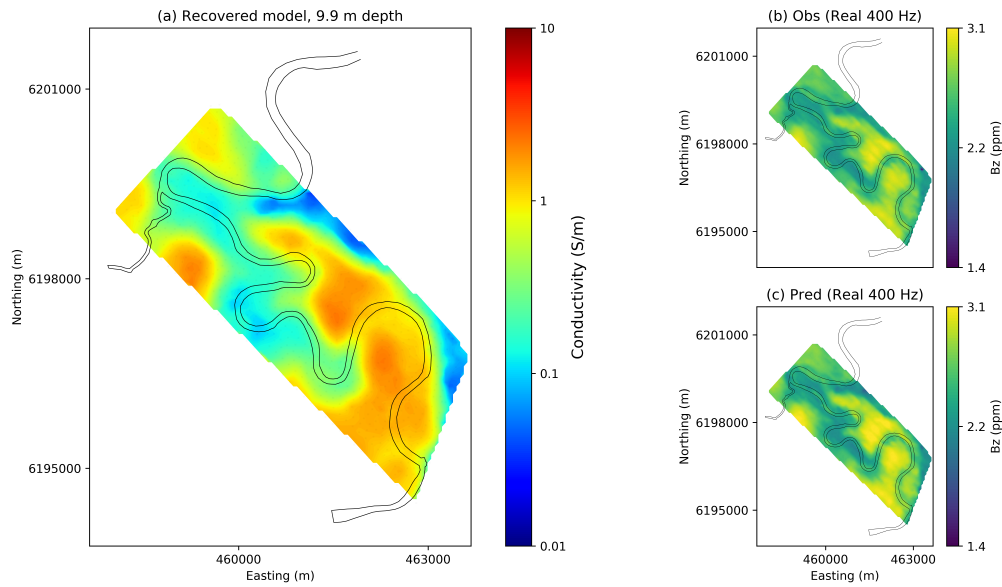


Figure D.10: (a) Conductivity model 9.9m below the surface from a stitched 1D inversion of RESOLVE data. (b) Real component of the observed RESOLVE data at 400Hz. (c) Real component of the predicted data at 400Hz.

D.5.3 Steel-Cased Well: Sensitivity Analysis for a Parametric Model

The purpose of this example is to demonstrate the modular implementation of sim-pegEM and how it can be used to experiment with simulation and inversion approaches. Conducting electromagnetic surveys in settings where steel casing is present is growing in interest for applications such as monitoring hydraulic fracturing or enhanced oil recovery (Hoversten et al., 2015; Um et al., 2015; Commer et al., 2015; Hoversten et al., 2014; Marsala et al., 2015; Cuevas, 2014a; Weiss et al., 2015; Yang et al., 2016). Steel is highly conductive ($\sim 5.5 \times 10^6 \text{ S/m}$), has a significant magnetic permeability ($\sim 50\mu_0 - 100\mu_0$) (Wu and Habashy, 1994). This is a large contrast to typical geologic settings, with conductivities typically less than 1 S/m and permeabilities similar to that of free space, μ_0 . In addition to the large physical property contrast, the geometry of well casing also presents a significant computational challenge. Well casing is cylindrical in shape and only millimeters thick, while the geologic structures we aim to characterize are on the scale of hundreds of meters to kilometers. Inverting electromagnetic data from such settings requires that we have the ability to accurately simulate and compute sensitivities for models with casing and 3D geologic variations. One strategy that may be considered is using a primary- secondary approach, simulating the casing in a simple background and using these fields to construct a source for the secondary problem which considers the 3 dimensional structures of interest (Heagy et al., 2015). Here, we demonstrate how the framework can be employed to implement this approach and compute the sensitivities. The parametric representation of the model allows us to investigate the expected data sensitivity to specific features of the model such as the location, spatial extent and physical properties of a geologic target. Such an analysis may be used to investigate how well we expect certain features of the model to be resolved

in an inversion and it could be employed as a survey design tool. In what follows, we outline the general approach and then discuss a specific implementation. The script used to generate this example is available at: <https://doi.org/10.6084/m9.figshare.5036123>.

Approach

In this example we design a survey to resolve a conductive body in a reservoir layer in the presence of a vertical, steel-cased well as shown in Figure D.11. To calculate the sensitivity of the data with respect to each model parameter requires that we be able to simulate and calculate derivatives of each component used to simulate data.

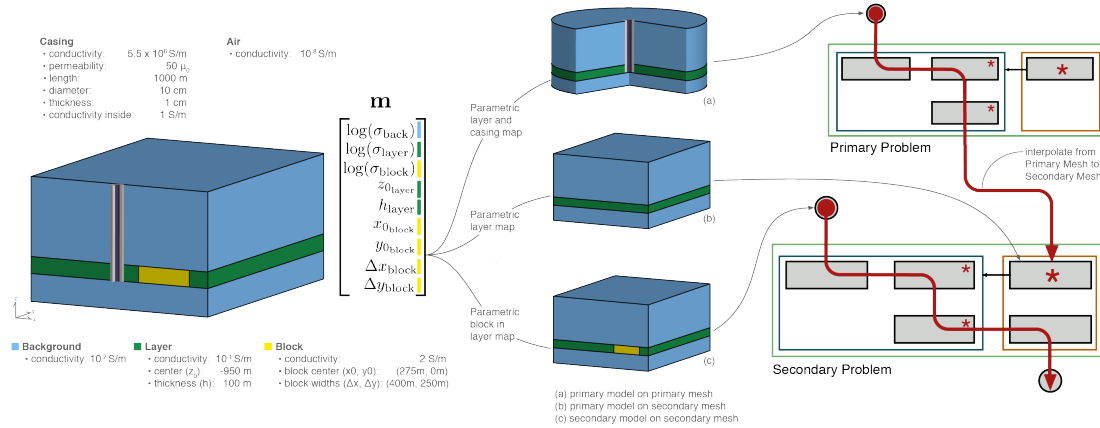


Figure D.11: Setup of parametric models and calculation of the sensitivity for a primary secondary approach of simulating 3D geology and steel casing.

We use a primary-secondary approach, as described in Heagy et al. (2015). The physical properties, fields and fluxes are composed of two parts, a primary and a secondary part. For example in the E-B formulation, $\sigma = \sigma^{\mathcal{P}} + \sigma^{\mathcal{S}}$, $\mu = \mu^{\mathcal{P}} + \mu^{\mathcal{S}}$, $\vec{E} = \vec{E}^{\mathcal{P}} + \vec{E}^{\mathcal{S}}$, $\vec{B} = \vec{B}^{\mathcal{P}} + \vec{B}^{\mathcal{S}}$. A primary problem, which includes the cylindrically

symmetric part of the model (casing, source, and layered background) is defined

$$\begin{aligned}\vec{\nabla} \times \vec{E}^{\mathcal{P}} + i\omega \vec{B}^{\mathcal{P}} &= 0 \\ \vec{\nabla} \times \mu^{-1} \vec{B}^{\mathcal{P}} - \sigma^{\mathcal{P}} \vec{E}^{\mathcal{P}} &= \vec{s}_e.\end{aligned}\tag{D.24}$$

This primary problem is solved on a cylindrically symmetric mesh with cells fine enough to capture the width of the casing and its solution yields the primary fields. The primary fields are then interpolated to a 3D tensor mesh, suitable for discretizing 3D reservoir-scale features. The primary fields are used to construct the source current density for the secondary problem, given by

$$\begin{aligned}\vec{\nabla} \times \vec{E}^{\mathcal{S}} + i\omega \vec{B}^{\mathcal{S}} &= 0 \\ \vec{\nabla} \times \mu^{-1} \vec{B}^{\mathcal{S}} - \sigma \vec{E}^{\mathcal{S}} &= \vec{q} \\ \vec{q} &= (\sigma - \sigma^{\mathcal{P}}) \vec{E}^{\mathcal{P}}.\end{aligned}\tag{D.25}$$

By solving the secondary problem, we then obtain secondary fields and fluxes. These are sampled by the receivers to create predicted data.

In equation D.25, we see that the source term, \vec{q} has model dependence through σ , $\sigma^{\mathcal{P}}$ and $\vec{E}^{\mathcal{P}}$. Typically primary-secondary approaches are used when the background is assumed to be known, as it is captured in the primary. Here, however, we do not wish to assume that the background is known; in practice it may be constrained, but it is not generally well known. The primary solution is used instead to separate the contributions of the casing and the block so that we can avoid a potentially crippling assumption. This approach allows an appropriately tailored mesh to be constructed for each problem. Thus, we require derivatives not only on the 3D secondary mesh, but also derivatives of the primary fields (in this case on a cylindrically symmetric mesh). To

implement this type of primary-secondary problem, we construct a Primary-Secondary source which solves the primary problem to provide the primary fields. Since all derivatives are implemented for the primary problem, when computing sensitivities for the secondary problem, the derivatives due to the primary problem are accounted for in the contributions of the source term to the derivative. This is conceptually shown in Figure D.11.

For this example, we wish to investigate how sensitive the specified survey is to aspects of the model which we might want to resolve in a field survey, such as the geometry and location of the anomalous body, as well as the physical properties of the geologic units. A voxel-based description of the model does not promote investigation of these questions, so we will instead apply a parametric description of the model. The model is parameterized into nine parameters which we consider to be unknowns ($\log(\sigma_{\text{background}})$, $\log(\sigma_{\text{layer}})$, $\log(\sigma_{\text{block}})$, $z_{0\text{layer}}$, h_{layer} , $x_{0\text{block}}$, Δx_{block} , $y_{0\text{block}}$, Δy_{block}). In what follows, we examine the sensitivity of the data with respect to these model parameters.

Implementation

The model we use is shown in Figure D.11. It consists of a 1km long vertical steel cased well (diameter: 10 cm, thickness: 1cm) with conductivity $\sigma = 5.5 \times 10^6$ S/m, and magnetic permeability $\mu = 50\mu_0$. The casing is assumed to be filled with fluid having a conductivity of 1S/m. The background has a resistivity of $100\Omega\text{m}$, and the 100m thick reservoir layer has a resistivity of $10\Omega\text{m}$. The target of this survey is the conductive block (2S/m) with dimensions $400\text{m} \times 250\text{m} \times 100\text{m}$. The source used consists of two grounded electrodes, a positive electrode coupled to the casing at a depth of 950m, and a return electrode 10km from the wellhead on the surface. We consider a frequency-domain experiment at a transmitting frequency of 0.5Hz and 1A current. For

data, we consider two horizontal components (x and y) of the real part of the electric field measured at the surface.

To accomplish this simulation and sensitivity calculation, we construct 3 mappings, shown conceptually in Figure D.11, in order to obtain: (1) $\sigma^{\mathcal{P}}$ on the primary (cylindrical) mesh, (2) $\sigma^{\mathcal{P}}$ on the secondary mesh (as is needed in equation D.25) and (3) σ on the secondary mesh. Differentiability of the electrical conductivity models with respect to each of the 9 parameters is achieved by constructing the model using arctangent functions (cf. Aghasi et al. (2011); McMillan et al. (2015b)). Each of these parameterizations can be independently tested for second-order convergence to check the validity of the computation of the derivatives (cf. Haber (2014b)).

The source term for the secondary fields requires that we simulate the primary fields. For this, we use the mapping of \mathbf{m} to $\sigma^{\mathcal{P}}$ on the primary mesh and employ the H-J formulation of Maxwell's equations in the frequency domain in order to describe a vertically and radially oriented current density and a rotational magnetic field. In this simulation, we also consider the permeability of the casing. The source consists of a wire-path terminating downhole at -950m where it is coupled to the casing. At the surface, the return electrode is 10km radially away from the well³. With these parameters defined, we have sufficient information to solve the primary problem and thereby obtain the primary electric field everywhere in the simulation domain. The real, primary current density for this example is shown in Figure D.12.

This primary field is described on the cylindrical mesh, so in order to use it to construct the source term for the secondary problem, we interpolate it to the 3D tensor mesh. The remaining pieces necessary for the definition of the secondary source on the 3D

³Due to the symmetry employed, the return electrode is a disc. Numerical experiments over a half-space show that the real, radial electric field from the cylindrical simulation exhibits the same character as the 3D simulation but is slightly reduced in magnitude.

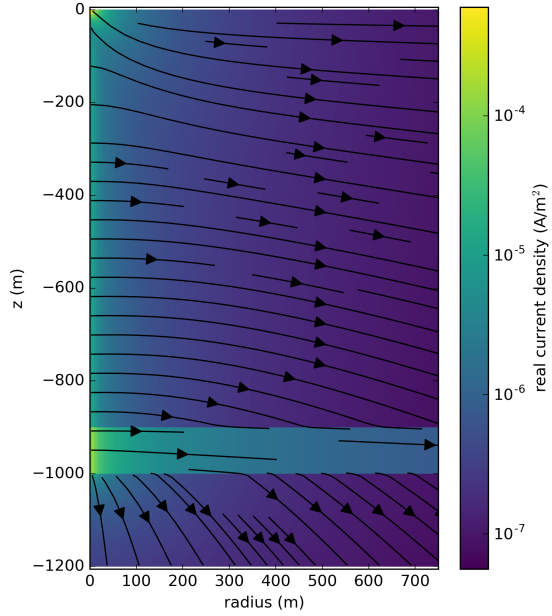


Figure D.12: Cross sectional slice of primary (casing + background) real current density. The colorbar is logarithmically scaled and shows the amplitude of the real current density.

mesh are defining σ and $\sigma^{\mathcal{P}}$; this is achieved through the mappings defined above. The primary problem and source, along with the mapping required to define $\sigma^{\mathcal{P}}$, are used to define a primary-secondary source, which solves a forward simulation to compute the secondary source-current, \mathbf{s}_e , shown in Figure D.13. Note that the source current density is only present where there are structures in the secondary model that were not captured in the primary, in this case, where the conductive block is present.

With the source term for the secondary problem defined, the secondary problem is then solved resulting in the predicted data at the surface. Here, we focus our attention to the real x, y components of the electric field, as shown in Figure D.14. The top two panels show the total (casing and conductive target) x-component (a) and y-component (b) of the electric field while the bottom two panels show the secondary (due to the conductive target, outlined in white) x-component (c) and y-component (d) of the electric

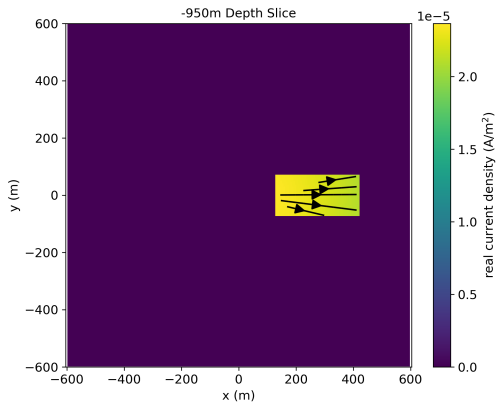


Figure D.13: Depth slice at $z=-950\text{m}$ showing the source current density for the secondary problem.

field. As expected, the total electric field is dominated by the source that is located in the casing. As shown in Figure D.12 the majority of the current is exiting into the layer at depth, but current is still emanating along all depths of the casing. Measured electric fields at the surface are sensitive to the currents that come from the top part of the casing and hence the observed fields are strongest closest to the pipe and they fall off rapidly with distance. The behavior of the secondary electric field is, to first order, like that expected from a dipole at depth oriented in the x -direction. It has a broad smooth signature at the surface.

Now that the pieces are in place to perform the forward simulation, we want to compute the sensitivity. Generally, we do not form the full sensitivity when performing an inversion as it is a large, dense matrix. Here however, since the inversion model is composed of only nine parameters, the final sensitivity matrix is small (nine by number of data). The steps followed to stitch together and compute the sensitivity are shown in the diagram in Figure D.11. To check the simulation approach for this example, the sensitivity is tested for second-order convergence (cf. Haber (2014b)).

Figures D.15, D.16 and D.17 shows the sensitivity of both the real E_x (left), and real

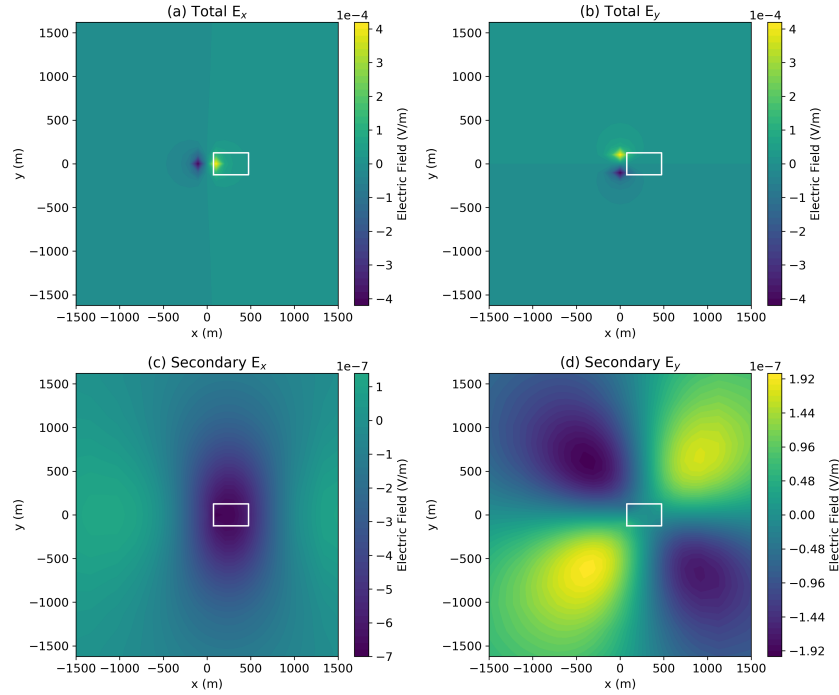


Figure D.14: Simulated real electric field data as measured at the surface using a primary secondary approach for casing and a conductive target (outlined in white). The upper panels show the total E_x (a) and E_y (b); the lower panels show the secondary (due to the conductive block) E_x (c) and E_y (d). Note that the colorbars showing the secondary electric fields are not on the same scale. The limits of the colorbars have been set so that the zero-crossing is always shown in the same color.

E_y (right) data with respect to each of the 9 model parameters. Note that the colorbars are not identical in each image and the units of the sensitivity are dependent on the parameter under consideration. In each image, the white outline shows the horizontal location of the block.

In Figure D.15, we focus on the physical properties of the background layer and block, all parametrized in terms of $\log(\sigma)$. Clearly, the conductivity of the background has the largest influence on the data, in particular near the well (at the origin), followed by the conductivity of the layer, where the injection electrode is situated. There are 4

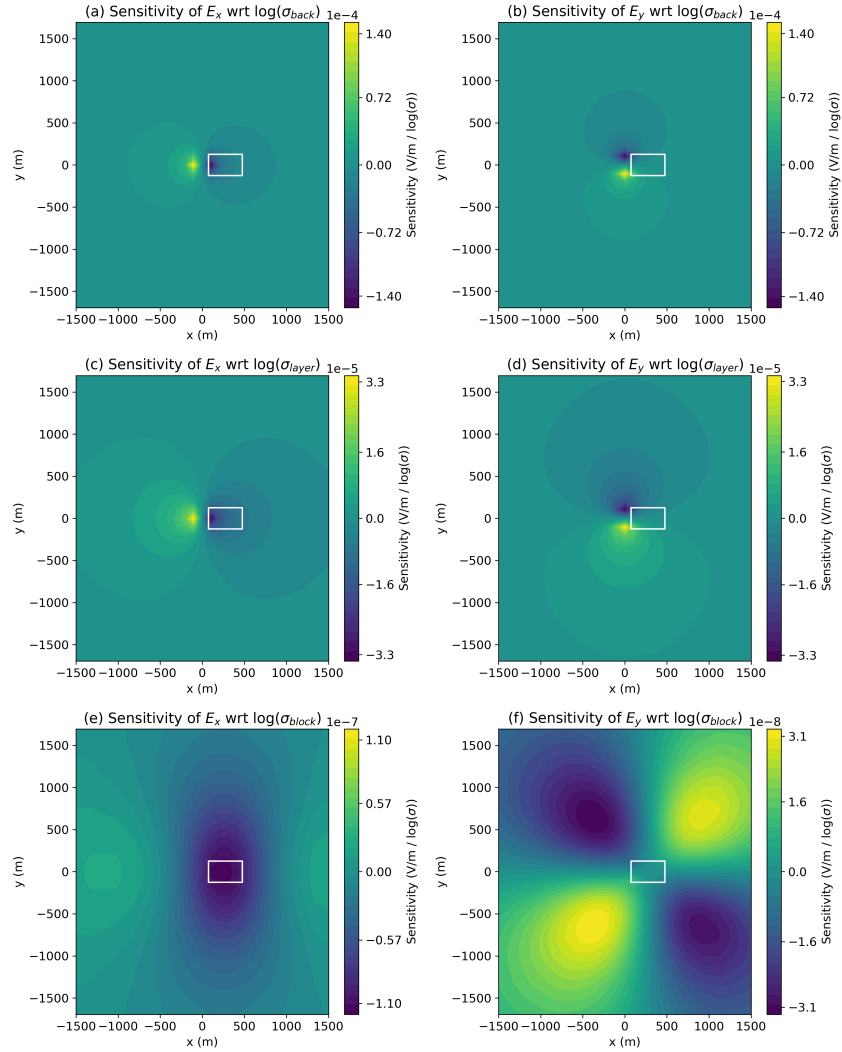


Figure D.15: Sensitivity of surface real E_x (left) and E_y (right) data with respect to the physical properties, $((V/m)/(\log(\sigma)))$

orders of magnitude difference between the maximum sensitivity of the data with respect to the conductivity of the block and that of the background. This indicates that in order to resolve such an anomalous body, the background must be well-constrained. When looking at Figure D.15 (f), we see that the areas of largest sensitivity of the E_y data with respect to the physical properties of the block are spatially distant from the body and the well. This indicates that if one is designing a survey, it may be advantageous to collect

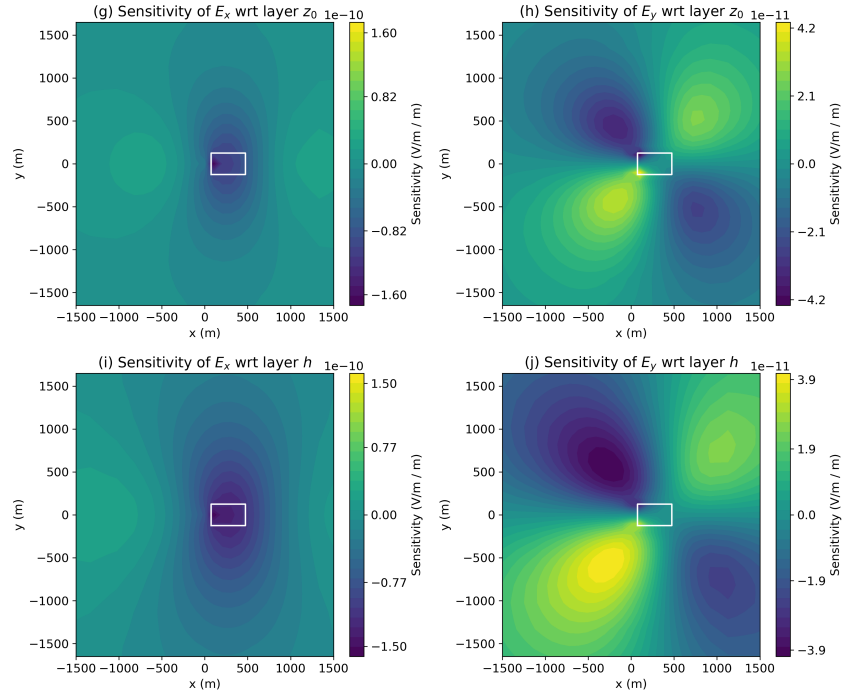


Figure D.16: Sensitivity of surface real E_x (left) and E_y (right) data with respect to the layer geometry, $((V/m)/m)$

data in these regions as these are also regions where the influence of the properties of the background are less dominant.

In Figure D.16, we focus on the depth and thickness of the layer. Note that the depth and thickness of the block are constrained to be the same as the layer, so the character of the sensitivity is influenced by the presence of the block. Here, the units of the sensitivity are $(V/m)/m$. Similarly, Figure D.17 shows the sensitivity with respect to the geometric properties of the block.

To compare between the physical properties and geometry of the model, the scales of interest must be taken into consideration. In Table D.1, we show the maximum amplitude of the sensitivity with respect to each individual model parameter. From this, we approximate the sensitivity as linear about the true model and compute the perturbation

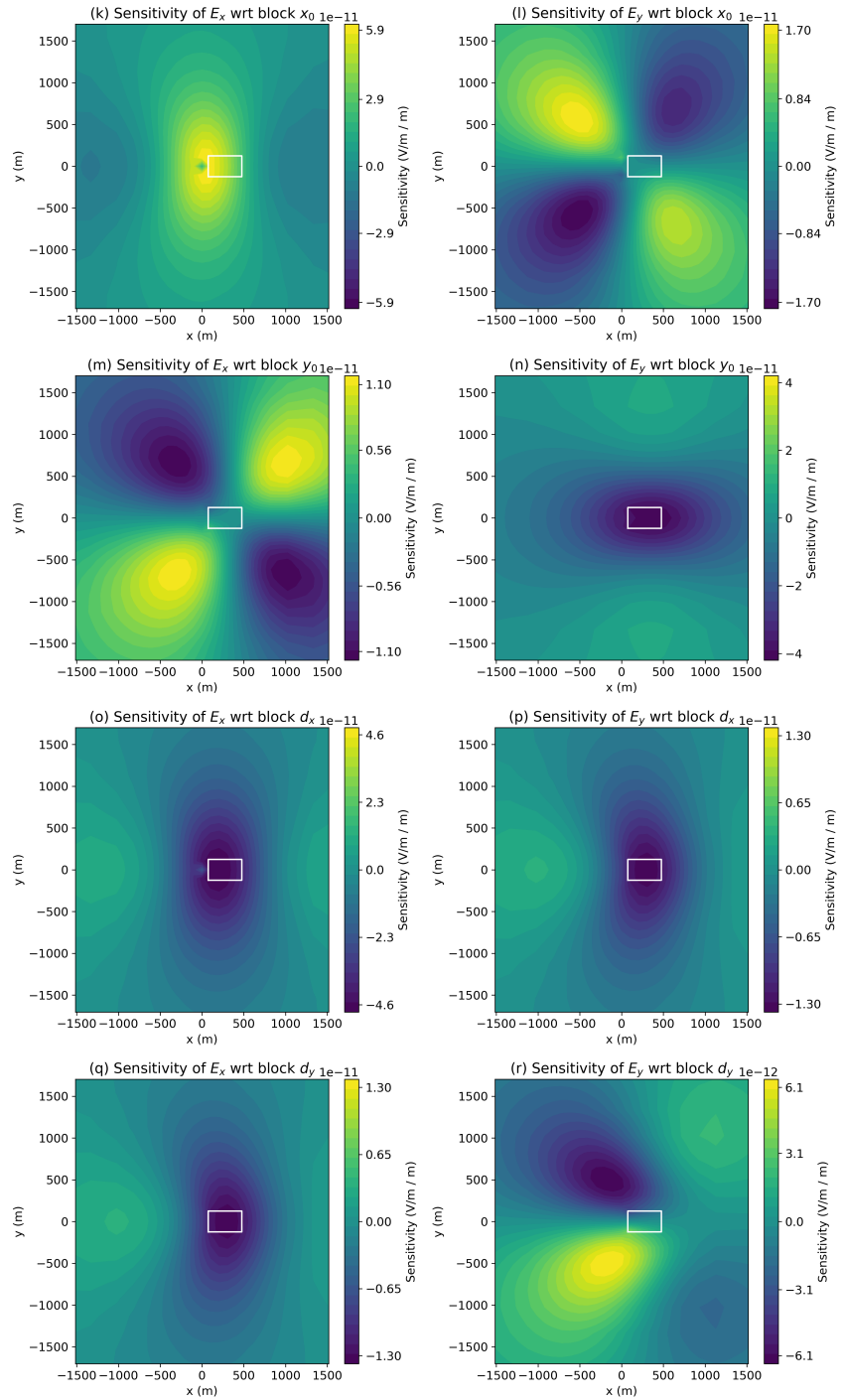


Figure D.17: Sensitivity of surface real E_x (left) and E_y (right) data with respect to the block geometry, $((V/m)/m)$

required to cause a change of 10^{-9} V/m in the data ($\Delta\mathbf{m}_i = 10^{-9}/\max|\mathbf{J}_i|$). For ease of comparison, the perturbations in the log-conductivity of the background, layer, and block were converted to linear conductivity by

$$\Delta\sigma_{\text{unit}} = \frac{\exp[\log(\sigma)_{\text{unit}} + \Delta\log(\sigma)_{\text{unit}}] - \exp[\log(\sigma)_{\text{unit}} - \Delta\log(\sigma)_{\text{unit}}]}{2}. \quad (\text{D.26})$$

In table D.1, we see that to cause a perturbation in the E_x data by $\sim 10^{-9} \text{ V/m}$, requires a 0.007% change in the conductivity of the background, while the conductivity of the block would need to change by 0.8% to have a comparable impact in the E_x data. In comparing between physical properties and geometric features of the model, we see that a change in the conductivity of the block by 0.8% has a similar impact in the E_x data as moving x_0 of the block by $\sim 16 \text{ m}$. For a change in y_0 of the block to have a comparable impact in the E_x data would require that it be perturbed by $\sim 85 \text{ m}$. However, the E_y data are more sensitive to y_0 ; a perturbation of $\sim 24 \text{ m}$, about 1/3 of that required in the E_x data, would result in a $\sim 10^{-9} \text{ V/m}$ change in the measured responses.

Examining the nature of the sensitivity with respect to parameters describing the target of interest provides insight both into how one might design a survey sensitive to the target, and how well we may be able to resolve various geometric features or physical properties in the model. For the example shown here, we see that it may be advantageous to collect data away from the well and hundreds of meters offset from the block. These are regions where both the E_x and E_y data have high sensitivity to features of the target and are distant from the steel-cased well, where we have the highest sensitivity to the background. Thus, data collected in these regions may improve our ability to resolve the target of interest. The parametric definition of the model provides a mechanism for examining how well we might expect to resolve various aspects of the target, such

as its spatial extent. There are clearly further questions that may be investigated here, including exploring survey parameters such as the impact of varying the frequency on our ability to resolve the block, or performing the same analysis for a time-domain survey. A modular framework, with accessible derivatives, is an asset for exploring these types of questions.

D.6 Conclusion

The framework we have laid out has rigorously separated out various contributions to the electromagnetic equations in both time and frequency domain. We have organized these ideas into an object oriented hierarchy that is consistent across formulations and attends to implementation details and derivatives in a modular way. The organization of the EM framework and numerical implementation are designed to reflect the math. The goal is to create composable pieces such that electromagnetic geophysical inversions and forward simulations can be explored and experimented with by researchers in a combinatorial, testable manner.

We strive to follow best practices in terms of software development including version control, documentation unit testing, and continuous integration. This work and the SIMPEG project are open-source and licensed under the permissive MIT license. We believe these practices promote transparency and reproducibility and we hope that these promote the utility of this work to the wider geophysics community.

parameter	Units of Sensitivity, \mathbf{J}_i	$\max \mathbf{J}_i $ wrt E_x	perturbation required to cause $\pm 10^{-9}V/m$ in E_x	$\max \mathbf{J}_i $ wrt E_y	perturbation required to cause $\pm 10^{-9}V/m$ in E_y
$\log(\sigma_{\text{back}})$	$(V/m)/\log(\sigma)$	1.5e-04	6.6e-08 S/m (6.6e-04%)	1.5e-04	6.6e-08 S/m (6.6e-04%)
$\log(\sigma_{\text{layer}})$	$(V/m)/\log(\sigma)$	3.5e-05	2.9e-06 S/m (2.9e-03%)	3.4e-05	2.9e-06 S/m (2.9e-03%)
$\log(\sigma_{\text{block}})$	$(V/m)/\log(\sigma)$	1.2e-07	1.7e-02 S/m (8.4e-01%)	3.3e-08	6.1e-02 S/m (3.1e+00%)
$z_0\text{layer}$	$(V/m)/m$	1.7e-10	5.8e+00 m	4.4e-11	2.3e+01 m
h_{layer}	$(V/m)/m$	1.6e-10	6.2e+00 m	4.1e-11	2.4e+01 m
$x_0\text{block}$	$(V/m)/m$	6.2e-11	1.6e+01 m	1.8e-11	5.6e+01 m
$y_0\text{block}$	$(V/m)/m$	1.2e-11	8.5e+01 m	4.2e-11	2.4e+01 m
Δx_{block}	$(V/m)/m$	4.8e-11	2.1e+01 m	1.5e-11	6.6e+01 m
Δy_{block}	$(V/m)/m$	1.4e-11	7.3e+01 m	6.5e-12	1.5e+02 m

Table D.1: Comparison of the maximum amplitude of the sensitivity with respect to each model parameter, and the approximate perturbation in that parameter required to produce a $10^{-9} V/m$ change in the measured data. The conversion from a perturbation in log-conductivity to conductivity is given by equation D.26. The perturbation in conductivity is also provided in terms of a percentage of the true model conductivity.

Appendix E

Open source practices for education

E.1 Introduction

Just as visualizing and interacting with simulation results is useful in a research context, it can be a powerful mechanism by which learners can build their understanding on concepts in geophysics. With the availability of tools such as Jupyter (Perez et al., 2015), as well as platforms like Binder (Project Jupyter et al., 2018) which provide hosting and computational resources, software developed in a research context can be readily repurposed and used in a teaching context. Much of the difference between learning in an educational context and learning in a research context is essentially whether the concepts being learned are well-established in the field, or at the edge of our knowledge. As such, a common set of tools can be used to serve both purposes.

Beyond the ability to interact with content, hosting resources on the web provides the opportunity for multiple contributors to be involved in the development, maintenance and curation of the resources. Unlike print textbooks, which are static, open-source web based resources can be continually updated as mistakes are found, new examples generated and explanations improved. Further, there are a host of tools within the open

source software ecosystem that enable interactive content, which connect computation to images and explanations, to be built.

In the GeoSci.xyz project (<https://geosci.xyz>), we have been working to take practices for open-source software development and apply them to the development of educational resources. GeoSci.xyz is a collection of collaboratively developed resources for research and education in the geosciences. To date, it includes three modules that each have “textbook” component and a collection of Jupyter-notebook apps associated with them:

- GPG: Geophysics for practicing geoscientists (<https://gpg.geosci.xyz>)
- EM: Electromagnetic geophysics (<https://em.geosci.xyz>)
- Toolkit: Geophysical toolkit for geologists (<http://toolkit.geosci.xyz>)

The GPG is targeted at the undergraduate level and provides introductory material and an overview of the physical principles governing geophysical methods including magnetics, seismic, ground penetrating radar and electromagnetics. This is used as the primary textbook in the course EOSC 350: *Environmental, Geotechnical and Exploration Geophysics I* offered at the University of British Columbia.

The EM module is an in-depth resource for electromagnetics. It covers fundamentals, starting at Maxwell’s equations, through to the suite of electromagnetic geophysical techniques (e.g. DC resistivity, Induced Polarization, Airborne Electromagnetics,). It also includes case-histories which methodically walk through an application of electromagnetics to answer a geoscientific question. In 2017, the Society of Exploration Geophysics Distinguished Instructor Short Course (SEG DISC) on *Geophysical Electromagnetics: Fundamentals and Applications* was given by Dr. Douglas Oldenburg, myself and Dr. Seogi Kang; em.geosci.xyz served as the main resource for participants.

The Toolkit is the most recent addition to the GeoSci.xyz ecosystem. This module is the result of a collaborative project between the Mineral Deposits Research Unit (MDRU) and the Geophysical Inversion Facility (GIF) at the University of British Columbia. It is intended to be a resource for geologists who are interested in incorporating geophysical data into their interpretation workflow. The main focus is on techniques for incorporating magnetic data into a geologic interpretation.

Each of the GeoSci.xyz modules bring together text, images, software, live-computation and practices from open source software development to create training and educational resources. The contents is open-source, licensed under the Creative Commons Attribution 4.0 International (CC BY 4.0) license which allows reuse and adaptation of the content. The development and maintenance of these resources follows open development practices including version control, issue tracking, and testing. Suggested edits and enhancements to the resources can be made by anyone, and all content additions or changes are peer-reviewed prior to updating each module. Source-code used to generate figures is captured with those figures; it is tested upon each update to any of the modules and accessible to users so that they can reproduce the results or change the inputs. These same codes are connected are used to generate “apps” using Jupyter notebooks and the ipywidgets package which allow users to interact with a numerical simulations through slide-bars and toggle buttons.

This appendix provides an overview of the underlying technology and some of the implications of capturing content in a modern, web-based framework that interoperates with open-source software. Section E.2 discusses the technology used to build the “textbook” component of each of the modules, including how source-code is captured to ensure figures are reproducible. Section E.3 demonstrates how Jupyter notebooks are used to make interactive content that connects live numerical simulations with widgets

and visualizations. Finally, Section E.4 discusses open development practices including peer-review, testing, and collaboration.

E.2 GeoSci.xyz Textbooks

More than two decades ago, Claerbout and Karrenbach (1992) articulated the potential for using web-technology to improve reproducibility, particularly of computational work. Since then, the open-source software ecosystem has grown significantly. As a result, there are many more high-quality tools that are freely available and interoperable with one another, simplifying the task of creating reproducible web-based content.

All of the GeoSci.xyz content is hosted and maintained on GitHub (<https://github.org/geoscixyz>). The GeoSci.xyz modules leverage a common python documentation generator, Sphinx (<http://sphinx-doc.org>), to build the websites. Each site is built and maintained as a collection of simple text-files that are compiled to the html website that users see. The pages can be edited in any text editor or directly on GitHub.

There are several Sphinx-extensions which we make use of in order to capture scientific content, including to manage bibliographies and to create plots from code. Figure E.1 shows a page on em.geosci.xyz that discusses the solution for a conductive sphere in a whole-space subject to a uniform electric field. The plot compares total and secondary electric fields for both conductive and resistive spheres. This plot is built from Python code; the text-file from which this page is built is shown in Figure E.2. Rather than storing the image file, the source- code is written into the page and compiled when the site is built. In this way, readers can always access the source code, and engaged readers can download the code, update the input parameters, run the computation, and explore the impact on the resultant image. In terms of maintenance, if errors are found in the computation or mistakes in labels or annotations of the figure, the source code can be

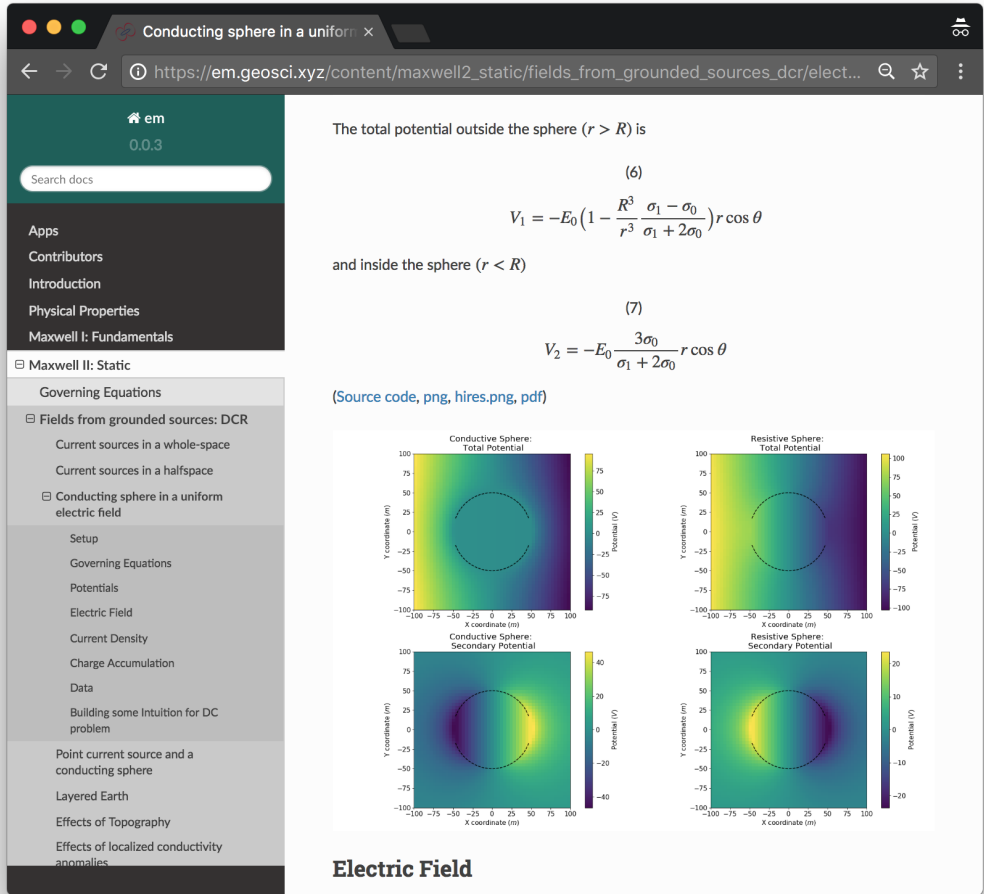


Figure E.1: Web-page on a conducting sphere in a uniform electric field (https://em.geosci.xyz/content/maxwell2_static/fields_from_grounded_sources_dcr/electrostatic_sphere.html). The plot shown on this page is compiled from Python code and can be downloaded and run by users, or update by maintainers if there are improvements that can be made.

altered and the figure rebuilt.

Simple sites, without intensive computation can be hosted on the free documentation hosting service ReadTheDocs (<https://readthedocs.org>). Several of the examples on the GeoSci.xyz sites involve simulations of Maxwell's equations, and have thus exceeded

The screenshot shows a GitHub repository page for 'geoscixyz / em'. The current file is 'electrostatic_sphere.rst'. The code editor displays a Python script with several code blocks. Lines 134 through 153 are highlighted in red, indicating they are part of a plot directive. The code uses the 'em_examples' module to import 'sphereElectrostatic_example' as 'electrostatic_sphere'. It defines parameters like conductivity values (sig0, sig1, sig2), radius (R), field strength (E0), and discretization levels (n, dx, dy, dz). It then creates a 3D grid (XYZ) and plots the total potential (ax[0]).

```

129 ... math::
130     V_2 = -E_0 \frac{3\sigma_0}{(\sigma_1+2\sigma_0)r} \cos\theta
131     :label: totalP_inside
132
133
134 ... plot::
135
136     from em_examples import sphereElectrostatic_example as electrostatic_sphere
137
138     sig0 = 10.**-3. # conductivity of the whole-space in S/m
139     sig1 = 10.**-1. # conductivity of the sphere in S/m
140     sig2 = 10.**-5. # conductivity of the sphere in S/m
141     R = 50. # radius of the sphere in m
142     E0 = 1. # inducing field strength in V/m
143     n = 50 # level of discretization
144     xr = np.linspace(-2.*R, 2.*R, n) # X-axis discretization
145     yr = xr.copy() # Y-axis discretization
146     dx = xr[1]-xr[0] # mesh spacing
147     dy = yr[1]-yr[0] # mesh spacing
148     dz = np_r_[0] # identical to saying `zr = np.array([0])`
149     XYZ = electrostatic_sphere.ndgrid(xr, yr, zr) # Space Definition
150
151     fig, ax = plt.subplots(2, 2, figsize=(18, 12))
152     ax = electrostatic_sphere.mkvc(ax)
153     ax[0] = electrostatic_sphere.Plot_Total_Potential(XYZ, sig0, sig1, R, E0, ax[0])

```

Figure E.2: Text source from which the web-page shown in Figure E.1 is built.
The code used to build the plot starts under the plot-directive on line 134.

the resource limits on ReadTheDocs, so instead we build the modules on a continuous integration service and deploy to a Google App Engine website.

E.3 Interactive content

Static figures can be made dynamic and interactive by connecting them with a live computational environment. The Jupyter Notebook combines text, images, lines of code, outputs and interactive widgets into a single “computational narrative” (Perez et al., 2015). Much of the research conducted in this thesis relied on Jupyter Notebooks and

benefited from the iterative workflow it supports as well as the widget architecture that allows computation to be connected to visualization through slide-bars and toggle buttons. Millions of researchers, data analysts, and journalists have adopted the Jupyter notebook (or similar computational notebooks) as a tool for authoring computational workflows and analyses (Rule et al., 2018).

The ability to include narrative text to document a workflow, visualize results inline, and conduct iterative analyses are all reasons that the Jupyter Notebook is a valuable research tool. For many of the same reasons, it is a powerful medium for developing and delivering educational content. Text which provides instructions or prompts questions to guide a learner can be included in the Notebook and provide context for the “app” or simulation tool. Depending on the purpose of the exercise, lines of code can be displayed, for example if the aim of the exercise is to walk through how to discretize the DC resistivity problem. Alternatively, if the physics is the central focus, the code can be abstracted-away, and the learner provided with widgets to run a simulation (see Figure E.3).

To date, there are 17 Notebooks associated with the GPG, > 30 with the EM module, and 10 for the Toolkit. We provide instructions for downloading the Notebooks and setting up the necessary software environment to run them. However, many of the learners we are working to reach are not necessarily familiar with setting up a software environment or launching applications from the command-line, and so these steps present a significant overhead. To overcome this barrier, we use Binder (<http://mybinder.org>, Project Jupyter et al. (2018)), which is a web-service that provides cloud-based hosting of Jupyter notebooks. As notebook authors, we provide the set of dependencies required to run the notebooks, and these are automatically installed when the user follows the Binder-url to the notebooks. The user is then served the Notebook in a live computa-

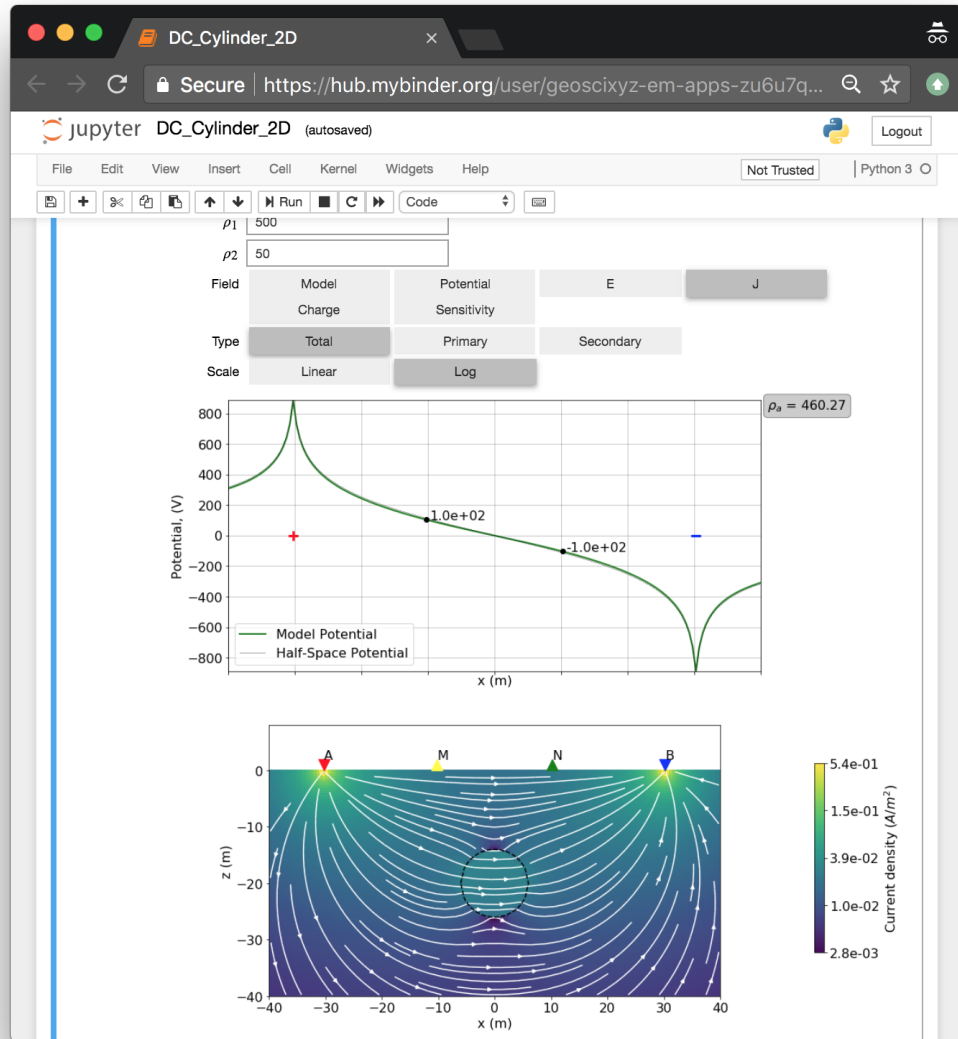


Figure E.3: A sample Jupyter notebook “app” that simulates a DC resistivity over a halfspace with a cylinder. The widgets control the visualization. The user can change the model parameters (e.g. the resistivity of the cylinder and of the background), the survey geometry, and select the visualization (e.g. electric field, currents, charges, etc.)

tional environment that is accessed from their web-browser. Using services like Binder means that learners do not need to open a command-prompt nor do they need to be familiar with how to manage a software environment. The focus then, can remain on the content.

Using Jupyter Notebooks as the medium for authoring educational content has the added benefit that many researchers and graduate students are already familiar with Notebooks. The simulation tools and tutorials are built on research code such as SimPEG, that are already a part of many of the contributors research toolbox. This removes the need for contributors to learn a new set of tools for the sole purpose of sharing educational content. In the long-run, we hope that by bringing research codes into education, engaged learners then have a trajectory to move beyond using the “apps” for learning a concept in geophysics and can further explore the computational steps taken to run those same simulations.

E.4 Open development

Best practices in open-source software development have enabled the growth and maintenance of software tools for that support large communities of researchers (e.g. Astropy in astronomy (Astropy Collaboration et al., 2013), SciPy in scientific computing Oliphant (2007)). In many of these projects, it is a handful of “core developers” who are responsible for generating the majority of the software, but each benefits from the minor enhancements, bug-fixes, and additions made by the “long tail” of contributors. In contrast, most educational resources are authored and maintained by a individual instructors. There is minimal opportunity for feedback or improvements to be made by others in a scalable way. Seeing the success of the open-source software ecosystem, we have sought to adopt many of the same practices in the hopes of fostering a commu-

nity of educators and learners around open-source educational material. This section outlines some of those practices.

Modern version control using git and GitHub (or similar) is an essential tool for allowing multiple contributors to productively work on different aspects of a project and have their improvements incorporated back into the main project. New content or edits on existing content incorporated into the module through a pull-request process. A pull-request shows a comparison between the main version of the module and the version containing the suggested changes and provides the opportunity for peer-review. Suggested changes to any of the GeoSci.xyz modules are peer-reviewed on GitHub prior to being merged into the main version of the module. Each web-page in the GeoSci.xyz textbooks has an “edit on GitHub” button that allows anyone to edit the current page and submit a pull request for their edits to be included in the live-site.

Issue trackers are used in software projects to notify developers of bugs that are found in the software and to keep track of the progress of a bug-fix, or similarly, to submit and track feature requests. The same concepts can be applied to the development of educational content. For example, some mathematical typos are subtle and require discussion to sort-out; prior to suggesting an edit, a contributor might create an issue to prompt that discussion.

When multiple contributors are working on a single code-base, testing is important to ensure that changes do not break existing functionality. For the GeoSci.xyz textbook-modules, we test that the website compiles. This ensures that no syntax errors have been introduced into the text and that the code used to build the figures runs without error. We also test that all of the external links that the site points to for additional resources are valid. If, for some reason, a web-page that we were referencing is taken-down, the testing provides an alert and we can find a new resource or remove the broken link. All

of the associated Jupyter notebooks are also tested. These tests execute all of the code in each of the notebooks and alert us if any errors are raised. Each of the GeoSci.xyz modules is tested on a monthly basis using TraviCI (<https://travis-ci.org/>), a continuous integration and testing service that is free for open source projects. This ensures that the website continues to compile and provides alerts if there have been changes in upstream software dependencies that cause any computations included in the resource to fail.

In addition to the practices state above, there are also best practices that can be learned from a well-architected code-base. Aspects of a well-designed code-base include modularity and the use of inheritance to promote a consistent structure across the project. If a software package is well-structured and well-organized, it becomes easier to invite contributors as it is evident where their contribution fits into the project. The case-histories in em.geosci.xyz are one place where we have used the concept of inheritance, in which a base-class provides the outline or template of the content, to provide structure. Each case history is structured in seven steps, as shown in Figure E.4. As a contributor, this is a well-structured template that can be followed and filled-in. As a learner, this structure provides consistency across content that is contributed by multiple authors and a framework in which to organize concepts.

E.5 Conclusions and outlook

Applied geophysics is a relatively small community. There are not many methods-oriented textbooks or resources available. As a result there is significant duplication of efforts as many educators develop their own set of resources, often in isolation. Even if these resources are captured and made available in the form of a textbook, the content rapidly becomes out-of-date as instrumentation and data analyses techniques continually improve. An open-source approach to the development of software has enabled

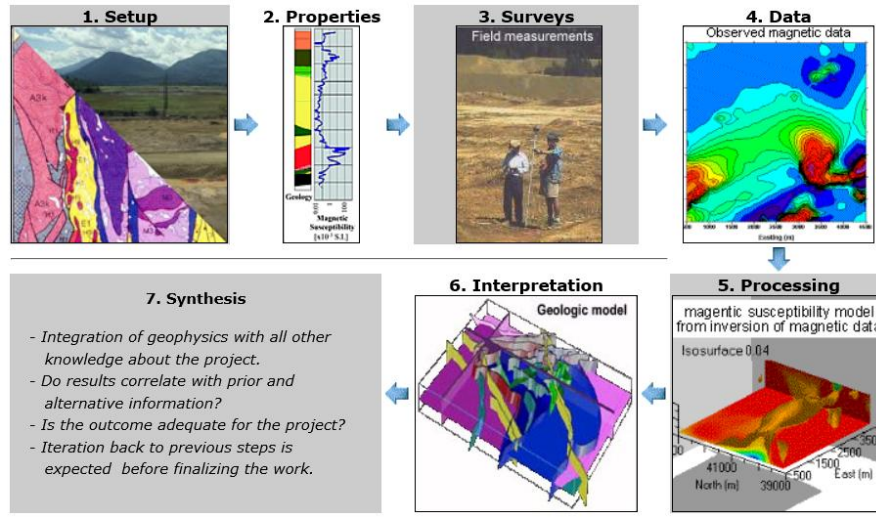


Figure E.4: Seven step framework used for the case histories in <https://em.geosci.xyz>. (1) Setup: describe the geoscientific question and objectives that are to be addressed. (2) Properties: identify the diagnostic physical properties (e.g. density, electrical conductivity, magnetic susceptibility, etc.). (3) Survey: design a survey that is suitable for detecting the physical property contrasts relevant to the application. (4) Data: carry out the field survey and collect the data set(s). (5) Processing: plot the data and apply the analysis steps needed to interpret the data (e.g. invert the data). (6) Interpretation: interpret the results in terms of the identified physical properties and original geoscience objective. (7) Synthesis: integrate the interpretation with geologic and other information relevant to the application in order to address the original geoscience objective. This image and caption are adapted from: https://em.geosci.xyz/content/geophysical_surveys/fundamentals/seven_steps.html

widespread collaboration on the tools that support communities of researchers. Our hope is that an open-source approach to the development of educational resources can catalyze a similar community in the geosciences.